Ln(III) Metallacrown Complexes: Novel Systems and Single-Molecule Magnet (SMM) Properties

Dissertation

A Dissertation Submitted to the Department of Chemistry, Pharmacy and Earth Sciences Based on the Requirements for the Degree of Doctor of Science in Chemistry

by

Angeliki Athanasopoulou

Born in Karditsa, Greece

Mainz, 2019

Dedicated to my parents who have always supported and encouraged me regardless any geographical distance.

Αφιερωμένο στους γονείς μου, οι οποίοι πάντα και παντού είναι δίπλα μου.

Acknowledgements

‘Ithaka’

As you set out for Ithaka
hope your road is a long one,
full of adventure, full of discovery.
Laistrygonians, Cyclops,
angry Poseidon—don’t be afraid of them:
you’ll never find things like that on your way
as long as you keep your thoughts raised high,
as long as a rare excitement
stirs your spirit and your body.
Laistrygonians, Cyclops,
wild Poseidon—you won’t encounter them
unless you bring them along inside your soul,
unless your soul sets them up in front of you.

Hope your road is a long one.
May there be many summer mornings when,
with what pleasure, what joy,
you enter harbors you’re seeing for the first time;
may you stop at Phoenician trading stations
to buy fine things,
mother of pearl and coral, amber and ebony,
sensual perfume of every kind—
as many sensual perfumes as you can;
and may you visit many Egyptian cities
to learn and go on learning from their scholars.

Keep Ithaka always in your mind.
Arriving there is what you’re destined for.
But don’t hurry the journey at all.
Better if it lasts for years,
so you’re old by the time you reach the island,
wealthy with all you’ve gained on the way,

not expecting Ithaka to make you rich.

Ithaka gave you the marvelous journey.
Without her you wouldn't have set out.
She has nothing left to give you now.

And if you find her poor, Ithaka won’t have fooled you.
Wise as you will have become, so full of experience,
you’ll have understood by then what these Ithakas mean.

By Constantinos P. Kavafis

(Translated by Edmund Keeley)

Declaration

Erklärung

Die vorliegende Arbeit wurde in der Zeit von März 2016 bis Juni 2019 unter Anleitung von [redacted] im Institute für Anorganische und Analytische Chemie der Johannes Gutenberg-Universität, Mainz angefertigt.

Ich erkläre hiermit, dass ich die vorliegende Arbeit selbstständig und ohne fremde Hilfe verfasst habe. Alle verwendeten Quellen und Hilfsmittel sind vollständig angegeben.

---------- ----------

Datum und Ort Angeliki Athanasopoulou

Dekan: [redacted]

Erster Berichterstatter: [redacted]

Zweiter Berichterstatter: [redacted]

Prüfer: [redacted]

Abstract

This Thesis deals with the synthesis and characterization of new Ga/Ln and 3d/Ln 12-Metallacrown-4 complexes, using salicylhydroxamic acid ($shaH_2$) as a bridging-chelating organic ligand. After establishing a successful way for the synthesis of the aforementioned complexes, magnetic studies took place and evaluation of the magnetic data are presented. The results that are presented in Chapter 2 and 3 are already published, while the work presented in Chapter 4 has been submitted for publication. Chapter 5 includes a bank of unpublished results which have been examined and reported.

In Chapter 1 an introduction into the topic of Metallacrowns and Single-molecule magnets (SMMs) is provided. Metallacrowns is a special family of complexes that our group finds great interest in since these molecules can retain their integrity in solution, they are easily modified according to our synthetic demands and needs as well as they can be used as excellent candidates at various applications such as molecular recognition, surface applications, etc. As such, the present Thesis has focused on the synthesis of these molecules with a strong interest into their magnetic properties.

Chapter 2 deals with the synthesis and magnetic characterization of a new family of 12-MC-4 complexes, namely $({}^{t}Bu_4N)\{[Ln^{III}(O_2CBu^{t})_4][12\text{-}MC\text{-}_{Mn(III)N(shi)}\text{-}4]\}\bullet 5CH_2Cl_2$ (Ln = Gd (**1**) and Tb (**2**)) and $({}^{t}Bu_4N)_2\{[Y^{III}(O_2CBu^{t})_4][12\text{-}MC\text{-}_{Mn(III)N(shi)}\text{-}4]\}(ClO_4)$ (**3**). These compounds have been structurally and magnetically investigated, while the magnetic exchange interactions within the 12-MC-4 ring as well as the Mn(III)-Gd(III) exchange interaction (J) have been presented and evaluated. The members of this family of complexes do not show any alternating-current (ac) magnetic susceptibility signals, meaning that our complexes do not behave as SMMS.

Chapter 3 involves the isolation and characterization of a new family of isostructural $\{Fe_6Ln\}$ complexes, $(pipH)_3\{Fe_6Ln(shiH)_3(shi)_6\}\cdot 1.5\ pip\cdot xH_2O$ (Ln = Gd (**1**), Dy (**2**), Tb (**3**) and Y (**4**), pip = piperidine, and shi^{3-} = salicylhydroxamic acid). This family of compounds possesses a unique structural metallacrown-like motif, while they also resemble the structure of metallacrypates. Magnetic studies have been performed and they demonstrated that the $\{Fe_6Dy\}$ analogue shows frequency-dependent ac signals. Thus the Dy-analogue belongs to the SMM family.

Chapter 4 focuses on the synthesis and magnetic characterization of the first Ga/Dy double-decker or sandwich 12-MC-4 complex ever to be reported. The compound possesses a general formula of ($^{t}Bu_4N$) [$Ga^{III}_8Dy^{III}(OH)_4(shi)_8$] (**1**) and its structural features have been also highlighted and analyzed. This is the first report of a pure Ga/Ln double-decker 12-MC-4 system to be presented while at the same time the complex does show interest SMM behavior with an anisotropy barrier U_{eff} = 40 K.

Finally Chapter 5 includes unpublished results that have been synthesized and characterized. Six new compounds are presented, five of which are Ga/Ln-based complexes, whilst a Fe/Ln compound is also introduced. All complexes have been structurally analyzed and some of them have been found to possess interesting magnetic properties. Detailed discussion concerning the importance of the used starting materials in inorganic synthesis is also provided and will be presented thoroughly throughout this chapter.

Table of Contents

List of Abbreviations

SMMs	Single-molecule Magnets
SIMs	Single-ion Magnets
{$Mn_{12}Ac$}	$[Mn_{12}O_{12}(O_2CMe)_{16}(H_2O)_4]$
dc	direct-current
ac	alternating-current
T_B	blocking temperature
U_{eff}	effective energy barrier of magnetization reversal
S	spin ground state
D	axial zero-field splitting parameter
E	transverse or rhombic zero-field parameter
m_s	magnetic microstates
QTM	quantum tunneling of magnetization
M	magnetization
H	field
MCs	Metallacrowns
ω	angular frequency
ν	ordinary frequency
χ	dynamic susceptibility
χ'	in-phase dynamic susceptibility
χ''	out-of-phase dynamic susceptibility
K_B	Boltzmann constant
T	temperature
μ_B	Bohr magneton
Pc	phthalocyanine ligand
Bu_4N^+	tertbutyl ammonium cation

J	spin-orbit quantum number
Ln	lanthanides
K	Kelvin
cm^{-1}	wavenumber
Oe	Oersted
s	second
3d	transition metal ions
4f	lanthanide ions
$shiH_3$	salicylhydroxamic acid
H_2picHA	picoline hydroxamic acid
$H_2quinHA$	quinoline hydroxamic acid
OAc^-	acetate anions
DMF	dimethylsulfoxide
NH_4^+	ammonium cation
DFT	Density Functional Theory
SQUID	Superconductive Quantum Interface Device

Chapter 1 Introduction

1.1 Single-molecule Magnets (SMMs)

At the beginning of the 1990s, a new phenomenon made its appearance within the class of Natural Sciences bringing, at that point, a big change in the field of Chemistry and Physics. It was the early 1990s when the revelation, that a single molecule could retain its magnetization at low temperatures (at liquid helium temperatures) even in the absence of an external magnetic field, was made and that contributed to the birth and growth of the field of Molecular Magnetism.[1,2] From that time onwards the field of the so-called Single-molecule Magnets (SMMs) started flourishing.

Single-molecule Magnets (SMMs) are magnetically bistable complexes, which show slow relaxation of magnetization even in the absence of an external magnetic field and they are able to retain this magnetization as long as it is kept below a characteristic blocking temperature (T_B).[3] The first molecule, in which this phenomenon was observed, was the well-known $[Mn^{III}_8Mn^{IV}_4O_{12}(O_2CMe)_{16}(H_2O)_4]$ or $Mn_{12}Ac$ cluster, which was in turn the first Single-molecule Magnet to be investigated and extensively studied. These molecules, nowadays, are considered excellent candidates for various novel technological applications such as high density storage data or as segments of spintronic devices or as quantum bits for quantum computation applications and others.[4–8]

SMMs can display hysteresis loops in diagrams of magnetization (M) versus field (H) at temperatures that correspond to the blocking temperature (T_B), which is the highest temperature in which an SMM can exhibit hysteresis loops. Under these conditions, an SMM can retain its magnetization for a broad amount of time, as long as the magnetization of the molecule is held below the blocking temperature.[3] The first investigations considering this Single-molecule Magnetism behaviour, had focused solely on the use of transition metal ions (3*d* metals). In 3d-SMMs the magnitude of the energy barrier, U_{eff}, for the magnetization reversal or else anisotropy barrier, is dependent on the blocking temperature. This magnitude is equal to $S^2|D|$ for integer spin systems or $(S^2\text{-}1/4)|D|$ for half-integer spin systems. From these equations it becomes clear that the two most important parameters that block the magnetization reversal are the total spin moment of the molecule, *S* and the Ising-type or easy axis magnetic anisotropy (anisotropy along the z axis), which can be manifested by the axial zero-field splitting parameter (ZFS), *D*.

At zero field, the projection of the total spin produces [2S +1] m_s microstates which are in turn split and when D < 0, the $m_s = \pm S$ lie lowest in energy. Flipping of the spin from the $m_s = +S$ to the $m_s = -S$ leads to relaxation of magnetization which occurs over the barrier, following the thermally-assisted process up to the point where a thermal equilibrium is reached, always by increments of 1 ($m_s = \pm 1$). Besides the thermal relaxation process, there is another process that can take place between two degenerate m_s microstates and this is the resonant quantum tunneling of magnetization (QTM). This phenomenon can be experimentally observed via the characteristic steps in the *M* vs *H* hysteresis diagrams and it is only possible when two microstates have the same energy.

The famous $Mn_{12}Ac$ compound, which was extensively investigated over the years, was found to have a U_{eff} = 51 cm^{-1}, deriving from a combination of *S* = 10 and *D* = -0.51 cm^{-1} (Figure 1.1.1).

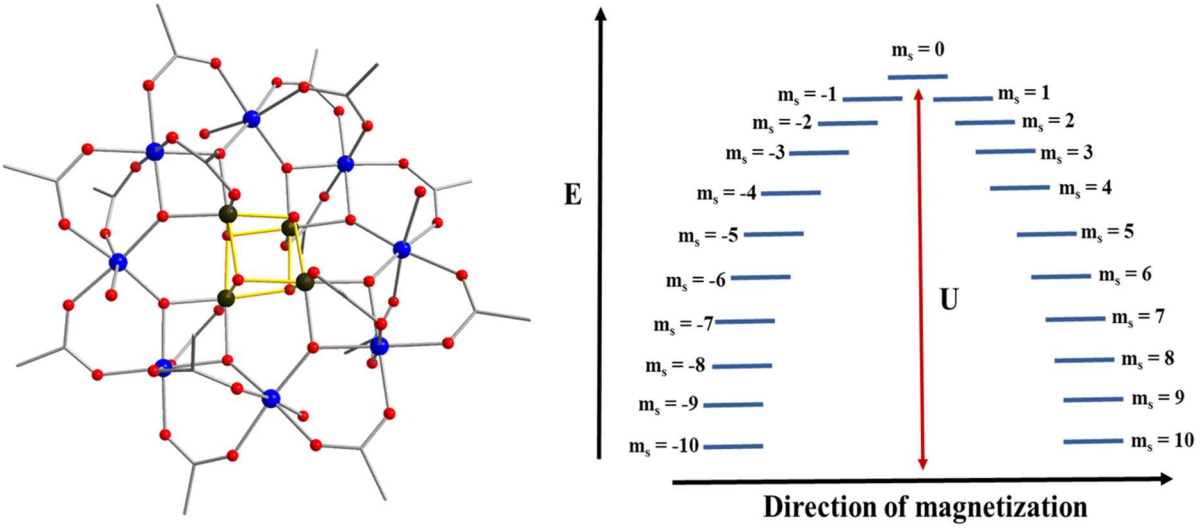

Figure 1.1.1 (left) Schematic representation of $Mn_{12}Ac$. Color scheme: Mn^{III}, blue; Mn^{IV}, olive green; O, red; N, blue; C, grey. H atoms are omitted for clarity. (right) Energy diagram of the $Mn_{12}Ac$ SMM with *S* = 10.

An important technique, which is used for the investigation of the SMM behaviour is the magnetization (*M*) vs field (*H*) measurements due to the fact that a single-molecule magnet shows hysteresis loops (Figure 1.1.3).

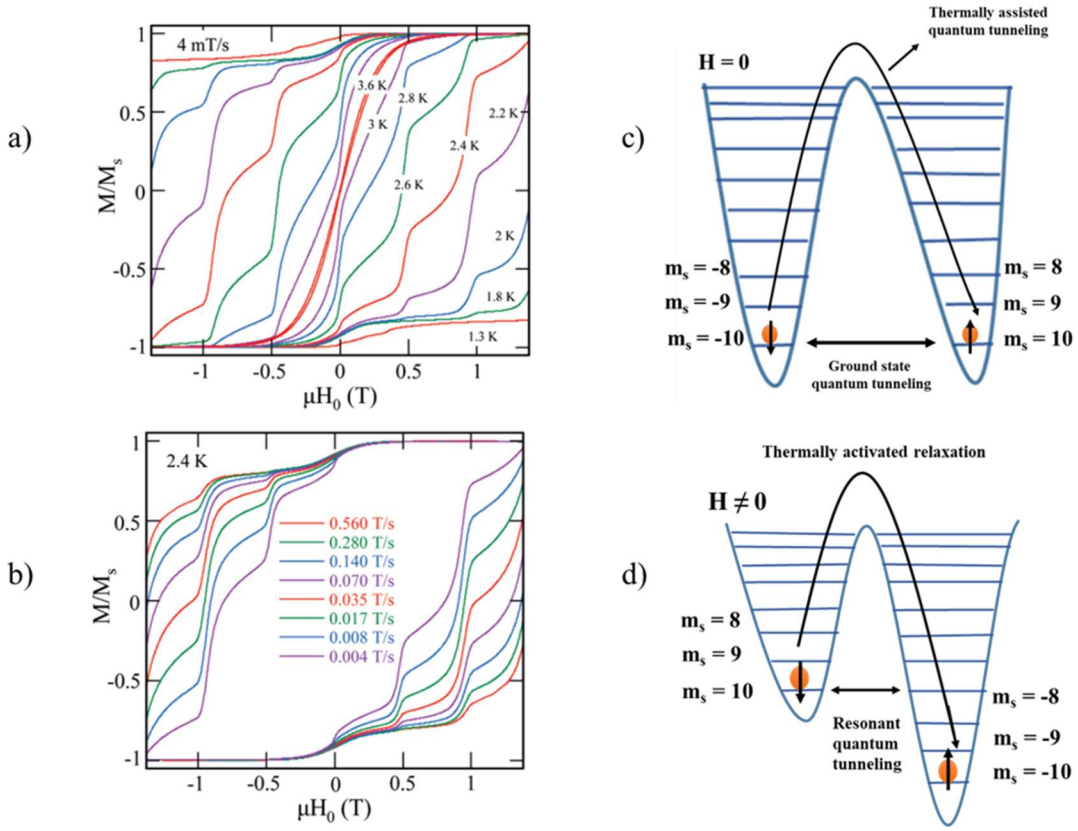

Figure 1.1.3: a) Magnetization hysteresis loops of a single crystal of $Mn_{12}Ac$ in a fixed scan rate of 4mT/s showing the temperature dependence and b) hysteresis loops of a single $Mn_{12}Ac$ crystal showing the sweep rate dependence at a fixed temperature of 2.4 K[9], c) double-well (energy) potential diagram of an $S = 10$ spin ground state at the absence of an external magnetic field and d) double-well (energy) potential diagram of an $S = 10$ spin ground state at the presence of an external magnetic field. Reproduced from Ref. 13 with permission from American Chemical Society (ACS).

As mentioned before, the steps that appear in the hysteresis loops diagram are due to the quantum tunneling of magnetization (QTM) and it is important to be noted that QTM is a quantum property of molecular magnetic systems. This phenomenon appears due to the presence of rhombic or transverse anisotropy (*E*) which leads to superposition of the magnetic states of the barrier with a tunneling splitting. The rhombic or transverse anisotropy (*E*) along with some other Zeeman terms, mixes the m_s microstates while the axial anisotropy (*D*) separates the m_s levels. The bigger the rhombic anisotropy, the bigger the mixing of the m_s

microstates and that leads to higher possibilities of quantum tunneling and magnetization in turn relaxes with really fast rates. For that reason, scientists thought about applying an external direct-current (*dc*) field in order to intervene into the energies of the microstates and change or modify them. Since QTM is allowed only between states that have the same energy, the application of the external dc field undoubtedly improves the magnetization relaxation as it changes the energies of the microstates and thus QTM is not easy to occur from the lowest in energy states or else from the ground state (ground state quantum tunneling). Thus, QTM can only occur at specific points when the field is swept and therefore we have the appearance of the steps in the hysteresis loops. The temperature and the sweep rate of the field are two very important parameters since the hysteresis loops that SMMs often possess are highly dependent on these two factors, with the coercivity of the loops increasing with decreasing temperature and decreasing with increasing sweep rates.

Experimentally the Single-molecule Magnet behaviour can be also detected and quantitatively examined with the use of alternating-current (*ac*) magnetic susceptibility studies. The dynamic susceptibility or else magnetic dynamics of a sample, can be probed by *ac* measurements via the employment of an oscillating magnetic field (equation 1.1.1). The dynamic susceptibility, χ, consists of two components that are dependent on the ω parameter which stands for the angular frequency of the *ac* field and is usually converted to $2\pi\nu$ units, where ν is the ordinary frequency. As it can be seen in equation 1.1.1, frequency dependent χ is a quantity with a real (dispersion) and an imaginary (absorption) counterpart.[10]

$$\chi(\omega) = \chi'(\omega) - i\chi''(\omega) \qquad \text{(Eq 1.1.1)}$$

For the thermally activated region, the relaxation of magnetization complies with the Arrhenius law since this is also a kinetic process, according to the equation 1.1.2:

$$\tau = \tau_0 \exp(U_{eff}/k_B T) \qquad \text{(Eq 1.1.2)}$$

where τ is the relaxation time, τ_0 is the pre-exponential factor or else the relaxation rate between attempts of thermal excitations over the energy barrier, k_B is the Boltzmann constant, T is the temperature and U_{eff} is the effective energy barrier of magnetization. By constructing then a plot of $\ln(\tau)$ vs 1/T, the effective energy barrier U_{eff} can be precisely calculated from the slope of the Arrhenius diagram.[11,12] In general lines, the in-phase susceptibility (χ) decreases as the *ac* frequency reaches the relaxation rate of the molecules and in turn, the out-of-phase counterpart will increase. When there is a single relaxation process in SMMs, a peak maxima

can be observed in a χ'' vs T plot, which shifts to higher temperatures[1,2,13] at the time the *ac* frequency increases (Figure 1.1.2).

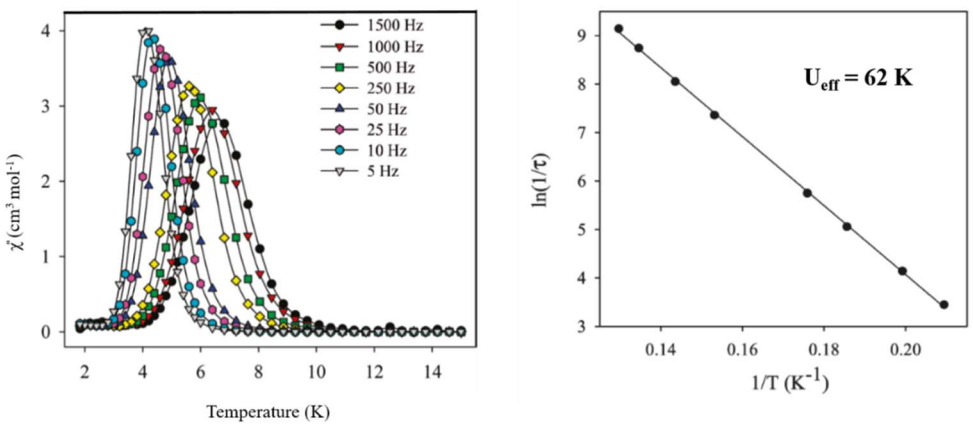

Figure 1.1.2 (left) Out-of-phase *ac* signals of $Mn_{12}Ac$ at various frequencies and (right) Arrhenius plot which derives from the peak maxima and their given temperatures, following the equation $\ln\tau = \ln\tau_0 + U_{eff}/k_BT$. Reproduced from Ref. 13 with permission from American Chemical Society (ACS).

For many years after the discovery of the $Mn_{12}Ac$ single-molecule magnet, the scientific community had turned its interest and had intensified its efforts towards the isolation of new polynuclear transition metal (3*d*) complexes, having as an ultimate goal the achievement of large U_{eff} values. The logic behind this was based on the idea that the accumulation of larger U_{eff} values would assist also with the maximization of the relaxation time of the resulting compound. That's the reason the main focus of synthetic chemists the years that followed until recently, was the maximization of the spin ground state (sum of the spins of the molecule), which would help with the promotion of the higher U_{eff} values based on the equations explained above in the text. This technique was determined to be widely debatable later on and we will focus on that at the next chapters.[14] Nevertheless, many beautiful 3*d* polynuclear compounds were synthesized, characterized and found to belong to the SMM family.[15–19]

One of the first and most studied molecular complexes with SMM behavior is the $[Fe^{III}_8O_2(OH)_{12}(tacn)_6]\cdot Br_7(H_2O)\cdot Br\cdot 8H_2O$ or else, as commonly known, the $\{Fe_8\}$ cluster, where tacn = 1,4,7-triazacyclonane (Figure 1.1.4).[15,16] The complex consists of eight high spin Fe^{III} centers (S = 5/2) and upon performing temperature dependant magnetic susceptibility studies ($\chi_M T$ vs T), is was highly suggested that the spin ground state of the system is $S = 10$,

which results when six spins are up and two spins are down. In the case of {Fe_8} it can be easily observed that the structural topology of the compound contains several triangular units which lead to spin frustration effects.[20]

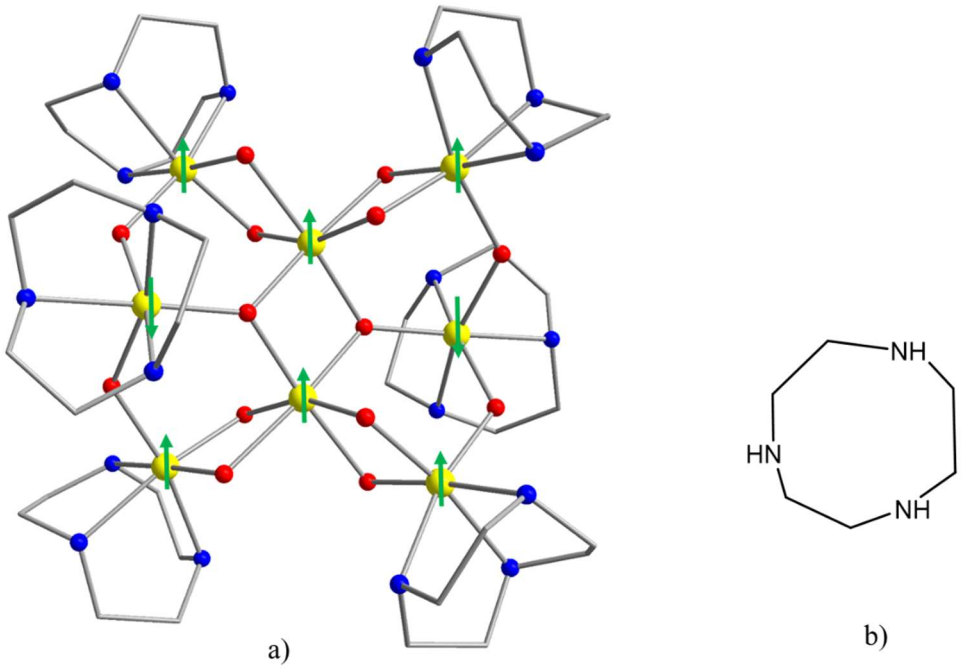

Figure 1.1.4: a) Schematic representation of molecular structure of $[Fe^{III}_8O_2(OH)_{12}(tacn)_6]^{8+}$. Color scheme: Fe^{III}, yellow; O, red; N, blue; C, grey. H atoms are omitted for clarity. Green arrows represent spin carriers and their arrangement within the complex according to magnetostructural correlations.[15] b) Schematic representation of tacn or 1, 4,7-triazacyclononane.

Since there are several triangles within the exchange pathway units linking the Fe(III) centers, frustration effects[21] appear meaning that the ground state cannot be properly characterized by assigning the spin vectors up and down. However, researchers after performing polarised neutron scattering techniques were able to gain a picture of the spin density which allowed them to observe that the spin density on Fe3 and Fe4 is negative, while in all other Fe(III) centers is positive. These data were an extra confirmation of the temperature dependence magnetic susceptibity ($\chi_M T$ vs T) and magnetization data (Figure 1.1.5) which indicated an $S = 10$ spin ground state as well.

The SMM behavior of the {Fe_8} was also extensively investigated over the years and from magnetic hysteresis measurements the temperature and field sweep rate dependence was undoubtedly visible (Figure 1.1.6).[22] During the measurement the field was swept in the easy axis direction of magnetization and from the graph we can clearly observe the appearance of steps in the hysteresis loops, which correspond to tunneling processes that take place under these specific conditions. More specifically, magnetization tunnels very fast at these particular field values and the height of the steps are evidently changing when a constant transverse field is applied as it can be distinctly observed at Figure 1.1.6.

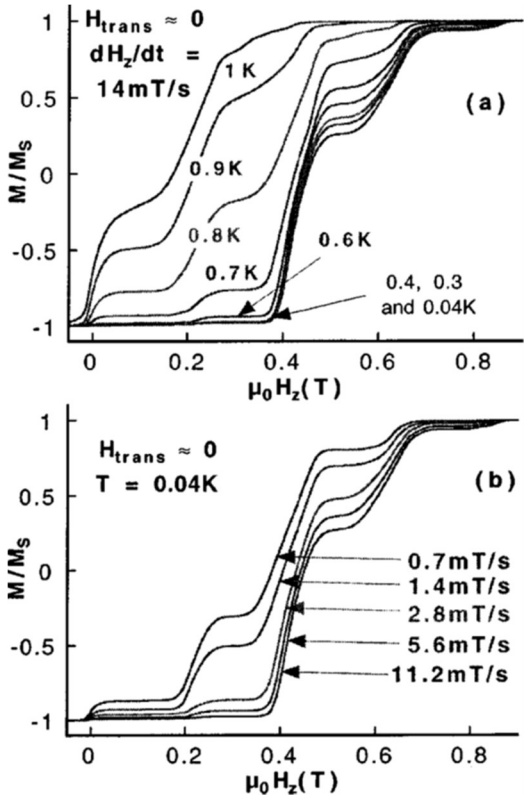

Figure 1.1.6: Hysteresis loops diagrams showing a) the temperature and b) field sweep rate dependence of magnetization of the {Fe_8} compound. Reproduced from Ref. 22 with permission from American Institute of Physics (AIP).

Evidently, the discovery of the single-molecule magnet (SMM) phenomenon brought a new insight into molecular nanoscience and molecular electronics. Since 1993 and until now the field is constantly progressing and new developments come to surface. It is undeniable that the field of Chemistry has emerged with the field of Physics, in the sense that Molecular Magnetism requires the strong collaboration between both these sectors of science and that has undoubtedly led to major breakthroughs, some of which will be later discussed.

1.2 Lanthanide-based Single-Molecule Magnets (SMMs)

For many years after the discovery of {Mn_{12}}, researchers were trying to isolate and magnetically characterize polynuclear 3*d*-metal complexes, which could potentially possess SMM properties. It was not before 2003 though, that a new breakthrough paper was published and from that time onwards started shaping a new era concerning the requirements of SMM design. In 2003 Ishikawa *et al.*, found out that a bis(phthalocyaninato) terbium double-decker complex $[Pc_2Tb]^{-\cdot}(Bu_4N)^+$, (where $Bu_4N^+ = [N(C_4H_9)_4]^+$) could function as a magnet at molecular level (Figure 1.2.1)[23]. In this case the origin of the magnetic behavior was determined to be deriving from both the spin and angular momenta of a single lanthanide ion, when subjected into a ligand field which stabilizes at the lowest sublevels a large $|J_z|$ value.

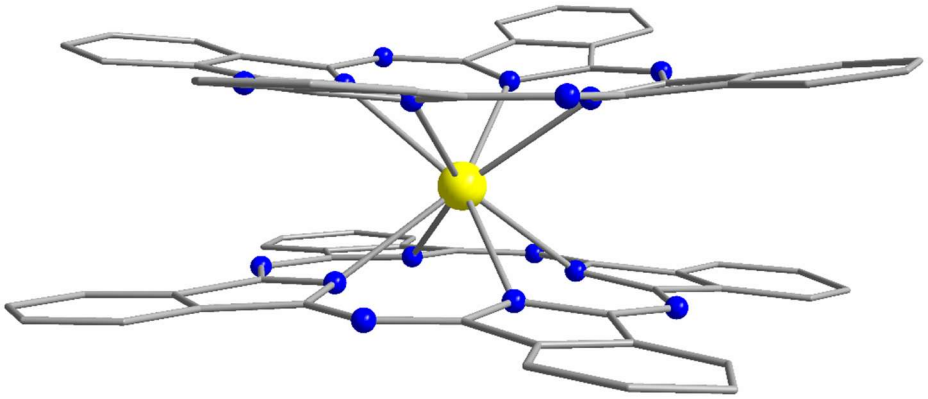

Figure 1.2.1: Schematic representation of molecular structure of $[Pc_2Tb](TBA)$. Color scheme: Tb: yellow; N: blue; C:grey.

As mentioned in the first chapter the ground state bistability, which is essential for securing the relaxation of magnetization, in 3*d* SMMs is generated from the total spin *S* and the ensuing [2*S* + 1] m_s microstates. In the case of Ln-SMMs now, the ground state bistability arises from the [2*J* + 1] m_j microstates within the spin-orbit coupled ground term $^{2S+1}L_J$. This is a feature that places lanthanides into a unique category since for most lanthanides the orbital contribution to the magnetic moment is large and cannot be easily quenched. Therefore, effects of ligand field in lanthanide compounds can be considered small but nevertheless still an important

perturbation.[24,25] The second parameter which secures and promotes the SMM behavior in lanthanides (even though is not a rigid requirement) is that the lowest in energy state or else ground state should preferably have a large m_j value, which would in turn secure a considerable magnetic moment. Based on that, the most commonly lanthanides used for the synthesis on new Ln(III) Single-molecule magnets are Dy(III), Tb(III), Ho(III) and Er(III) (Table 1.2.1).

	Gd^{3+}	Tb^{3+}	Dy^{3+}	Ho^{3+}	Er^{3+}
$4f^n$	$4f^7$	$4f^8$	$4f^9$	$4f^{10}$	$4f^{11}$
spin-orbit ground term	$^8S_{7/2}$	$^7F_6$	$^6H_{15/2}$	$^5I_8$	$^4I_{15/2}$
Free ion g value	2	3/2	4/3	5/4	6/5

Table 1.2.1: Electronic information of Ln(III) Ions.

Terbium(III) and Dysprosium(III) ions are widely used due to the high anisotropy that they possess. This has to do with some factors that will be discussed shortly but it worths mentioning that indeed the number of Tb(III) or Dy(III) SMMs is rapidly growing. It can be also observed that the Dy(III)-based SMMs are in general more in number compared to the Tb(III) ones, nevertheless both of these lanthanides have given us many beautiful molecular complexes for studying and deeper understanding of the SMM phenomenon.

In 2011 *Rinehart et al.*, published a paper that provided a lucid and scientific explanation towards the question 'Why do lanthanides give us this great SMM performance?'.[26] Till that moment, scientists would isolate and magnetically characterize Ln(III) complexes with tremendous satisfaction, since they were the recipients of results with great SMM performance, without though really understanding the reason behind. Jeffrey R. Long and Jeffrey R. Rinehart provided solid explanations on the aforementioned question by making, for the first time, the already existing literature understandable to a wider audience.

As mentioned above, the electronic structure of lanthanide ions is way more complicated than the one of transition metal ions, since the spin-orbit coupled quantum number *J* is responsible for ensuing the magnetic bistability. The crystal field effect in lanthanide ions is smaller than the spin-orbit coupling energy and as such, the crystal field acts as a perturbation to the spin-orbit interaction. This was found to be the key factor towards the question of why lanthanides

have this great SMM performance, even though this perturbation of the crystal field to the spin-orbit interaction is small. What really happens is that the ground spin-orbit coupled *J* state is influenced with the crystal field in a way that this interaction leads to the appearance of the magnetic anisotropy barrier in which the orientations of the spin ground state are split. Having as an example the widely used Dy(III) ion, we can see that its ground state, as a free ion, is sixteen-fold degenerate since the ground state *J* term of Dy(III) is 15/2. Considering the [2*J* +1] manifold we can easily understand that the magnetic microstates of Dy(III) are the following: $m_J = \pm 15/2, \pm 13/2, \pm 11/2, \pm 9/2, \pm 7/2, \pm 5/2, \pm 3/2, \pm 1/2$ (Figure 1.2.2). This [2*J* +1] degeneracy of the ground state can be removed and influenced differently according to the crystal field in which the lanthanide ion is placed. Thus, the orientation of the spin along with the strength and symmetry of the field are deeply associated with the splitting of the m_J microstates meaning that we can get better SMM performance, as long as we increase the single-ion anisotropy of the lanthanide ions by choosing carefully the appropriate ligand field.

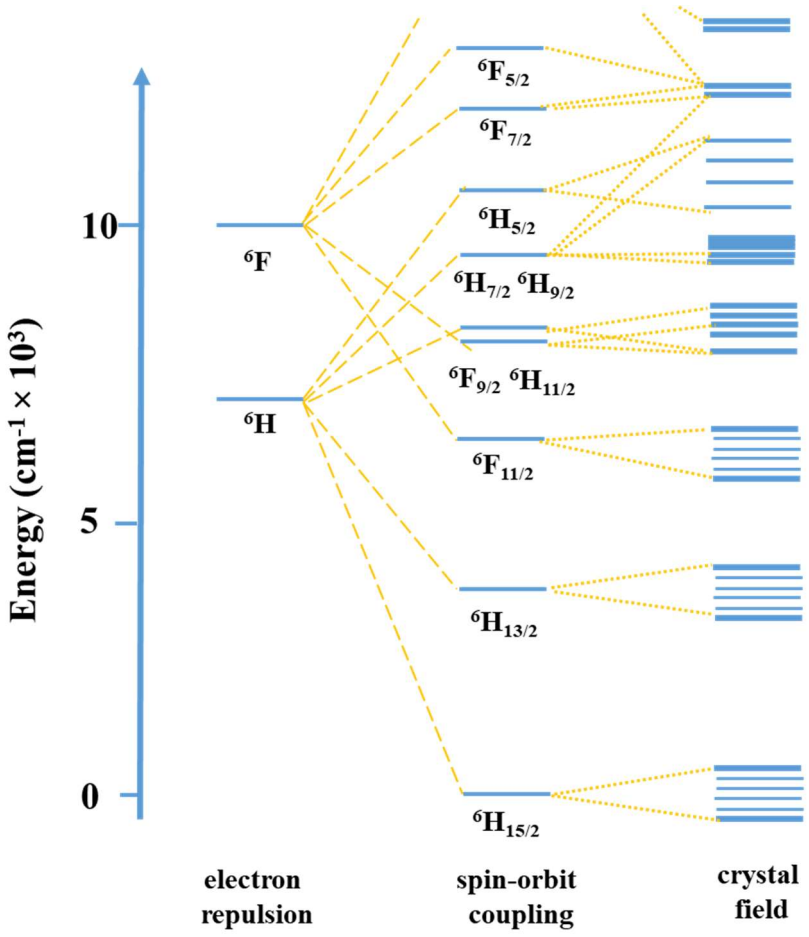

Figure 1.2.2: Low energy diagram of the electronic structure of a Dy(III) free ion with different perturbations of electron repulsions, spin-orbit coupling and the crystal field.

Long & coworkers, categorized lanthanides according to the quadrupole moment of their *f*-electron cloud to oblates (equatorially expanded), prolates (axially elongated) or isotropic (spherical) based on the previous work of Sievers *et. al*.[27] The strong angular dependence of the *f* orbitals is actually responsible for this shape variation of the *f* electron cloud and a depiction of the shape of the lanthanide ions can be observed at Figure 1.2.3.

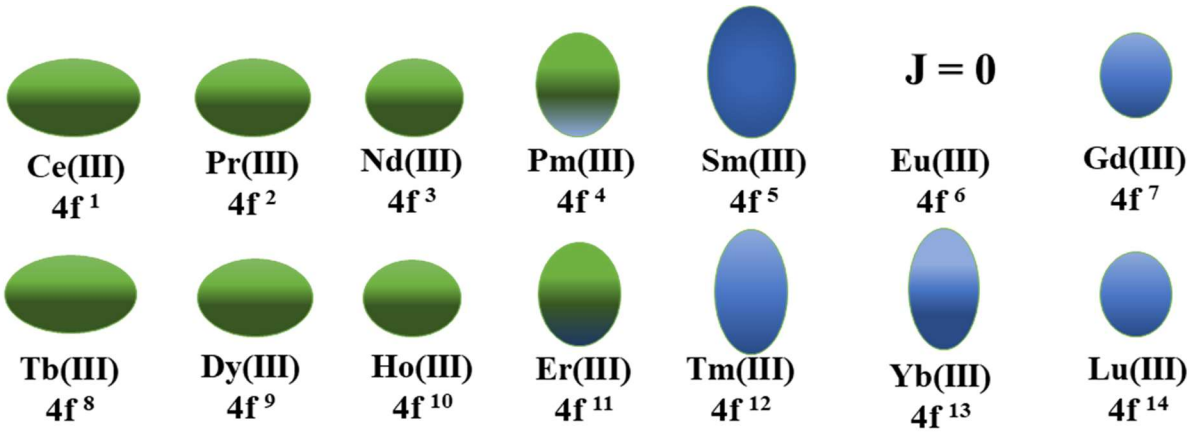

Figure 1.2.3: Schematic representation of the quadrupole moments of lanthanide ions base on approximations of their 4*f* electron charge clouds. No figure of Europium(III) is provided since its ground state is diamagnetic, $J = 0$.

Having all the above at hands, it was easy to start thinking about the design of new techniques that would lead to better or optimal SMM performance. These techniques are based on the shape of the lanthanide ion and the ultimate goal of scientists is to find the appropriate ligand field that will surround the 4*f* ion. In general, in order to enlarge the anisotropy of a prolate ion we must place it into an equatorially coordinating geometry so that the charge contact with the axial *f* electron density will be minimized. On the same ground, the anisotropy of an oblate ion can be maximized when we place it in a crystal field in which the electron density of the ligand is gathered above and below the xy plane. Sandwich-type organic moieties belong to this category of ligands and have been extensively studied due to the fact that the $[Pc_2Tb]^-$ compound was the first that the SMM behavior was observed possessing a central Tb(III) ion and two phthalocyanine ligands above and below the plane.

In fact, that model of Rinehart *et al.,* gave an easily comprehensible insight towards understanding many factors of the SMM behavior as for example the fact that most of the SMMs that exist in the literature

are Dy(III)-based molecules. The main explanation to that is that the Dy(III) ion is a Kramers ion which means that the ground state of Dy(III) is always bistable (regardless the crystal field) and furthermore it possesses a large moment at the ground state, ($^6H_{15/2}$). Thus bistability can be ensured from the beginning without the need of finding the appropriate ligand environment that would cause the splitting of the ground state.

Coming back to the $[Pc_2Ln]^-$ complex (where Ln(III) = Tb, Dy, Ho, Er, Tm, or Yb) magnetic measurements were performed and only the Dy(III) and the Tb(III) were found to have slow relaxation of magnetization. Out-of-phase signals of the aforementioned compounds are depicted in Figure 1.2.4, where it can be clearly observed that the magnetization cannot keep up with the oscillating field indicating thus, the presence of an anisotropy or effective energy barrier, U_{eff}.

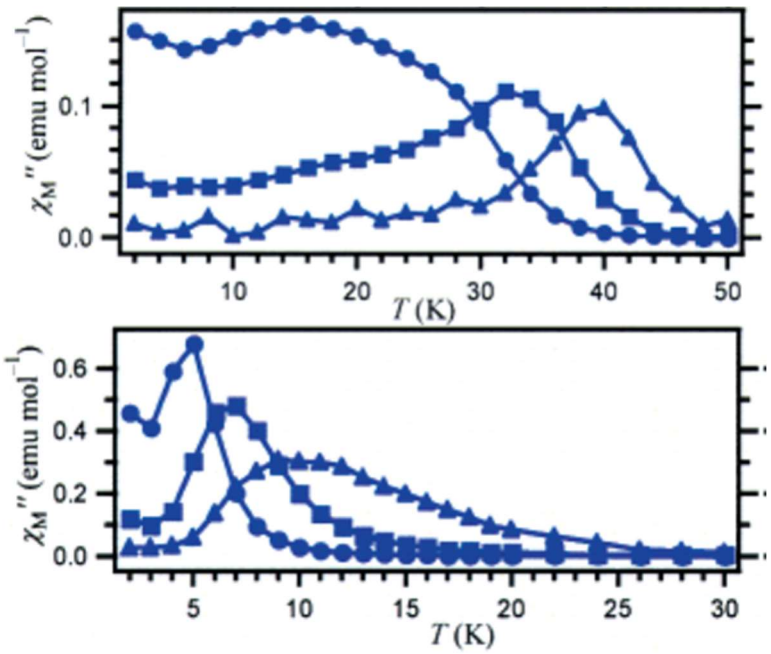

Figure 1.2.4: Diagrams showing the χ_M'' vs T plots of $[Pc_2Tb]^{-}\cdot(Bu_4N)^+$ (upper diagram) and $[Pc_2Dy]^{-}\cdot(Bu_4N)^+$ at 10 Hz, 100 Hz and 997 Hz.[23] Reproduced from Ref. 23 with permission from American Chemical Society (ACS).

Ishikawa *et al.*, realized that there must be a correlation between the rising of the temperature up to 40 K (depicted at the upper diagram of Figure 1.2.4) and the m_J microstates of the lanthanide ions, since up to that point, no 3*d* SMM had surpassed in χ_M'' vs T plots the limit-temperature of 8 K. Suddenly, a huge rise was visible and thus after performing some calculations[28,29] they were able to quantify the separation energies between the m_J states of the complexes (Figure 1.2.5).

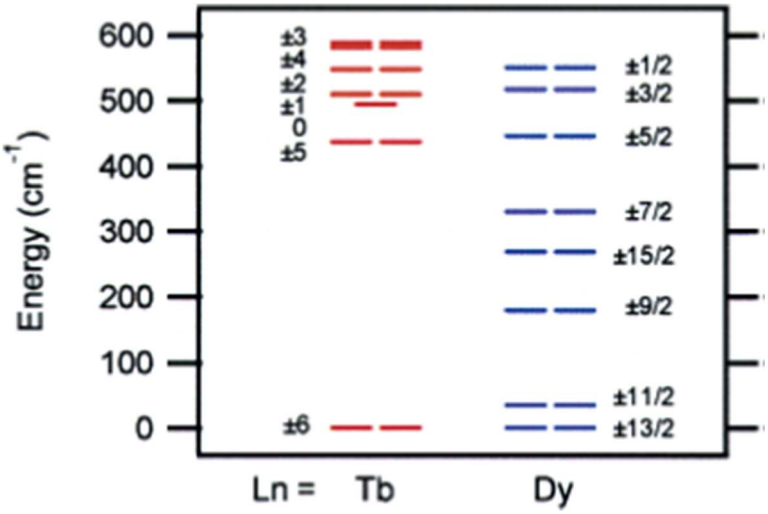

Figure 1.2.5: Energy and m_J values of $[Pc_2Tb]^{-}\cdot(Bu_4N)^{+}$ and $[Pc_2Dy]^{-}\cdot(Bu_4N)^{+}$ complexes. Reproduced from Ref. 23 with permission from American Chemical Society (ACS).

In the case of the Tb(III)-analogue, the energy separation between the $m_J = \pm 6$ and $m_J = \pm 5$ is more than 400 cm^{-1} and if we think that the relaxation of magnetization is a 'step' process (J, J±1) then this large gap is crucial. In the Dy-analogue, on the other hand, the energy separation between the ±13/2 and ±11/2 is extremely small and that implies that relaxation of magnetization will inevitably be faster leading to smaller U_{eff} values. Indeed, fitting of the data using the Arrhenius law gave a $U_{eff} = 230$ cm^{-1} for the $[Pc_2Tb]^{-}\cdot(Bu_4N)^{+}$ and a $U_{eff} = 28$ cm^{-1} for the $[Pc_2Dy]^{-}\cdot(Bu_4N)^{+}$. Nevertheless, this was the first example of lanthanide-based SMMs reported in the literature and that made the field of molecular magnetism to progress tremendously till these days, where mononuclear Ln-based molecules with large U_{eff} values and hysteresis up to 80 K are reported. [30]

Before coming to the most recent and breakthrough published examples of Ln(III)-based SMMs, I will shortly refer to the more complicated relaxation mechanisms that have been found to take place in lanthanide complexes. The most discussed relaxation mechanisms in the literature are four and have to do with relaxation theories involving QTM and spin-lattice mechanisms. The spin-lattice mechanism supports that a system can be seen as two parts, the spin system and the lattice system. Both of them can retain a thermal equilibrium until an oscillating field is applied parallel to a steady field on the sample, at which time exchanges of energy are produced and thus magnetic relaxation occurs.[31] The spin lattice mechanisms

include the Orcbach, Raman and direct processes. We can further categorize these relaxation pathways according to their dependence from the temperature and-or the field. Orbach and Raman processes are temperature dependent mechanisms while QTM and direct process are field dependant mechanisms. The relation between the relaxation time and the different mechanisms that can take place can be seen at the Equation 1.2.1.[32,33]

$$\tau^{-1} = AH^{m}T + \frac{B_1}{1+FH^2} + CT^{n} + \tau_0^{-1}\exp(-\frac{Ueff}{KT}) \qquad \text{Equation 1.2.1}$$

Parameters A, C and τ_0 are constant and they relate to three different relaxation mechanisms namely direct, Raman and Orbach and they all contribute at the same time to the rate of relaxation, τ^{-1}. The Orbach process involves excitation of an electron to the following m_s state, while interacting with lattice phonons, passing over the barrier. The direct process is a single-phonon mechanism, dealing with phonons of the same energy and it allows the spin flip without fully overcoming the energy barrier. On the contrary, the Raman process is a two-phonon mechanism which includes excitation to a virtual state and relaxation can follow afterwards (Figure 1.2.6).

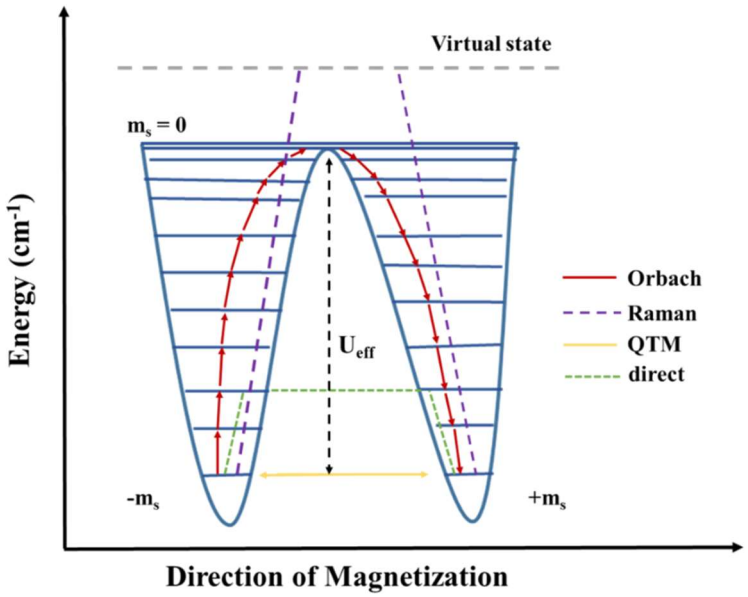

Figure 1.2.6: Schematic representation of the different relaxation mechanisms as described in the text.

Normally, QTM, direct and Raman process are mechanisms which reduce the U_{eff} of a complex. Therefore, these processes should be minimized or supressed in order to extend or force the system to follow a thermal relaxation pathway, which in the end can lead to higher U_{eff} values and relaxation times. The most commonly used methods in order to succeed in that task is the application of an external dc magnetic field and the modification of the ligand field around the metal ions in order to maximize as much as possible the axial anisotropy.[34,35] Thus, when scientists take into serious account the ligand field around the metal ion and the single-ion anisotropy that it possesses, it may lead to complexes with an overall high molecular anisotropy, which along with the appropriate surrounding ligand field can induce extraordinary SMM or SIM (single-ion magnet, when only one ion contributes as a magnetic core) behavior.

The most recent and cutting-edge example of a molecule that shows slow relaxation of magnetization at very high temperatures, is a compound published in *Science* by Layfield *et al*. last December.[36–38] The article describes the synthesis and magnetic characterization of a dysprosium metallocene complex which was found to possess an effective energy barrier to magnetization reversal of U_{eff} = 1451 cm^{-1} and a magnetic hysteris above liquid nitrogen temperatures, up to 80 K. The target complex has a general formula of $[(\eta^5\text{-Cp*})Dy(\eta^5\text{-Cp}^{i\text{Pr}5})][B(C_6F_5)_4]$, abbreviated as $[Dy\text{-}5^*][B(C_6F_5)_4]$ and is depicted at Figure 1.2.7.

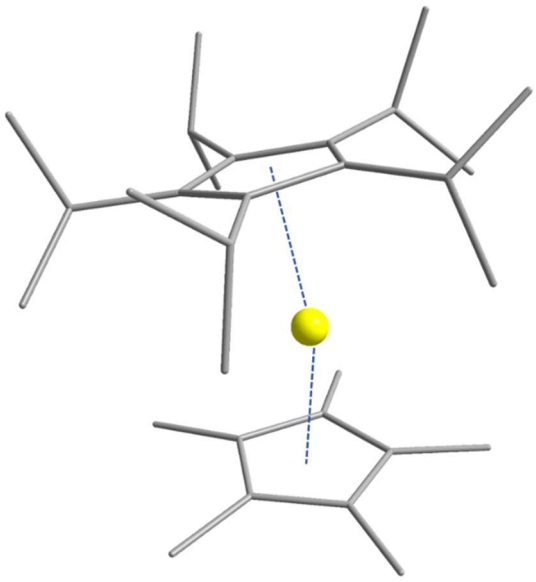

Figure 1.2.7: Schematic representation of molecular structure of $[Dy\text{-}5^*][B(C_6F_5)_4]$. Color scheme: Dy, yellow; C, grey.

The SMM properties of the complex were revealed after performing alternating-current (ac) susceptibility studies, where an oscillating field of 5 Oe and zero applied dc field were used. The in-phase (χ'_M) and out-of phase (χ''_M) components were employed in order to construct the Cole-Cole plots of the complex at different temperature regimes (Figure 1.2.8.).

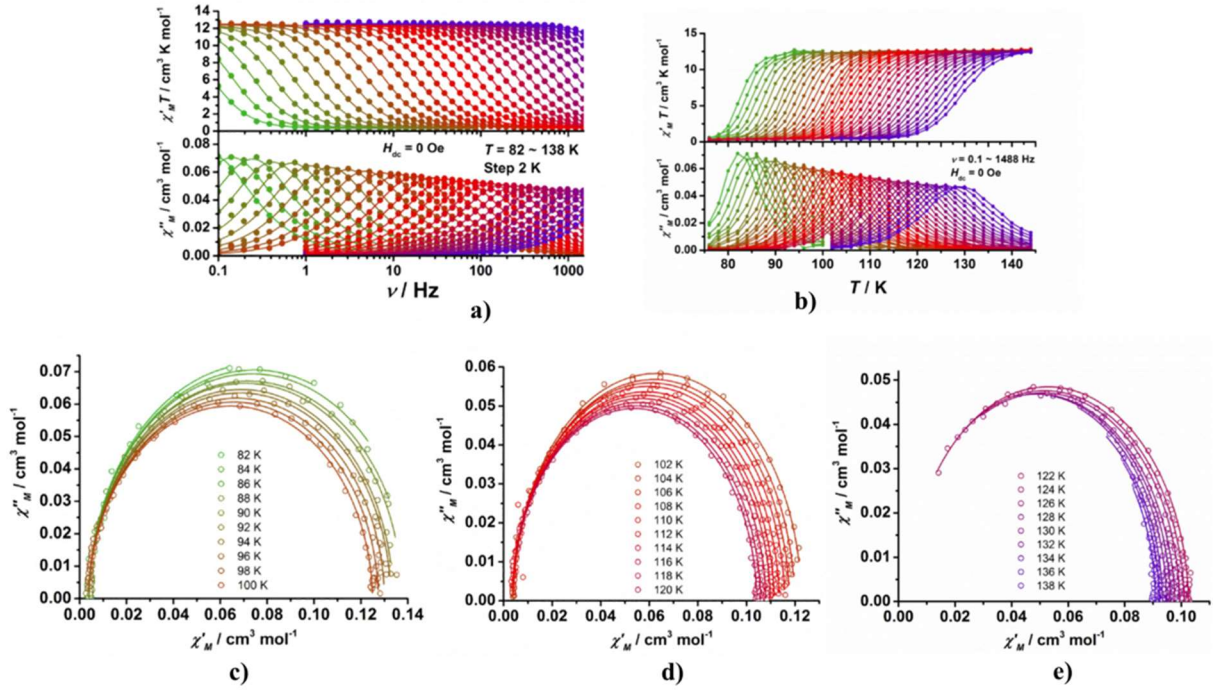

Figure 1.2.8: a) Frequency-dependant out-of-phase signals of the Dysprosium metallocene complex at zero field using frequencies from 0.1 till 1488 Hz, from 82 K (green) till 138 K (purple). Solid lines represent fitting of the data. b) Temperature dependence of out-of-phase signals of the complex at zero field collected at temperatures of 76 to 144 K and frequencies of 0.1 till 1488 Hz. Solid lines represent fitting of the data. c,d,e) Cole-Cole plots for the [Dy-5*][$B(C_6F_5)_4$]complex at temperatures of 82-100 K (c), 102-120 K (d) and 122-138 K. Solid lines represent fitting of the data. Reproduced from Ref. 36 with permission from American Association for the Advancement of Science (AAAS).

The temperature dependence of the relaxation time for the [Dy-5*][$B(C_6F_5)_4$] complex is also available at Figure 1.2.9 along with the depiction of the magnetic hysteresis of the complex. These data were fit using the $\tau^{-1} = \tau_0^{-1} \exp\left(-\frac{Ueff}{KT}\right) + CT^n + \tau_{QTM}^{-1}$ equation and the following values were derived: $\tau_0 = 4.2 \times 10^{-12}$ s, $U_{eff} = 1541$ cm^{-1}, C = 3.1×10^{-8} s^{-1}K^{-n} where n = 3.0 and $\tau_{QTM} = 2.5 \times 10^4$ s. Tests for magnetic hysteresis were also performed since the storage memory devices really depend on the development of magnetic hysteresis with an appreciable coercivity. Therefore, it was observed that magnetic hysteresis was indeed visible at

temperatures from 2 till 85 K using a field sweep rate of 200 $Oe \cdot s^{-1}$, with the loops closing as the temperature rises.

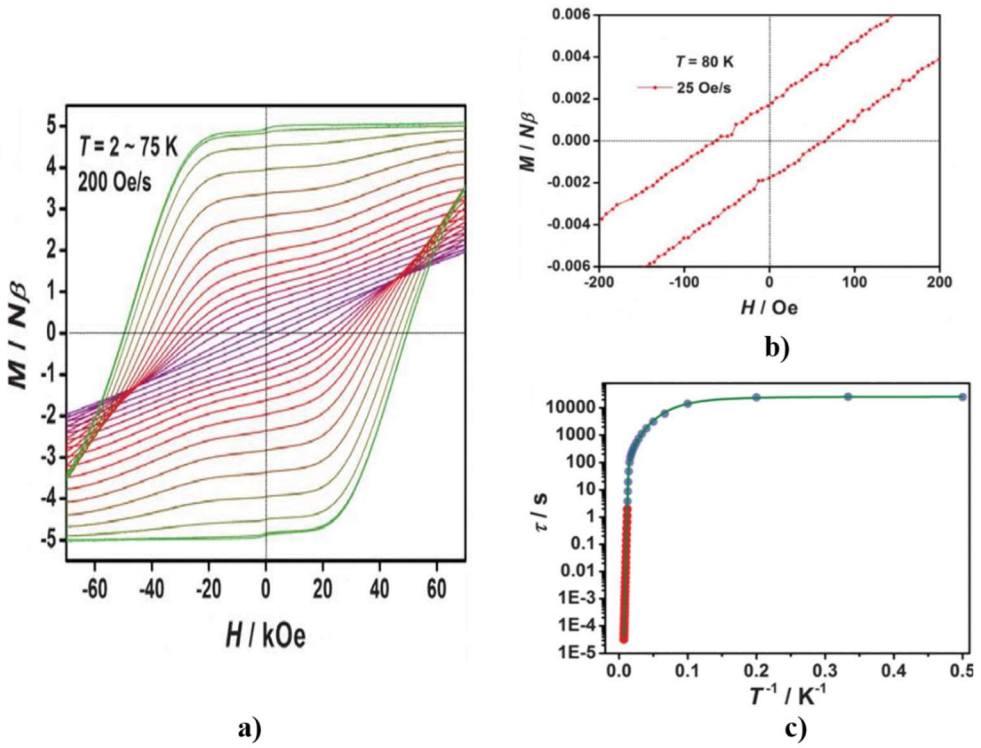

Figure 1.2.9: a) Magnetization versus field plot of [Dy-5*][$B(C_6F_5)_4$] in the temperature range of 2-75 K with a 200 $Oe \cdot s^{-1}$ field sweep rate. b) Magnetization versus field plot of dysprocenium compound at 80 K using a flied sweep rate of 25 $Oe \cdot s^{-1}$. c) Temperature dependence of relaxation time for complex [Dy-5*][$B(C_6F_5)_4$]. The colored solid lines represent fitting of the data based on the equation described in the text. Reproduced from Ref. 36 with permission from American Association for the Advancement of Science (AAAS).

This is an extraordinary example of a molecular complex that functions as a magnet at temperatures above liquid nitrogen (above 77 K) and it gives us great hopes that the field has found the right path through which one day the blocking temperature will be risen even more. The discovery of that compound and the resulting properties measured mark a new era within the Single-molecule Magnet family, which will hopefully soon pay off in terms of technological applications, since there is a great need for devices with possibilities of even bigger storage information.

1.3 Metallacrowns

In 1989, a new class of compounds started gaining more and more attention when Pecoraro *et al.* described their synthesis and classification.[39] These compounds are of particular interest since the structural predictability and versatility, integrity in solution and combination of properties that they can posses, make them excellent candidates for extensive investigations with potential applications in various fields of research such as molecular magnetism, host-guest chemistry, molecular recognition.[40]

Metallacrowns (MCs) have some unique structural characteristics that have been thoroughly analyzed, throughout the years, in coordination/cluster chemistry. They are cyclic molecules, structurally analogue to crown ethers, possessing a $–[M\text{-}N\text{-}O]_n$- repeating unit, in contrary to the characteristic and well-known $–[C\text{-}C\text{-}O]_n$- motif of crown ethers (Figure 1.3.1). Similar to crown ethers, the naming of metallacrowns is based on the number of the atoms comprising the ring size, as well as the number of the donating oxygen atoms within the ring.

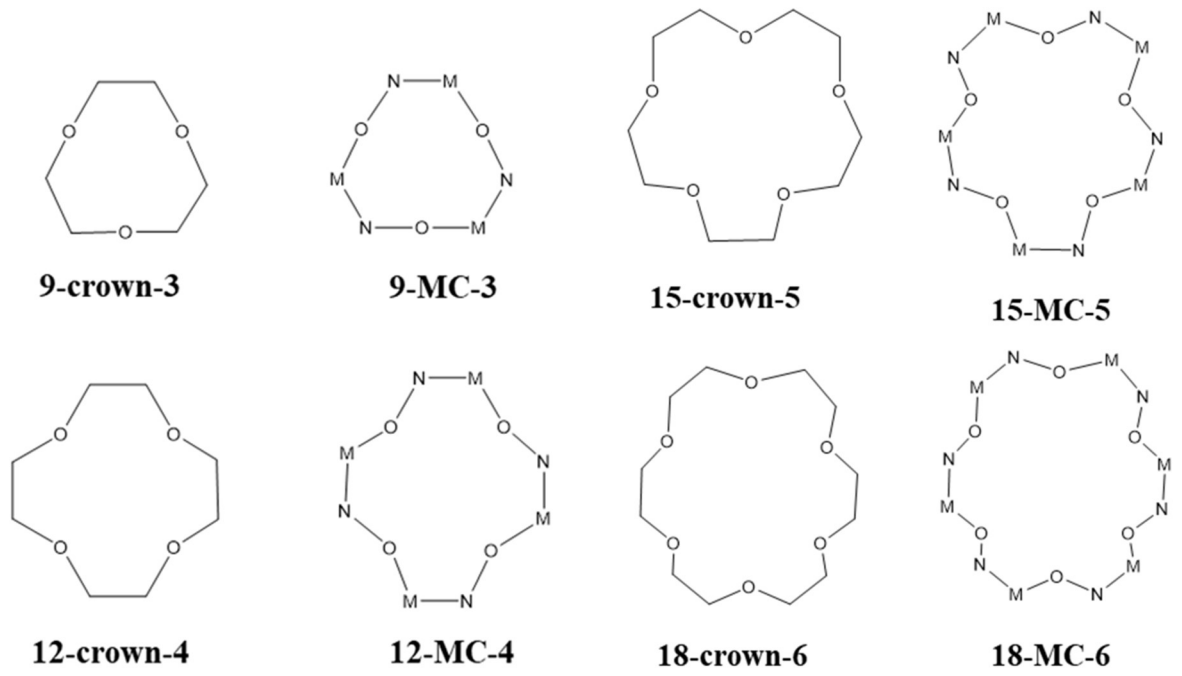

Figure 1.3.1: Schematic representation of different metallacrown size motifs existing in the literature and the respecting crown ether analogue.

For instance, a 12-MC-4, where MC is referring to metallacrown, is a 12-membered ring consisting of four continuous –[M-N-O]- units with 4 oxygen donor atoms. A more descriptive naming can be also given when we want to be more precise about the central metal ion, the ligand we have used and any further coordinating or non-coordinating ions existing in the structure. The general formula that describes the above is the following:

$$\{M_1B[\text{ring size-MC}_{M2X(L)}\text{-oxygens of the rings}]Y\},$$

where M1 is the metal ion in cavity of the ring along with its oxidation state, B refers to the coordinating ions, M2 refers to the ring metal ion and its oxidation state, X refers to the third heteroatom of the ring, L refers to the ligand used and Y refers to the non-coordinating ions.[40,41] In general, these complexes can be found in many structural conformations spanning from 9-MC-3 till 60-MC-20 but the most commonly used and well established ring sizes are the 9-MC-3, the 12-MC-4, the 15-MC-5 and 18-MC-6.[41]

Apart from metallacrowns, nowadays, quite many complexes have been published belonging to the family of azametallacrowns or aza-MCs, which consist of the -$[M\text{-}N\text{-}N]_n$- repeating unit. Moreover, there are also macrocycle complexes reported that are part of the expanded MCs network possessing a repeating unit of –$[M\text{-}N\text{-}C\text{-}O]_n$- , while the category of metallacoronates posses the repeating unit of –$[M\text{-}O\text{-}C\text{-}O]_n$, in which both the heteroatoms have been replaced by oxygen atoms.[42,43] Another quite usually observed motif within the class of MCs is the inverse type of MCs where the molecules possess the –[M-O-N-M-N-O]- repeating unit. In this structural conformation normally the ring metal ions look at the cavity of the MC which can also include coordinating anions.[44] Finally, there is also the possibility that a metallacrown will crystallize having no coordinating metal ion in the central cavity and when that happens the term ‘vacant’ is normally used.[45,46]

Nowadays, the most common forms of Metallacrowns present in the literature are the homometallic 3*d*[39,47] and the heterometallic 3*d*/4*f* MCs[46], even though there have been also some heterometallic 3*d*/5*f* MCs presented.[48] All of these variations, in terms of metal ions, have been and still are under thorough investigation since there are many exciting properties such as magnetic ones, photoluminesce, etc, that need to be better understood. This variation of metal ion along with the different structural conformation that MCs could potentially adopt, places these molecules to a unique category of coordination compounds with exciting structural motifs and interesting magnetic behavior.

A very important factor that dictates the final structural conformation of the resulting Metallacrown is the organic moiety or ligand that is used. This is a big synthetic asset for coordination chemists because by varying the organic counterpart they know to which structural form of the MC they will end up. This sense of synthetic control over the final product is a big advantage of these complexes because even though we are discussing about coordination complexes that crystallize out of solution reactions, a high sense of control is still available. More specifically, by focusing exclusively on the 12-MC-4 and 15-MC-5 structural conformations there have been some ligands, and substituted analogs of these ligands, that have been repeatedly seen promoting these specific geometrical arrangements. For example, salicylhydroxamic acid ($shiH_3$) and derivatives have been known to promote the 12-MC-4 conformation since they form a 90° angle which when repeated four times it assists on the shaping of the square-like 12-MC-4 compound. Following the same principle, ligands such as picoline hydroxamic acid (H_2picHA) and quinoline hydroxamic acid ($H_2quinHA$) promote the 15-MC-5 structural arrangement by shaping subunits that possess a perfect 108° angle. Thus, repetition of these subunits by five leads to the formation of a pentagonal structure as it can be seen at Figure 1.3.2 (below).

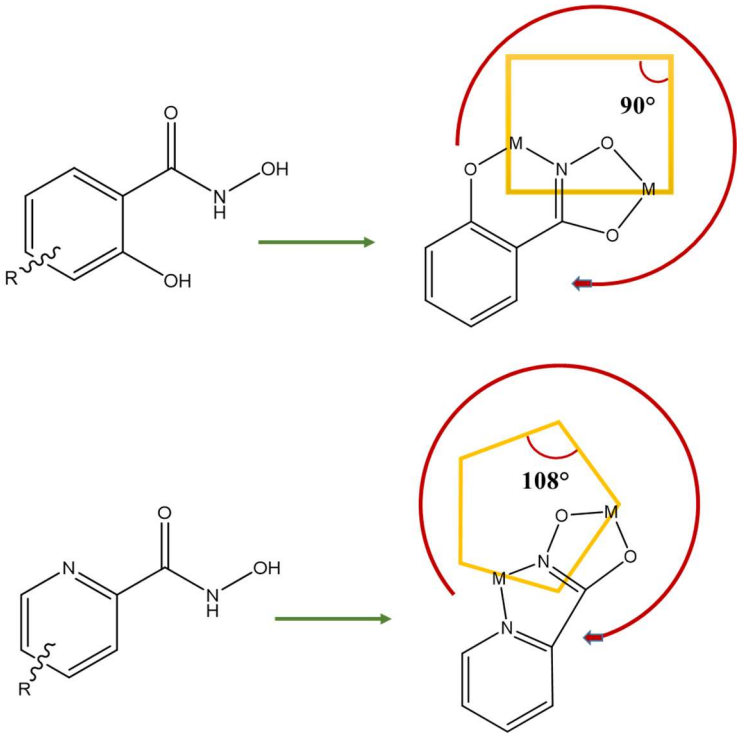

Figure 1.3.2: Schematic representation of design strategy of Metallacrowns based on the ligand used. (above) 12-MC-4 conformation produced by ligands that form 90° internal angles; salicylhydroxamic acid is depicted. (below) 15-MC-5 conformation produced by ligands that form 108° internal angles; picoline hydroxamic acid is depicted.

Even though the choice of the organic ligand is of great importance, other variables such as metal ions used, solvents, counterions, stoichiometry and concentration of the reaction solution have a great impact on the crystallization product. Especially for the choice of metal ion, an extra care should be taken considering the number of protons of the ligand used. For example, it is wiser to use trivalent metal ions when tripotic ligands are the ligands of choice or divalent metal ions when working with diprotic ligands etc, for charge balance considerations.[49] Thus, when all considerations are correctly and prudently used, there is still a high level of control that synthetic chemists can extract and impose on the MC synthesis.

As mentioned at the beginning of this subchapter, the first metallacrown was described in the literature in 1989 by Pecoraro *et al.*[39] and this was a 12-MC-4 manganese metallacrown with the general formula of $\{Mn^{II}[Mn^{III}(shi)]_4(OAc)_2(DMF)_6\}\cdot 2DMF$, where shi^{3-} = salicylhydroxamic acid, OAc^- = acetate, DMF = dimethylsulfoxide (Figure 1.3.3). The compound consists of four Mn^{III} ring metal ions which are coordinated to four triply deprotonated salicylhydroxamic ligands, two acetate ions acting as bridging moieties between Mn^{II} and Mn^{III} ions, with the Mn^{II} ion sitting in the cavity of the metallacrown and six DMF molecules terminally bound to the four Mn^{III} ions. The periphery Mn^{III} ions are all six-coordinate with distorted octahedral geometries while the central Mn^{II} is six-coordinate with distorted trigonal prismatic geometry.

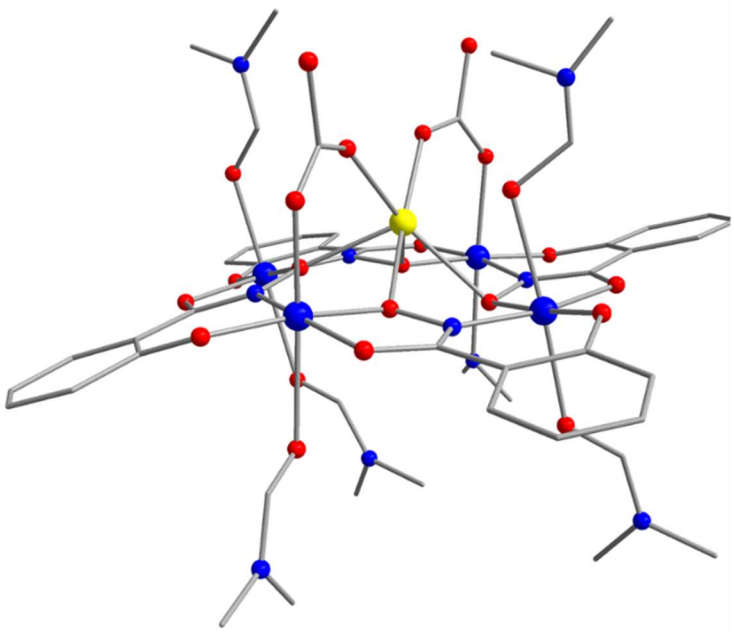

Figure 1.3.3: Schematic representation of $\{Mn^{II}[Mn^{III}(shi)]_4(OAc)_2(DMF)_6\}\cdot 2DMF$. Solvate molecules and H atoms are omitted for claritz reasons. Color scheme: Mn^{III}, blue; Mn^{II}, yellow; O, red; N, blue; C, grey.

The focus of this Thesis will be the synthesis and characterization of 12-MC-4 complexes and as such a more detailed explanation of this molecular conformation is provided in Figure 1.3.4. Taking as an example the molecular structure of $\{Mn^{II}[Mn^{III}(shi)]_4(OAc)_2(DMF)_6\}\cdot 2DMF$, the important parameters for the synthesis of these complexes are marked in Figure 1.3.4. 12-MC-4 compounds consist of four ring metal ions that occupy the periphery of the molecule and one central metal ion that sits in the cavity. For charge balance issues, the organic chelating/bridging ligand that is assisting with the formation of the skeleton of the molecule, has to be matching with the charge of the periphery metal ions used.[49] It is also important to take care of the solvents used since in many cases they can coordinate as solvate terminal ligands. Lastly, the nature of the used metal salt is of crucial significance as most of the times, the anions can participate in the structure as coordinating bridging co-ligands.

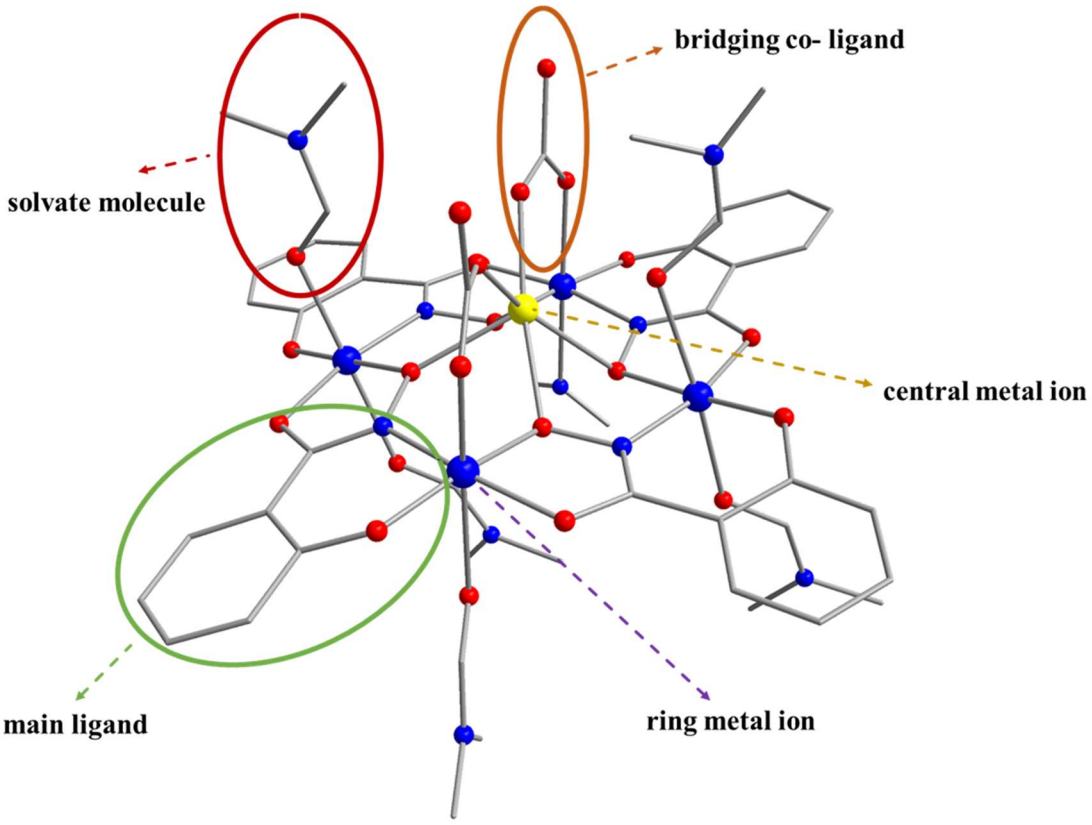

Figure 1.3.4: Schematic representation of synthetic variables used in order to optimize the crystallization and properties of the molecules. Color scheme: Mn^{III}, blue; Mn^{II}, yellow; O, red; N, blue; C, grey.

It, thus, became apparent that these compounds possess a large number of advantages based on the amount of synthetic parameters that can be adjusted. All these variations of choices have a great impact on the addressable properties that scientists would want to study according to their area of interest. Therefore, there have been many different type of metallacrowns presented and discussed in the literature. These, at the beginning, included mainly half-sandwich or sandwich-type molecules consisting of primarily 3*d* elements such as Vanadium(V), Manganese(II)/(III), Iron(III), Cobalt(III), Copper(II), Nickel(III) and Zinc(II).[41,42] Later on, the field started progressing towards the synthesis of 3d/4f MC complexes and that as a result brought into the surface a whole new series of interesting advances, in terms of properties.[41]

Pecoraro and coworkers, apart from being the first ones to extensively analyze these complexes, were and still are, the ones that have emphasized and analyzed this unique scaffold of Metallacrowns focusing mainly on luminescent properties, as such "scratching only the tip" of their magnetic properties. Lately, many beautiful complexes have been published and investigated for luminescent properties with the latest example being a $[LnGa^{III}_4(shi)_4(C_6H_5CO_2)_4(C_5H_5N)(CH_3OH)]$ (Ln^{III} = Sm, Eu, Gd, Tb, Dy, Ho, Er, Tm, Yb) (Figure 1.3.5).

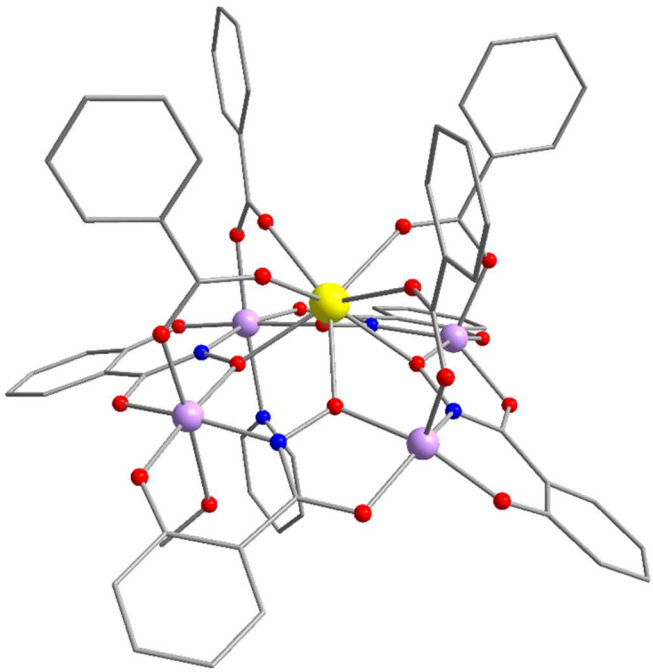

Figure 1.3.5: Schematic representation of molecular structure of $[DyGa^{III}_4(shi)_4(C_6H_5CO_2)_4(C_5H_5N)(CH_3OH)]$. Color scheme: Dy^{III}, yellow; Ga^{III}, purple; O, red; N, blue; C, grey.

In that paper, a new family of visible and NIR-emitting Metallacrowns with Ga^{III}/Ln^{III} is reported, while the Dy^{III} and Sm^{III} analogues of these compounds can emit in both regions. More detailed information is given at the publication itself, where a deeper description of the phenomenon is provided.[50]

Getting away from the luminescent properties of these molecules, that have been thoroughly studied, and focusing now on their magnetic properties, it is obvious enough that not much investigation was done in this area. 3*d*/4*f* MCs provide an excellent approach for SMMs behavior since both the magnetic characters of the paramagnetic 3*d* and the highly anisotropic 4*f* ions can be combined. There are not too many reports discussing so far in depth the magnetic behavior of Metallacrowns, nevertheless the most dissertated motif, up to now, is the heterometallic Mn/4f MCs.[51–54]

In 2016 Boron *et al.*, reported a nice publication that was dealing with the effect of the bridging anion on the magnetic properties of MCs. [51] The SMM properties of a $DyX_4M(12\text{-}MC_{Mn}{}^{III}{}_{(N)shi}\text{-}4)$ Metallacrown were investigated (X = salicylate, acetate, benzoate, trimethylacetate, M = Na^I or K^I) (Figure 1.3.6). The main scaffold of the MCs remained the same, while the bridging ligands and the counterions used, were varied. The only complex that showed frequency dependent tails of signals, in the out-of-phase diagram, was the $Dy(Hsal)_4M$ 12-MC-4 compound. That was a further confirmation, that the nature of the bridging ligands can strongly affect the out-of-phase magnetic properties, confirming again the relation of dependence that exist between the synthetic adjustable MC variables and SMM properties.

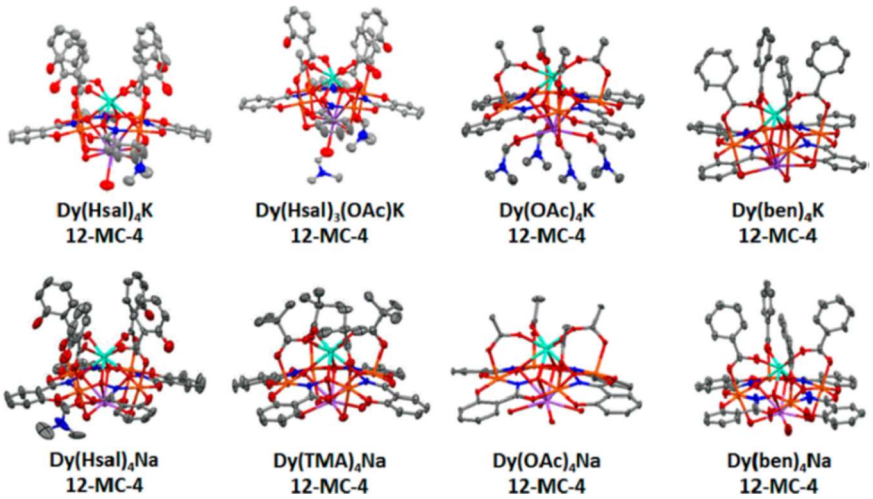

Figure 1.3.6: Molecular structure of different MC series discussed from Boron *et al.* [51] Reproduced from Ref. 51 with permission from American Chemical Society (ACS).

To summarize, it is important to understand that the MC scaffold is a special tool that will help us study and understand further more the SMM properties. Apart from that, it is imperative for us to investigate the synthetic challenges that follow the MC synthesis because through that, better knowledge will be gained. There have been already many articles focusing on the synthetic strategies, the stability of MCs in solution, luminescent properties etc and thus now the time has come, for a better understanding of the magnetic properties of these complexes that will help us understand even better, some of the crucial requirements of the SMM phenomena.

1.4 Metallacryptates

As the analogy of crown ethers to metallacrowns has been demonstrated and discussed in the previous chapter, here at this section another class of metallamacrocycles is discussed. The so-called metallacrypates or metallacryptands are the inorganic analogues of the famous cryptands.[55] In 1987 Jean Marie Lehn, Donald Cram and Charles Pedersen received the Nobel prize for the synthesis of cryptands and their contribution to the growth of supramolecular chemisty. The term cryptand suggests that a substrate or else an element is kept or bound in the 'crypt', entombing it to the cavity of the cryptand. These compounds are three-dimentional analogues of crown ethers and can easily host different ions in their central empty space. Host-guest chemistry flourished due to the discovery of these complexes that have been proposed for a variety of applications such as sensors[56], catalysis[57] and as chiral blocks for 2D and 3D solids.[58,59]

The most well-known cryptand is the $N[CH_2CH_2OCH_2CH_2OCH_2CH_2]_3N$ or [2.2.2]cryptand for short (Figure 1.4.1). The notation in the formula stands for the number of ether oxygen atoms or else coordination sites, in every bridge between the nitrogen atoms. Most of the amine based cryptands have a high coordination-binding preference towards alkaki metals[60] as it has been observed so far, and most of the times these are accommodated in the cavity of cryptands as guests.

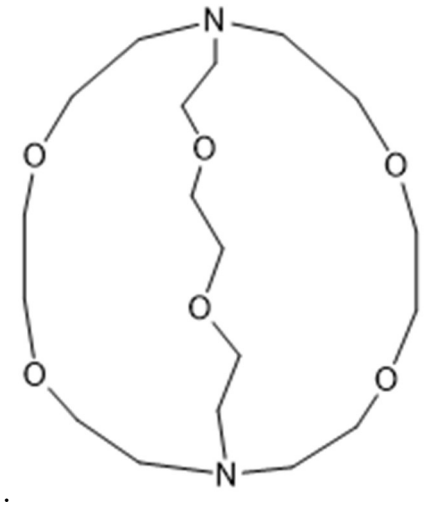

Figure 1.4.1: Schematic representation of a [2.2.2]Cryptand.

More specifically, this three dimensional space that is created in the cavity of cryptands can be either seen as a binding site or as host for 'guest' ions. The complex that is formed from the cryptand and the cationic guest is called cryptate. One characteristic of cryptands is that they can easily compose compounds with a variety of cations such as alkali metals, lanthanides and alkaline earth elements, while they can coordinate to guest ions (NH^{4+}), using both nitrogen and oxygen atoms.

Metallacryptands have appeared in the literature already a few times by now.[61] There are some worth-mentioning examples such as a double decker compound of two 12-$MC_{Ga}{}^{III}{}_{N(shi)}$-4 complexes that encapsulate a sodium cation in a cage-like structure[62] and a metallacryptand compound consisting of manganese and 2,2'-dipyridylketonediolate which embodies a core of manganese oxide, exhibiting interesting SMM behavior.[63] The latest example featuring a metallacryptand structural motif appeared in the literature in May 2018.[64] Pecoraro and coworkers, addressed the synthesis and characterization of a $[LnGa_6(H_2shi)(Hshi)(shi)_7(C_5H_5N)]$ (shi^{3-} = salicylhydroximate, Ln(III) = Pr, Nd, Sm, Eu, Gd, Tb, Dy, Ho, Er, Yb) or else Ln(III){[3.3.1]Ga(III) Metallacryptate} as shown in Figure 1.4.2. That was the first example of a Ln(III)-based metallacryptate in which SMM properties were observed.

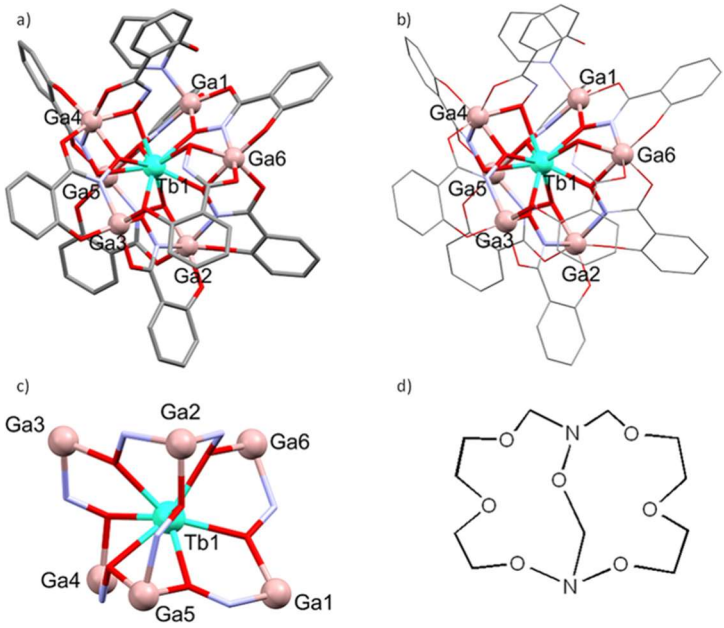

Figure 1.4.2: a) Schematic representation of molecular structure of $[TbGa_6(H_2shi)(Hshi)(shi)_7(C_5H_5N)]$; b) highlighted core of the Terbium analogue of the metallacryptate; c) inorganic core of $[TbGa_6(H_2shi)(Hshi)(shi)_7(C_5H_5N)]$; d) cryptand representation for comparison. Reproduced from Ref. 64 with permission from Wiley.

The compound consists of six Ga(III) ions bridged together via the oximate moieties of seven triply, one doubly and two singly deprotonated shiH_3 ligands while the Ln(III) ion sits at the cavity of the metallacryptand. Four of the Ga(III) ions are six-coordinate with distrorted octahedral geometries and the remaining two, are five-coordinate with their geometry being closer to a square pyramidal one as confirmed by the Addison tau criteria.[65] The central lanthanide is nine-coordinate possessing a tricapped trigonal prism geometry.

Magnetic studies were performed for all isostructural complexes but only the Dysprosium analogue was found to possess out-of-phase ac signals at zero field and thus only this compound will be more extensively discussed. Magnetic susceptibility studies were performed and are shown in a $\chi_M T$ vs T plot for the Dysprosium metallacryptate in Figure 1.4.3. The $\chi_M T$ value of the complex at 300 K is 13.48 $cm^3mol^{-1}K$, lower than the expected value for a non-interacting Dy(III) ion (14.17 $cm^3mol^{-1}K$, $^6H_{15/2}$, S = 5/2, L = 5, g = 4/3, J = 15/2). This is most likely due to the presence of long range antiferromagnetic interactions within the crystal.[66] The $\chi_M T$ product decreases steadily with decreasing temperature before it reaches a value of 9.18 $cm^3mol^{-1}K$ at 2 K. This behavior can be most likely attributed to depopulation of ground J sublevels and/or the presence of intermolecular antiferromagnetic interactions.[67,68] In Figure 1.2.3b the isothermal magnetization of the compound at 2 K from 0 T to 7 T is depicted. The magnetization increases to a saturation value of 5.55 Nβ which is much lower than the expected value of 10 Nβ normally observed for a single Dy(III) ion. This is due to the presence of low lying excited stated and additional influences from the crystal field.[69,70]

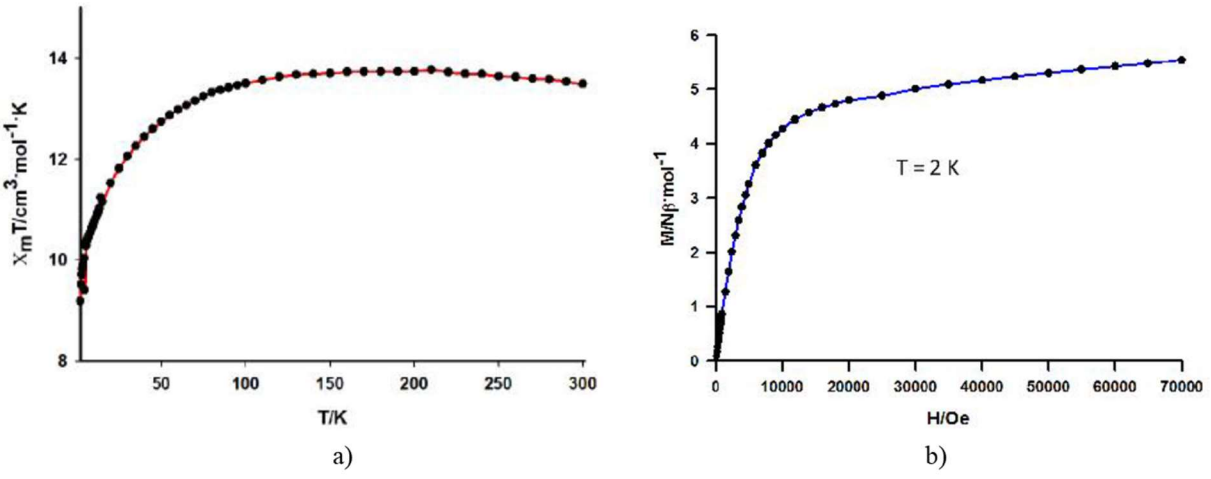

Figure 1.4.3: a) $\chi_M T$ vs T diagram of Dysprosium Metallacryptate ; b) Magnetization diagram of same complex at 2 K. Reproduced from Ref. 64 with permission from Wiley.

Alternating-current (ac) studies are also extensively discussed in the paper. The Dysprosium Metallacrypate at zero field showed tails of signals and thus an applied field of 750 Oe was used. Upon application of the external field the peak maxima was observed due to suppression of the QTM (Figure 1.4.4)

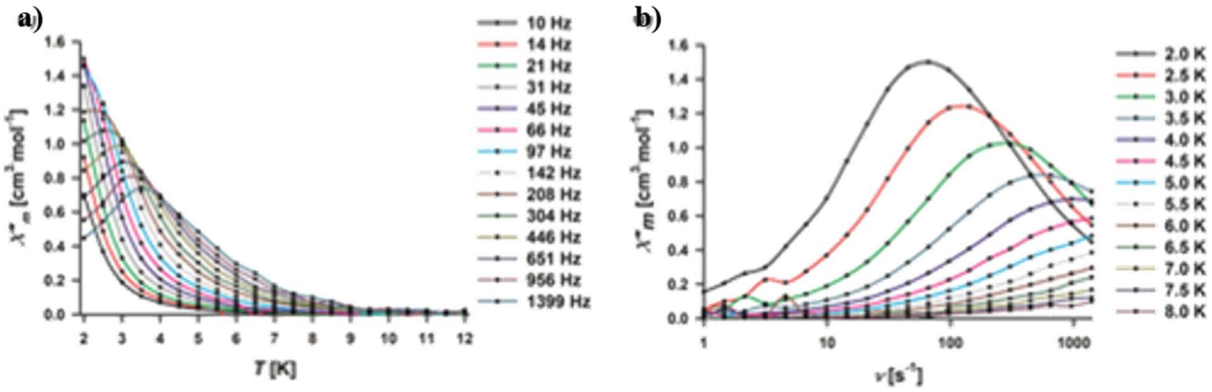

Figure 1.4.4: a) Frequency dependent ac signals; b) Temperature dependent ac signals. Reproduced from Ref. 64 with permission from Wiley.

Upon constructing the Cole-Cole plots, it was observed from the shape of the semicircles that one process is present. Thus, constructing the Arrhenius plot and fitting the data assuming only the Orbach process as the present relaxation pathway helped the authors to extract a good and reliable fit (Figure 1.4.5). Fitting of the data gave an effective energy barrier of U_{eff} = 12.7 K and a pre-exponential factor of $\tau_0 = 3.6\times10^{-6}$ s^{-1}.

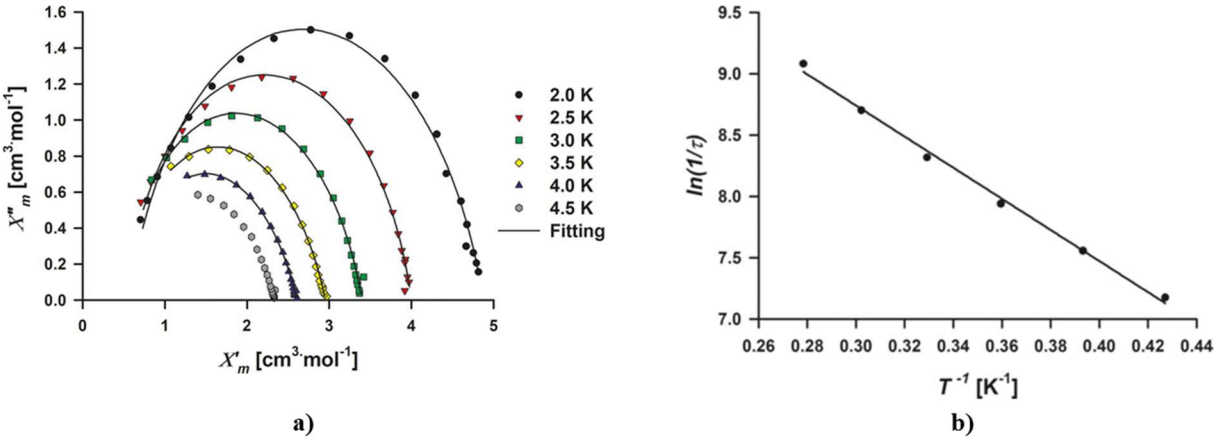

Figure 1.4.5: a) Cole-Cole plot of Dysprosium metallacryptand; b) Arrhenius plot of Dysprosium complex. Black line represents fitting of the data. Reproduced from Ref. 64 with permission from Wiley.

It is, thus, obvious from the aforementioned example that this structural type of metallacryptands or metallacrown cages can lead to compounds with beautiful architectures and interesting magnetic properties. This class of complexes definitely require more exploration and investigation structurally and magnetically, since there are not many examples reported in the literature up to now. However, more and more research groups lately focus their interest towards this direction and many more exciting complexes are awaiting to be discovered and will be unveiled the coming years. One such example will be presented and analyzed in the coming sections.

1.5 The choice of the metal ions

One of the greatest requirements, widely known and accepted among the chemists and physicists working either at the field of bulk magnetism or molecular nanoscale systems, is the paramagnetic nature of the metal ions used in any kind of magnetic material. In other words spin is necessary to be present. As such, the metal ions that are used for the construction of such materials, dictate the overall physical properties and more precisely the magnetic behavior of the final compound.

In the field of molecular magnetism all these years, the most widely used metal ions for the synthesis and characterization of single-molecule magnets (SMMs) or single-ion magnets (SIMs) were the first raw transition metal ions at the beginning, while later on the focus was turned into lanthanides. Thus, all these examples that have been studied already, always include at least one paramagnetic metal center with preferably anisotropic electronic structure. These factors helped the field to progress towards the use of 4*f* metal ions which are paramagnetic and highly anisotropic, at the same time. Most examples in the literature are either homometallic or heterometallic compounds of Dy(III), which is a Kramer ion. Kramer ions are ions with non-integer spin and they are a favorite choice of synthetic chemists since ground-state bistability is always ensured.[26,28,29] However, there are many high energy barriers reported in the literature, from complexes composed by Tb(III) ions (non-Kramer ion), nevertheless in these cases other factors ensured the bistability of the ground state of the compound.[27,28]

In the present thesis, complexes of heterometallic Mn^{III}/Ln, Fe^{III}/Ln and Ga^{III}/Ln will be presented. Manganese belongs to the first row transition metal ions and in the +3 oxidation state has a [Ar]3d^4 electronic configuration. This +3 oxidation state of Manganese is also known to be highly anisotropic since Jahn-Teller effects take place. Thus, our aim towards the use of Mn(III) ions along with Ln(III) ions, was the synthesis and characterization of new 3d/4f 12-MC-4 metallacrown complexes in order to investigate and possibly evaluate the final magnetic behavior. Iron ions also belong to the first row transition metals and in the + 3 oxidation state they possess a [Ar]$3d^5$ configuration. Fe(III) is known to have a preference adopting a six-coordinate mode thus it is almost always in octahedral geometry. When in octahedral geometry, Fe(III) possess a spin of 5/2 making these ions highly paramagnetic along with Mn(II) ions (S

= 5/2). The fact that always the +3 oxidation of metal ions used was preferred, has to do with the organic ligand used considering the structural requirements in terms of charge balance considerations, as discussed in previous chapters. In the present Thesis, the results that will be presented have been obtained by the exclusive use of salicylhydroxamic acid abbreviated as $shiH_3$ (Figure 1.5.1) which is a triprotic ligand. As such, for the construction of metallacrown compounds it was considered necessary to use exclusively ring metal ions that would be in the +3 oxidation state.

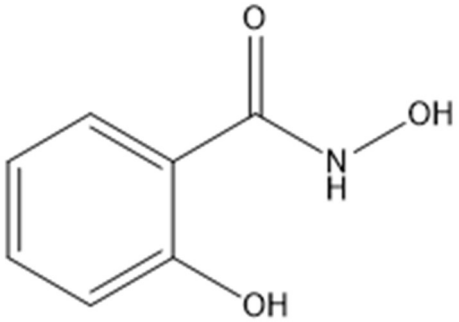

Figure 1.5.1: Schematic representation of salicylhydroxamic acid, abbreviated as $shiH_3$.

Apart from the use of paramagnetic metal ions, in this Thesis results using Ga(III) ions, as ring metal ions in Metallacrowns complexes, will be presented. Gallium belongs to group 13 (Boron group) and in the +3 oxidation state it possees a $[Ar]3d^{10}$ electronic configuration, like Zn(II). In 2014, there was a very interesting paper that appeared in the literature, discussing the effect of diamagnetic metal ions in the enhancement of the effective energy barrier.[71] According that paper, diamagnetic Zn(II) metal ions can enhance the effective energy barrier of SMMs. Upadhyay *et al*, synthesized a $[ZnDy(NO_3)_2(L)_2(CH_3CO_2)]$ and a $[Dy(HL)_2(NO_3)_3]$ complex using the Schiff base 2-methoxy-6-[(E)-phenyliminomethyl]phenol as a ligand (Figure 1.5.2) and performed experimental and theoretical studies of both complexes. Experimentally, it was observed that the complex possessing Zn(II) had a larger U_{eff} value than the mononuclear dysprosium compound. Searching for an explanation they performed DFT (Density Functional Theory) calculations and they discovered that the presence of the diamagnetic Zn(II) ions was causing larger polarization effects on the O atoms of the coordinating ligand and that in turn was leading to larger electrostatic interactions on the Dysprosium ion.

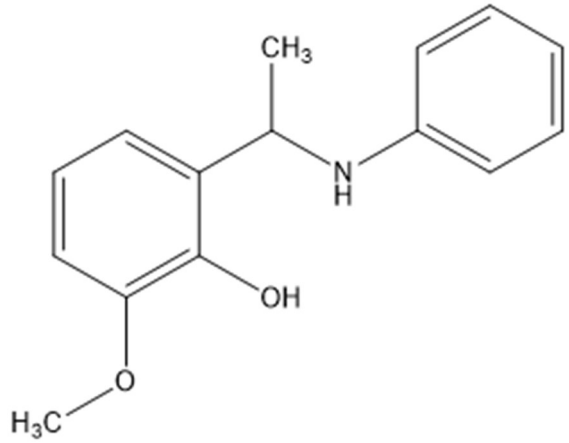

Figure 1.5.2: Schematic representation of 2-methoxy-6-[(E)-phenyliminomethyl]phenol discussed in the text.

This resulted, according to their findings, in the destabilization of the excited states which led to a bigger gap between the ground state and the first excited state. Thus, they concluded that this effect helps with the enhancement of the anisotropy barrier, U_{eff} which was established by their experiments.[71]

Having all these things in mind and by observing that, by that time, no Ga(III)/Ln(III) had been published in the literature, my aims were turned into the synthesis and magnetic characterization of new 12-MC-4 Ga(III)/Ln(III) MCs hoping to be able to observe an enhanced anisotropy barrier compared to the other MCs published, which were based on paramagnetic ring metal ions. By that time, there were some Metallacrowns reported using Zn(II) as ring metal ions but not in the 12-MC-4 motif, not with salicylhydroxamic ligand as the organic counterpart and most importantly non of these complexes had been magnetically investigated.[72–74]

1.6 Scope of this Thesis

As discussed at the above sections of Introduction, it is clear, that the field of Molecular Magnetism is a rapidly developing field since the demand on storage applications gets higher and higher. The field has progressed immensely since 1993, reaching today the moment having molecules operating at temperatures above 77 K which is the temperature that nitrogen liquefies.[30] A promising scaffold, for exploring the SMM behavior within the class of magnetic molecules, is the wide-known Metallacrown scaffold. The reasons for that have been extensively explained at section 1.3, nevertheless it is worth mentioning again that Metallacrowns have a great topology for combining both transition metal ions and lanthanides, taking advantage of the assets of both categories. Thus, the objective at this Thesis will be the synthesis and magnetic characterization of new Ln(III) 12-MC-4 Metallacrown complexes in terms of validating the hypothesis mentioned above. The fact that the Metallacrown scaffold seems like a promising motif for investigating the magnetic properties of molecules, is something that seems quite obvious, however, not many examples exist in the literature that verify that.

The main aim of this Thesis is the synthesis and characterization of 12-MC-4 MCs using salicylhydroxamic acid as a bridging/chelating ligand. This ligand has been used quite extensively by now and has proven to posses the correct geometry that leads to the formation of the 12-MC-4 complexes. The choice of the ring metal ion developed after thorough consideration, concerning what would be the interest of investigation every time, and a general overview of the chapters below explains the rational behind.

Chapter 2 deals with the synthesis, structural and magnetic characterization of a new family of Mn(III)/Ln(III) 12-Metallacrown-4 complexes. The synthesis and magnetic characterization is thoroughly reported, while fitting of the exchange coupling parameters is also provided. The fitting of the magnetic data is the salient feature of that paper, since no fitting scheme and results had been previously reported, concerning the strength of the magnetic exchange interactions at Metallacrowns scaffolds. Nevertheless, the complexes found to possess no alternating-current (ac) data, at the operating temperature of our SQUID (Superconductive Quantum Interface Device) magnetometer and as a result the obtained family of complexes could not be further

investigated since they do not show any SMM behavior at the temperature ranges our SQUID allows.

Chapter 3 covers the synthesis and magnetic investigation of a family of a mixed Fe(III)/ Ln(III) 9-MC-3/12-MC-4 complexes or else a [3.3.1] Metallacryptand family of compounds. The structural conformation of these complexes and the choice of the metal ions, in combination with the organic ligand used, are of great interest since not many examples have been reported having this type of structural motif.[75,76] All compounds have been tested for SMMs properties and the {Fe_6Dy} analogue exhibits frequency dependent out-of-phase signals. Cole-cole plots were constructed for the molecule and fitting of the Arrhenius law gave an effective energy barrier of 10.4 K. Fitting of the {Fe_6Y} compound revealed also the presence of both antiferromagnetic and slightly ferromagnetic interactions between the metals spin carriers. More details are give at the corresponding chapter.

Chapter 4 discuss the synthesis and characterization of the fist double-decker Ga(III)/Dy 12-MC-4 compound ever to be reported. So far, no other sandwich type or double-decker complex has been reported in the literature. The chapter deals firstly with the synthesis of the compound and extensively discusses its structural features. Alternating-current (ac) susceptibility studies were also performed and they showed that the pioneer {Ga_8Dy} compound belongs to the SMM family. Fitting of the Arrhenius law gave an effective energy barrier of U_{eff} = 40 K. Theoretical calculations were also performed and showed that the ground state wave function is mainly composed by the $|\pm 11/2>$ in the easy axis direction that being consistent with the appearance of slow relaxation of magnetization in our {Ga_8Dy} complex.

Chapter 5 contains a library of unpublished results of compounds that have been isolated and will be later on published. The majority of these compounds are Ga(III) centred while there is also a family of Fe(III)/Ln(III) complexes reported. All of the complexes that will be discussed in this chapter have been structurally and magnetically characterized. More details will be found in the corresponding chapter.

1.7 References

[1] R. Sessoli, D. Gatteschi, A. Caneschi, M. A. Novak, *Nature* **1993**, *365*, 141–143.

[2] R. Sessoli, H. L. Tsai, A. R. Schake, S. Wang, J. B. Vincent, K. Folting, D. Gatteschi, G. Christou, D. N. Hendrickson, *Journal of the American Chemical Society* **1993**, *115*, 1804–1816.

[3] D. Gatteschi, R. Sessoli, J. Villain, *Molecular Nanomagnets*, Oxford University Press, **2006**.

[4] A. A. Athanasopoulou (2015) 'Polynuclear Ni(II) Complexes with Schiff Bases as Bridging Ligands: A Molecular Approach to Nanoscience', MSc Thesis, Brock University Digital Repository, brock.10464.7089.

[5] R. Vincent, S. Klyatskaya, M. Ruben, W. Wernsdorfer, F. Balestro, *Nature* **2012**, *488*, 357–360.

[6] L. Bogani, W. Wernsdorfer, *Nature Materials* **2008**, *7*, 179–186.

[7] K. Katoh, H. Isshiki, T. Komeda, M. Yamashita, *Coordination Chemistry Reviews* **2011**, *255*, 2124–2148.

[8] K. Katoh, H. Isshiki, T. Komeda, M. Yamashita, *Chemistry - An Asian Journal* **2012**, *7*, 1154–1169.

[9] R. Bagai, G. Christou, *Chemical Society Reviews* **2009**, *38*, 1011.

[10] Y.-N. Guo, G.-F. Xu, Y. Guo, J. Tang, *Dalton Transactions* **2011**, *40*, 9953.

[11] M. A. Novak, W. S. D. Folly, J. P. Sinnecker, S. Soriano, *Journal of Magnetism and Magnetic Materials* **2005**, *294*, 133–140.

[12] C. Lampropoulos, G. Redler, S. Data, K. A. Abboud, S. Hill, G. Christou, *Inorganic Chemistry* **2010**, *49*, 1325–1336.

[13] N. E. Chakov, S-C. Lee, A. G. Harter, P. L. Kuhns, A. P. Reyes, S. O. Hill, N. S. Dalal, W. Wernsdorfer, K. A. Abboud, G. Christou, *Nature* **1996**, *383*, 145–147.

[14] F. Neese, D. A. Pantazis, *Faraday Discuss.* **2011**, *148*, 229–238.

[15] D. Gatteschi, R. Sessoli, A. Cornia, *Chemical Communications* **2000**, 725–732.

[16] K. Weighardt, K. Pohl, I. Jibril, G. Huttner, *Angewandte Chemie International Edition in English* **1984**, *23*, 77–78.

[17] C. J. Milios, A. Vinslava, W. Wernsdorfer, S. Moggach, S. Parsons, S. P. Perlepes, G. Christou, E. K. Brechin, *Journal of the American Chemical Society* **2007**, *129*, 2754–2755.

[18] G. Aromí, S. Parsons, W. Wernsdorfer, E. K. Brechin, E. J. L. McInnes, *Chemical Communications* **2005**, 5038.

[19] K. Chakarawet, P. C. Bunting, J. R. Long, *Journal of the American Chemical Society* **2018**, *140*, 2058–2061.

[20] C. Delfs, D. Gatteschi, L. Pardi, R. Sessoli, K. Wieghardt, D. Hanke, *Inorganic Chemistry* **1993**, *32*, 3099–3103.

[21] C. A. Christmas, H. L. Tsai, L. Pardi, J. M. Kesselman, P. K. Gantzel, R. K. Chadha, D. Gatteschi, D. F. Harvey, D. N. Hendrickson, *Journal of the American Chemical Society* **1993**, *115*, 12483–12490.

[22] W. Wernsdorfer, R. Sessoli, A. Caneschi, D. Gatteschi, A. Cornia, D. Mailly, *Journal of Applied Physics* **2000**, *87*, 5481–5486.

[23] N. Ishikawa, M. Sugita, T. Ishikawa, S. Koshihara, Y. Kaizu, *Journal of the American Chemical Society* **2003**, *125*, 8694–8695.

[24] B. Wybourne, *Spectroscopic Properties Of Rare Earths*, **1965**.

[25] A. Abragam, B. Bleaney, *Electron Paramagnetic Resonance of Transition Ions*, Oxford University Press, Oxford, **2012**.

[26] J. D. Rinehart, J. R. Long, *Chemical Science* **2011**, *2*, 2078.

[27] J. Sievers, *Zeitschrift f*[illegible]*r Physik B Condensed Matter* **1982**, *45*, 289–296.

[28] N. Ishikawa, T. Iino, Y. Kaizu, *The Journal of Physical Chemistry A* **2002**, *106*, 9543–9550.

[29] N. Ishikawa, M. Sugita, T. Okubo, N. Tanaka, T. Iino, Y. Kaizu, *Inorganic Chemistry* **2003**, *42*, 2440–2446.

[30] F.-S. Guo, B. M. Day, Y.-C. Chen, M.-L. Tong, A. Mansikkamäki, R. A. Layfield, *Science* **2018**, eaav0652.

[31] W. Haase, S. Wróbel, in *Relaxation Phenomena* (Eds.: W. Haase, S. Wróbel), Springer Berlin Heidelberg, Berlin, Heidelberg, **2003**, pp. 1–9.

[32] *Magnetochemistry*, Springer Berlin Heidelberg, Berlin, Heidelberg, **1986**.

[33] J. M. Zadrozny, M. Atanasov, A. M. Bryan, C.-Y. Lin, B. D. Rekken, P. P. Power, F. Neese, J. R. Long, *Chem. Sci.* **2013**, *4*, 125–138.

[34] L. Ungur, J. J. Le Roy, I. Korobkov, M. Murugesu, L. F. Chibotaru, *Angewandte Chemie International Edition* **2014**, *53*, 4413–4417.

[35] S.-D. Jiang, B.-W. Wang, G. Su, Z.-M. Wang, S. Gao, *Angewandte Chemie International Edition* **2010**, *49*, 7448–7451.

[36] F.-S. Guo, B. M. Day, Y.-C. Chen, M.-L. Tong, A. Mansikkamäki, R. A. Layfield, *Science* **2018**, eaav0652.

[37] F.-S. Guo, B. M. Day, Y.-C. Chen, M.-L. Tong, A. Mansikkamäki, R. A. Layfield, *Angewandte Chemie International Edition* **2017**, *56*, 11445–11449.

[38] C. A. P. Goodwin, F. Ortu, D. Reta, N. F. Chilton, D. P. Mills, *Nature* **2017**, *548*, 439.

[39] M. S. Lah, V. L. Pecoraro, *Journal of the American Chemical Society* **1989**, *111*, 7258–7259.

[40] G. Mezei, C. M. Zaleski, V. L. Pecoraro, *Chemical Reviews* **2007**, *107*, 4933–5003.

[41] A. A. Athanasopoulou, C. Gamer, L. Völker, Eva Rentschler, *NOVEL MAGNETIC NANOSTRUCTURES: Unique Properties and Applications.*, ELSEVIER, S.L., **2018**.

[42] M. Ostrowska, I. O. Fritsky, E. Gumienna-Kontecka, A. V. Pavlishchuk, *Coordination Chemistry Reviews* **2016**, *327–328*, 304–332.

[43] V. L. Pecoraro, *Inorganica Chimica Acta* **1989**, *155*, 171–173.

[44] A. J. Stemmler, J. W. Kampf, V. L. Pecoraro, *Inorganic Chemistry* **1995**, *34*, 2271–2272.

[45] M. Remelli, D. Bacco, F. Dallavalle, E. Lazzari, N. Marchetti, M. Tegoni, *Dalton Transactions* **2013**, *42*, 8018.

[46] P. Happ, C. Plenk, E. Rentschler, *Coordination Chemistry Reviews* **2015**, *289–290*, 238–260.

[47] T. C. Stamatatos, S. Dionyssopoulou, G. Efthymiou, P. Kyritsis, C. P. Raptopoulou, A. Terzis, R. Vicente, A. Escuer, S. P. Perlepes, *Inorganic Chemistry* **2005**, *44*, 3374–3376.

[48] A. J. Stemmler, J. W. Kampf, V. L. Pecoraro, *Angewandte Chemie International Edition in English* **1996**, *35*, 2841–2843.

[49] C. Y. Chow, E. R. Trivedi, V. Pecoraro, C. M. Zaleski, *Comments on Inorganic Chemistry* **2015**, *35*, 214–253.

[50] C. Y. Chow, S. V. Eliseeva, E. R. Trivedi, T. N. Nguyen, J. W. Kampf, S. Petoud, V. L. Pecoraro, *Journal of the American Chemical Society* **2016**, *138*, 5100–5109.

[51] T. T. Boron, J. C. Lutter, C. I. Daly, C. Y. Chow, A. H. Davis, A. Nimthong-Roldán, M. Zeller, J. W. Kampf, C. M. Zaleski, V. L. Pecoraro, *Inorganic Chemistry* **2016**, *55*, 10597–10607.

[52] M. R. Azar, T. T. Boron, J. C. Lutter, C. I. Daly, K. A. Zegalia, R. Nimthong, G. M. Ferrence, M. Zeller, J. W. Kampf, V. L. Pecoraro, et al., *Inorganic Chemistry* **2014**, *53*, 1729–1742.

[53] F. Cao, S. Wang, D. Li, S. Zeng, M. Niu, Y. Song, J. Dou, *Inorganic Chemistry* **2013**, *52*, 10747–10755.

[54] A. Athanasopoulou, L. Carrella, E. Rentschler, *Inorganics* **2018**, *6*, 66.

[55] D. Phlip, *Advanced Materials* **1996**, *8*, 866–868.

[56] H. Piotrowski, K. Polborn, G. Hilt, K. Severin, *Journal of the American Chemical Society* **2001**, *123*, 2699–2700.

[57] M. Fujita, Y. J. Kwon, S. Washizu, K. Ogura, *Journal of the American Chemical Society* **1994**, *116*, 1151–1152.

[58] J. J. Bodwin, V. L. Pecoraro, *Inorganic Chemistry* **2000**, *39*, 3434–3435.

[59] M. Moon, I. Kim, M. S. Lah, *Inorganic Chemistry* **2000**, *39*, 2710–2711.

[60] J. Kim, A. S. Ichimura, R. H. Huang, M. Redko, R. C. Phillips, J. E. Jackson, J. L. Dye, *Journal of the American Chemical Society* **1999**, *121*, 10666–10667.

[61] C. M. Zaleski, E. C. Depperman, C. Dendrinou-Samara, M. Alexiou, J. W. Kampf, D. P. Kessissoglou, M. L. Kirk, V. L. Pecoraro, *Journal of the American Chemical Society* **2005**, *127*, 12862–12872.

[62] M. S. Lah, B. R. Gibney, D. L. Tierney, J. E. Penner-Hahn, V. L. Pecoraro, *Journal of the American Chemical Society* **1993**, *115*, 5857–5858.

[63] C. Dendrinou-Samara, M. Alexiou, C. M. Zaleski, J. W. Kampf, M. L. Kirk, D. P. Kessissoglou, V. L. Pecoraro, *Angewandte Chemie International Edition* **2003**, *42*, 3763–3766.

[64] J. C. Lutter, S. V. Eliseeva, J. W. Kampf, S. Petoud, V. L. Pecoraro, *Chemistry - A European Journal* **2018**, *24*, 10773–10783.

[65] A. W. Addison, T. N. Rao, J. Reedijk, J. van Rijn, G. C. Verschoor, *J. Chem. Soc., Dalton Trans.* **1984**, 1349–1356.

[66] C. Benelli, D. Gatteschi, *Chemical Reviews* **2002**, *102*, 2369–2388.

[67] M. L. Kahn, R. Ballou, P. Porcher, O. Kahn†, J.-P. Sutter, *Chemistry - A European Journal* **2002**, *8*, 525–531.

[68] G. Abbas, Y. Lan, G. E. Kostakis, W. Wernsdorfer, C. E. Anson, A. K. Powell, *Inorganic Chemistry* **2010**, *49*, 8067–8072.

[69] S. Osa, T. Kido, N. Matsumoto, N. Re, A. Pochaba, J. Mrozinski, *Journal of the American Chemical Society* **2004**, *126*, 420–421.

[70] J. Tang, I. Hewitt, N. T. Madhu, G. Chastanet, W. Wernsdorfer, C. E. Anson, C. Benelli, R. Sessoli, A. K. Powell, *Angewandte Chemie International Edition* **2006**, *45*, 1729–1733.

[71] A. Upadhyay, S. K. Singh, C. Das, R. Mondol, S. K. Langley, K. S. Murray, G. Rajaraman, M. Shanmugam, *Chem. Commun.* **2014**, *50*, 8838–8841.

[72] J. Jankolovits, C. M. Andolina, J. W. Kampf, K. N. Raymond, V. L. Pecoraro, *Angewandte Chemie International Edition* **2011**, *50*, 9660–9664.

[73] J. Jankolovits, J. W. Kampf, V. L. Pecoraro, *Chinese Chemical Letters* **2015**, *26*, 444–448.

[74] E. R. Trivedi, S. V. Eliseeva, J. Jankolovits, M. M. Olmstead, S. Petoud, V. L. Pecoraro, *Journal of the American Chemical Society* **2014**, *136*, 1526–1534.

[75] W. Yang, H. Yang, S.-Y. Zeng, D.-C. Li, J.-M. Dou, *Dalton Transactions* **2017**, *46*, 13027–13034.

[76] T. Lou, H. Yang, S. Zeng, D. Li, J. Dou, *Crystals* **2018**, *8*, 229.

Chapter 2

This chapter deals with the synthesis and characterization of a novel family of Mn(III)/Ln(III) 12-MC-4 complexes, in which, a 1-J and a 2-J fitting coupling model has been employed and reported for the first time in 3*d*/4*f* MCs. This paper has already been published in Inorganics by the reference details Athanasopoulou *et al.*, Inorganics **2018**, *6*, 66 with the corresponding DOI: 10.3390/inorganics6030066.

Synthesis, Structural and Magnetic Characterization of a Mixed 3*d*/4*f* 12-Metallacrown-4 Family of Complexes

Angeliki A. Athanasopoulou[1,2], Luca M. Carrella [1] and Eva Rentschler [1,*]

1 Institute of Inorganic and Analytical Chemistry, Johannes Gutenberg University Mainz, Duesbergweg 10-14, D-55128 Mainz, Germany; aathanas@uni-mainz.de

2 Graduate School Materials Science in Mainz, Staudinger Weg 9, D-55128 Mainz, Germany

* Correspondence: rentschl@uni-mainz.de; Tel.: +49 6131 39 25491

Author Contributions

Angeliki A. Athanasopoulou designed and performed the experiments regarding the isolation of complex **1-3**. She also performed infrared (IR), UV-Vis studies as well as collected and prepared the samples for elemental analysis and SQUID magnetometry. Single-crystal X-ray measurements were performed from Dr. Dieter Schollmeyer while the refinement of collected data was performed by Dr. Luca M. Carrella. Evaluation of magnetic studies was done by Angeliki A. Athanasopoulou along with the assistance of Dr. Luca M. Carrella. The manuscript was written by Angeliki A. Athanasopoulou while important input was added by Luca M. Carrella and Eva Rentschler. Finally, Eva Rentschler had the overall supervision in the interpretation of data throughout the manuscript process.

2.1 Abstract

A new family of complexes ($^{t}Bu_4N$){[$Ln^{III}(O_2CBu^{t})_4$][12-MC-$_{Mn(III)N(shi)}$-4]}•$5CH_2Cl_2$ (Ln = Gd (**1**) and Tb (**2**)), ($^{t}Bu_4N)_2${[$Y^{III}(O_2CBu^{t})_4$][12-MC-$_{Mn(III)N(shi)}$-4]}(ClO_4) (**3**); where $shiH_3$= salicylhydroxamic acid; $Bu^{t}CO_2^-$ = pivalate ions; $^{t}Bu_4N$= tetrabutylammonium and ClO_4^- = perchlorate ions, has been isolated. The reaction of salicylhydroxamic acid with

$Mn(O_2CBu^t)_2 \cdot 2H_2O$, $Ln(NO_3)_3 \cdot xH_2O$, $^tBu_4NClO_4$ in the presence of morpholine (C_4H_9NO) led to the isolation of compounds **1-3**. The complexes belong to the 12-MC-4 family of Metallacrowns (MCs) possessing a central $\{Mn_4^{III}Ln^{III}(\mu\text{-}NO)_4\}^{11+}$ core with the four Mn^{III} atoms occupying the periphery positions, while the formed [Mn-N-O] repeating unit, assists in the accommodation of the Ln^{III} atom in the center of the ring. Peripheral ligation is provided by four $\eta^1:\eta^1:\mu$ pivalate ions. Direct current magnetic susceptibility (dc) measurements revealed the presence of predominant antiferromagnetic exchange interactions within the metal centers. A 1-*J* fitting model was used in order to quantify the Mn^{III}-Mn^{III} interactions and fitting of the data, for the diamagnetic Y^{III} analogue, gave J = -3.74 cm^{-1} and $g_{Mn(III)} = 2.07$. Fitting of the $\{Mn_4Gd\}$ compound using a 2-*J* model, counting additionally for the Mn^{III}-Gd^{III} interactions, revealed values of J_1 = -3.52 cm^{-1}, J_2 = -0.45 cm^{-1} and $g_{Mn(III)} = 1.99$.

Keywords: metallacrowns; single-molecule magnets (SMMs); heterometallic complexes; inorganic synthesis; coordination chemistry

2.2 Introduction

Heterometallic 3*d*/4*f* complexes continue to attract the interest of scientific community since they have been proven good candidates for possible applications in various fields such as optics [1,2], catalysis [3] and molecular magnetism [4]. In the field of molecular magnetism, the use of paramagnetic 3*d* metal ions in combination with highly anisotropic lanthanides such as Dy^{III} or Tb^{III} with large and unquenched orbital angular momenta [5], can lead to single-molecule magnetism (SMM) behavior with large anisotropy barriers (or energy barriers) for the magnetization reversal. In a common understanding, an SMM is able to retain its magnetization, only as long as it is kept below a characteristic blocking temperature, T_B, in the absence of an applied magnetic field [6]. The magnitude of the energy barrier to spin reversal (U_{eff}) in 3*d* SMMs is equal to $S^2|D|$ for integer and $(S^2 - 1/4)|D|$ for half-integer spin systems, where D is the zero-field splitting parameter. Thus, the total spin of the molecule, S, and the Ising-type magnetic anisotropy, are the two factors that block the magnetization reversal. In transition metal complexes the ground state bistability arises from the total spin S with the ensuing $[2S+1]m_s$ microstates while in lanthanides the spin-orbit-coupled ground term $^{2S+1}L_J$ splits into

[2J +1] m_J microstates which are responsible for the magnetic bistability of those complexes[5]. Experimentally, we can detect the slow magnetic relaxation of SMMs by performing alternating-current (ac) susceptibility measurements and most importantly by the observation of hysteresis loops, which is the ultimate diagnostic property of bulk classical magnets [7]. Recently, quantum tunneling of magnetization (QTM) [8,9] and quantum interference promote the discussion of SMMs as being ideal candidates for even more advanced applications such as spintronics and quantum computing [9–11].

Metallacrowns (MCs) is a class of compounds that since their discovery has attracted the immense attention of the scientific community [12–14]. Most of these complexes have repeatedly demonstrated their ability to encapsulate a central metal ion in their MC cavity, similar to crown ethers, and till now a wide range of MC sizes has been reported [15]. The first example of a 12-MC-4 was reported in 1989 by Pecoraro and Lah, and it was a $Mn(OAc)_2$[12-MC-$_{MnIII(N)shi}$-4] complex where $^{-}$OAc is acetate ions and shi^{3-} is salicylhydroximate ions [13]. Pecoraro and coworkers have exceedingly demonstrated that salicylhydroxamic acid ($shaH_2$, Scheme 1) can possibly be subjected to a metal assisted 2-amide-iminol tautomerism, which leads to salicylhydroxime ($shiH_3$, Scheme 1); the latter being an excellent chelating-bridging ligand which has also been shown to possess the appropriate geometry to afford the 12-MC-4 motif [1,15]. The formed repeating unit of [Mn^{III}-N-O], along with the triply deprotonated salicylhydroximate, the central Mn^{II} ion and the two acetate bridges were responsible for the aforementioned configuration. Usually, in the central MC cavity sits a transition metal ion, even though there are also reports where alkali and alkaline earth metals occupy the cavity[15,16]. Lately, the focus has been turned into the incorporation of lanthanide ions in the center, since these compounds have been proposed as excellent candidates for molecular recognition [17,18], molecular magnetism [19] and luminescent [1,19–22] technologies.

Although there have been numerous 12-MC-4 complexes reported to date, only a few comprise the 3d/4f motif with salicylhydroxamic acid ($shiH_3$) [23–25]. If we further restrict the above requirements, by exclusively using Mn^{III} as the periphery ring metal ion, only a very few papers have been published featuring the above qualifications. Pecoraro and Zaleski reported a complex with the general formula being $Ln^{III}M^{I}(OAc)_4$[12-MC-$_{MnIII(N)shi}$-4]$(H_2O)4\cdot6DMF$ where M^{I} = Na^{I} and K^{I} and Ln= various lanthanides [26–28]. This family of compounds has been extensively structurally studied but the authors did focus their investigations mainly towards the effect that the Na^{I} or K^{I} ions had on magnetic measurements and not on the pure $\{Mn_4^{III}Ln^{III}(\mu\text{-}NO)4\}^{11+}$ magnetic core, without emphasizing on the evaluation of exchange

interactions by fitting of the data. Our group has a great interest on the synthesis and magnetic characterization of MCs and so far has dealt with the isolation of homometallic and heterometallic ones based on transition metal ions [29–32]. Herein, we report the synthesis, crystal structures and magnetic studies of a rare family of isostructural ($^{t}Bu_4N$){[$Ln^{III}(O_2CBu^{t})_4$][12-MC-$_{Mn(III)N(shi)}$-4]}·$5CH_2Cl_2$ (Ln = Gd (**1**) and Tb (**2**)) and a ($^{t}Bu_4N$)$_2${[$Y^{III}(O_2CBu^{t})_4$][12-MC-$_{Mn(III)N(shi)}$-4]}·(ClO_4) (**3**) compound. This is an unprecedented example of Ln(III)[12-MC-$_{Mn(III)N(shi)}$-4] without the presence of any alkali or alkaline earth metals.

2.3 Crystal structures of compounds 1-3

The general reaction of $Mn(O_2CBu^{t})_2·2H_2O$, $M(NO_3)_3·xH_2O$ (M = Gd^{III}, Tb^{III}, Y^{III}), $shaH_2$, $^{t}Bu_4NClO_4$ and morpholine, in a 4:1:4:1:4 molar ratio, in CH_2Cl_2 gave dark brown solutions which were layered with hexanes to give dark brown crystals of ($^{t}Bu_4N$){[$Ln^{III}(O_2CBu^{t})_4$][12-MC-$_{Mn(III)N(shi)}$-4]}•$5CH_2Cl_2$ for **1** and **2** and ($^{t}Bu_4N$)$_2${[$Y^{III}(O_2CBu^{t})_4$][12-MC-$_{Mn(III)N(shi)}$-4]}(ClO_4) for **3** in high yields (> 59%). The chemical and structural identities of the compounds were confirmed with by single-crystal X-ray crystallography, elemental analyses (C, H, N) and IR spectral data (SI).

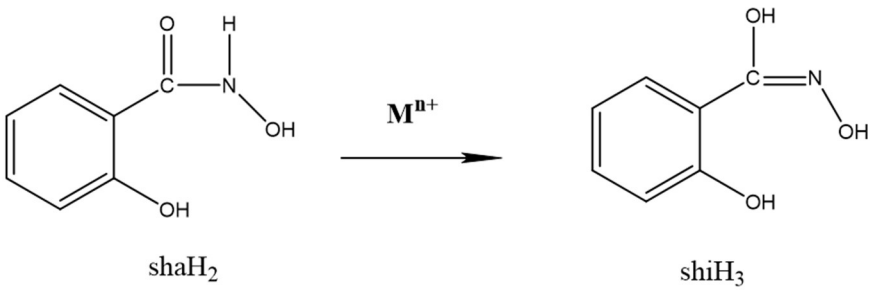

Scheme 1: Illustrative representation and abbreviation of organic molecules discussed in the text.

Single-crystal diffraction studies revealed that compounds **1** and **2** are isostructural and crystallize in the *P*4/*n* tetragonal space group, while complex **3** crystallizes in the *P*4cc tetragonal space group (Table 1, SI). Although complex **3** is not isostructural with complexes **1** and **2**, still it does possess the same core with them and thus, only complex **2** will be thoroughly

described for simplicity reasons. The structure of **2** consists of a $[Tb^{III}(O_2CBu^t)_4][12\text{-}MC\text{-}_{Mn(III)N(shi)}\text{-}4]\}^-$ anion (Fig. 1), one $^tBu_4N^+$ cation and, five non-coordinated CH_2Cl_2 molecules. Its asymmetric unit features one quarter of the $[Tb^{III}(O_2CBu^t)_4][12\text{-}MC\text{-}_{Mn(III)N(shi)}\text{-}4]\}^-$ anion, with the C_4 axis passing through the central Tb^{III} ion. There are two isomers in the structure and only the main part will be discussed. Selected interatomic distances and angles for all complexes are listed in Tables S2 and S3. The core of **2** comprises four Mn^{III} and one Tb^{III} atoms arranged in a square pyramidal-like topology with the Tb atom occupying the apical position of the pyramid and the Mn atoms completing the base (Fig.S1).

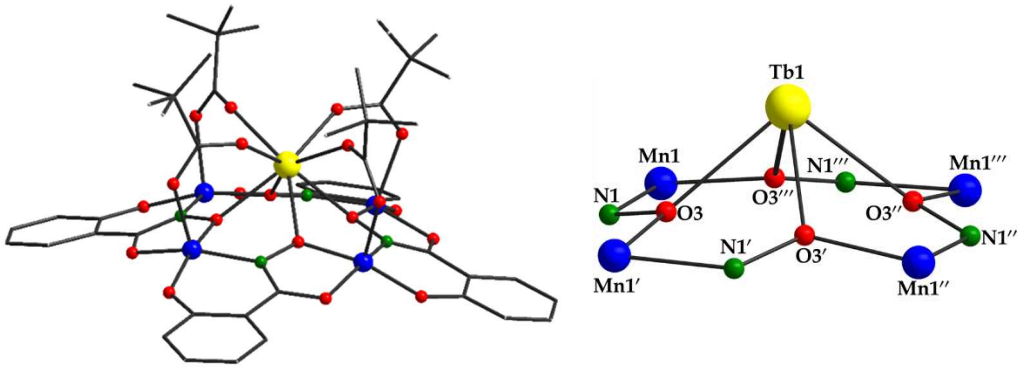

Figure 2.3.1: Schematical representation of molecular structure and labeled schematic representation of the core $\{Mn_4^{III}Ln^{III}(\mu\text{-}NO)_4\}^{11+}$ of complex **2**. Color scheme: Tb, yellow; Mn^{III}, blue; N, green; O, red. H atoms are omitted for clarity.

The basal Mn^{III} atoms are bridged by diatomic oximate bridges provided by the shi^{3-} ligand, giving a Mn…Mn separation of 4.642(9) Å. Note that the coordinated anion of shi^{3-} was generated in situ from the metal ion-assisted transformation of $shaH_2$ under basic conditions. The large Mn–N–O–Mn torsion angle (173.3(4)°), which is very close to the ideal linearity of 180°, is responsible for the approximately ideal planarity of the Mn4 assembly, whilst the Tb^{III} atom lies 1.789(8) Å out of the Mn4 plane. The connection between the basal Mn^{III} and the Tb^{III} atoms is provided by the oximate O atoms of the shi^{3-} ligand resulting in a Mn…Tb separation of 3.739(2) Å. Further ligation is provided by four $\eta^1{:}\eta^1{:}\mu$ bridging pivalate ions (Fig. 1). The coordination sphere around the Mn atoms is completed by the alkoxido and phenoxido O atoms provided by the organic moiety which possesses a $\eta^1{:}\eta^1{:}\eta^1{:}\eta^2{:}\mu_3$ coordination mode leading to an overall inorganic core of $\{Mn_4^{III}Ln^{III}(\mu\text{-}NO)4\}^{11+}$ (Fig.S2, SI).

All Mn^{III} ions are five-coordinate with almost perfect square pyramidal geometry. This has been confirmed by the analysis of the shape-determining bonds and angles using the Reedjik and Addison *et al.* method [33], which gives us a trigonality index, τ, of 0.11 for the four Mn^{III} ions. The τ = 0.1 value is consistent with a square pyramidal geometry, as for a perfect square pyramidal geometry a τ value of 0 is expected, while a τ value of 1 is consistent for a trigonal bipyramidal geometry. The oxidation states of Mn atoms were established by charge balance considerations, metric parameters and bond-valence sum (BVS) calculations [34], with the last providing us with a value of 3.03 for Mn1. Note that the oxidation of Mn^{II} to Mn^{III} occurs undoubtedly by the atmospheric O_2 under the prevailing basic conditions [35,36]. Finally, the central lanthanide ion is eight-coordinate possessing a slightly distorted square antiprismatic geometry with a continuous shape measurement factor of CshM = 0.71 (Figure 1) [37]. The closest this number is to zero, the closest is the geometry of the lanthanide to the ideal one.

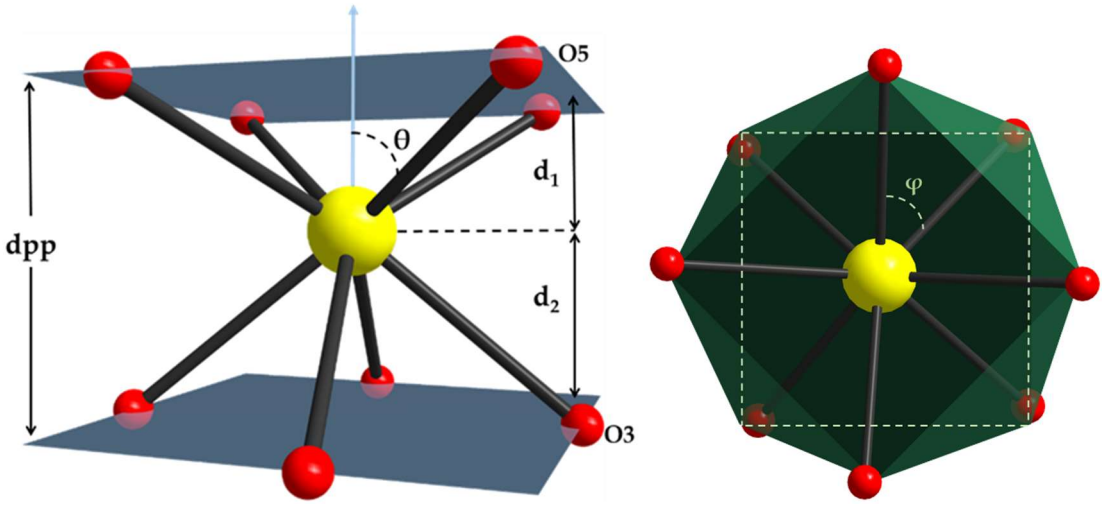

Figure 2.3.2: Details of structural parameters discussed in the text for complex **2**.

Several pivotal geometrical parameters were obtained for complex **2** in order to gain a better understanding of the inner coordination sphere around the lanthanide ion (Fig.2). To be more descriptive, the angle between the four-fold axis and the Ln-O bond direction, θ, corresponds to compression or elongation along the tetragonal axis, depending on its value. The magic value for perfect square-antiprismatic (SAP) geometry is θ = 54.74°, while smaller angles correspond to elongation and wider ones lead to compression [38–40]. In complex **2**, the average value of θ was found to be 56.15°, indicating axial compression. The distance between the upper and lower O_4-planes, interplanar distance (dpp), was found to be 2.639(0) A˚, while the distances

d_1 and d_2 were found to be 1.103(4) A˚ and 1.535(6) A˚, counting for the plane spaned by the carboxylate oxygen atom (O5) and the one by the oximate oxygen (O3),respectively. The symmetry of lanthanide's coordination geometry can be further described by another important parameter which is called skew or twist angle. This is the φ angle which basically defines the angle between the diagonals of the two O_4-planes. This is a vital parameter for the determination of point group symmetry at the lanthanide site, which consequently leads to assisting on the description of the crystal field substate composition of lanthanide complexes. When φ = 0 an ideal square prismatic geometry is expected, while when φ = 45° an ideal square antiprismatic geometry is observed. In complex **2** an average φ value of 43.28(4)° was calculated, further supporting the square antiprismatic geometry of the Tb^{III} ion.

2.4 Magnetic studies of complexes 1-3

Solid state, direct-current (dc) magnetic susceptibility (χ_M) measurements were collected in the temperature range of 2.0-300 K for freshly prepared crystalline samples of **1**, **2** and **3,** under an applied field of 0.1 T. The obtained data are presented as a $\chi_M T$ *vs* T plot in Figure 3. The experimental values at 300 K for all complexes (18.1 $cm^3mol^{-1}K$ for **1**, 21.1 for **2** $cm^3mol^{-1}K$ and 11.4 $cm^3mol^{-1}K$ for **3***)* are lower than the theoretical ones (19.88 $cm^3\ mol^{-1}\ K$ for **1**, 23.82 $cm^3\ mol^{-1}\ K$ for **2** and 12.0 $cm^3\ mol^{-1}\ K$ for **3**) expected for four non-interacting Mn^{III} ions ($S = 2$, g = 2) and one Gd^{III} ($^8S_{7/2}$, $S = 7/2$, $L = 0$, g = 2,), one Tb^{III} ($^7F_6$, $S = 3$, $L = 3$, g = 3/2), or one diamagnetic Y^{III} ion [41]. All complexes possess a similar magnetic behavior, with the $\chi_M T$ steadily decreasing with decreasing tempetarure from 300 K till 2 K, where it reaches values of 6.95 $cm^3\ K\ mol^{-1}$ for **1**, 3.30 $cm^3\ K\ mol^{-1}$for **2** and 0.2 $cm^3\ K\ mol^{-1}$for **3**, respectively. The shape of the $\chi_M T$ *vs* T plots for all complexes indicates the presence of predominant antiferromagnetic exchange interactions within the metal centers. This is further supported by the fact that the $\chi_M T$ values at 300 K for all complexes are lower than the expected theoritical ones.

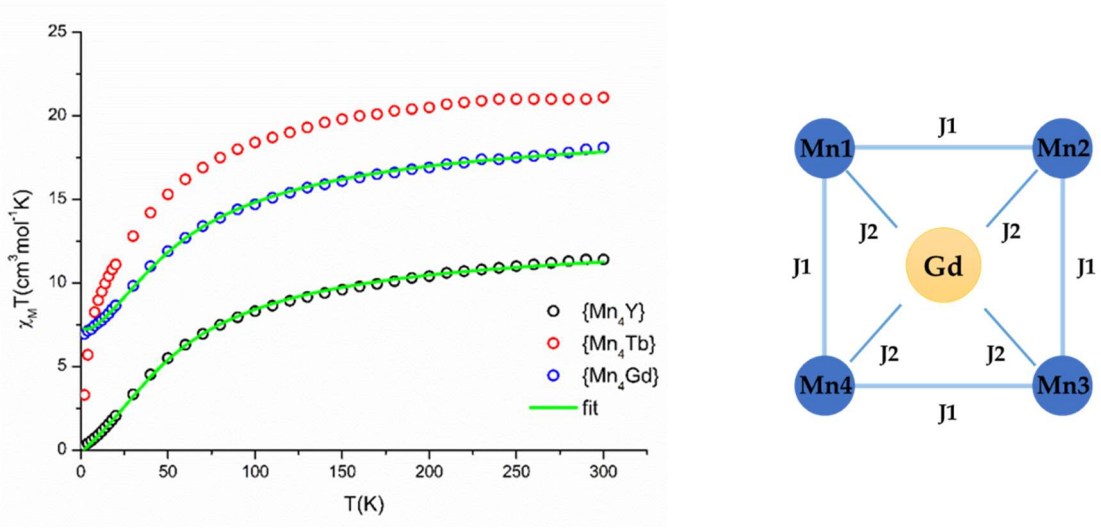

(a) (b)

Figure 2.4.1: (a) Temperature dependance of magnetic susceptibility for complexes **1**, **2** and **3**. Green solid line represents simulation of the data in complex **1** and **3**; see text for details and fitting parameters. (**b**) fitting model for complex **1**.

In order to gain better insight in the strength of the intramolecular Mn^{III} - Mn^{III} magnetic exchange interactions, the magnetic susceptibility data of complex **3** were fit using PHI [42] program. The magnetic susceptibility data of complex **3**, which comprises the diamagnetic Y^{III} ion in the central cavity, were fit using a 1-*J* model according to the spin Hamiltonian:

$$\hat{H} = -2J\,(\hat{S}_{Mn1}\cdot\hat{S}_{Mn2} + \hat{S}_{Mn2}\cdot\hat{S}_{Mn3} + \hat{S}_{Mn3}\cdot\hat{S}_{Mn4} + \hat{S}_{Mn4}\cdot\hat{S}_{Mn1})$$

An excellent simulation of the data (solid green line, Fig. 3) was achieved with a $J = -3.74$ cm^{-1} and g = 2.07. The antiferromagnetic exchange interactions are anticipated for a system that is exclusively coupled via oximate bridges that give very large Mn-N-O-Mn torsion angles, which are known to promote antiferromagnetic exchange interactions [43].

In order to also quantify the nature of the Mn^{III}-Ln^{III} exchange interactions, complex **1** was also fit, using a 2-*J* model, which counts for the outer Mn^{III}-Mn^{III} (J_1) interactions as well as for inner the Mn^{III}-Gd^{III} (J_2) interaction, shown in Figure 3 (b). The data were fit according to the spin Hamiltonian shown below:

$$\hat{H} = -2J_1\,(\hat{S}_{Mn1}\cdot\hat{S}_{Mn2} + \hat{S}_{Mn2}\cdot\hat{S}_{Mn3} + \hat{S}_{Mn3}\cdot\hat{S}_{Mn4} + \hat{S}_{Mn4}\cdot\hat{S}_{Mn1}) - 2J_2(\hat{S}_{Mn1}\cdot\hat{S}_{Gd} + \hat{S}_{Mn2}\cdot\hat{S}_{Gd} + \hat{S}_{Mn3}\cdot\hat{S}_{Gd} + \hat{S}_{Mn4}\cdot\hat{S}_{Gd})$$

An excellent fit of the data (solid green line, Fig.3) could be obtained with J_1 = -3.35 cm^{-1}, J_2 = -0.45 cm^{-1} and $g_{Mn(III)}$ = 1.99. The values of both models are in an excellent agreement. Note that antiferromagnetic exchange interactions, in Mn^{III}-Gd^{III} and other 3*d*-Gd^{III} species, possesing the $3d_{x2-y2}$ orbital unoccupied, are quite often observed [44–47]. Here is the first time that fitting of the magnetic susceptibility data for 3*d*/Gd^{III} interactions has been reported, within the MC family of complexes.

Field-dependent magnetization measurements were also performed for complexes **1** and **2** at temperatures between 2 and 10 K over the range of 0-7 T (Fig. 4 and Fig. S7). The magnetization of **1** and **2** shows a rapid increase below 1 T followed by a slow, nearly linear increase without reaching saturation. The lack of saturation in magnetization of **1** and **2** indicates the presence of magnetic anisotropy and/or population of the Ln^{III} low-lying excited states, as well as the effect from some weak antiferromagnetic components between the metal centers.

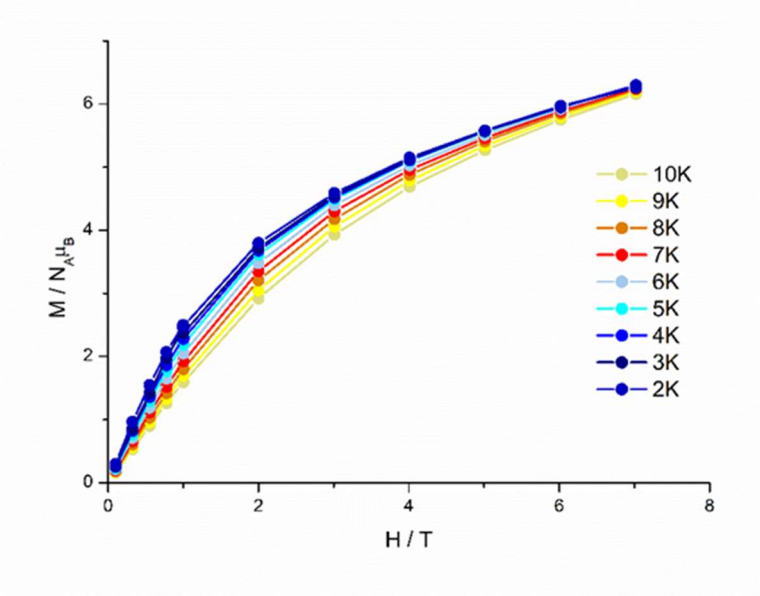

Figure 2.4.2: M vs H plots for complex 2 in various temperatures as indicated. Solid lines are guidelines for the eyes.

2.5 Materials and Methods

2.5.1 General Information

All chemicals and solvents used for synthesis were of reagent grade and used as purchased without further purification. The starting material $Mn(O_2CBu^t)_2{\cdot}2H_2O$ was synthesized using literature procedures [48]. C, H and N elemental analyses were carried out on a Foss Heraeus Vario EL at the Institute of Organic Chemistry at the Johannes Gutenberg University Mainz. Infrared absorption spectra were recorded at room temperature in a range of 3,000-400 cm^{-1} on a Thermo Fischer NICOLET Nexus FT/IR-5700 spectrometer equipped with Smart Orbit ATR Diamond cell. UV-Vis absorption measurements were performed between for complexes **1**, **2** and **3** in MeCN between 200 and 1000 nm on a JASCO V-570 UV/Vis/NIR spectrophotometer (Fig.6, SI).

A similar procedure has been used to isolate compounds **1** - **3**.

$(^tBu_4N)\{[Gd^{III}(O_2CBu^t)_4][12\text{-}MC\text{-}_{Mn(III)N(shi)}\text{-}4]\}^{\bullet}5CH_2Cl_2$ (**1**$^{\bullet}5CH_2Cl_2$): To an almost colorless solution of $shiH_3$ (30.50 mg, 0.2 mmol) and morpholine (18 µL, 0.2mmol) in CH_2Cl_2 was added $Mn(O_2CBu^t)_2{\cdot}2H_2O$ (55.00 mg, 0.2 mmol) followed by stirring for 5 min. To the resulting dark brown almost clear solution $Gd(NO_3)_3{\cdot}H_2O$ (6.00 mg, 0.025 mmol) was added along with $^tBu_4NClO_4$ (26.00 mg, 0.075 mmol) and left for stirring for another 40 min. The solution was subsequently filtered and left for crystallization. Layering hexane gave diffraction quality crystals of **1**$^{\bullet}5CH_2Cl_2$ after 5 days which were collected by filtration, washed with hexanes (3 x 5 mL) and dried in air. Yield: 0.032 g (59%) based on the Gd^{III} ion. The air-dried solid was analyzed as (**1**): C, 47.32; H, 5.46; N, 4.31 %. Found: C, 47.44; H, 5.49; N, 4.38 %. Selected ATR data (cm^{-1}): 2961 (w), 2292 (w), 2875 (w), 1598 (w), 1569 (s), 1538 (w), 1421 (w), 1096 (m), 867 (w), 768 (w), 683 (s), 649 (w), 617 (m), 482 (m).

$(^tBu_4N)\{[Tb^{III}(O_2CBu^t)_4][12\text{-}MC\text{-}_{Mn(III)N(shi)}\text{-}4]\}{\cdot}5CH_2Cl_2$ (**2**$^{\bullet}5CH_2Cl_2$): Compound **2**$^{\bullet}5CH_2Cl_2$ was synthesized with the similar procedure as compound **1**$^{\bullet}5CH_2Cl_2$, except that $Tb(NO_3)_3{\cdot}H_2O$ (8.50 mg, 0.025 mmol) was used instead of $Gd(NO_3)_3{\cdot}H_2O$. Yield: 0.039 g (76%) based on the Tb^{III} ion. The air-dried solid was analyzed as (**2**): C, 47.27; H, 5.46; N, 4.31 %. Found: C, 47.38; H, 5.52; N, 4.34 %. Selected ATR data (cm^{-1}): 2961 (w), 2929 (w), 2874 (w), 1597 (w), 1568 (s), 1537 (w), 1421 (w), 1099 (m), 865 (w), 771 (w), 721 (s), 649 (w), 683 (s), 600 (m), 482(m).

($^{t}Bu_4N)_2\{[Y^{III}(O_2CBu^{t})_4][12\text{-}MC\text{-}_{Mn(III)N(shi)}\text{-}4]\}\cdot(ClO_4)$ (**3**): Compound **3** was synthesized with the similar procedure as compound **1** and **2**, except that this time $Y(NO_3)_3\cdot H_2O$ (0.01 mg, 0.025 mmol) was used. Yield: 0.028 g (59%) based on the Y^{III} ion. The air-dried solid was analyzed as (**3**): C, 50.63; H, 6.59; N, 4.43 %. Found: C, 50.74; H, 6.71; N, 4.51 %. Selected ATR data (cm^{-1}): 2961 (w), 2929 (w), 2874 (w), 1596 (w), 1569 (m), 1424 (w), 1099 (m), 865 (w), 771 (w), 684 (s), 649 (w), 600 (m), 482 (m).

2.5.2 X-Ray Crystallography

X-ray diffraction data for the structure analysis were collected from suitable single crystals on a Bruker SMART with an APEX II CCD detector (**1**, **2**) and on a STOE IPDS 2T (**3**) equipped with an Oxford cooling system operating at 173(2) K (**1**, **2**) and at 120(2)K (**3**), respectively. Graphite-monochromated Mo-Kα radiation (λ = 0.71073 Å) from long-fine focus sealed X-ray tube was used throughout. Data reduction and absorption correction were done with Bruker Apex v3.0 [49,50] and SADABS[x11] (**1**, **2**) or with STOE X-RED[51] (**3**). Structures were solved with SHELXT [52] and refined by full-matrix least-squares on F-squared using SHELXL [53], interfaced through Olex2 [54]. All non-hydrogen atoms were refined with anisotropic displacement parameters, while all hydrogen atoms have been placed on idealized positions using a riding model. In complexes **1**, **2** and **3** the anionic (metallacrown) part show isomerism and are disordered over two positions. The metallacrowns can be arranged clockwise [M-NO-M] or anticlockwise [M-ON-M], with slightly different position for the transition metal ions, while the central lanthanide ions remains on its position in both isomers. The site occupation factor of the isomers were refined free to 0.82/0.18, 0.80/0.20 and 0.91/0.09 for **1, 2** and **3**, respectively. While in **1** and **2** the whole anionic part was refined over two positions, in **3** only the manganese ions were refined over two positions, due to the low occupancy of the second isomer. The cationic counter ions Bu_4N^+ were refined over two positions with a fixed ratio of 0.6/0.4 in **1** and **2**. CCDC 1849727-1849729 (**1**-**3**) contains the supplementary crystallographic data for the structure reported in this paper.

2.5.3 Magnetic Measurements

Variable-temperature direct current (dc) magnetic susceptibility measurements were performed on polycrystalline samples with the use of Quantum Design SQUID magnetometer MPMS-7 equipped with a 7 T magnet. The samples were embedded in eicosane to avoid orientation of the crystallites under applied field. Experimental susceptibility data were corrected for the underlying diamagnetism using Pascal's constants [55]. The temperature dependent magnetic contribution of the holder and of the embedding matrix eicosane were experimentally determined and substracted from the measured susceptibility data. Variable temperature susceptibility data were collected in a temperature range of 2-300K under an applied field of 0.1 Tesla, while magnetization data were collected between 2 and 10 K and magnetic fields up to 7 Tesla. Alternating-current (ac) measurements were performed with an oscillating magnetic field of 3 Oe at frequencies ranging from 1 to 1400 Hz.

2.6 Conclusions

In summary, we reported a new family of Mn^{III}/Ln^{III} 12-MC-4 complexes, derived from the reaction of $Mn(O_2CBu^t)_2 \cdot 2H_2O$ with various nitrate salts of lanthanides in the presence of salicylhydroxamic acid. Direct-current (dc) magnetic susceptibility studies revealed the presence of antiferromagnetic exchange interactions between the metal centers, while fitting of the data using the $\{Mn_4Y\}$ complex allowed us to quantify the strength of the interactions within the outer Mn^{III} ions, which was found to be J = -3.74 cm^{-1} with g = 2.07. Moreover, fitting of the $\{Mn_4Gd\}$ (**1**) data gave an extra insight into the strength of the magnetic exchange interactions, especially for the Mn^{III}-Gd^{III} intramolecular interaction, revealing values of $J_{Mn\text{-}Mn}$ = -3.35 cm^{-1}, $J_{Mn\text{-}Gd}$ = -0.45 cm^{-1} and $g_{Mn(III)}$ = 1.99. Note that this is the first example within the family of metallacrowns (MCs), where simulation of the magnetic data has been reported. In-phase and out-of-phase (ac) magnetic susceptibility measurements as a function of temperature did not reveal any slow relaxation in fields of H_{dc}= 0-3000 Oe. In order to further improve the magnetic properties of such compounds, the chemistry will be broadened to the use of other magnetic or diamagnetic 3*d* and 4*f* metal ions, by means of modifying the structural and/or physical properties of the resulting molecular compounds.

Supplementary Materials: Supplementary materials are available online at www.mdpi.com/xxx/s1 and check cif files of compounds **1**, **2** and **3**, Table S1: Crystallographic date for complexes **1**-**3**, Figure S1: coordination modes of ligands in complex **2**, Figure S2: Labeled schematic representation of the core $\{Mn_4^{III}Ln^{III}(\mu\text{-}NO)_4\}^{11+}$ of complex **2**. Color scheme: Tb, yellow; Mn^{III}, blue; N, green; O, red, Table S2: Selected bond Lengths for complex **2**., Selected Bond Angles for **2**,Table S4: Shape measurements of the 8-coordinate lanthanide coordination polyhedra. The bold numbers indicate the closest polyhedron according to SHAPE calculations, Figure S3: IR spectrum for complex **1**, Figure S4: IR spectrum for complex **2**, Figure S5: IR spectrum for complex **3**, Figure S6: UV-Vis spectra of 1 (black), 2 (red), 3 (blue), and $shiH_3$ (green) in MeCN, Figure S7: *M* vs *H* plots for complex **1** in various temperatures as indicated. Solid lines are guidelines for the eyes.

Author Contributions: Angeliki A. Athanasopoulou designed and performed the experiments. She analyzed most of the data and wrote the paper. Luca M. Carrella refined the structures and helped a lot with his knowledgeable input throughout the paper-writing process. Eva Rentschler was involved during the writing of the paper to every step of the process giving valuable feedback.

Funding: This research received no external funding.

Acknowledgments: We are very greateful to Regine Jung-Pothmann and Dr. Dieter Schollmeyer for the collection of the X-ray diffraction data of all our complexes. Angeliki A. Athanasopoulou is a member of (SFB/TRR) 173 “Spin+X – Spin its collective environment” and a fellow of the Excellence Initiative by the Graduate School Materials Science in Mainz, Germany (DFG/GSC 266), both initiated by the Deutsche Forschungsgemeinschaft (DFG, GermanResearchFoundation).

Conflicts of Interest: The authors declare no conflict of interest.

2.7 References

(1) Chow, C. Y.; Trivedi, E. R.; Pecoraro, V.; Zaleski, C. M. Heterometallic Mixed *3d - 4f* Metallacrowns: Structural Versatility, Luminescence, and Molecular Magnetism. *Comments Inorg. Chem.* **2015**, *35* (4), 214–253.

(2) Jia, R.; Li, H.-F.; Chen, P.; Gao, T.; Sun, W.-B.; Li, G.-M.; Yan, P.-F. Synthesis, Structure, and Tunable White Light Emission of Heteronuclear Zn_2Ln_2 Arrays Using a Zinc Complex as Ligand. *CrystEngComm* **2016**, *18* (6), 917–923.

(3) Evangelisti, F.; Moré, R.; Hodel, F.; Luber, S.; Patzke, G. R. 3d–4f $\{Co^{II}_3Ln(OR)_4\}$ Cubanes as Bio-Inspired Water Oxidation Catalysts. *J. Am. Chem. Soc.* **2015**, *137* (34), 11076–11084.

(4) Rosado Piquer, L.; Sañudo, E. C. Heterometallic 3d–4f Single-Molecule Magnets. *Dalton Trans.* **2015**, *44* (19), 8771–8780.

(5) Woodruff, D. N.; Winpenny, R. E. P.; Layfield, R. A. Lanthanide Single-Molecule Magnets. *Chem. Rev.* **2013**, *113* (7), 5110–5148.

(6) Christou, G.; Gatteschi, D.; Hendrickson, D. N.; Sessoli, R. Single-Molecule Magnets. *MRS Bull.* **2000**, *25* (11), 66–71.

(7) Bagai, R.; Christou, G. The Drosophila of Single-Molecule Magnetism: [Mn12O12(O2CR)16(H2O)4]. *Chem. Soc. Rev.* **2009**, *38* (4), 1011.

(8) Friedman, J. R.; Sarachik, M. P.; Tejada, J.; Ziolo, R. Macroscopic Measurement of Resonant Magnetization Tunneling in High-Spin Molecules. *Phys. Rev. Lett.* **1996**, *76* (20), 3830–3833.

(9) Thomas, L.; Lionti, F.; Ballou, R.; Gatteschi, D.; Sessoli, R.; Barbara, B. Macroscopic Quantum Tunnelling of Magnetization in a Single Crystal of Nanomagnets. *Nature* **1996**, *383* (6596), 145–147.

(10) Bogani, L.; Wernsdorfer, W. Molecular Spintronics Using Single-Molecule Magnets. *Nat. Mater.* **2008**, *7* (3), 179–186.

(11) Urdampilleta, M.; Klyatskaya, S.; Cleuziou, J.-P.; Ruben, M.; Wernsdorfer, W. Supramolecular Spin Valves. *Nat. Mater.* **2011**, *10* (7), 502–506.

(12) Lah, M. S.; Kirk, M. L.; Hatfield, W.; Pecoraro, V. L. The Tetranuclear Cluster Fe III [Fe III (Salicylhydroximato)(MeOH)(Acetate)]3 Is an Analogue of M3+(9-Crown-3). *J. Chem. Soc. Chem. Commun.* **1989**, No. 21, 1606.

(13) Lah, M. S.; Pecoraro, V. L. Isolation and Characterization of {MnII[MnIII(Salicylhydroximate)]4(Acetate)2(DMF)6}.Cntdot.2DMF: An Inorganic Analog of M2+(12-Crown-4). *J. Am. Chem. Soc.* **1989**, *111* (18), 7258–7259.

(14) Dutton, J. C.; Murray, K. S.; Tiekink, E. R. T. Magnetism of Oxovanadium(IV) Complexes of Binucleating Ligands. Oxidation to and Structure of a Mononuclear Oxovanadium(V) Complex of N,N′-(Pentan-3-Ol) Bis(Salicylaldimine). *Inorganica Chim. Acta* **1989**, *166* (1), 5–8.

(15) Mezei, G.; Zaleski, C. M.; Pecoraro, V. L. Structural and Functional Evolution of Metallacrowns. *Chem. Rev.* **2007**, *107* (11), 4933–5003.

(16) Tegoni, M.; Furlotti, M.; Tropiano, M.; Lim, C. S.; Pecoraro, V. L. Thermodynamics of Core Metal Replacement and Self-Assembly of Ca^{2+} 15-Metallacrown-5 †. *Inorg. Chem.* **2010**, *49* (11), 5190–5201.

(17) Jones, L. F.; Kilner, C. A.; Halcrow, M. A. A Cobalt Metallacrown Anion Host with Guest-Dependent Redox Activity. *Chem. - Eur. J.* **2009**, *15* (18), 4667–4675.

(18) Jones, L. F.; Barrett, S. A.; Kilner, C. A.; Halcrow, M. A. Ammonium, Alkylammonium, and Amino Acid Complexes of a Hexacopper Fluoro-Metallacrown Cavitand. *Chem. - Eur. J.* **2008**, *14* (1), 223–233.

(19) Chow, C. Y.; Eliseeva, S. V.; Trivedi, E. R.; Nguyen, T. N.; Kampf, J. W.; Petoud, S.; Pecoraro, V. L. Ga^{3+} /Ln^{3+} Metallacrowns: A Promising Family of Highly Luminescent Lanthanide Complexes That Covers Visible and Near-Infrared Domains. *J. Am. Chem. Soc.* **2016**, *138* (15), 5100–5109.

(20) Trivedi, E. R.; Eliseeva, S. V.; Jankolovits, J.; Olmstead, M. M.; Petoud, S.; Pecoraro, V. L. Highly Emitting Near-Infrared Lanthanide "Encapsulated Sandwich" Metallacrown Complexes with Excitation Shifted Toward Lower Energy. *J. Am. Chem. Soc.* **2014**, *136* (4), 1526–1534.

(21) Ostrowska, M.; Fritsky, I. O.; Gumienna-Kontecka, E.; Pavlishchuk, A. V. Metallacrown-Based Compounds: Applications in Catalysis, Luminescence, Molecular Magnetism, and Adsorption. *Coord. Chem. Rev.* **2016**, *327–328*, 304–332.

(22) A. A. Athanasopoulou; C. Gamer; L. Völker; Eva Rentschler. *NOVEL MAGNETIC NANOSTRUCTURES: Unique Properties and Applications.*; ELSEVIER: S.l., 2018.

(23) Qin, Y.; Gao, Q.; Chen, Y.; Liu, W.; Lin, F.; Zhang, X.; Dong, Y.; Li, Y. Four Mixed 3d-4f 12-Metallacrown-4 Complexes: Syntheses, Structures and Magnetic Properties. *J. Clust. Sci.* **2017**, *28* (3), 891–903.

(24) Cao, F.; Wang, S.; Li, D.; Zeng, S.; Niu, M.; Song, Y.; Dou, J. Family of Mixed 3d–4f Dimeric 14-Metallacrown-5 Compounds: Syntheses, Structures, and Magnetic Properties. *Inorg. Chem.* **2013**, *52* (19), 10747–10755.

(25) Lou, T.; Yang, H.; Zeng, S.; Li, D.; Dou, J. A New Family of Heterometallic LnIII[12-MCFeIIIN(Shi)-4] Complexes: Syntheses, Structures and Magnetic Properties. *Crystals* **2018**, *8* (5), 229.

(26) Azar, M. R.; Boron, T. T.; Lutter, J. C.; Daly, C. I.; Zegalia, K. A.; Nimthong, R.; Ferrence, G. M.; Zeller, M.; Kampf, J. W.; Pecoraro, V. L.; et al. Controllable Formation of Heterotrimetallic

Coordination Compounds: Systematically Incorporating Lanthanide and Alkali Metal Ions into the Manganese 12-Metallacrown-4 Framework. *Inorg. Chem.* **2014**, *53* (3), 1729–1742.

(27) Travis, J. R.; Zeller, M.; Zaleski, C. M. Facile Carboxylate Ligand Variation of Heterotrimetallic 12-Metallacrown-4 Complexes. *Polyhedron* **2016**, *114*, 29–36.

(28) Boron, T. T.; Lutter, J. C.; Daly, C. I.; Chow, C. Y.; Davis, A. H.; Nimthong-Roldán, A.; Zeller, M.; Kampf, J. W.; Zaleski, C. M.; Pecoraro, V. L. The Nature of the Bridging Anion Controls the Single-Molecule Magnetic Properties of DyX $_4$ M 12-Metallacrown-4 Complexes. *Inorg. Chem.* **2016**, *55* (20), 10597–10607.

(29) Happ, P.; Rentschler, E. Enforcement of a High-Spin Ground State for the First 3d Heterometallic 12-Metallacrown-4 Complex. *Dalton Trans* **2014**, *43* (41), 15308–15312.

(30) Happ, P.; Plenk, C.; Rentschler, E. 12-MC-4 Metallacrowns as Versatile Tools for SMM Research. *Coord. Chem. Rev.* **2015**, *289–290*, 238–260.

(31) Plenk, C.; Krause, J.; Beck, M.; Rentschler, E. Rational Linkage of Magnetic Molecules Using Click Chemistry. *Chem. Commun.* **2015**, *51* (30), 6524–6527.

(32) Happ, P.; Sapozhnik, A.; Klanke, J.; Czaja, P.; Chernenkaya, A.; Medjanik, K.; Schuppler, S.; Nagel, P.; Merz, M.; Rentschler, E.; et al. Analyzing the Enforcement of a High-Spin Ground State for a Metallacrown Single-Molecule Magnet. *Phys. Rev. B* **2016**, *93* (17).

(33) Addison, A. W.; Rao, T. N.; Reedijk, J.; van Rijn, J.; Verschoor, G. C. Synthesis, Structure, and Spectroscopic Properties of Copper(II) Compounds Containing Nitrogen–sulphur Donor Ligands; the Crystal and Molecular Structure of Aqua[1,7-Bis(N-Methylbenzimidazol-2′-Yl)-2,6-Dithiaheptane]Copper(II) Perchlorate. *J Chem Soc Dalton Trans* **1984**, No. 7, 1349–1356.

(34) Liu, W.; Thorp, H. H. Bond Valence Sum Analysis of Metal-Ligand Bond Lengths in Metalloenzymes and Model Complexes. 2. Refined Distances and Other Enzymes. *Inorg. Chem.* **1993**, *32* (19), 4102–4105.

(35) Alaimo, A. A.; Koumousi, E. S.; Cunha-Silva, L.; McCormick, L. J.; Teat, S. J.; Psycharis, V.; Raptopoulou, C. P.; Mukherjee, S.; Li, C.; Gupta, S. D.; et al. Structural Diversities in Heterometallic Mn–Ca Cluster Chemistry from the Use of Salicylhydroxamic Acid: {Mn $^{III}_4$ Ca $_2$ }, {Mn $^{II/III}_6$ Ca $_2$ }, {Mn $^{III/IV}_8$ Ca}, and {Mn $^{III}_8$ Ca $_2$ } Complexes with Relevance to Both High- and Low-Valent States of the Oxygen-Evolving Complex. *Inorg. Chem.* **2017**, *56* (17), 10760–10774.

(36) Stoumpos, C. C.; Gass, I. A.; Milios, C. J.; Lalioti, N.; Terzis, A.; Aromí, G.; Teat, S. J.; Brechin, E. K.; Perlepes, S. P. A Mn $^{II}_4$ Cubane and a Novel Mn $^{II}_{10}$ Mn $^{III}_4$ Cluster from the Use of Di-2-Pyridyl Ketone in Manganese Acetate Chemistry. *Dalton Trans* **2009**, No. 2, 307–317.

(37) Alvarez, S.; Alemany, P.; Casanova, D.; Cirera, J.; Llunell, M.; Avnir, D. Shape Maps and Polyhedral Interconversion Paths in Transition Metal Chemistry. *Coord. Chem. Rev.* **2005**, *249* (17–18), 1693–1708.

(38) Sorace, L.; Benelli, C.; Gatteschi, D. Lanthanides in Molecular Magnetism: Old Tools in a New Field. *Chem. Soc. Rev.* **2011**, *40* (6), 3092.

(39) Baldoví, J. J.; Cardona-Serra, S.; Clemente-Juan, J. M.; Coronado, E.; Gaita-Ariño, A.; Palii, A. Rational Design of Single-Ion Magnets and Spin Qubits Based on Mononuclear Lanthanoid Complexes. *Inorg. Chem.* **2012**, *51* (22), 12565–12574.

(40) Sørensen, M. A.; Weihe, H.; Vinum, M. G.; Mortensen, J. S.; Doerrer, L. H.; Bendix, J. Imposing High-Symmetry and Tuneable Geometry on Lanthanide Centres with Chelating Pt and Pd Metalloligands. *Chem. Sci.* **2017**, *8* (5), 3566–3575.

(41) Benelli, C.; Gatteschi, D. Magnetism of Lanthanides in Molecular Materials with Transition-Metal Ions and Organic Radicals. *Chem. Rev.* **2002**, *102* (6), 2369–2388.

(42) Chilton, N. F.; Anderson, R. P.; Turner, L. D.; Soncini, A.; Murray, K. S. PHI: A Powerful New Program for the Analysis of Anisotropic Monomeric and Exchange-Coupled Polynuclear *d* - and *f* -Block Complexes. *J. Comput. Chem.* **2013**, *34* (13), 1164–1175.

(43) Milios, C. J.; Piligkos, S.; Brechin, E. K. Ground State Spin-Switching via Targeted Structural Distortion: Twisted Single-Molecule Magnets from Derivatised Salicylaldoximes. *Dalton Trans* **2008**, No. 14, 1809–1817.

(44) Papatriantafyllopoulou, C.; Abboud, K. A.; Christou, G. Carboxylate-Free $Mn^{III}_2 Ln^{III}_2$ (Ln = Lanthanide) and $Mn^{III}_2 Y^{III}_2$ Complexes from the Use of (2-Hydroxymethyl)Pyridine: Analysis of Spin Frustration Effects. *Inorg. Chem.* **2011**, *50* (18), 8959–8966.

(45) Savva, M.; Skordi, K.; Fournet, A. D.; Thuijs, A. E.; Christou, G.; Perlepes, S. P.; Papatriantafyllopoulou, C.; Tasiopoulos, A. J. Heterometallic $Mn^{III}_4 Ln_2$ (Ln = Dy, Gd, Tb) Cross-Shaped Clusters and Their Homometallic $Mn^{III}_4 Mn^{II}_2$ Analogues. *Inorg. Chem.* **2017**, *56* (10), 5657–5668.

(46) Liu, S.-J.; Xie, X.-R.; Zheng, T.-F.; Bao, J.; Liao, J.-S.; Chen, J.-L.; Wen, H.-R. Three-Dimensional Two-Fold Interpenetrated Cr^{III}–Gd^{III} Heterometallic Framework as an Attractive Cryogenic Magnetorefrigerant. *CrystEngComm* **2015**, *17* (38), 7270–7275.

(47) Gómez, V.; Vendier, L.; Corbella, M.; Costes, J.-P. Tetranuclear $[Co–Gd]_2$ Complexes: Aiming at a Better Understanding of the 3d-Gd Magnetic Interaction. *Inorg. Chem.* **2012**, *51* (11), 6396–6404.

(48) Yu, S. B.; Lippard, S. J.; Shweky, I.; Bino, A. Dinuclear Manganese(II) Complexes with Water and Carboxylate Bridges. *Inorg. Chem.* **1992**, *31* (17), 3502–3504.

(49) Bruker Apex 3 2016; Brucker AXS Inc., Madison, Wisconsin, USA.

(50) Sheldrick G. M. SADABS-2016/2 2016, Bruker AXS Inc., Madison, Wisconsin, USA.

(51) Stoe & Cie X-RED 2002, Stoe & Cie, Darmstadt, Germany.

(52) Sheldrick, G. M. *SHELXT* – Integrated Space-Group and Crystal-Structure Determination. *Acta Crystallogr. Sect. Found. Adv.* **2015**, *71* (1), 3–8.

(53) Sheldrick, G. M. Crystal Structure Refinement with *SHELXL*. *Acta Crystallogr. Sect. C Struct. Chem.* **2015**, *71* (1), 3–8.

(54) Dolomanov, O. V.; Bourhis, L. J.; Gildea, R. J.; Howard, J. A. K.; Puschmann, H. *OLEX2* : A Complete Structure Solution, Refinement and Analysis Program. *J. Appl. Crystallogr.* **2009**, *42* (2), 339–341.

(55) Bain, G. A.; Berry, J. F. Diamagnetic Corrections and Pascal's Constants. *J. Chem. Educ.* **2008**, *85* (4), 532.

2.8 Supporting Information

Table S1. Crystallographic data for complexes **1-3**.

Complex	**1**	**2**	**3**
Empirical formula	$C_{69}H_{98}Cl_{10}Mn_4N_5O_{20}Tb$	$C_{69}H_{98}Cl_{10}Mn_4N_5O_{20}Gd$	$C_{80}H_{124}ClMn_4N_6O_{24}Y$
Formula weight	2050.70	2049.03	1897.96
Temperature/K	173(2)	173(2)	120(2)
Crystal system	tetragonal	tetragonal	tetragonal
Space group	P4/n	P4/n	P4cc
a/Å	18.9040(14)	18.9025(9)	21.8159(6)
b/Å	18.9040	18.9025	21.8159
c/Å	12.3051(9)	12.2959(6)	18.6491(7)
α/°	90	90	90
β/°	90	90	90
γ/°	90	90	90
Volume/Å^3	4397.4(7)	4393.4(5)	8875.7(6)
Z	2	2	4
ρ_{calc}g/cm^3	1.549	1.549	1.420
μ/mm^{-1}	1.722	1.674	1.305
F(000)	2084	2082	3976
Crystal size/mm^3	0.5 × 0.44 × 0.1	0.5 × 0.4 × 0.05	0.21 × 0.167 × 0.09
Radiation	MoK\α (λ = 0.71073)	MoK\α (λ = 0.71073)	MoK\α (λ = 0.71073)
2Θ range for data collection/°	1.523 to 25.994	1.524 to 25.000	2.356 to 25.996
Index ranges	-23 ≤ h ≤ 23 -23 ≤ k ≤ 23 -15 ≤ l ≤ 15	-22 ≤ h ≤ 22 -22 ≤ k ≤ 22 -14 ≤ l ≤ 14	-23 ≤ h ≤ 26 -24 ≤ k ≤ 7 -23 ≤ l ≤ 20
Reflections collected	42710	33112	10893
Independent reflections	R_{int} = 0.0612 R_{sigma} = 0.0286	R_{int} = 0.0680 R_{sigma} = 0.0337	R_{int} = 0.0677 R_{sigma} = 0.0631
Data/restraints/ parameters	4332 / 196 / 453	3880 / 175 / 447	8346 / 159/ 571
Goodness-of-fit on F^2	1.262	1.220	1.072
Final R^{a,b} indexes [I>=2σ (I)]	R_1 = 0.0473 wR_2 = 0.1271	R_1 = 0.0431 wR_2 = 0.1039	R_1 = 0.0762 wR_2 = 0.1752
Final R^{a,b} indexes [all data]	R_1 = 0.0546 wR_2 = 0.1306	R_1 = 0.0524 wR_2 = 0.1077	R_1 = 0.1110 wR_2 = 0.1983
Largest diff. peak /hole / e Å^{-3}	0.702 / -1.294	0.649/ -0.986	0.751/ -0.374

[a] $R_1 = \Sigma(||F_o| - |F_c||)/\Sigma|F_o|$. [b] $wR_2 = [\Sigma[w(F_o^2 - F_c^2)^2]/\Sigma[w(F_o^2)^2]]^{1/2}$, $w = 1/[\sigma^2(F_o^2) + (ap)^2 + bp]$, where $p = [\max(F_o^2, 0) + 2F_c^2]/3$.

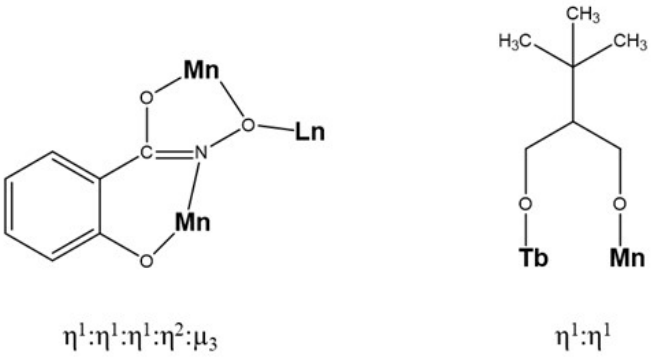

Figure S1. Coordination modes of ligands in complex **2**.

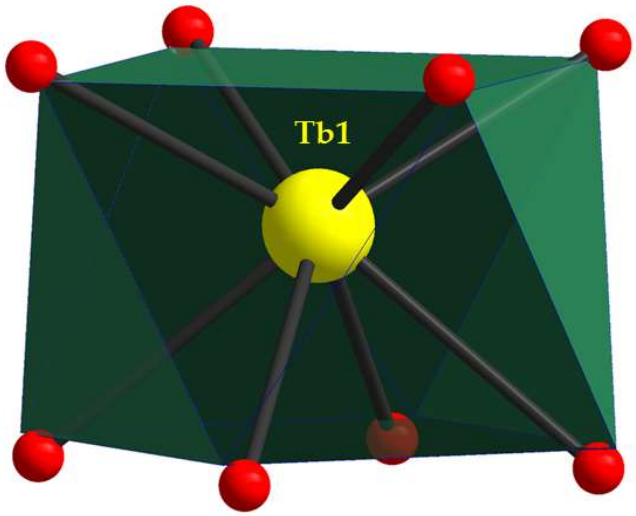

Figure S2. Square antiprismatic geometry of Tb1 in the structure of complex **2**. The points connected by the blue lines define the vertices of the ideal polyhedron**.** Color scheme: Tb, yellow; O, red.

Table S2 Selected Bond Lengths for complex **2.**

Atom	Atom	Length/Å
Tb1	O3	2.424(4)
Tb1	O5	2.320(4)
Mn1	O1	1.843(5)
Mn1	O2[1]	1.941(5)
Mn1	O3[1]	1.903(4)
Mn1	O4	2.086(5)
Mn1	N1	1.965(5)
O3	N1	1.405(8)

[1]+Y,1/2-X,+Z; [2]1/2-X,1/2-Y,+Z; [3]1/2-Y,+X,+Z; [4]-1/2+Y,1-X,-Z; [5]1-Y,1/2+X,-Z; [6]1/2-X,3/2-Y,+Z

Table S3 Selected Bond Angles for **2.**

Atom	Atom	Atom	Angle/°
O5	Tb1	O3	82.59(15)
O5	Tb1	O3[3]	76.94(15)
O5	Tb1	O3[1]	145.95(14)
O5	Tb1	O3[2]	137.02(14)
O3	Tb1	O3[1]	66.33(11)
O3	Tb1	O3[2]	101.4(2)
O5	Tb1	O5[1]	76.93(10)
O5	Tb1	O5[2]	123.2(2)
O1	Mn1	O4	97.1(2)
O1	Mn1	O2[3]	94.86 (19)
O1	Mn1	O3[3]	165.5(2)
O2[3]	Mn1	O4	95.8(2)
O2[3]	Mn1	N1	158.7(3)
O3[3]	Mn1	O2[3]	80.72(17)
O3[3]	Mn1	O4	97.03(19)
O3[3]	Mn1	N1	88.9(3)
O1	Mn1	N1	90.6(3)
N1	Mn1	O4	104.0(3)
N1	O3	Tb1	122.0(4)
O3	N1	Mn1	116.9(5)

[1]1/2-Y,+X,+Z; [2]1/2-X,1/2-Y,+Z; [3]+Y,1/2-X,+Z; [4]-1/2+Y,1-X,-Z; [5]1-Y,1/2+X,-Z; [6]1/2-X,3/2-Y,+Z

Table S4. Shape measurements of the 8-coordinate lanthanide coordination polyhedra. The bold numbers indicate the closest polyhedron according to SHAPE calculations.[97]

Polyhedron[c]	Tb1	Gd1	Y1	Y2
OP-8	31.55	31.61	30.59	29.56
HPY-8	23.76	23.74	23.92	24.09
HBPY-8	15.66	15.73	15.68	15.90
CU-8	7.93	8.01	7.95	8.19
SAPR-8	**0.72**	**0.73**	**0.59**	**0.45**
TDD-8	2.39	2.42	2.33	2.33
JGBF-8	16.92	16.97	16.76	16.68
JETBPY-8	30.21	30.24	29.90	29.57
JBTPR-8	3.12	3.12	3.01	2.89
BTPR-8	2.12	2.09	2.08	2.05
JSD-8	5.82	5.85	5.69	5.58
TT-8	8.81	8.88	8.83	9.07
ETBPY-8	25.23	25.28	24.90	24.59

[c] Abbreviations: OP-8, octagon; HPY-8, heptagonal pyramid; HBPY-8, hexagonal bipyramid; CU-8, cube; SAPR-8, square antiprism; TDD-8, triangular dodecahedron; JGBF-8, Johnson gyrobifastigium; JETBPY-8, Johnson elongated triangular bipyramid; JBTPR-8, Johnson biaugmented trigonal prism; BTPR-8, biaugmented trigonal prism; JSD-8, Johnson snub diphenoid; TT-8, triakis tetrahedron; ETBPY-8, elongated trigonal bipyramid.

Infrared Absorption Spectroscopy

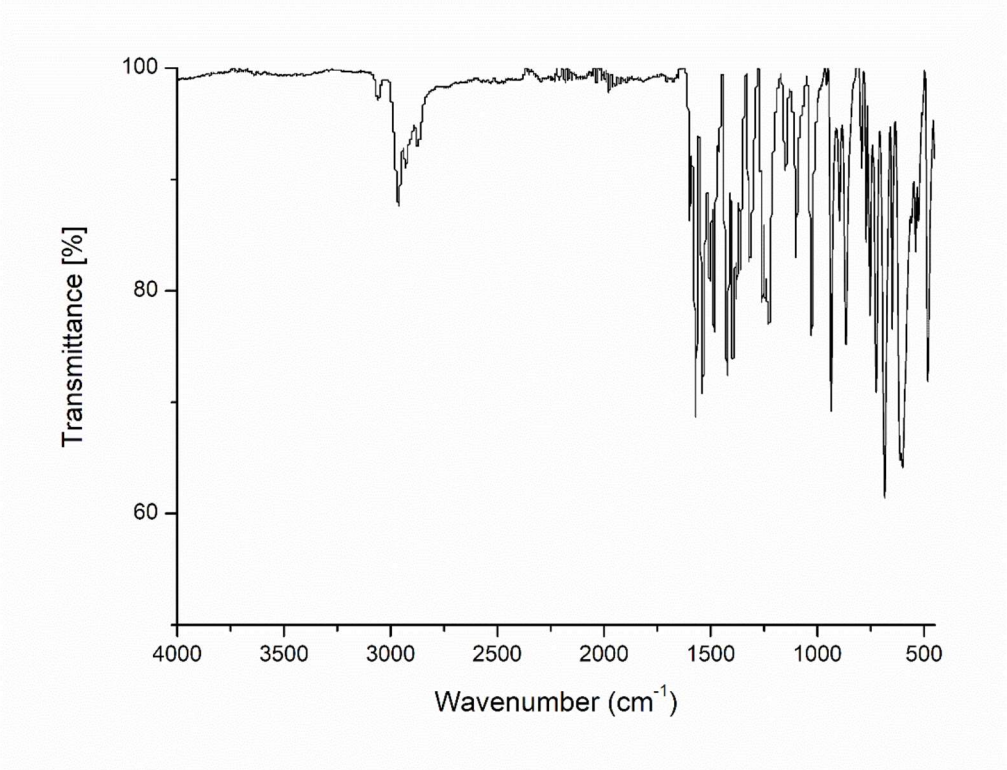

Figure S3: IR spectrum for complex **1**.

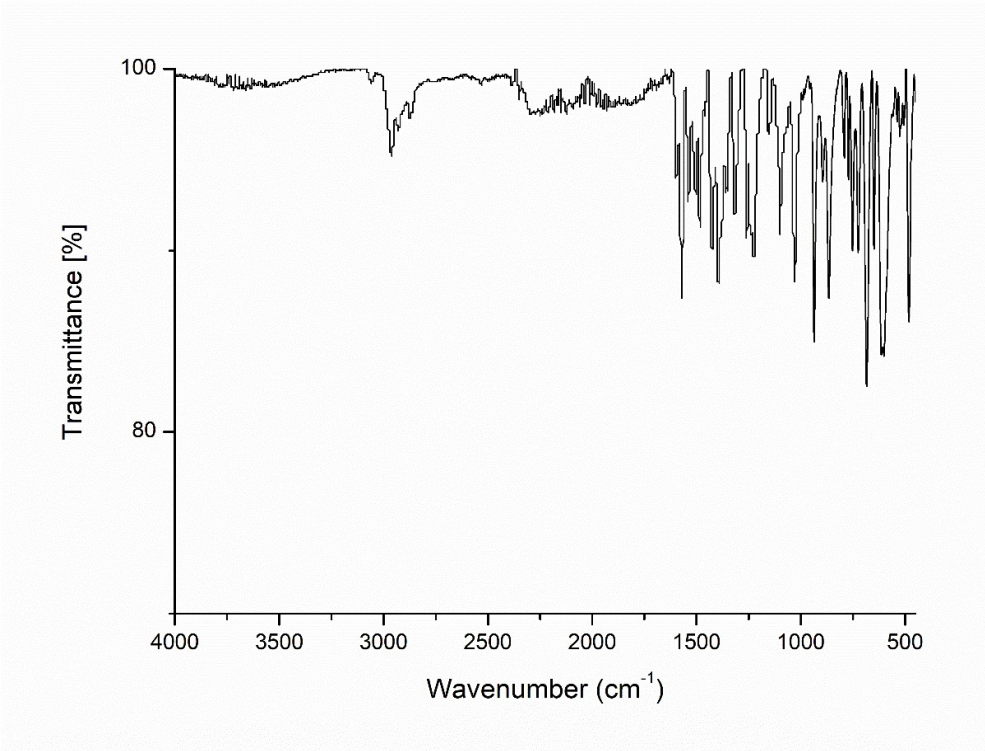

Figure S4: IR spectrum for complex **2**.

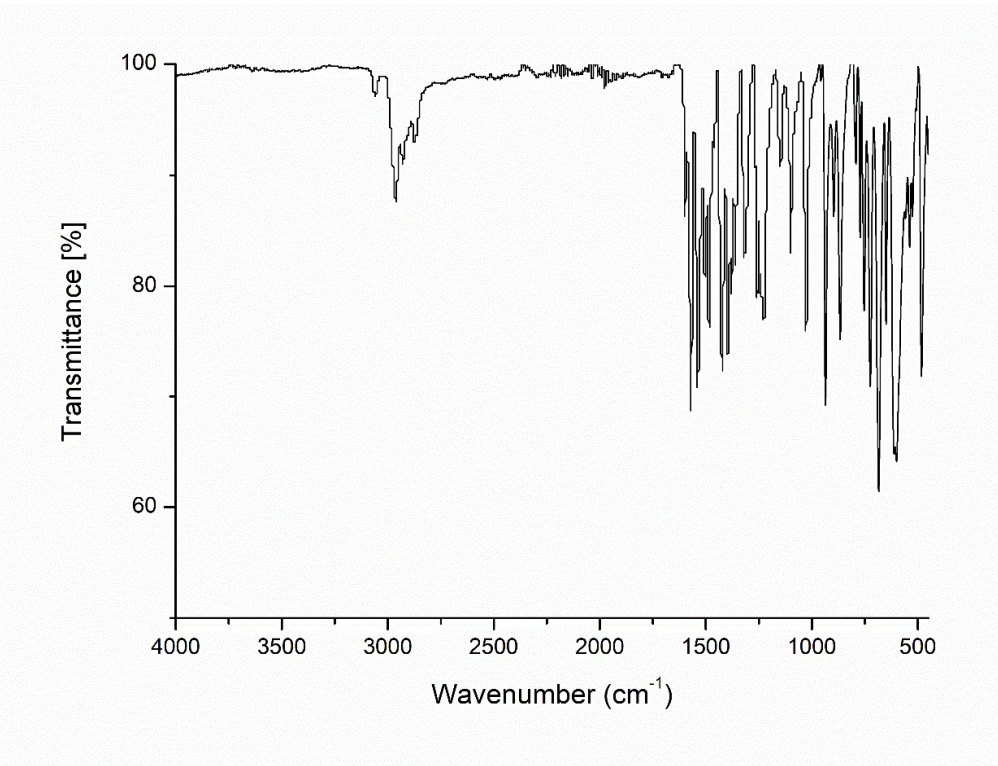

Figure S5: IR spectrum for complex **3**.

UV-Vis Absorption Spectroscopy

The ligand ($shiH_3$) has two main bands at 227 nm and 318 nm, which appear to be also present at all the complexes. These ligand-centered transitions, that can be assigned to excitations within the delocalized π-system of the coordinated hydroxamic acid, are observed at 209 and 250 nm for **1**, at 209 and 271 nm for **2** and at 208 and 271 nm for **3**. The light absorption by **1** , **2** and **3** at around ~357 nm is characteristic for ligand-to-metal charge-transfer (LMCT) transitions [[115]].

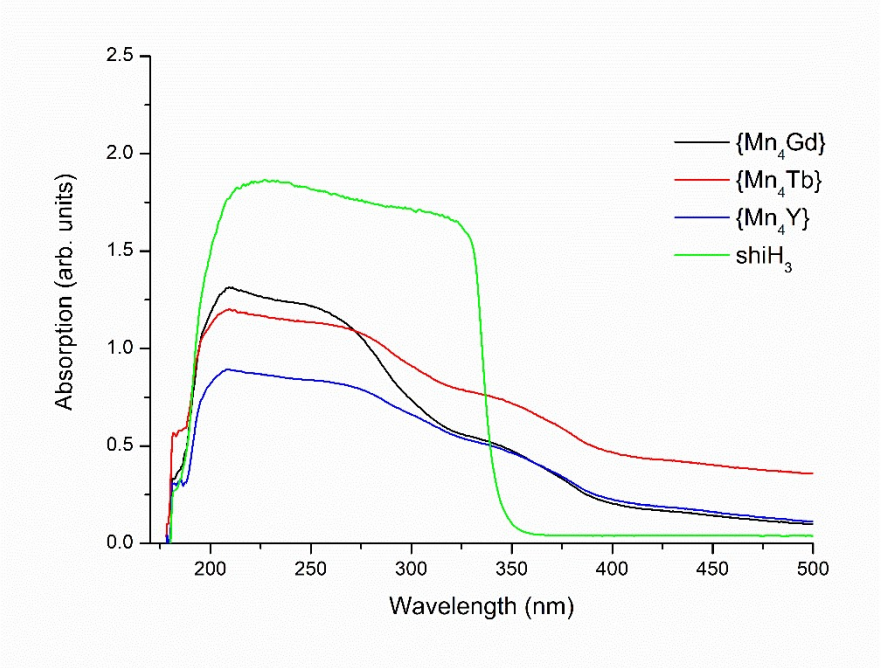

Figure S6: UV-Vis spectra of **1** (black), **2** (red), **3** (blue), and $shiH_3$ (green) in MeCN.

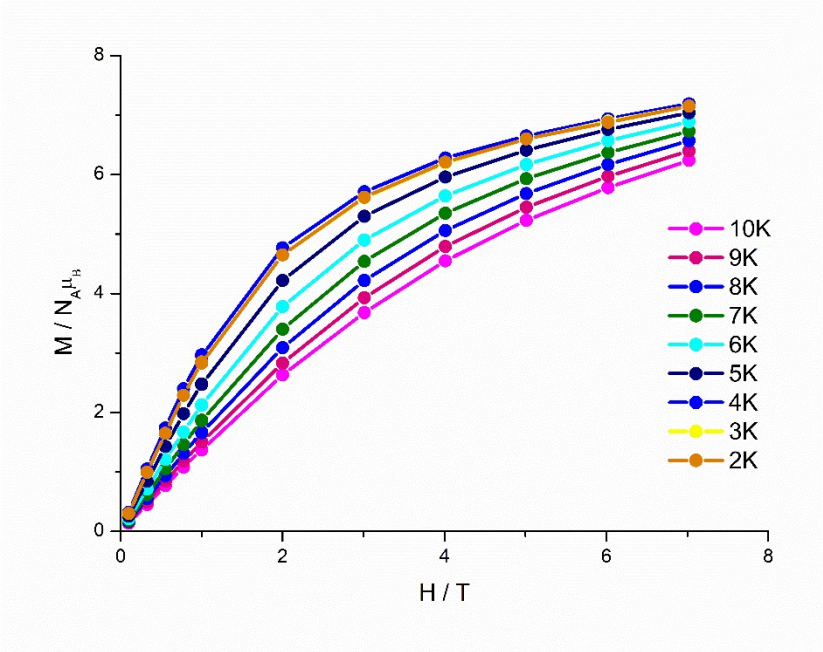

Figure S7: *M* vs *H* plots for complex **1** in various temperatures as indicated. Solid lines are guidelines for the eyes.

References:

(1) Alvarez, S.; Alemany, P.; Casanova, D.; Cirera, J.; Llunell, M.; Avnir, D. Shape Maps and Polyhedral Interconversion Paths in Transition Metal Chemistry. *Coord. Chem. Rev.* **2005**, *249* (17–18), 1693–1708.

(2) Gliemann, G. A. B. P. Lever: Inorganic Electronic Spectroscopy, Vol. 33 Aus: Studies in Physical and Theoretical Chemistry, Elsevier, Amsterdam, Oxford, New York, Tokio 1984. 863 Seiten, Preis: $ 113, 50. *Berichte Bunsenges. Für Phys. Chem.* **1985**, *89* (1), 99–100.

Chapter 3

In this chapter the synthesis and characterization of a new Fe(III)/Ln(III) of mixed 9-MC-3/12-MC-4 or a new metallacryptate family of complexes is reported. This is the first Fe(III)/Ln(III) metallacryptate family of compounds, using salicylhydroxamic acid, reported. The compounds have been structurally and magnetically investigated, while it has been observed that the {Fe_6Dy} analogue belongs to the SMM family. This paper has been published in Dalton Transactions by the reference details Athanasopoulou *et al.*, Dalton Trans **2019,** *48*, 4779 – 4783 and DOI: 10.1039/C9DT00552H.

Slow Relaxation of Magnetization in a {Fe_6Dy} Complex Deriving from a Family of Highly Symmetric Metallacryptands

Angeliki A. Athanasopoulou,[a,b] Luca M. Carrella[a] and Eva Rentschler *[a]

a. Institute of Inorganic and Analytical Chemistry, Johannes Gutenberg University Mainz, Duesbergweg 10-14, D-55128 Mainz, Germany, rentschl@uni-mainz.de

b .Graduate School Materials Science in Mainz, Staudinger Weg 9, D-55128 Mainz, Germany.

†Electronic Supplementary Information (ESI) available: Full synthetic and crystallographic discussion, figures, and magnetic data. CCDC **(1)**, **(2), (3)** and **(4).** For ESI and crystallographic data in CIF or other electronic format see DOI: 10.1039/C9DT00552H.

Author Contributions

Angeliki A. Athanasopoulou designed and performed the experiments regarding the isolation of complex **1-4**. She also performed infrared (IR), UV-Vis studies as well as collected and prepared the samples for elemental analysis and SQUID magnetometry. Single-crystal X-ray measurements were performed from Dr. Dieter Schollmeyer while the refinement of collected data was performed by Dr. Luca M. Carrella. Evaluation of magnetic studies was done by Angeliki A. Athanasopoulou along with the assistance of Dr. Luca M. Carrella. The manuscript was written by Angeliki A. Athanasopoulou while important input was added by Luca M. Carrella and Eva Rentschler. Finally, Eva Rentschler had the overall supervision in the interpretation of data throughout the manuscript process.

3.1 Abstract

The synthesis and characterization of a new family of isostructural {Fe_6Ln} complexes, $(pipH)_3\{Fe_6Ln(shiH)_3(shi)_6\}\cdot 1.5\ pip\cdot xH_2O$ (Ln = Gd (1), Dy (2), Tb (3) and Y (4), pip = piperidine, and shi^{3-} = salicylhydroxamic acid) is reported. The resulting compounds possess an exceptionally unique stucture of a metallacrown-like motif while the overall complexes feature more the structure of metallacryptates. Magnetic studies are reported and reveal that the {Fe_6Dy} analogue belongs to the single-molecule magnet (SMM) family.

3.2 Introduction

Single-molecule magnets (SMMs)[1–3] are being intensively discussed for possible applications such as high-density data storage, quantum computation and spintronics.[4–7] High magnetic anisotropy is considered to be the crucial requirement for the appearance of a high energy barrier of the magnetization reversal in SMMs. However, the basic prediction and manipulation of magnetic anisotropy has proven to be extremely difficult, as it is determined by several factors such as molecular symmetry, ligand field strength, zero-field splitting and spin-orbit coupling. In 2003, the breakthrough [Pc_2Tb] (Pc = pthalocyanine) complex turned the focus to the use of 4*f* elements.[8] Today energy barriers (U_{eff}) as high as 1541 cm^{-1} are reported for dysprosocenium complexes, showing magnetic hysteresis close to or even above liquid nitrogen (77K).[9–11]

The design of new SMMs focuses on the use of pure 3d metal ions, 3d/4f heterometallic metal ions and homometallic 4f ions. Compounds with solely homometallic 3d metal ions can afford large spin ground states but nevertheless they usually possess a small axial anisotropy. The inclusion of 4f metal ions on the other hand, leads to complexes with large thermal energy barriers (U_{eff}) due to the high intrinsic magnetic anisotropy and the large spin-orbit coupling of the 4f ions.[12–14] Thus, aiming for a better magnetization performance, the field has progressed towards the isolation of 3d/4f complexes since the combination of transition metals and 4*f* ions can lead to considerably large energy barriers (U_{eff}) and relaxation times (τ) [9,10,15,16] and therefore much endeavor has been focused on the isolation and characterization of heterometallic 3d/4f SMMs.[17–21]

Metallacrown complexes (MCs), are inorganic analogues of organic crown ethers, with the continuous repetition of a $[\text{-M-N-O}]_n$ unit. Similar to crown ethers, metallacrowns

are named following the ring size and the number of the donating oxygen atoms. The first metallacrown was reported in 1989, by Pecoraro and Lah[22] and since then a flourishing development of MCs make this group of compounds exhibiting numerous structural types varying from 9-MC-3 to 60-MC-20.[23] In 3d/4f MCs, the ring positions are occupied by a 3d metal ion while a 4f ion is located in the cavity of the MC ring. This structural type is a promising scaffold for SMM behavior, since it easily combines the inherent magnetic character of both 3d and 4f ions, with most common and most documented being the heterometallic Mn/4f MCs.[18,24–27]

The structural and magnetic properties of Fe/4f MCs are not highly discussed, since there are only a few complexes reported to date.[28,29] Lou *et al*., have recently reported a new Fe/Ln 12-MC-4 complex using salicylhydroxamic acid ($shiH_3$, Scheme 1, ESI) as a ligand, which has been extensively structurally and magnetically studied. In the direction of further broadening the field of Fe/Ln MCs, we have synthesized a series of a new family of isostructural $(pipH)_3\{Fe_6Ln(shiH)_3(shi)_6\}\cdot 1.5\ pip\cdot xH_2O$ (Ln = Gd (**1**), Dy (**2**), Tb (**3**) and Y (**4**), pip = piperidine, and shi^{3-} = salicylhydroxamic acid). These molecules belong to a new category of metallacrown-like complexes in which the MC compounds resemble more the structure of cryptands whilst maintaining the characteristic metallacrown [M-N-O] binding mode. Thus, these compounds can be considered as a combination of 9-MC-3 and 12-MC-4 complexes (Fig.1) placing this family to the leading edge of such Metallacrown-type molecules while at the same time they can also relate to the structure of cryptands. Recently, Pecoraro *et al.*, reported a $[LnGa_6(H_2shi)(Hshi)(shi)_7(C_5H_5N)]$ (shi3- = salicylhydroximate; Ln = Pr, Nd, Sm – Yb) that has been best described as a metallacryptate . Focusing exclusively on the Fe-based clusters though, this is the second Fe/Ln/shi^{3-} cluster reported to date, the first being a Ln(III)[12-$MC_{Fe(III)N(shi)}$-4] metallacrown assembled from the use of salicylhydroxamic acid and the first Fe/Ln/shi^{3-} complex comprising this unique highly symmetric metallacryptand structure.[29]

3.3 Crystal structures of complexes 1-4

The general reaction of $Fe(acac)_3$, $Ln(NO_3)_3{\cdot}xH_2O$ (Ln = Gd^{III}, Dy^{III}, Tb^{III}, Y^{III}), $shaH_2$, $^tBu_4NClO_4$ and piperidine in a 4:1:4:1:4 molar ratio, in MeOH gave dark brown plates of $(pipH)_3\{Fe_6Ln(shiH)_3(shi)_6\}\cdot 1.5\ pip\cdot xH_2O$ (Ln = Gd (**1**), Dy (**2**), Tb (**3**) and Y (**4**)) in good yields (~65%). The chemical and structural identities of the complexes were confirmed by X-ray crystallography, elemental analyses (C, H, N) and IR spectroscopy (ESI).

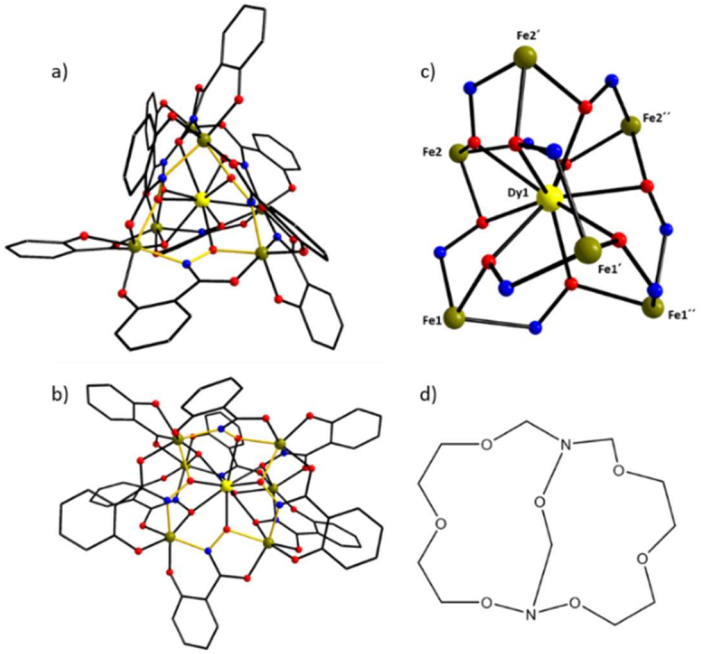

Figure 3.2.1: (a) and (b) Schematic representation of complex **2** highlighting its two distinct structural portrayals of the 9-MC-3 and 12-MC-4 conformation; c) metallacryptate core; d) depiction of cryptand for comparison. Color scheme: Dy^{III}, yellow; Fe^{III}, dark yellow; N, blue; O, red. H atoms are omitted for clarity.

Single-crystal diffraction studies revealed that complexes **1**, **2**, **3** and **4** are all isostructural and crystallize in the $P\bar{3}c1$ trigonal space group (Table S1, ESI). Therefore, only complex **2** will be extensively described for simplicity reasons. The final oxidation states in **2** were based on charge balance considerations, metric parameters and BVS calculations.[30] The structure of **2** consists of a $[Fe_6Dy(shiH)_3(shi)_6]^{3-}$ anion (Fig. 1), three piperidine cations and water molecules in the lattice, while a 3-fold (C_3) passes through the central Ln atom. The $^tBu_4NClO_4$ that was used for charge balance considerations does not participate in the crystal structure. Nevertheless is essential for the

crystallization of the final product since it appears to play an important role on the concentration of the reacting solution. Selected interatomic distances and angles for all complexes are listed in Table S2 and S3 (ESI). The core of **2** (Fig.2) comprises 6 Fe^{III} and one Dy^{III} atoms arranged in a trigonal prism-like topology with the Dy atom being placed in the center of the prism. The Fe1···Fe1′···Fe1′′ and Fe2···Fe2′···Fe2′′ distances at the vertices of the trianglular prism, are 4.896(1) Å and 4.711(1) Å, respectively, while the distance of the three other rectangular faces that are completing the prism, is 4.787 (1) Å. The connection between the Fe^{III} and the Dy^{III} atoms is provided by the oximate O atoms of the shi^{3-} ligand resulting in Fe^{III}···Dy^{III} separations of 3.581(1) and 3.714(1) Å. The 6 Fe^{III} ions are bridged by 9 μ-NO bridges as well as the phenoxide and carbonyl fragments of 3 doubly and 6 triple deprotonate salicylhydroxamic ligands. The salicylhydroxamate ligand adopts the same $\eta^1:\eta^1:\eta^1:\eta^2:\mu_3$ coordination mode assisting in the formation of the [Fe-N-O] repeating unit, which leads to the unprecedented mixed 9-MC-3/12-MC-4 motif of the compound (Fig.S1, ESI). Complex **2** can be also described as an Fe(III)[3:3:1]metallacryptand, where Fe2' and Fe1' are regarded to be analogous to the N atoms in a cryptand (Fig. 1). The six Fe(III) metal ions and the nine (shi^{3-}/$shiH^{2-}$) ligands build up the metallacryptand, in which Dy1 occupies the central position. The oxidation states of Fe ions were derived from charge balance, bond length and BVS calculations as six Fe^{III} ions (Table S4, ESI). All Fe atoms are six-coordinate with distorted octahedral geometries.

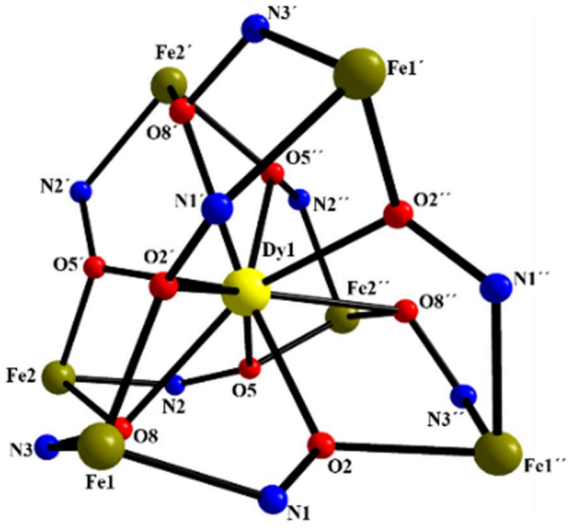

Figure 3.2.2: Labeled schematic representation of the inorganic core $\{Fe^{III}_6Dy^{III}(\mu\text{-}NO)_9\}^{12+}$ of complex **2**. Color scheme: Dy^{III}, yellow; Fe^{III}, dark yellow; N, blue; O, red.

Dy1 is encapsulated in the cavity of the mixed 9-MC-3/12-MC-4 metallamacrocycle or metallacryptand and all the Dy-O bond distances are in the range of 2.361(4) to 2.548(4) Å. The Dy atom is 9-coordinate and in order to evaluate the closer coordination polyhedron defined by the donor atoms around it, the program SHAPE was employed.[31,32] In this case, it was found that Dy1 has a CShM=1.13 possessing an almost ideal spherical tricapped trigonal prism geometry with an oximato bridge from shi^{3-} (N3′ and O8′, Fig. 2) serving as the capping atoms (Fig. S2, ESI). As expected, the Ln atoms in all complexes possess the same coordination geometry (Table S5, ESI). Moreover, SHAPE calculations were employed, exclusively for the Fe(III) ions of the $\{Fe_6Dy\}$ core as a whole and they showed that the disposition of the six outer Fe(III) ions possess an almost ideal trigonal prismatic geometry with a CShM=0.88 (Fig. S3). The triangular phases of the trigonal prism are slightly twisted, with respect to each other, and thus the distortion angle φ was calculated. In ideal trigonal prismatic geometries φ is 0° while in our case φ was found to be 13.97°, demonstrating once more the small distortion from the ideal geometry.

3.4 Magnetic studies of complexes 1-4

Variable-temperature direct-current (dc) magnetic susceptibility measurements were performed on freshly prepared and analytical pure (see ESI) microcrystalline samples of **1 - 4** in the temperature range of 2-300K under an applied field of 0.1T. The obtained data are presented as a $\chi_M T$ vs. T plot in Fig. 3. The experimental values at 300 K for all complexes (26.7 $cm^3mol^{-1}K$ for **1**, 23.3 $cm^3mol^{-1}K$ for **2**, 32.2 $cm^3mol^{-1}K$ for **3** and 23.2 $cm^3mol^{-1}K$ for **4**) are lower than the theoretical spin only values (34.13 $cm^3mol^{-1}K$ for **1**, 40.42 $cm^3mol^{-1}K$ for **2**, 38.07 $cm^3mol^{-1}K$ for **3** and 26.25 $cm^3mol^{-1}K$ for **4**) expected for six non-interacting Fe^{III} ions (S = 5/2, g = 2) and one Gd^{III} ($^8S_{7/2}$, S = 7/2, L = 0, g = 2), one Dy^{III} ($^6H_{15/2}$, S = 5/2, L = 5, J = 15/2, g = 4/3), one Tb^{III} ($^7F_6$, S = 3, L = 3, g = 3/2), or one diamagnetic Y^{III} ion. For all complexes, the $\chi_M T$ product decreases with decreasing temperature indicating the presence of predominant antiferromagnetic

exchange interactions within the metal centres. This behaviour is further highlighted by the fact that the $\chi_M T$ values at 300 K for all compounds, are lower than the expected theoretical ones. For complex **4**, the extrapolation of $\chi_M T$ to 0 K is approaching zero, implying the presence of a diamagnetic spin ground state (S_T=0) arising from dominating antiferromagnetic exchange interactions between the Fe^{III} spin centres. The presence of antiferromagnetic exchange interactions within the metal spin carriers is common in Fe^{III}/Ln^{III} MCs complexes, as it is observed in the literature.[28,29] The fitting of the magnetic susceptibility data was not fully satisfactory due to the substantial number of metal centres that possess large spin moments. Nevertheless, we tried to fit the experimental data using the CLUMAG[33] program and the results of the best-fit parameters obtained, can be shown in detail at the ESI (Fig. S4). As a general remark it was seen that J_1, which corresponds to the interaction associated within the 9-MC-3 scaffold, is slightly positive. This is anticipated considering the triangular conformation that is formed, which inevitably leads to non well-defines spin states.[34] On the other hand, J_2 which corresponds to the interactions that comprise the base of the pyramid or else the 12-MC-4 scaffold, was found to be negative which is consistent with the large torsion angles present in the structure (Table S3).

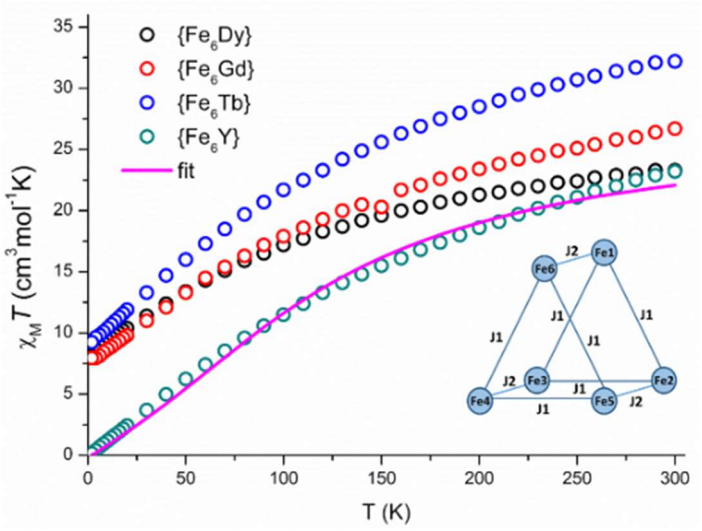

Figure 3.4.1: Temperature dependence of magnetic susceptibility for complexes 1 – 4 and fitting of the $\{Fe_6Y\}$ complex. In the inset the fitting model used can be also observed.

The field dependence of magnetization for compounds **1-3** were measured in the temperature range of 2 - 10 K over the range of 0 - 7 T (Fig. S3-S5, ESI). As

demonstrated in Fig. S3-S5 (ESI), the values of magnetization increase acutely at low field, and after that a more linear increase is observed for complexes **2** and **3**, while a more continuous increase is observed for compound **1**. In all cases, saturation is not reached at 7 T with the magnetization values being 6.73 μ_B for **1**, 5.57 μ_B for **2** and 4.95 μ_B for **3** at 2 K, respectively. The lack of saturation in magnetization is indicative of the presence of magnetic anisotropy and/or population of the Ln^{III} low-lying excited states, while it can be also attributed to the presence antiferromagnetic interactions between the metal centres.

To probe the magnetic dynamics for complexes **1**-**3**, alternating-current magnetic susceptibility studies (ac) were performed in zero-applied dc field for all complexes, with a 3.0 Oe ac field oscillating at frequencies between 1-1400 Hz and in the temperature range of 1.9-4.7 K. Compounds **1** and **3** do not show any out-of-phase χ''_M signals either at zero or applied dc field. The {Fe_6Dy} analogue exhibits frequency-dependent tails of signals below ~5 K at zero field, suggestive of the magnetization relaxation of a fast-relaxing SMM meaning that the slow magnetic relaxation and a part of quantum tunnelling coincide (Fig. S9, SI). For complex **2**, we observed a lack of χ''_M peak maxima at zero field and thus in order to shift the peaks and supress the quantum tunnelling (QTM), an applied field was used. Upon pursuing field-scan measurements an optimum external field of 800 Oe was chosen to be used for further magnetic investigations. The SMM behaviour of complex **2** is clearly visible after the application of the external dc field since the χ'_M and χ''_M values are significantly increased and the maxima of the peaks are observed (Fig. 4). The dependence of χ''_M signals on the ac frequency at each different temperature (Fig. 4) permitted us to fit the data using a generalized Debye function and extract the temperature dependent relaxation times (τ). These data were employed to construct an Arrhenius-type plot and evaluate the effective energy barrier, U_{eff}, and the pre-exponential factor, τ_0, based on the equation $\ln\tau = \ln\tau_0 + U_{eff}/k_BT$. The best-fit parameters obtained for the thermally-activated regime gave the following values: $U_{eff} = 7.23$ cm^{-1} (10.4 K) and $\tau_0 = 2.08 \times 10^{-6}$ s (Fig. 5).

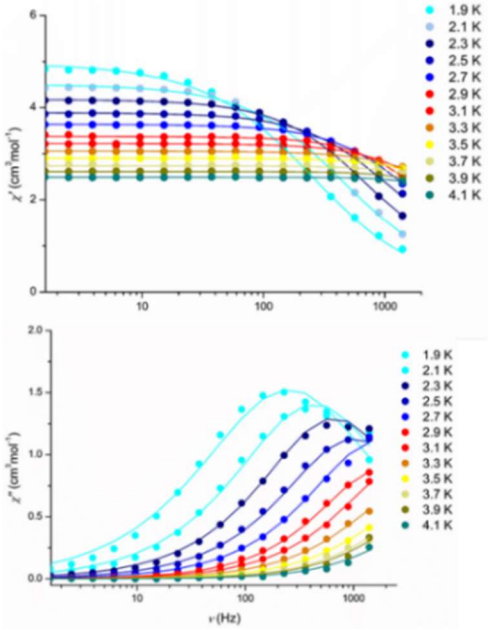

Figure 3.4.2: Frequency-dependent ac susceptibilities in an applied field of 800 Oe for complex 2. The solid lines represent fitting of the data.

When Kramers ions (i.e Dy^{III}) are present in a molecular complex, then the presence of an easy-axis anisotropy, dipole-dipole and hyperfine interactions allow the mixing of the ground states of the Kramers ions in zero dc field, thus advancing the QTM over thermal relaxation processes.[35,36] In order to reduce or even remove the QTM, an external (optimum dc field) was employed. The Cole-Cole plots for **2** in the temperature range of 1.9 K – 4-1 K display semicircular shapes and fitting of the data was possible using the generalized Debye model (here the Cole-Cole model was used).[37,38]

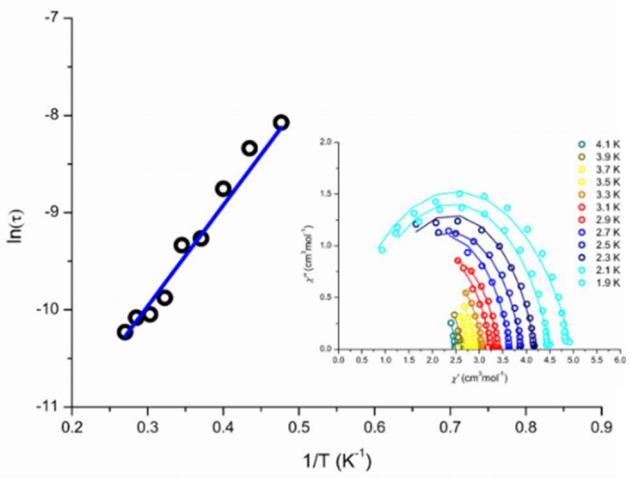

Figure 3.4.3: (left) Arrhenius plot showing the magnetization relaxation of 2 under an applied field of 800 Oe.(right) Cole-Cole plots for complex 2 using the ac susceptibility data under a field of 800 Oe from 1.9 K to 4.1 K. The solid lines represent the best fit obtained using the generalized Debye model.

This uncommon metallacryptand or else combined 9-MC-3/12-MC-4 conformation of the complexes makes this classification of molecules the first among the family of metallacrowns or metallacrown-like compounds, with such a unique architectural motif.

3.5 Conclusions

In conclusion, we have shown that the reaction of $Fe(acac)_3$ with various lanthanides in the presence of salicylhydroxamic acid has led to the isolation of an unprecedented family of metallacryptates or mixed 9-MC-3/12-MC-4 metallacrown-like complexes, with interesting magnetic properties. The complexes are highly symmetric possessing a trigonal prism-like topology with the 3-fold (C_3) axis passing through the central lanthanide, assisting in the formation of the overall mixed metallacrown-like form of the complex while it was also shown, by SHAPE calculations, that the outer Fe(III) centres are arranged in an almost ideal trigonal prismatic geometry as well. The SMM nature of the $\{Fe_6Dy\}$ analogue was confirmed by experimental measurements, giving an effective energy barrier of $U_{eff} = 7.23$ cm^{-1} (10.4 K) and a relaxation time $\tau_0 = 2.08 \times 10^{-6}$ s. Work in progress includes the isolation and characterization of other members of the $\{Fe_6Ln\}$ family, such us the Ho^{III} and Er^{III} analogues, as well as the substitution of Fe^{III} from Mn^{III} or Cr^{III} as a means of obtaining complexes with high molecular anisotropy which can in turn enhance the overall magnetic properties of the resulting compounds.

Acknowledgements

We would like to thank Dieter Schollmeyer for the collection of the X-Ray diffraction data of all our complexes. Angeliki A. Athanasopoulou is a member of (SFB/TRR) 173 ″Spin+X -Spin its collective environment″ and a fellow of the Excellence Initiative by the Graduate School of Excellence Materials Science in Mainz, Germany (DFG/GSC

266), both initiated by the Deutsche Forschungsgemeinschaft (DFG, GermanResearchFoundation).

Conflicts of interest

"There are no conflicts to declare".

3.6 References

1 D. Gatteschi, R. Sessoli and J. Villain, *Molecular nanomagnets*, New York Oxford University Press, 2006.

2 R. Winpenny and G. Aromí, Eds., *Single-molecule magnets and related phenomena*, Springer, Berlin ; New York, 2006.

3 G. Christou, D. Gatteschi, D. N. Hendrickson and R. Sessoli, *MRS Bulletin*, 2000, **25**, 66–71.

4 Y.-N. Guo, G.-F. Xu, Y. Guo and J. Tang, *Dalton Transactions*, 2011, **40**, 9953.

5 N. F. Chilton, S. K. Langley, B. Moubaraki, A. Soncini, S. R. Batten and K. S. Murray, *Chemical Science*, 2013, **4**, 1719.

6 R. J. Blagg, F. Tuna, E. J. L. McInnes and R. E. P. Winpenny, *Chemical Communications*, 2011, **47**, 10587.

7 Y.-Z. Zheng, G.-J. Zhou, Z. Zheng and R. E. P. Winpenny, *Chem. Soc. Rev.*, 2014, **43**, 1462–1475.

8 N. Ishikawa, M. Sugita, T. Ishikawa, S. Koshihara and Y. Kaizu, *Journal of the American Chemical Society*, 2003, **125**, 8694–8695.

9 F.-S. Guo, B. M. Day, Y.-C. Chen, M.-L. Tong, A. Mansikkamäki and R. A. Layfield, *Angewandte Chemie International Edition*, 2017, **56**, 11445–11449.

10 C. A. P. Goodwin, F. Ortu, D. Reta, N. F. Chilton and D. P. Mills, *Nature*, 2017, **548**, 439.

11 F.-S. Guo, B. M. Day, Y.-C. Chen, M.-L. Tong, A. Mansikkamäki and R. A. Layfield, *Science*, 2018, eaav0652.

12 P. Happ, C. Plenk and E. Rentschler, *Coordination Chemistry Reviews*, 2015, **289**–**290**, 238–260.

13 Y. Kishi, F. Pointillart, B. Lefeuvre, F. Riobé, B. Le Guennic, S. Golhen, O. Cador, O. Maury, H. Fujiwara and L. Ouahab, *Chemical Communications*, 2017, **53**, 3575–3578.

14 F. Habib and M. Murugesu, *Chemical Society Reviews*, 2013, **42**, 3278.

15 J. Liu, Y.-C. Chen, J.-L. Liu, V. Vieru, L. Ungur, J.-H. Jia, L. F. Chibotaru, Y. Lan, W. Wernsdorfer, S. Gao, X.-M. Chen and M.-L. Tong, *Journal of the American Chemical Society*, 2016, **138**, 5441–5450.

16 Y.-S. Ding, N. F. Chilton, R. E. P. Winpenny and Y.-Z. Zheng, *Angewandte Chemie International Edition*, 2016, **55**, 16071–16074.

17 R. Sessoli and A. K. Powell, *Coordination Chemistry Reviews*, 2009, **253**, 2328–2341.

18 T. T. Boron, J. C. Lutter, C. I. Daly, C. Y. Chow, A. H. Davis, A. Nimthong-Roldán, M. Zeller, J. W. Kampf, C. M. Zaleski and V. L. Pecoraro, *Inorganic Chemistry*, 2016, **55**, 10597–10607.

19 S. T. Liddle and J. van Slageren, *Chemical Society Reviews*, 2015, **44**, 6655–6669.

20 S. K. Langley, D. P. Wielechowski, V. Vieru, N. F. Chilton, B. Moubaraki, B. F. Abrahams, L. F. Chibotaru and K. S. Murray, *Angewandte Chemie International Edition*, 2013, **52**, 12014–12019.

21 X. Zhang, S. Liu, V. Vieru, N. Xu, C. Gao, B.-W. Wang, W. Shi, L. F. Chibotaru, S. Gao, P. Cheng and A. K. Powell, *Chemistry - A European Journal*, 2018, **24**, 6079–6086.

22 M. S. Lah, M. L. Kirk, W. Hatfield and V. L. Pecoraro, *Journal of the Chemical Society, Chemical Communications*, 1989, 1606.

23 G. Mezei, C. M. Zaleski and V. L. Pecoraro, *Chemical Reviews*, 2007, **107**, 4933–5003.

24 M. R. Azar, T. T. Boron, J. C. Lutter, C. I. Daly, K. A. Zegalia, R. Nimthong, G. M. Ferrence, M. Zeller, J. W. Kampf, V. L. Pecoraro and C. M. Zaleski, *Inorganic Chemistry*, 2014, **53**, 1729–1742.

25 F. Cao, S. Wang, D. Li, S. Zeng, M. Niu, Y. Song and J. Dou, *Inorganic Chemistry*, 2013, **52**, 10747–10755.

26 T. T. Boron, J. W. Kampf and V. L. Pecoraro, *Inorganic Chemistry*, 2010, **49**, 9104–9106.

27 A. Athanasopoulou, L. Carrella and E. Rentschler, *Inorganics*, 2018, **6**, 66.

28 W. Yang, H. Yang, S.-Y. Zeng, D.-C. Li and J.-M. Dou, *Dalton Transactions*, 2017, **46**, 13027–13034.

29 T. Lou, H. Yang, S. Zeng, D. Li and J. Dou, *Crystals*, 2018, **8**, 229.

30 W. Liu and H. H. Thorp, *Inorganic Chemistry*, 1993, **32**, 4102–4105.

31 S. Alvarez, P. Alemany, D. Casanova, J. Cirera, M. Llunell and D. Avnir, *Coordination Chemistry Reviews*, 2005, **249**, 1693–1708.

32 A. Ruiz-Martínez, D. Casanova and S. Alvarez, *Chemistry - A European Journal*, 2008, **14**, 1291–1303.

33 D. Gatteschi and L. Pardi, *Gazz. Chim. Ital.*, 1993, **123**, 231.

34 C. A. Christmas, H. L. Tsai, L. Pardi, J. M. Kesselman, P. K. Gantzel, R. K. Chadha, D. Gatteschi, D. F. Harvey and D. N. Hendrickson, *Journal of the American Chemical Society*, 1993, **115**, 12483–12490.

35 C. Benelli and D. Gatteschi, *Chemical Reviews*, 2002, **102**, 2369–2388.

36 J. D. Rinehart and J. R. Long, *Chemical Science*, 2011, **2**, 2078.

37 K. S. Cole and R. H. Cole, *The Journal of Chemical Physics*, 1941, **9**, 341–351.

38 M. Grahl, J. Kötzler and I. Seßler, *Journal of Magnetism and Magnetic Materials*, 1990, **90**–**91**, 187–188.

3.7 Supporting Information

Experimental Section

All manipulations were performed under aerobic conditions using materials (reagent grade) and solvents as received.

C, H and N elemental analyses were carried out on a Foss Heraeus Vario EL at the Institute of Organic Chemistry at the Johannes Gutenberg University Mainz. Infrared absorption spectra were recorded at room temperature in a range of 3,000-400 cm^{-1} on a Thermo Fischer NICOLET Nexus FT/IR-5700 spectrometer equipped with Smart Orbit ATR Diamond cell. UV-Vis absorption measurements were performed between for complexes 1, 2, 3 and 4 in MeCN between 200 and 1000 nm on a JASCO V-570 UV/Vis/NIR spectrophotometer (Fig.S10, ESI) Variable-temperature direct current (dc) magnetic susceptibility measurements were performed on polycrystalline samples with the use of Quantum Design SQUID magnetometer MPMS-7 equipped with a 7 T magnet. The samples were embedded in eicosane to avoid orientation of the crystallites under applied field. Experimental susceptibility data were corrected for the underlying diamagnetism using Pascal's constants.[114] The temperature dependent magnetic contribution of the holder and of the embedding matrix eicosane were experimentally determined and substracted from the measured susceptibility data. Variable temperature susceptibility data were collected in a temperature range of 2-300K under an applied field of 0.1 Tesla, while magnetization data were collected between 2 and 10 K and using magnetic fields up to 7 Tesla. Alternating-current (ac) measurements were performed with an oscillating magnetic field of 3 Oe at frequencies ranging from 1 to 1400 Hz. Field-dependence measurements were performed and they revealed an optimum dc field of 800 Oe. Using that optimum field further magnetic measurements were performed as described in the text.

3.7.1 Synthesis of reported compounds 1-4:

$(pipH)_3\{Fe_6Gd(shiH)_3(shi)_6\}\cdot 1.5\ pip\cdot xH_2O$ (1): To a stirred almost colorless solution of $shiH_3$ (30.50 mg, 0.2 mmol) and piperidine (20 μL, 0.2 mmol) in MeOH, $Fe(acac)_3$ (0.071 mg, 0.2 mmol) was added and left for stirring for 5 min. To the resulting dark red almost clear solution $Gd(NO_3)_3\cdot H_2O$ (7.00 mg, 0.025 mmol) was added along with $^tBu_4NClO_4$ (26.00 mg, 0.075 mmol) and was stirred for further 40 min. Then, the solution was filtered and the filtrate was layered with Et_2O/hexane. Slow mixing gave diffraction quality crystals of **1** after 5 days which were collected by filtration, washed with hexanes (3 × 5 mL) and dried in air. Yield: 0.045 g (72.5%) based on the Gd^{III} ion. The air-dried solid was analyzed as **$1\cdot 1.5pip\cdot 15H_2O$ ($Fe_6Gd_1H_{121.5}O_{42}C_{85.5}N_{13.5}$):** C, 40.99; H, 4.89; N, 7.55. Found: C, 41.05; H, 4.81; N, 7.54. Selected ATR data (cm^{-1}): 1593 (w), 1560 (w), 1485 (s), 1429 (w), 1305 (w), 1254 (s), 1035 (w), 916 (s), 848 (w), 664 (w), 582 (s), 541 (w).

$(pipH)_3\{Fe_6Dy(shiH)_3(shi)_6\}\cdot 1.5\ pip\cdot xH_2O$ (2): This complex was prepared in the same manner as complex **1** but using $Dy(NO_3)_3\cdot H_2O$ (9.00 mg, 0.025 mmol) instead of $Gd(NO_3)_3\cdot H_2O$. After 7 days dark brown crystals of **2** appeared; these were collected by filtration, washed with hexanes (3 × 5 mL) and dried in air. Yield: 0.042 g (68%) based on the Dy^{III} ion. The air-dried solid was analyzed as **$2\cdot 1.5pip\cdot 11H_2O$ ($Fe_6Dy_1H_{113.5}O_{38}C_{85.5}N_{13.5}$):** C, 42.20; H, 4.70; N, 7.77. Found: C, 42.28; H, 4.62; N, 7.74. Selected ATR data (cm^{-1}): 1591 (w), 1560 (w), 1485 (s), 1431 (w), 1305 (w), 1253 (s), 1035 (w), 917 (s), 849 (w), 666 (w), 581 (s), 541 (w).

$(pipH)_3\{Fe_6Tb(shiH)_3(shi)_6\}\cdot 1.5\ pip\cdot xH_2O$ (3): The complex was prepared in the same manner as the complexes above but using $Tb(NO_3)_3\cdot H_2O$ (9.00 mg, 0.025 mmol) as the lanthanide source . After 5 days dark brown crystals of **3**; these were collected by filtration, washed with hexanes (3 × 5 mL) and dried in air. Yield: 0.039 g (63%) based on the Tb^{III} ion. The vacuum-dried solid was analyzed as **$3\cdot 1.5pip\cdot 14H_2O$ ($Fe_6Tb_1H_{119.5}O_{41}C_{85.5}N_{13.5}$):** C, 41.29; H, 4.84; N, 7.60. Found: C, 41.28; H, 4.75; N, 7.49. Selected ATR data (cm^{-1}): 1592 (w), 1560 (w), 1485 (s), 1428 (w), 1305 (w), 1255 (s), 1036 (w), 916 (s), 848 (w), 665 (w), 582 (s), 542 (w).

(pipH)$_3${Fe$_6$Y(shiH)$_3$(shi)$_6$}·1.5 pip·xH$_2$O (4): The complex was prepared in the same manner as the complexes above but with the use of Y(NO$_3$)$_3$·H$_2$O (10.00 mg, 0.025 mmol) as the lanthanide source. After 8 days dark brown crystals of **4**; these were collected by filtration, washed with hexanes (3 × 5 mL) and dried in air. Yield: 0.039 g (52%) based on the Y^{III} ion. The vacuum-dried solid was analyzed as **4·1.5pip·11H$_2$O (Fe$_6$Y$_1$H$_{113.5}$O$_{38}$C$_{85.5}$N$_{13.5}$):** C, 43.09; H, 4.88; N, 7.92. Found: C, 43.19; H, 4.82; N, 7.81. Selected ATR data (cm^{-1}): 1592 (w), 1560 (w), 1485 (s), 1428 (w), 1305 (w), 1255 (s), 1036 (w), 916 (s), 848 (w), 665 (w), 582 (s), 542 (w).

3.7.2 Single-crystal X-ray diffraction studies.

X-ray diffraction data for the structure analysis were collected from suitable single crystals on a STOE IPDS 2T [2–5] equipped with an Oxford cooling system operating at 120(2)K (**1**) and at 193(**2**) K [3–5], respectively. Graphite-monochromated Mo-Kα radiation (λ = 0.71073 Å) from long-fine focus sealed X-ray tube was used throughout. Data indexing, reduction, integration and absorption correction were done with STOE X-AREA and STOE X-RED[2]. Structures were solved with SHELXT[3] and refined by full-matrix least-squares on F-squared using SHELXL[4], interfaced through OLEX2[5]. All non-hydrogen atoms were refined with anisotropic displacement parameters, while hydrogen atoms belonging to the main core have been placed on idealized position using a riding model. The hydrogen atoms of the doubly deprotonated ligands were placed according to charge balance considerations and geometrical reasons. For the solvent water molecules the hydrogen atoms were placed geometrical. For the solvent water molecules the hydrogen atoms cannot be located satisfactorily and were omitted. Although some water molecules can be located, still large solvent accessible voids are present in the structures. The highly disordered solvent molecules in these voids were squeezed with the routine SQUEEZE[6–8] implemented in Platon[7]. The piperidinium cation is disordered over two positions with a site occupation of 0.6/0.4. CCDC 1873575-1873578 contains the supplementary crystallographic data for the structure reported in this paper. These data can be obtained free of charge via www.ccdc.cam.ac.uk/conts/retrieving.html (or from the Cambridge Crystallographic Data Centre, 12 Union Road, Cambridge CB21EZ, UK; fax: (+44)1223-336-033; or deposit@ccdc.cam.ac.uk).

Table S1 Crystallographic data for complexes **1-4.**

Complex	**1**	**2**	**3**	**4**
Empirical formula	$C_{85.5}H_{91.50}Fe_6GdN_{13.5}O_{45}$	$C_{85.5}H_{93}DyFe_6N_{13.5}O_{43.5}$	$C_{85.5}H_{91.5}TbFe_6N_{13.5}O_{45}$	$C_{85.5}H_{91.5}YFe_6N_{13.5}O_{46.25}$
Formula weight	2520.59	2503.35	2522.26	2472.25
Temperature/K	120(2)	193(2)	193(2)	193(2)
Crystal system	trigonal	trigonal	trigonal	trigonal
Space group	P $\bar{3}$c 1	P $\bar{3}$c 1	P $\bar{3}$c 1	P $\bar{3}$c 1
a/Å	20.306(2)	20.474(3)	20.715(3)	20.6406(5)
b/Å	20.306(2)	20.474(3)	20.715(3)	20.6406(5)
c/Å	36.6668(4)	36.848(7)	37.100(7)	37.0102(11)
α/°	90	90	90	90
β/°	90	90	90	90
γ/°	120	120	120	120
Volume/Å^3	13094(3)	13377(5)	13787(5)	13655.2(8)
Z	3.99996	3.99996	3.99996	3.99996
ρ_{calc}g/cm^3	1.279	1.243	1.215	1.203
μ/mm^{-1}	1.222	1.258	1.193	1.115
F(000)	5116.0	5082	5120	5056.0
Crystal size/mm^3	0.23 × 0.157 × 0.12	0.18 × 0.16 × 0.13	0.42 × 0.393 × 0.34	0.26 × 0.137 × 0.06
Radiation	MoK\α (λ = 0.71073)	MoK\α (λ = 0.71073)	MoK\α (λ = 0.71073)	MoK\α (λ = 0.71073)
2Θ range for data collection/°	4.162 to 57.018	4.13 to 56.976	4.082 to 56.952	4.958 to 51.99
Index ranges	-21 ≤ h ≤ 27 -27 ≤ k ≤ 27 -46 ≤ l ≤ 48	-26 ≤ h ≤ 25 -24 ≤ k ≤ 27 -48 ≤ l ≤ 49	-27 ≤ h ≤ 26 -27 ≤ k ≤ 27 -49 ≤ l ≤ 48	-22 ≤ h ≤ 25 -25 ≤ k ≤ 22 -45 ≤ l ≤ 45
Reflections collected	48829	44898	68203	50806
Independent reflections	R_{int} = 0.0256 R_{sigma} = 0.0191	R_{int} = 0.0417 R_{sigma} = 0.0394	R_{int} = 0.0570 R_{sigma} = 0.0268	R_{int} = 0.1053 R_{sigma} = 0.0539
Data/restraints/ parameters	10867 / 114 / 562	11114/ 303/ 544	11553/ 120/ 553	8957/ 160/ 556
Goodness-of-fit on F^2	1.077	1.111	1.143	1.121
Final R^{a,b} indexes [I>=2σ (I)]	R_1 = 0.0533 wR_2 = 0.1436	R_1 = 0.0744 wR_2 = 0.1872	R_1 = 0.0572 wR_2 = 0.1699	R_1 = 0.0846 wR_2 = 0.2312
Final R^{a,b} indexes [all data]	R_1 = 0.0645 wR_2 = 0.1513	R_1 = 0.1169 wR_2 = 0.2189	R_1 = 0.0762 wR_2 = 0.1856	R_1 = 0.1292 wR_2 = 0.2695
Largest diff. peak /hole / e Å^{-3}	1.03 / -1.28	1.08/ -1.84	0.751/ -0.374	0.88/ -0.59

$^a R_1 = \Sigma(||F_o| - |F_c||)/\Sigma|F_o|$. $^b wR_2 = [\Sigma[w(F_o^2 - F_c^2)^2]/\Sigma[w(F_o^2)^2]]^{1/2}$, $w = 1/[\sigma^2(F_o^2) + (ap)^2 + bp]$, where $p = [\max(F_o^2, 0) + 2F_c^2]/3$.

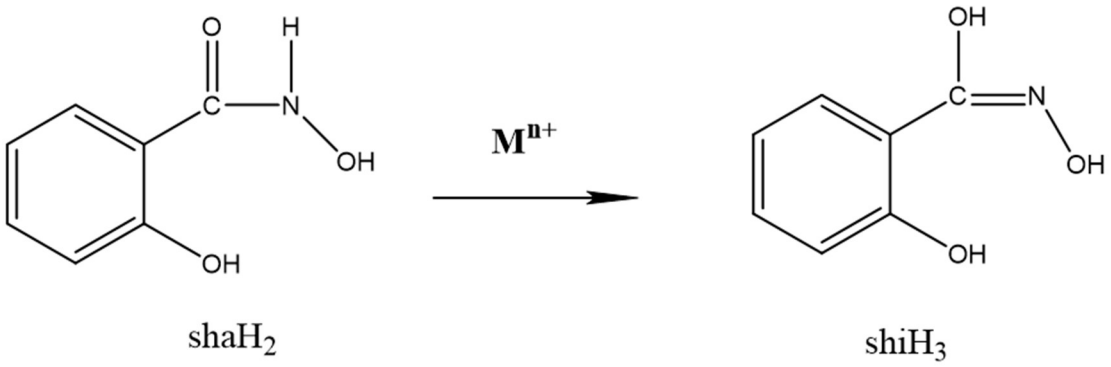

Scheme 1. Illustrative representation and abbreviation of organic molecules discussed in the text.

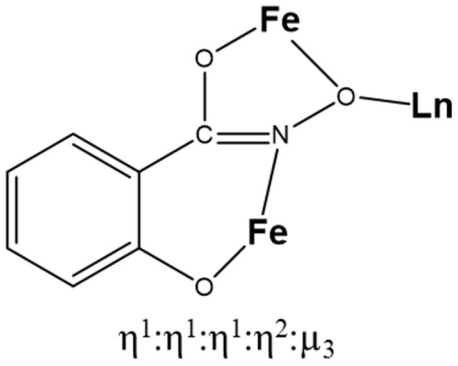

Figure S1: Coordination mode of shi^{3-} in complexes **1-4**.

Table S2 Selected Bond Lengths for complexes **1-4.**

Atom	Atom	Length/Å
Dy1	O2	2.373(4)
Dy1	O5	2.361(4)
Dy1	O8	2.548(4)
Fe1	O1[2]	1.999(4)
Fe1	O2[2]	2.037(4)
Fe1	O3	1.971(5)
Fe1	O9	1.989(5)
Fe1	N1	2.114(6)
Fe1	N3	2.064(5)
Fe2	O4[2]	2.032(4)
Fe2	O5[2]	2.014(4)
Fe2	O6	1.981(4)
Fe2	O7	1.950(5)
Fe2	O8	2.095(4)
Fe2	N2	2.027(6)
O2	N1	1.419(6)
O5	N2	1.408(6)
O8	N3	1.418(6)
Gd1	O2	2.386(2)
Gd1	O5	2.396(2)
Gd1	O8	2.549(3)
Fe1	O11	2.033(3)
Fe1	O21	2.010(3)
Fe1	O3	1.980(3)
Fe1	O8	2.096(2)
Fe1	O9	1.951(3)
Fe1	N1	2.032(3)
Fe2	O4[1]	2.008(3)
Fe2	O5[1]	2.029(2)
Fe2	O6	1.980(3)
Fe2	O7	1.985(3)
Fe2	N2	2.121(3)
Fe2	N3	2.070(3)
O2	N1	1.392(4)
O5	N2	1.413(4)
O8	N3	1.415(4)
Tb1	O2	2.388(3)
Tb1	O5	2.383(3)
Tb1	O8	2.558(3)
Fe1	O1[2]	2.001(3)
Fe1	O2[2]	2.035(3)
Fe1	O3	1.979(3)
Fe1	O9	1.992(3)
Fe1	N1	2.125(4)
Fe1	N3	2.066(4)
Fe2	O4[2]	2.031(3)

Fe2	O5[2]	2.013(3)
Fe2	O6	1.984(3)
Fe2	O7	1.951(3)
Fe2	O8	2.091(3)
Fe2	N2	2.031(4)
O2	N1	1.415(5)
O5	N2	1.393(5)
O8	N3	1.411(5)
Y1	O2	2.361(4)
Y1	O5[1]	2.373(4)
Y1	O8	2.545(4)
Fe1	O1[1]	2.029(5)
Fe1	O2[1]	2.016(5)
Fe1	O3	1.992(5)
Fe1	O7	1.957(5)
Fe1	O8	2.095(4)
Fe1	N1	2.024(6)
Fe2	O4[1]	2.003(5)
Fe2	O5[1]	2.037(5)
Fe2	O6	1.975(5)
Fe2	O9	1.990(5)
Fe2	N2	2.119(6)
Fe2	N3	2.059(5)
O2	N1	1.394(7)
O5	N2	1.421(6)
O8	N3	1.417(7)

[1]1+Y-X,1-X,+Z; [2]1-Y,+X-Y,+Z; [3]-Y+X,-Y,3/2-Z

Table S3 Selected Bond Angles for **1-4.**

Atom	Atom	Angle/˚
O2[1]	Dy1	O2	76.99(15)
O2	Dy1	O8	70.76(14)
O2[1]	Dy1	O8	77.51(14)
O2[2]	Dy1	O8[2]	70.76(14)
O2	Dy1	O8[1]	142.48(15)
O5	Dy1	O2[2]	130.48(13)
O5	Dy1	O2	88.35(15)
O5	Dy1	O2[1]	59.89(14)
O5	Dy1	O8	67.92(14)
O5	Dy1	O8[1]	129.17(14)
O8[1]	Dy1	O8	118.61(4)
O1[1]	Fe1	O2[1]	77.14(17)
O1[1]	Fe1	N1	96.75(19)
O1[1]	Fe1	N3	159.3(2)
O2[1]	Fe1	N1	83.56(19)
N3	O8	Dy1	115.6(3)
O2	N1	Fe1	122.6(3)
O2	N2	Fe2	116.5(4)
O2	Gd1	O2[1]	77.32(9)
O2	Gd1	O5[1]	145.32(8)
O2	Gd1	O5	88.27(8)
O2[1]	Gd1	O5	130.37(9)
O2	Gd1	O8	67.76(8)
O2	Gd1	O8[1]	128.82(8)
O2[1]	Gd1	O8	59.71(8)
O5	Gd1	O5[1]	77.26(9)
O5	Gd1	O8	70.82(8)
O5	Gd1	O8[1]	142.91(8)
O5	Gd1	O8[2]	77.70(8)
O8	Gd1	O8[1]	118.51(2)
O1[1]	Fe1	O8	149.11(11)
O2[1]	Fe1	O1[1]	76.39(10)
O2[1]	Fe1	O8	73.64(10)
O2[1]	Fe1	N1	90.37(12)
N3	O8	Gd	114.99(19)
N3	O8	Fe1	109.93(19)
O2	N1	Fe1	117.1(2)
O5	N2	Fe2	122.8(2)
O2	Tb1	O2[2]	76.96(11)
O2[1]	Tb1	O8	77.50(10)
O2	Tb1	O8[1]	142.83(10)
O2	Tb1	O8	71.27(10)

O5	Tb1	O2	88.33(11)
O5[1]	Tb1	O2	130.98(11)
O5	Tb1	O2[1]	144.78(11)
O5[1]	Tb1	O5	77.40(11)
O5	Tb1	O8	67.45(10)
O5	Tb1	O8	59.89(10)
O8[1]	Tb1	O8	118.48(3)
O1[1]	Fe1	O2[1]	76.90(13)
O1[1]	Fe1	N1	97.05(14)
O1[1]	Fe1	N3	159.11(15)
O2[1]	Fe1	N1	83.59(14)
N3	O8	Tb1	115.5(2)
N3	O8	Fe2	110.3(2)
O2	N1	Fe1	122.6(3)
O5	N2	Fe2	117.0(3)
O2	Y1	O2[1]	77.40(17)
O2	Y1	O5[1]	144.92(15)
O2	Y1	O5	88.25(15)
O2	Y1	O5[2]	130.78(16)
O2	Y1	O8[1]	129.01(15)
O2	Y1	O8[2]	59.86(15)
O2	Y1	O8	67.78(15)
O5	Y1	O5[1]	77.12(16)
O5	Y1	O8[2]	77.29(15)
O5	Y1	O8[1]	142.73(14)
O5	Y1	O8	71.08(15)
O8	Y1	O8[1]	118.56(4)
O1[1]	Fe1	O8	148.66(19)
O2[1]	Fe1	O1[1]	76.68(18)
O2[1]	Fe1	O8	73.22(17)
O2[1]	Fe1	N1	89.5(2)
N3	O8	Y1	115.8(3)
N3	O8	Fe1	110.1(4)
O2	N1	Fe1	117.0(4)
O5	N2	Fe2	122.8(4)

[1]1-Y,+X-Y,+Z; [2]1+Y-X,1-X,+Z; [3]-Y+X,-Y,3/2-Z

Table S4: Bond Valence Sum Calculations (BVS) for complexes **1**-**4**.

Atom	Complex **1**		Complex **2**		Complex **3**		Complex **4**	
	+2	**+3**	**+2**	**+3**	**+2**	**+3**	**+2**	**+3**
Fe1	2.65	**3.13**	2.63	**3.08**	2.60	**3.05**	2.63	**3.11**
Fe2	2.61	**3.06**	2.65	**3.13**	2.65	**3.13**	2.62	**3.07**

Table S5. Shape measurements of the 9-coordinate lanthanide coordination polyhedra. The bold numbers indicate the closest polyhedron according to SHAPE calculations.[97]

Polyhedron[c]	Gd1	Dy1	Tb1	Y1
EP-9	35.38	35.34	35.44	35.35
OPY-9	23.56	23.52	23.50	23.52
HBPY-9	19.89	19.95	20.09	20.03
JTC-9	12.76	12.73	12.76	12.81
JCCU-9	10.51	10.47	10.58	10.53
CCU-9	9.53	9.56	9.64	9.60
JCSAPR-9	2.54	2.49	2.49	2.48
CSAPR-9	1.76	1.77	1.74	1.75
JTCTPR-9	1.89	1.78	1.81	1.78
TCTPR-9	**1.13**	**1.14**	**1.11**	**1.12**
JTDIC-9	10.64	10.66	10.76	10.80
HH-9	12.63	12.65	12.65	12.66
MFF-9	2.02	2.05	2.01	2.02

[c] Abbreviations: EP-9, enneagon; OPY-9, octagonal pyramid; HBPY-9, heptagonal bipyramid; JTC-9, Johnson triangular cupola J3; JCCU-9,capped cube J8; CCU-9, spherical-relaxed capped cube; JCSAPR-9, capped square antiprism J10; CSAPR-9, spherical capped square antiprism; JTCTPR-9, tricapped trigonal prism J51; TCTPR-9, spherical tricapped trigonal prism; JTDIC-9,tridiminished icosahedron J63; HH-9, hula-hoop; MFF-9, muffin.

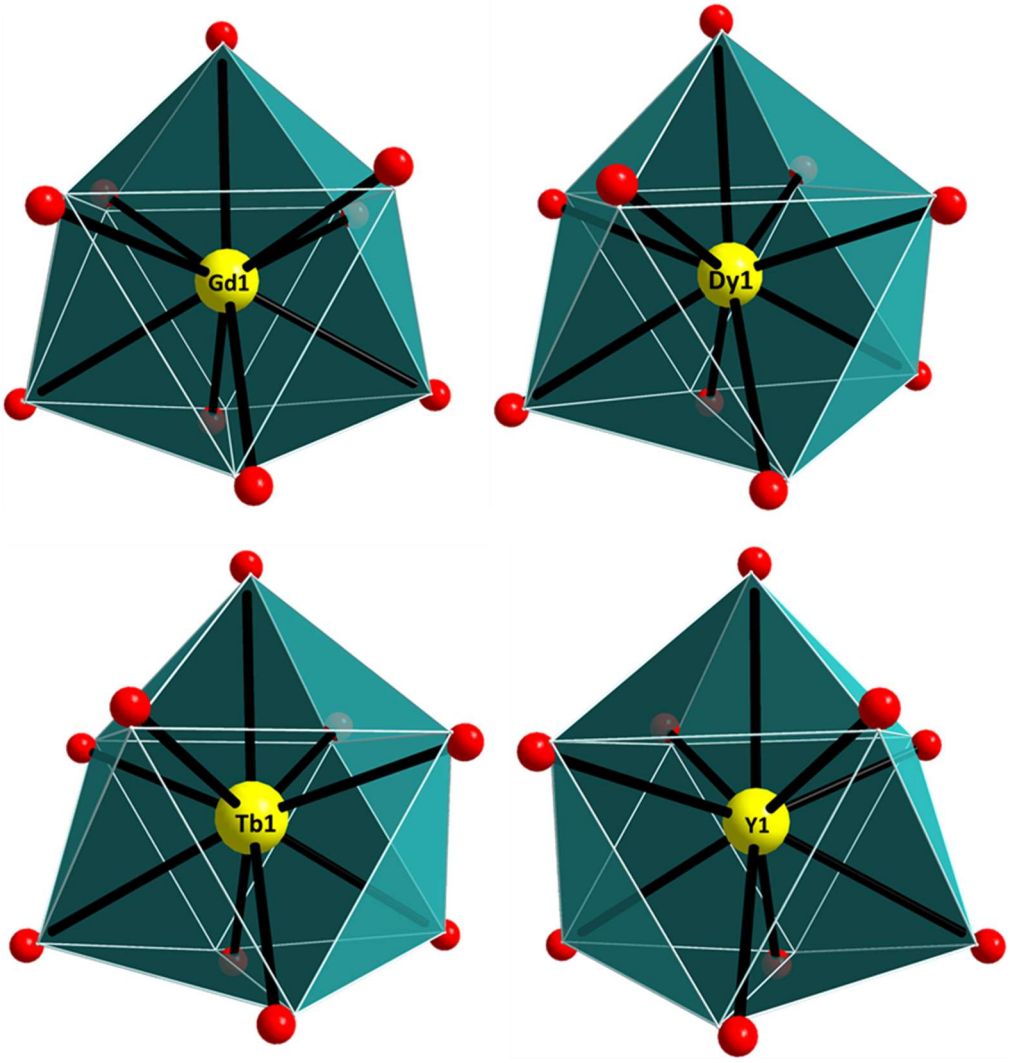

Figure S2: Spherical tricapped trigonal prismatic geometry of central lanthanide in complexes **1**-**4**. The points connected by the lighter lines define the vertices of the ideal polyhedron**.** Color scheme: Ln, yellow; O, red.

Table S6. Shape measurement of the 6 Fe(III) centers surrounding the lanthanide metal ion (in this case Dy) and respecting coordination polyhedra. The bold numbers indicate the closest polyhedron according to SHAPE calculations.

Polyhedron[c]	Fe_6
HP-6	34.32
PPY-6	17.55
OC-6	10.45
TPR-6	**0.88**
JPPY-6	21.71

[c] Abbreviations: HP-6, hexagon; PPY-6, pentagonal pyramid; OC-6, octahedron; TPR-6, trigonal prism; JPPY-6, Johnson pentagonal pyramid J2.

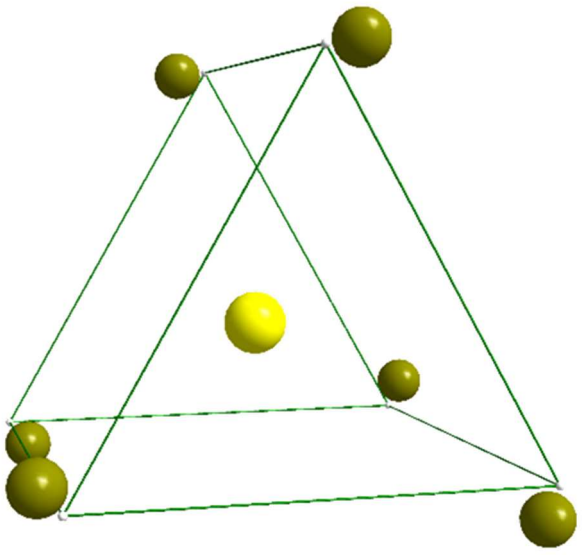

Figure S3: Trigonal prismatic geometry of Fe(III) ions in complex **2**. The points connected by the lighter lines define the vertices of the ideal polyhedron**.** Color scheme: Dy, yellow; Fe, dark yellow.

3.7.3 Magnetic Studies

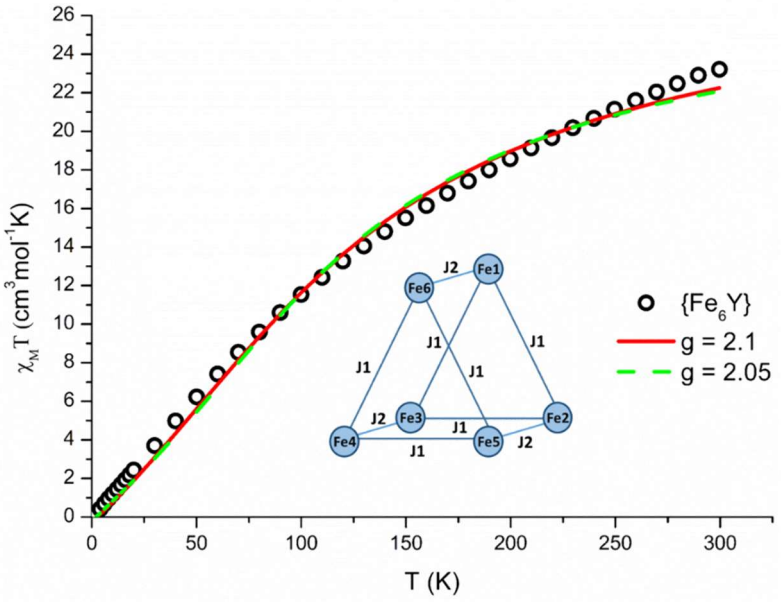

Figure S4: Temperature dependence of magnetic susceptibility for complex **4**. Red solid line and green dotted line represent fitting of the data in complex **4.** (Inset): fitting model for compound **4**.

Aiming to a better insight in the strength of the intramolecular Fe^{III} - Fe^{III} magnetic exchange interactions, the magnetic susceptibility data of complex **4** were fit using the CLUMAG[10] program. The magnetic susceptibility data of complex **4**, which comprises the diamagnetic Y^{III} ion in the central cavity, were fit using a 2-J model according to the spin Hamiltonian:

$$\hat{H} = -J_1 (\hat{S}_{Fe1}\cdot\hat{S}_{Fe2} + \hat{S}_{Fe2}\cdot\hat{S}_{Fe3} + \hat{S}_{Fe3}\cdot\hat{S}_{Fe1} + \hat{S}_{Fe4}\cdot\hat{S}_{Fe5} + \hat{S}_{Fe5}\cdot\hat{S}_{Fe6} + \hat{S}_{Fe4}\cdot\hat{S}_{Fe6}) - J_2(\hat{S}_{Fe1}\cdot\hat{S}_{Fe6} + \hat{S}_{Fe2}\cdot\hat{S}_{Fe5} + \hat{S}_{Fe3}\cdot\hat{S}_{Fe4})$$

Despite all our attempts for a better fitting of the data, the best fit parameters were obtained according to the depiction of the values on the graph above. The values that were obtained from the first attempt were J_1= +1.02 cm^{-1}, J_2 = - 9.60 cm^{-1} and g = 2.1, while the second best fitting attempt gave us J_1 = +1.86 cm^{-1}, J_2 = -9.40 cm^{-1} and g = 2.05. In both cases a TIP of 1.2*10-5 emu*mol^{-1} was employed. The g values in both cases are higher than expected for six-coordinate Fe(III) ions, with a d^5 electronic configuration, nevertheless no other fitting endeavors gave us more reliable results. A 1-J model was tested as well, considering the high symmetry of our molecule, with no success. Fitting attempts while employing more exchange coupling parameters were averted in order to avoid overparameterization, which in turn would not be reliable, based on the symmetric distances and angles of our compound.

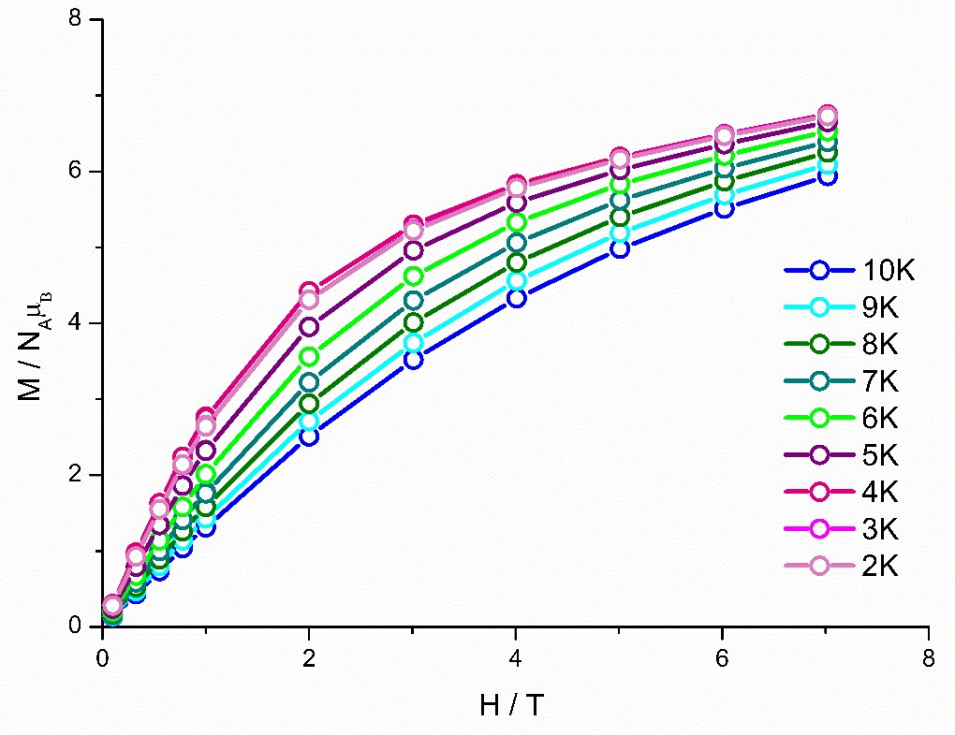

Figure S5: M vs H plots for complex **1** in various temperatures as indicated. Solid lines are guidelines for the eyes.

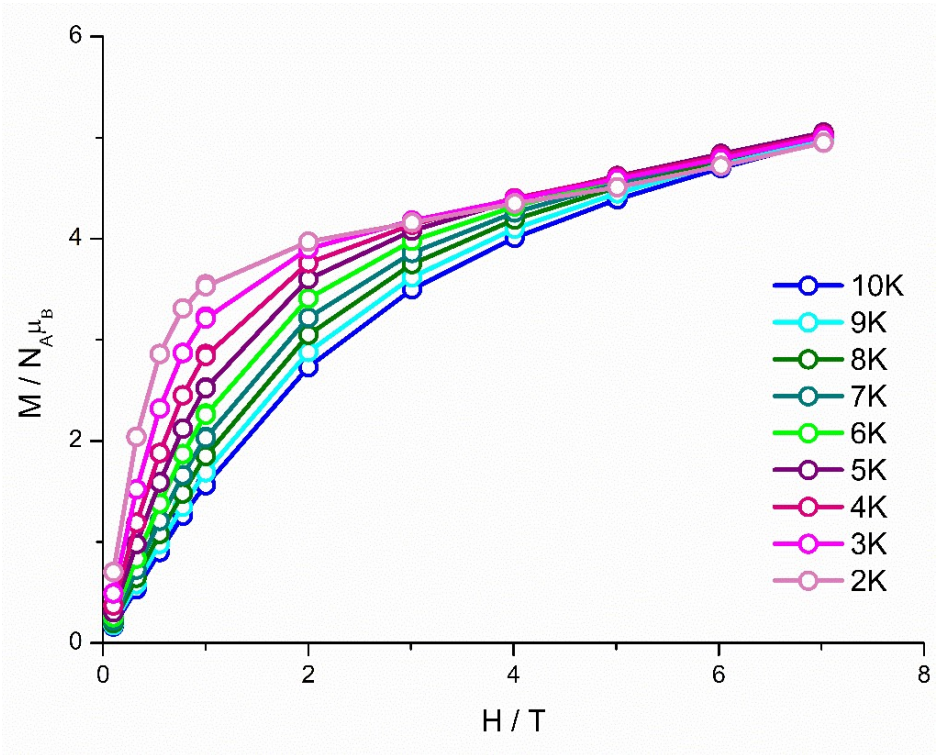

Figure S6: M vs H plots for complex **2** in various temperatures as indicated. Solid lines are guidelines for the eyes.

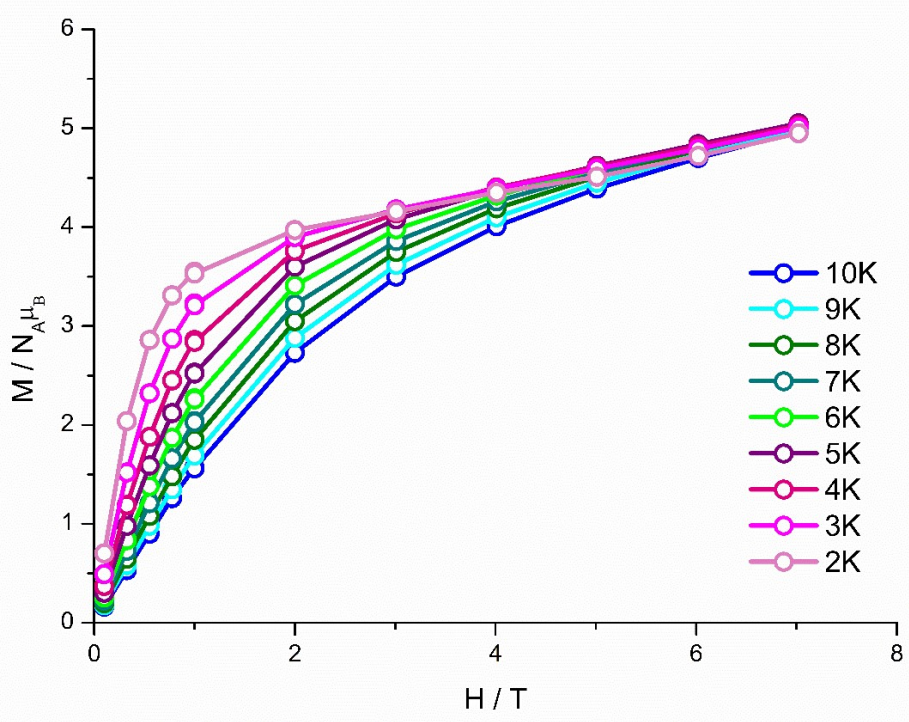

Figure S7: M vs H plots for complex **3** in various temperatures as indicated. Solid lines are guidelines for the eyes.

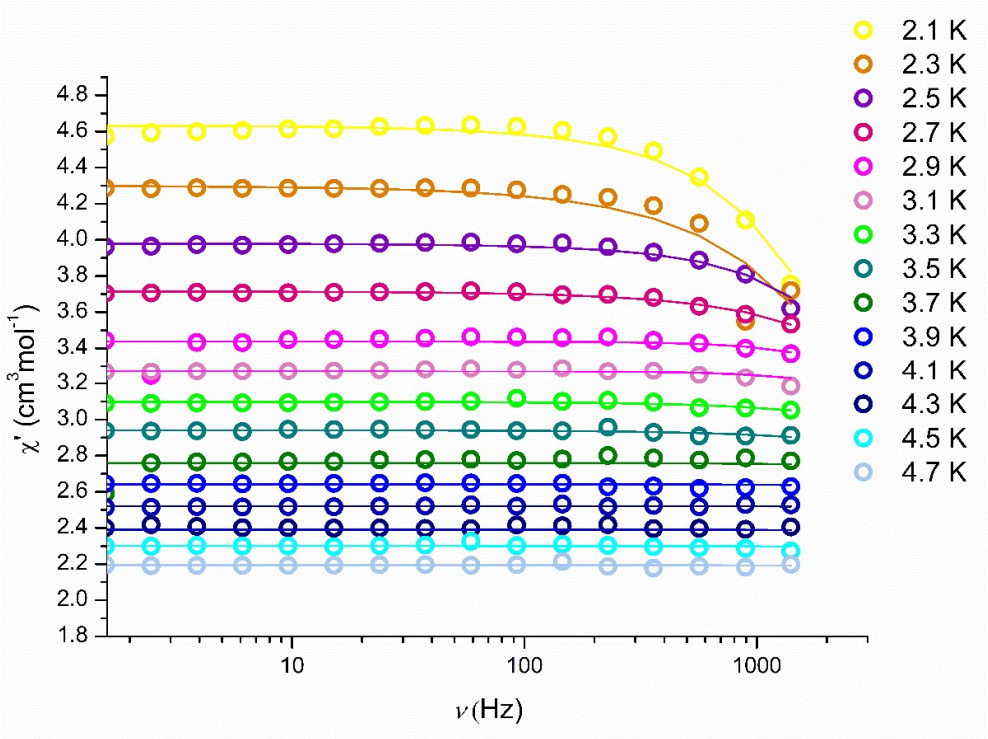

Figure S8: Frequency dependent in-phase susceptibility plot of for compound **2** (2.1 to 4.7 K) at zero field. Solid lines represent fit of the data.

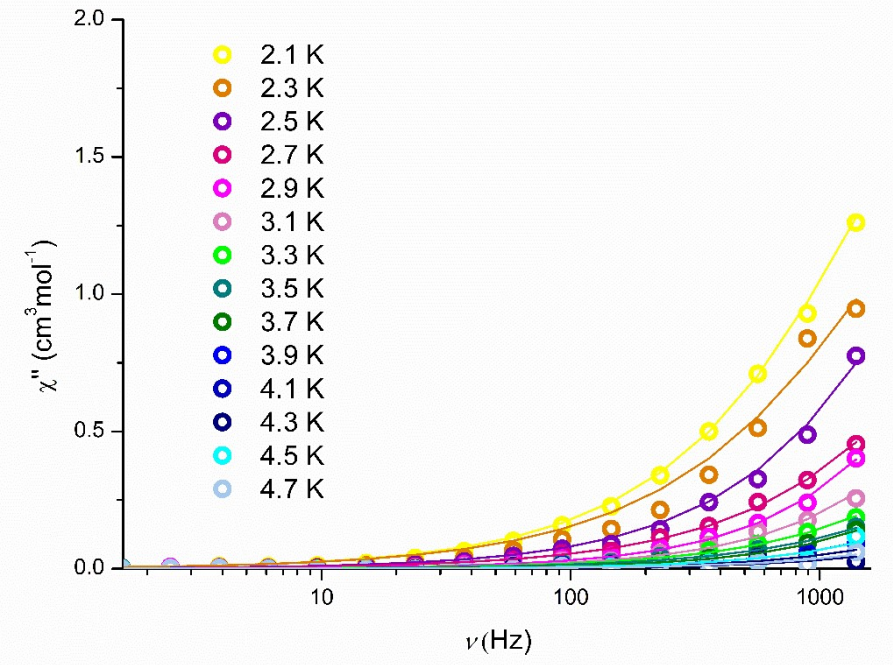

Figure S9: Frequency dependent out-of-phase susceptibility plot of for compound **2** (2.1 to 4.7 K) at zero field. Solid lines represent fit of the data.

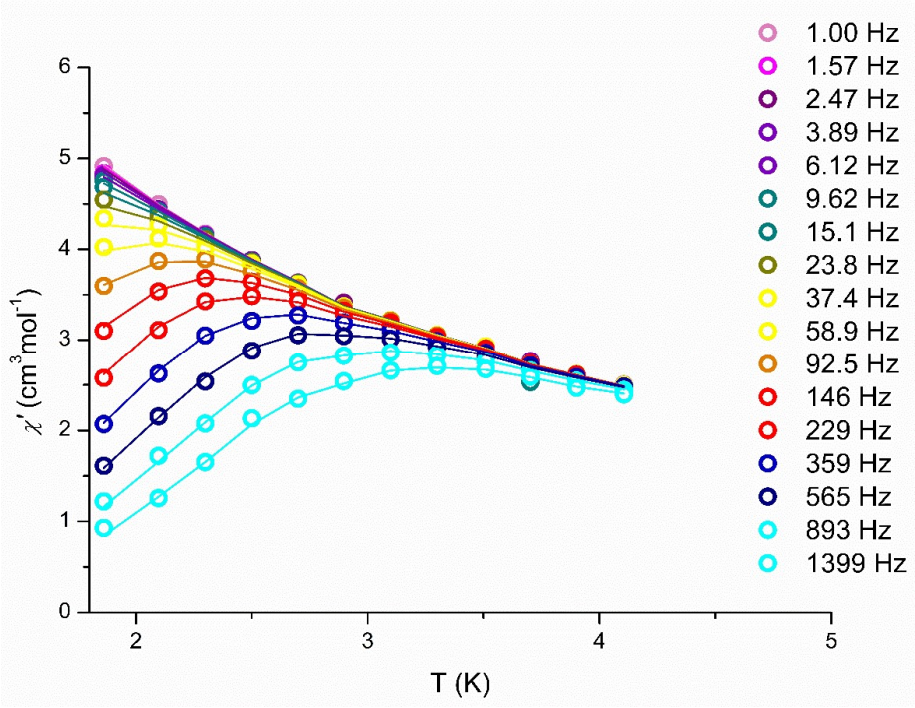

Figure S10: Temperature dependent in-phase susceptibility plot of for compound **2** (2.1 to 4.1 K) at 800 Oe. Solid lines represent fit of the data.

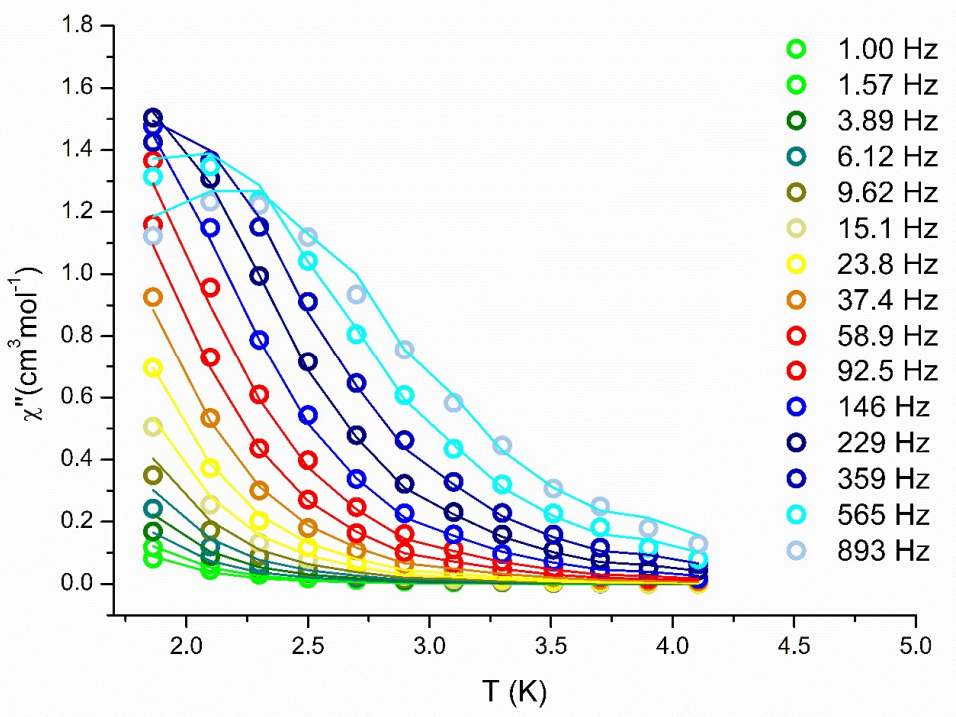

Figure S11: Temperature dependent out-of-phase susceptibility plot of for compound **2** (2.1 to 4.1 K) at 800 Oe. Solid lines represent fit of the data.

3.7.4 UV-Vis Absorption Spectroscopy

The ligand ($shiH_3$) has two main bands at 227 nm and 318 nm, which appear to be also present at all the complexes. These ligand-centered transitions, that can be assigned to excitations within the delocalized π-system of the coordinated hydroxamic acid, are observed at 210 and 307 nm for **1**, at 212 and 320 nm for **2**, at 219 and 312 nm for **3** and at 211 and 334 nm for **4**. The light absorption by **1** , **2**, **3** and **4** at around ~460 nm is characteristic for ligand-to-metal charge-transfer (LMCT) transitions.[11]

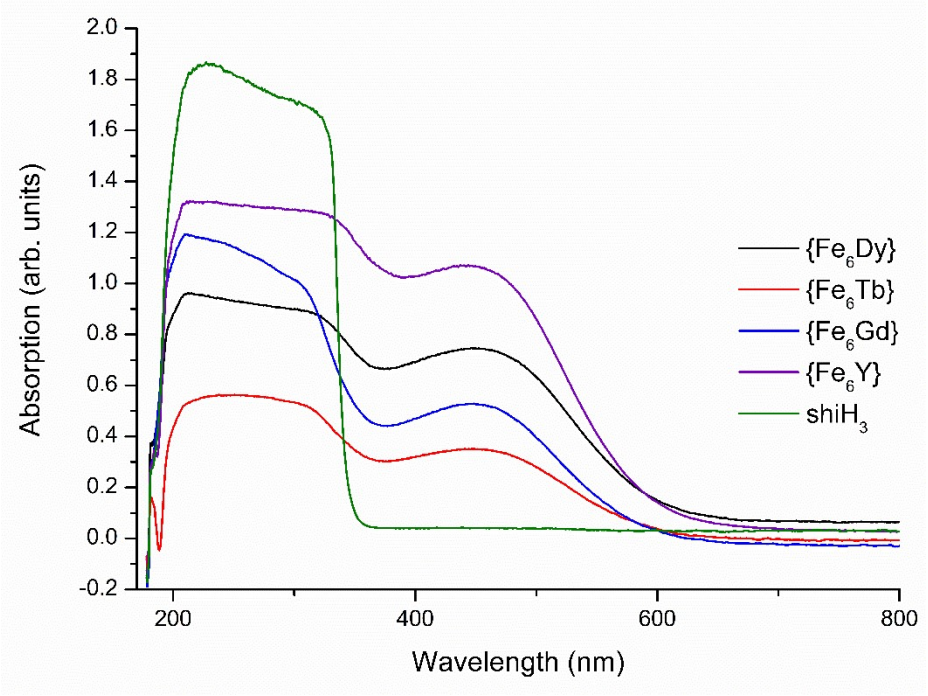

Figure S12: UV-Vis spectra of **1** (blue), **2** (black), **3** (red), **4** (purple) and $shiH_3$ (green) in MeCN.

3.7.5 Infrared Absorption Spectroscopy

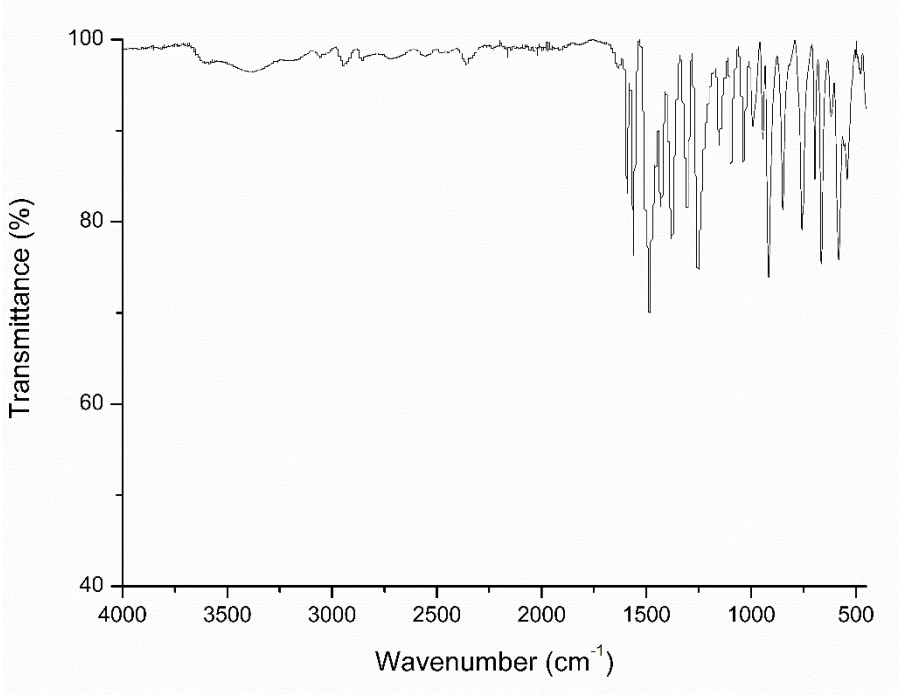

Figure S13: IR spectrum for complex **1**.

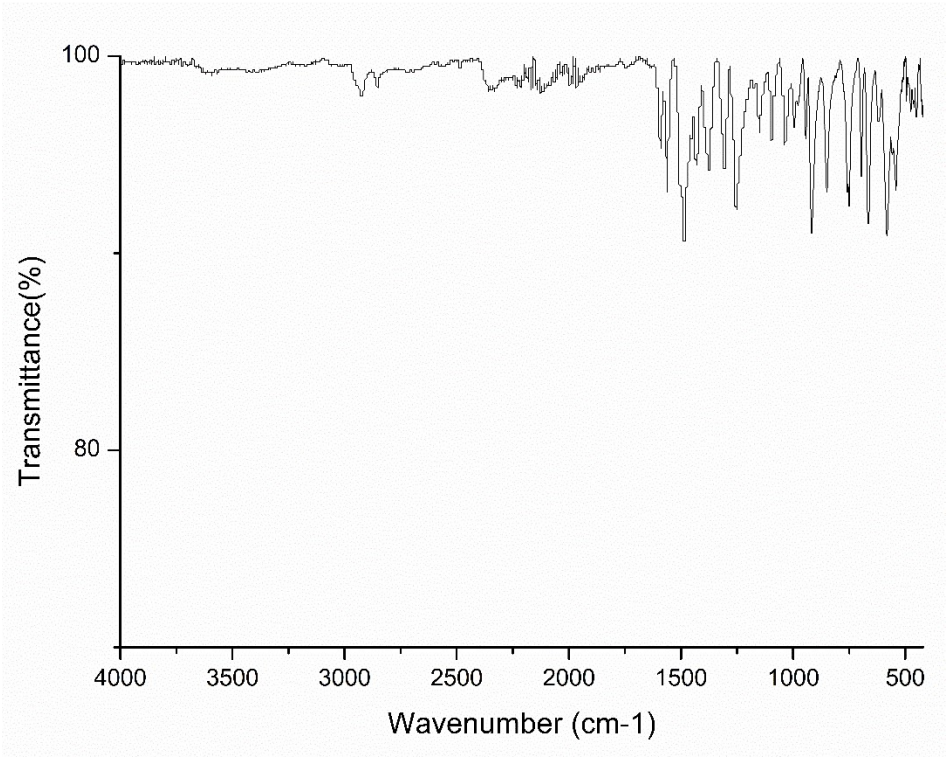

Figure S14: IR spectrum for complex **2**.

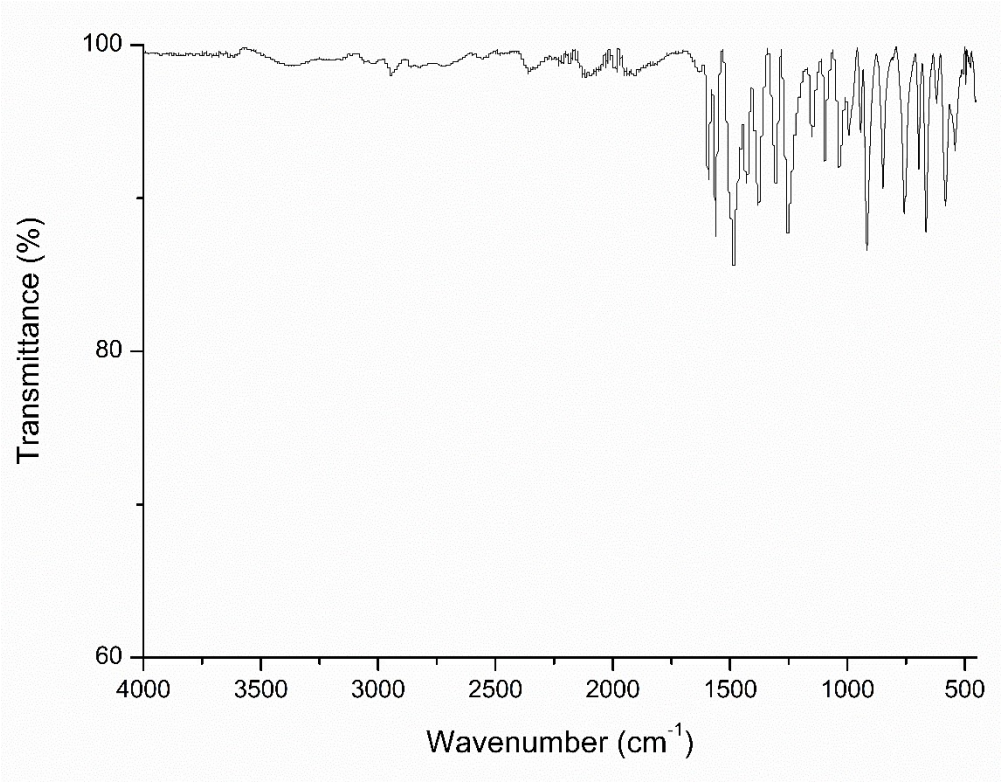

Figure S15: IR spectrum for complex **3**.

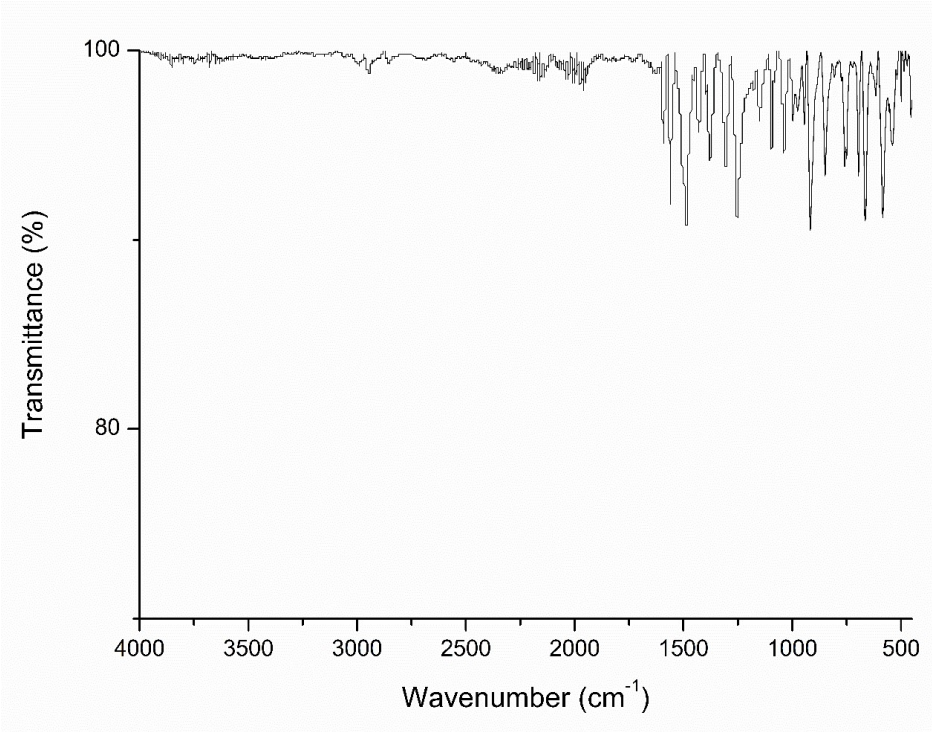

Figure S16: IR spectrum for complex **4**.

3.6.6 References

1 G. A. Bain and J. F. Berry, *Journal of Chemical Education*, 2008, **85**, 532.

2 Stoe & Cie X-AREA 2002, Stoe & Cie X-RED 2002, Stoe & Cie, Darmstadt, Germany.

3 G. M. Sheldrick, *Acta Crystallographica Section A Foundations and Advances*, 2015, **71**, 3–8.

4 G. M. Sheldrick, *Acta Crystallographica Section C Structural Chemistry*, 2015, **71**, 3–8.

5 O. V. Dolomanov, L. J. Bourhis, R. J. Gildea, J. A. K. Howard and H. Puschmann, *Journal of Applied Crystallography*, 2009, **42**, 339–341.

6 A. L. Spek, *Journal of Applied Crystallography*, 2003, **36**, 7–13.

7 A. L. Spek, *Acta Crystallographica Section D Biological Crystallography*, 2009, **65**, 148–155.

8 A. L. Spek, *Acta Crystallographica Section C Structural Chemistry*, 2015, **71**, 9–18.

9 S. Alvarez, P. Alemany, D. Casanova, J. Cirera, M. Llunell and D. Avnir, *Coordination Chemistry Reviews*, 2005, **249**, 1693–1708.

10D. Gatteschi and L. Pardi, *Gazz. Chim. Ital.*, 1993, **123**, 231.

11G. Gliemann, *Berichte der Bunsengesellschaft für physikalische Chemie*, 1985, **89**, 99–100.

Chapter 4

This chapter deals with the synthesis and characterization of the first double-decker Ga(III)/Ln(III) 12-MC-4 complex. The compound has been structurally and magnetically investigated. As it is observed, the complex exhibits frequency dependent tails of signals at 0 field, while upon application of an external dc field the out-of-phase peaks are visible. Fitting of the data gave a U_{eff} value of 40 K. Theoretical calculations were also performed in order to get a deeper insight towards the magnetic dynamics of our {Ga_8Dy} molecule. Finally, preliminary photoluminescence studies were performed and presented, where the Dy-based emission of the compound is clearly visible. This paper has been submitted for publication at Angewandte Chemie and the decision is still pending. The article will be presented as it has been submitted.

Author Contributions

Angeliki A. Athanasopoulou designed and performed the experiments regarding the isolation of complex **1**, which possesses the general formula of $(^tBu_4N)[Ga^{III}_8Dy^{III}(OH)_4(shi)_8]$. She also performed infrared (IR), UV-Vis, Photoluminescence (PL) studies as well as collected and prepared the samples for elemental analysis and SQUID magnetometry. Single-crystal X-ray measurements were performed from Dr. Dieter Schollmeyer while the refinement of collected data was performed by Dr. Luca M. Carrella. Evaluation of magnetic studies was done by Angeliki A. Athanasopoulou along with the assistance of Dr. Luca M. Carrella. Theoretical calculations were performed by Dr. José J. Baldoví. The manuscript was written by Angeliki A. Athanasopoulou while important input was added by José J. Baldoví, Luca M. Carrella and Eva Rentschler. Finally, Eva Rentschler had the overall supervision in the interpretation of data throughout the manuscript process.

Slow Magnetic Relaxation In a Unique Dy(III)-centered 12-Metallacrown-4 Double-Decker

Angeliki A. Athanasopoulou,[a,b] José J. Baldoví [c], Luca M. Carrella,[a] and Eva Rentschler*[a]

a] A. A. Athanasopoulou, Dr. L. M. Carrella, Prof. Dr. E. Rentschler
Institute of Inorganic and Analytical Chemistry, Johannes Gutenberg University, Duesbergweg 10-14, D-55128 Mainz, Germany
E-mail: rentschl@uni-mainz.de

[b] Graduate School of Excellence Materials Science in Mainz
Staudinger Weg 9, D-55128 Mainz, Germany

[c] Dr. J. J. Baldoví
Max Planck Institute for the Structure and Dynamics of Matter
Luruper Chaussee 149, D-22761 Hamburg, Germany

4.1 Abstract

Upon reacting $Dy(O_2CMe)_3 \bullet xH_2O$ and $Ga(NO_3)_3 \bullet xH_2O$ following a metallacrown synthetic routine, complex $(^tBu_4N)[Ga^{III}_8Dy^{III}(OH)_4(shi)_8]$ (**1**) was obtained. The compound possesses a unique structure enclosing the central magnetic Dy^{III} ion between diamagnetic Ga^{III} 12-MC-4 sandwich-type ligands. The Dy^{III} is coordinated in square antiprismatic geometry and the double-decker complex exhibits single-molecule magnet (SMM) behavior with an effective energy barrier (U_{eff}) of 40 K. Consistent with the observed slow relaxation of magnetization, theoretical calculations suggest a $|\pm 11/2>$ ground state in the easy axis direction.

4.2 Introduction

The high demand on miniaturization of components for the development of smaller and novel devices has led to the use of nanoscale systems. Single Molecule Magnets (SMMs) are individual molecules (of a few nanometers) that have been in the spotlight of researchers for over 25 years since they have proven to be promising candidates for various applications such as high-density data storage, quantum computation, magnetic refrigeration and spintronics.[8–11] While in the beginning the interest was focused on polynuclear 3*d*-based SMMs[5], right after

the discovery that the mononuclear [Pc_2Tb] (Pc=phthalocyanine) complex exhibits slow relaxation of magnetization, the 4*f* elements became the focal point, improving immensely the SMM performance.[6–9] This second generation of SMMs is based on the magnetic anisotropy of a single ion, which arises from the combination of spin-orbit coupling and the crystal field. The selection of the appropriate coordination environment, depending on both the electronic f-shell shape of the magnetic center[10,11] and an adequate choice of ligands (in order to minimize molecular vibrations that couple to the spin states),[12,13] are crucial factors for the enhancement of their properties. The latest example highlighting the aforementioned approach, is the report of a dysprosocenium complex possessing an energy barrier (U_{eff}) of 1,541 cm^{-1}, displaying magnetic hysteresis at temperatures above 77 K where nitrogen liquefies.[9]

The SMM behavior of monometallic phthalocyanine sandwich complexes of Tb^{III} and Dy^{III} showed that the organic ligand used is of great importance since the strength and the symmetry of the crystal field at the Ln^{III} ion is the key for the resulting slow relaxation of magnetization.[6,14] Hence, we decided to employ Metallacrowns (MCs) as ligands and coordinate them with lanthanides thus forming double-decker systems. Lately, it has been shown that the use of diamagnetic metal ions in combination with anisotropic paramagnetic ones can increase or enhance the effective energy barrier, with a few examples using Zn^{II}, Mg^{II}, Al^{III} and others, already reported.[15–21] The presence of diamagnetic metal ions advances larger polarization effects, which subsequently lead to enhanced larger electrostatic interactions on the lanthanide ions compared to systems using solely closed shell organic ligands. That assists on the destabilization of the excited states causing a bigger gap between them and the ground state.[22,23] Thus, the employment of a Ga(III)-based MC systems is a novel approach towards the synthesis of new 12-MC-4 complexes, having as an ultimate goal the magnetic investigation of such compounds.

Metallacrowns (MCs), firstly reported in 1989 by Pecoraro and Lah,[24] are inorganic analogues of organic crown ethers and they possess a repeating $[-M-N-O]_n$ unit which assists in the formation of the characteristic MC cyclic motif. The [N-O] moiety is provided by salicylhydroxamates and derivatives which is a class of organic shells well known for being excellent chelating-bridging ligands in coordination chemistry, as well as for adopting the suitable geometry that promotes the formation of the MC motif.[25–27] These complexes have the ability to encapsulate a central metal ion in their cavity, similar to crown ethers, and their ring size varies from 9-MC-3 to 60-MC-20.[25] Recently, the incorporation of 4*f* metal ions in the central cavity of those compounds, has brought them into the forefronts of the field since

these molecules can be excellent choices for molecular recognition,[28,29] molecular magnetism[30] and luminescent technologies[26,30–33].

Lately, the enhancement of the inherent luminescent properties of lanthanides using diamagnetic Ga(III) ions as periphery ring metal ions, are presented.[30,34–38] Pecoraro and coworkers have reported a Ga(III)/Ln(III) 12-MC-4 complex using salicylhydroxamic acid,[30] in which they have extensively investigated the structural features and luminescent properties. However, magnetic studies have not been reported. Herein, we report the synthesis, structural and magnetic characterization of the first double-decker Ga(III)/Dy(III) 12-MC-4 complex using salicylhydroxamic acid as an organic bridging/chelating ligand. Theoretical calculations were employed in order to assist with the deeper understanding of the magnetic behavior of our compound. To the best of our knowledge, no double-decker or sandwich-type Ln(III)-Metallacrown complex has been published up to now.

4.3 Crystal structure of complex 1

The general reaction of $Ga(NO_3)_3 \bullet H_2O$, $Dy(O_2CMe)_3 \bullet xH_2O$, $shaH_2$ (Scheme 1, SI), $^tBu_4NClO_4$ and piperidine in a 8:1:8:3:8 molar ratio, in MeOH gave a white suspension that under extended stirring remained undissolved. Upon filtration, the colorless solution was left to slowly evaporate and that led to the formation of small colorless plate crystals of $(^tBu_4N)[Ga^{III}_8Dy^{III}(OH)_4(shi)_8]$ (**1**) in ~35 %. The chemical and structural identity of complex **1** was proven by single-crystal X-ray crystallography, elemental analyses (C, H, N) and IR spectroscopy (Supporting Information).

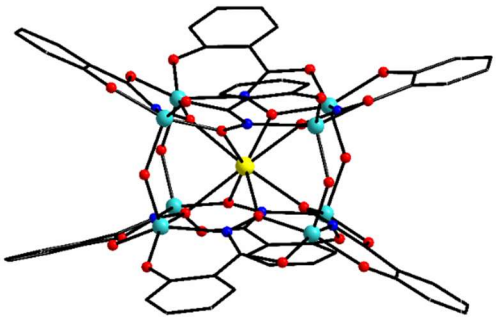

Figure 4.3.1: Schematic representation of complex **1**. Color scheme: Ga^{III}, aqua; Dy^{III}, yellow; N, blue; O, red; C, black. H atoms are omitted for clarity.

Single-crystal diffraction studies unveiled that complex **1** crystallizes in the monoclinic P2/*c* space group (Table S1). The oxidation states and the assignment of the ligands' protonation/deprotonation level in **1** were based on metric parameters and charge balance considerations. The compound consists of a $[Ga^{III}_8Dy^{III}(OH)_4(shi)_8]^-$ anion which is counterbalanced by a $^tBu_4N^+$ cation, while there are also MeOH and H_2O molecules in the lattice. The anion comprises eight Ga^{III} atoms and one Dy^{III} atom arranged in a sandwich-like topology. The Ga^{III} atoms are located above and below the planes of the central lanthanide ion. The basal Ga^{III} atoms are bridged via the oximate groups of eight triply deprotonated shi^{3-} ligands in a $\eta^1:\eta^1:\eta^1:\eta^2:\mu_3$ fashion, while the two deckers are connected to each other via the four μ-OH bridges. The oximato O atoms provided by the ligand are coordinated to the central Dy^{III} atom, serving as linkers of the two deckers. As a result, the Dy^{III} is enclosed by eight O atoms and possesses a square antiprismatic coordination geometry (CShM = 1.18, Figure S1, Table S4). All Ga atoms are five-coordinate with slightly distorted to almost perfect square pyramidal geometries (τ = 0.26 - 0.06) as it was defined by the trigonality index parameters.[39]

The overall $\{Ga^{III}_8Dy^{III}(\mu\text{-}OH)_4(\mu\text{-}NO)_8\}^{15+}$ core of **1** (Figure S2) reveals that the basal Ga•••Ga and the Ga•••Dy distances are in the ranges of 4.691(1)-4.714(1) and 3.716(1)-3.747(1) Å, respectively, while the Ga•••Ga distances between the two deckers are between 3.387(1) and 3.418(2) Å. The Ga-O-N-Ga torsion angles lie within the 165.3-176.4˚range. As it is observed the torsion angles are quite close to 180° and that explains the almost perfect planarity of the two 12-MC-4 planes.

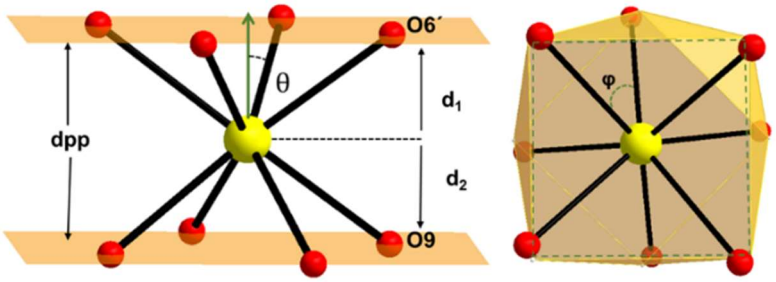

Figure 4.3.2: Structural parameters discussed in the text for complex **1**. Yellow ball: Dysprosium, red ball: oxygen.

Certain critical geometrical parameters were acquired for complex **1** in order to get a deeper understanding of the inner coordination sphere of the dysprosium ion (Figure 2). The θ angle, which corresponds to compression or elongation along the tetragonal axis depending on its value, is the angle between the four-fold axis and the Ln-O bond direction. The magic value for perfect eight-coordinate square antiprismatic systems is θ = 54.74˚, whilst larger angles are

consistent with compression and smaller ones correspond to elongation.[10,40,41] Complex **1** possess an average θ value of 54.29˚ revealing a slight axial elongation for the surrounding of the central lanthanide ion. Another important parameter that was calculated is the skew angle φ, which defines the angle between the diagonals of the two O_4-planes. When φ is 0 a perfect square prismatic geometry is expected, while when φ is 45˚ a perfect square antiprismatic geometry is anticipated. Complex **1** possesses an average φ value of 36.40˚ which further supports the distorted square antiprismatic geometry of the central Dy^{III} ion. The interplanar distance (dpp), was found to be 2.710(1) Å, while the distances d_1 and d_2 were both found to be 1.355(0) Å. Finally, compound **1** is the first and only example of a sandwich-type or double-decker lanthanide 12-MC-4 complex and the first possessing diamagnetic Ga^{III} metal ions as the periphery metal ions, encapsulating a paramagnetic Dy^{III} ion in the middle.

4.4 Magnetic studies of complex 1

Solid state, direct-current (dc) magnetic susceptibility studies were performed in the temperature range of 2 – 300 K on a freshly prepared and analytical pure (see Supporting Information for details) microcrystalline sample of **1**•$5H_2O$ under an applied field of 0.1 T. The $\chi_M T$ product at 300 K is 13.9 $cm^3mol^{-1}K$, very close to the value of 14.17 $cm^3mol^{-1}K$ expected for one non-interacting Dy^{III} ion ($^6H_{15/2}$, S = 5/2, L = 5, J = 15/2, g = 4/3) (Figure S3). The $\chi_M T$ product shows a slow and steady decrease upon cooling from 300 K till 50 K, while after that a more sharp decrease is observed till 2 K, where it reaches the value of 9.18 $cm^3mol^{-1}K$. The decrease at low temperature is characteristic for the depopulation of the Zeeman split crystal field levels. A small TIP correction of 5×10^{-4} cm^3mol^{-1} was added to the experimental susceptibility curve for correcting the unrealistic deviations at higher temperatures. The field dependence of magnetization was also measured for complex **1** in the temperature range of 2 - 10 K under a variety of magnetic fields of the 0 - 7 T range (Figure S4). As displayed in Figure S4, the values of magnetization increase sharply at low fields while after that a more continuous increase is observed for compound **1**. The value of magnetization of complex **1** at 2 K under the applied field of 7 T is 5.95 μ_B, not reaching saturation. The lack of saturation in magnetization is suggestive of the presence of magnetic anisotropy and/or population of the Dy^{III} low-lying states.

To further understand the observed magnetic behaviour of complex **1**, theoretical calculations were employed using the SIMPRE computational package.[42,43] The static magnetic susceptibility (Figure 5) was successfully simulated with a relative error of $E = 1.2 \cdot 10^{-4}$ using the Radial Effective Charge (REC) model (D_r = 1.26 Å and Z_i = 0.045) (see details in SI). The calculated magnetization curves are also in a good agreement with the experimental data.

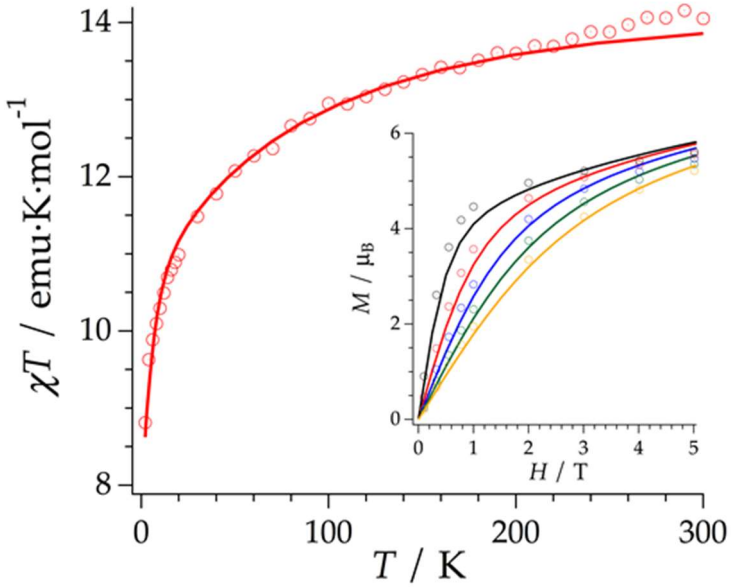

Figure 4.4.1: Experimental (symbols), fitted (solid line) thermal dependence of the magnetic susceptibility of complex **1** from 2 to 300 K measured at 1000 Oe. The inset shows experimental (symbols) and predicted (solid line) magnetization versus magnetic field at 2 (black), 4 (red), 6 (blue), 8 (green) and 10 K (orange).

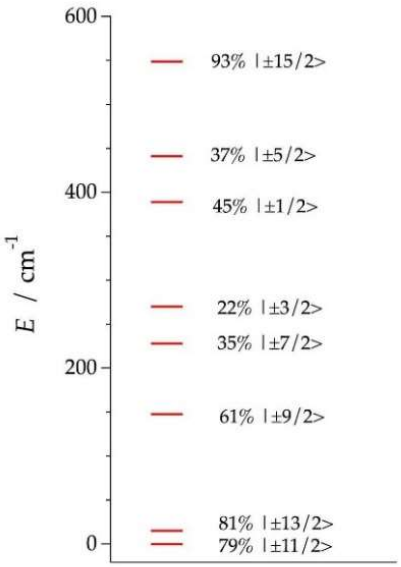

Figure 4.4.2: Energy diagram of Dy(III) electronic sublevels according to performed calculations.

According to the performed calculations, the ground state wave function is mainly composed by 79% of the |±11/2> microstates in the easy axis direction, which is congruent with the observed slow relaxation of the magnetization. The first excited doublet is located at about 15 cm^{-1}, showing a large contribution (81%) of another high spin microstate (±13/2) and widely separated from the rest of energy levels (Figure 4). The computed energy levels, wave functions and crystal-field parameters are available in the Supporting Information (Tables S5 and S6).

Alternating-current (ac) susceptibility measurements were performed for complex **1** in a zero-applied dc field, with a 3 Oe ac field oscillating at frequencies from 1-1400 Hz in the temperature range of 1.9-5.5 K. Complex **1** displays frequency-dependant tails of signals below 5.5 K at zero field, indicative of the presence of fast relaxation of magnetization (Figure S5-S8). This means that the slow relaxation of magnetization and quantum tunnelling (QTM) coexist. The lack of the appearance of the χ'' peak maxima at zero field led to further investigations, using the assistance of an optimum applied field of 1000 Oe (at frequencies from 1-1400 Hz and at a temperature range of 1.9-5.5 K) aiming to shift the peaks and supress the QTM. After the application of the external field the SMM behaviour of compound **1** is clearly pronounced since the χ' and χ'' values are significantly increased and the peaks maxima are clearly visible (Figure 5).

Plots of ln(τ) versus 1/T were produced (Figure 6) and a linear behaviour is observed for the high temperature regime, revealing the presence of a thermally activated Orbach pathway. A fit was obtained taking into account all possible relaxation processes using the equation $\tau^{-1} = \tau_{QTM}^{-1} + CT^n + \tau_0^{-1}\exp(-U_{eff}/K_BT)$, where τ_{QTM}^{-1} corresponds to the quantum tunnelling relaxation process, CT^n corresponds to the Raman relaxation and the last terms relate to the Orbach relaxation pathway.[154] The best fit parameters are n = 9, C = 0.0039 $s^{-1}K^{-9}$, Ueff = 40 K, τ_0 = 3.3 10^{-9} s and τ_{QTM} = 0.79 s (Figure 6).

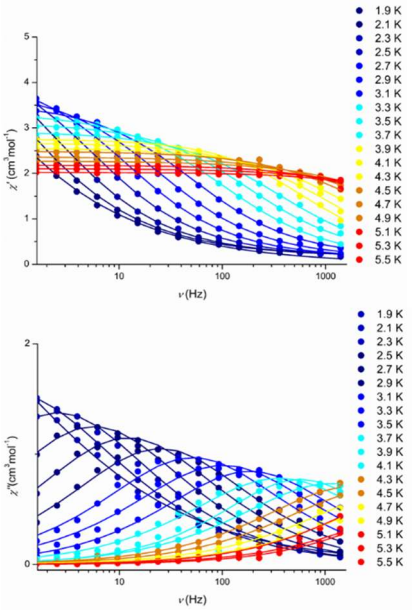

Figure 4.4.3: Frequency-dependent ac susceptibilities in an applied field of 1000Oe for complex **1**. The solid lines represent fitting of the data.

In zero dc field, the presence of an easy-axis anisotropy, the dipole-dipole and hyperfine interactions allow the mixing of the ground state of the Kramers ions thus advancing the QTM over thermal relaxation processes.[45,46] In order to reduce or even remove the QTM, an external (optimum dc field) was employed. The Cole-Cole plots for **1** in the temperature range of 1.9 K-5.5 K display semicircular shapes and a generalized Debye model (Cole-Cole model) was used for fitting of the data.[47,48]

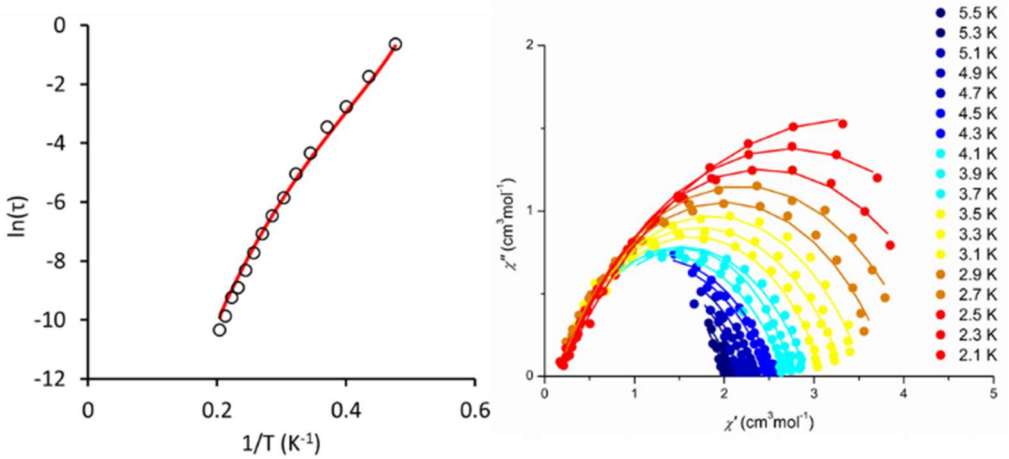

Figure 4.4.4: (left) Arrhenius plot showing the magnetization relaxation of **1** under an applied field of 1000 Oe. (right) Cole-Cole plots for compound **1** using the ac susceptibility data under a field of 1000 Oe from 2.1 K to 5.5 K. The solid lines represent the best fit obtained using the generalized Debye model.

The obtained α values are in the range of 0.47- 0.36, implying a distribution of relaxation times and possibly indicating the presence of multiple relaxation pathways due to a combination of thermally assisted processes and QTM, proven additionally from the fitting discussed. The observed slow relaxation of magnetization is most likely a combined result of the anisotropic central dysprosium ion and the surrounding diamagnetic Ga(III) ions, which induce electrostatic interactions, possibly assisting with the stabilization of the high multiplicity |±11/2> spin state.[22]

Preliminary photoluminescence studies have been performed, as shown in Figure 7. Complex **1** shows a strong blue emission upon maximum excitation at 340 nm. The broad band at ~375 nm is most likely due to a strong energy transfer from Dy^{III} to the ligand's excited state(s) causing the ligand's fluorescence, while the bands at 474, 581, 670 and 757 nm can be attributed to the characteristic $^4F_{9/2}\rightarrow{}^6H_{15/2}$, $^4F_{9/2}\rightarrow{}^6H_{13/2}$, $^4F_{9/2}\rightarrow{}^6H_{11/2}$ and $^4F_{9/2}\rightarrow{}^6H_{9/2}$ emission transitions of Dy^{III} ions, respectively.[49]

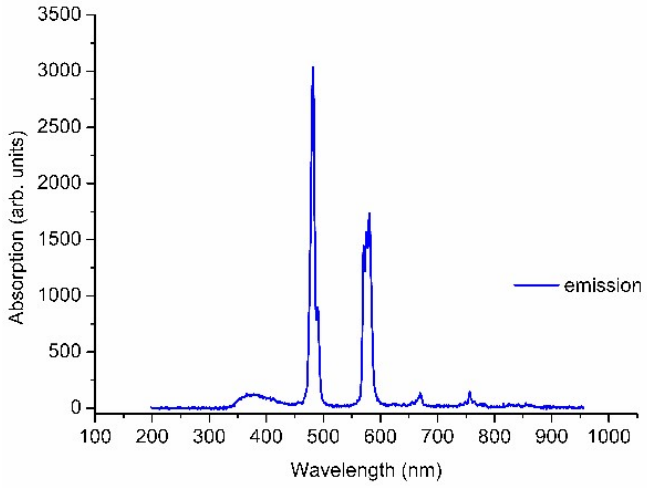

Figure 7. Room temperature emission spectra for **1** in MeCN. The excitation wavelength was 340 nm.

Up to now, neither fluorescence nor absorption spectra associated with lanthanide centers have been reported in Ln-based phthalocyanine (Pc) double-decker complexes.[50]

4.5 Conclusions

In conclusion, we have shown that the reaction of $Ga(NO_3)_3 \bullet H_2O$, and $Dy(O_2CMe)_3 \bullet xH_2O$ in the presence of salicylhydroxamic acid has led to the isolation of a novel Ln(III) double-decker 12-MC-4 or sandwich type complex, which shows slow relaxation of magnetization both at zero and with an applied magnetic field. Experimental measurements further confirmed the SMM nature of our $\{Ga_8Dy\}$ complex upon application of the optimum field of 1000 Oe, giving an effective energy barrier of U_{eff} = 40 K and a relaxation time $\tau_0 = 3.3\times10^{-9}$ s, while photoluminesce studies recorded the Dysprosium-based emission of the compound. Work in progress involves the isolation and characterization of more members of the lanthanide series, such us Tb^{III}, Ho^{III}, Er^{III}, as well as the substitution of the diamagnetic Ga(III) ions from paramagnetic ones, in order to compare the effect of diamagnetism over paramagnetism on the resulting energy barrier and the ensuing observed SMM behaviour or the new complexes.

Acknowledgements

We would like to thank Dr. Dieter Schollmeyer for the collection of the X-Ray diffraction data of our complex. A. A. A. is a member of (SFB/TRR) 173 ″Spin+X - Spin in its collective environment″ and a fellow of the Excellence Initiative by the Graduate School of Excellence Materials Science in Mainz, Germany (DFG/GSC 266), both initiated by the Deutsche Forschungsgemeinschaft (DFG, German Research Foundation). J. J. B. acknowledges the EU for a Marie Curie Fellowship (H2020-MSCA-IF-2016-751047)

Keywords: metallacrowns • single-molecule magnets • coordination chemistry • lanthanides • molecular magnetism

4.6 References

[1] Y.-N. Guo, G.-F. Xu, Y. Guo, J. Tang, *Dalton Transactions* **2011**, *40*, 9953.

[2] N. F. Chilton, R. P. Anderson, L. D. Turner, A. Soncini, K. S. Murray, *Journal of Computational Chemistry* **2013**, *34*, 1164–1175.

[3] R. J. Blagg, F. Tuna, E. J. L. McInnes, R. E. P. Winpenny, *Chemical Communications* **2011**, *47*, 10587.

[4] Y.-Z. Zheng, G.-J. Zhou, Z. Zheng, R. E. P. Winpenny, *Chem. Soc. Rev.* **2014**, *43*, 1462–1475.

[5] R. Sessoli, D. Gatteschi, A. Caneschi, M. A. Novak, *Nature* **1993**, *365*, 141–143.

[6] N. Ishikawa, M. Sugita, T. Ishikawa, S. Koshihara, Y. Kaizu, *Journal of the American Chemical Society* **2003**, *125*, 8694–8695.

[7] C. A. P. Goodwin, F. Ortu, D. Reta, N. F. Chilton, D. P. Mills, *Nature* **2017**, *548*, 439.

[8] F.-S. Guo, B. M. Day, Y.-C. Chen, M.-L. Tong, A. Mansikkamäki, R. A. Layfield, *Angewandte Chemie International Edition* **2017**, *56*, 11445–11449.

[9] F.-S. Guo, B. M. Day, Y.-C. Chen, M.-L. Tong, A. Mansikkamäki, R. A. Layfield, *Science* **2018**, eaav0652.

[10] J. J. Baldoví, S. Cardona-Serra, J. M. Clemente-Juan, E. Coronado, A. Gaita-Ariño, A. Palii, *Inorganic Chemistry* **2012**, *51*, 12565–12574.

[11] S. T. Liddle, J. van Slageren, *Chemical Society Reviews* **2015**, *44*, 6655–6669.

[12] M. Atzori, A. Chiesa, E. Morra, M. Chiesa, L. Sorace, S. Carretta, R. Sessoli, *Chemical Science* **2018**, *9*, 6183–6192.

[13] L. Escalera-Moreno, N. Suaud, A. Gaita-Ariño, E. Coronado, *The Journal of Physical Chemistry Letters* **2017**, *8*, 1695–1700.

[14] N. Ishikawa, *Polyhedron* **2007**, *26*, 2147–2153.

[15] A. Upadhyay, C. Das, S. Vaidya, S. K. Singh, T. Gupta, R. Mondol, S. K. Langley, K. S. Murray, G. Rajaraman, M. Shanmugam, *Chemistry - A European Journal* **2017**, *23*, 4903–4916.

[16] J. Ruiz, G. Lorusso, M. Evangelisti, E. K. Brechin, S. J. A. Pope, E. Colacio, *Inorganic Chemistry* **2014**, *53*, 3586–3594.

[17] E. Moreno Pineda, N. F. Chilton, F. Tuna, R. E. P. Winpenny, E. J. L. McInnes, *Inorganic Chemistry* **2015**, *54*, 5930–5941.

[18] A. Barge, M. Botta, U. Casellato, S. Tamburini, P. Alessandro Vigato, *European Journal of Inorganic Chemistry* **2005**, *2005*, 1492–1499.

[19] S. N. König, N. F. Chilton, C. Maichle-Mössmer, E. M. Pineda, T. Pugh, R. Anwander, R. A. Layfield, *Dalton Trans.* **2014**, *43*, 3035–3038.

[20] J. Goura, E. Colacio, J. M. Herrera, E. A. Suturina, I. Kuprov, Y. Lan, W. Wernsdorfer, V. Chandrasekhar, *Chemistry - A European Journal* **2017**, *23*, 16621–16636.

[21] S. K. Langley, N. F. Chilton, B. Moubaraki, K. S. Murray, *Chemical Communications* **2013**, *49*, 6965.

[22] A. Upadhyay, S. K. Singh, C. Das, R. Mondol, S. K. Langley, K. S. Murray, G. Rajaraman, M. Shanmugam, *Chem. Commun.* **2014**, *50*, 8838–8841.

[23] A. Chakraborty, J. Goura, P. Kalita, A. Swain, G. Rajaraman, V. Chandrasekhar, *Dalton Transactions* **2018**, *47*, 8841–8864.

[24] M. S. Lah, V. L. Pecoraro, *Journal of the American Chemical Society* **1989**, *111*, 7258–7259.

[25] G. Mezei, C. M. Zaleski, V. L. Pecoraro, *Chemical Reviews* **2007**, *107*, 4933–5003.

[26] C. Y. Chow, E. R. Trivedi, V. Pecoraro, C. M. Zaleski, *Comments on Inorganic Chemistry* **2015**, *35*, 214–253.

[27] P. Happ, C. Plenk, E. Rentschler, *Coordination Chemistry Reviews* **2015**, *289–290*, 238–260.

[28] L. F. Jones, C. A. Kilner, M. A. Halcrow, *Chemistry - A European Journal* **2009**, *15*, 4667–4675.

[29] L. F. Jones, S. A. Barrett, C. A. Kilner, M. A. Halcrow, *Chemistry - A European Journal* **2008**, *14*, 223–233.

[30] C. Y. Chow, S. V. Eliseeva, E. R. Trivedi, T. N. Nguyen, J. W. Kampf, S. Petoud, V. L. Pecoraro, *Journal of the American Chemical Society* **2016**, *138*, 5100–5109.

[31] E. R. Trivedi, S. V. Eliseeva, J. Jankolovits, M. M. Olmstead, S. Petoud, V. L. Pecoraro, *Journal of the American Chemical Society* **2014**, *136*, 1526–1534.

[32] M. Ostrowska, I. O. Fritsky, E. Gumienna-Kontecka, A. V. Pavlishchuk, *Coordination Chemistry Reviews* **2016**, *327–328*, 304–332.

[33] A. A. Athanasopoulou, C. Gamer, L. Völker, Eva Rentschler, *NOVEL MAGNETIC NANOSTRUCTURES: Unique Properties and Applications.*, ELSEVIER, S.L., **2018**.

[34] A. Athanasopoulou, L. Carrella, E. Rentschler, *Inorganics* **2018**, *6*, 66.

[35] Y. Qin, Q. Gao, Y. Chen, W. Liu, F. Lin, X. Zhang, Y. Dong, Y. Li, *Journal of Cluster Science* **2017**, *28*, 891–903.

[36] Q.-W. Li, J.-L. Liu, J.-H. Jia, Y.-C. Chen, J. Liu, L.-F. Wang, M.-L. Tong, *Chemical Communications* **2015**, *51*, 10291–10294.

[37] J. Jankolovits, J. W. Kampf, V. L. Pecoraro, *Inorganic Chemistry* **2013**, *52*, 5063–5076.

[38] M. S. Lah, B. R. Gibney, D. L. Tierney, J. E. Penner-Hahn, V. L. Pecoraro, *Journal of the American Chemical Society* **1993**, *115*, 5857–5858.

[39] A. W. Addison, T. N. Rao, J. Reedijk, J. van Rijn, G. C. Verschoor, *J. Chem. Soc., Dalton Trans.* **1984**, 1349–1356.

[40] L. Sorace, C. Benelli, D. Gatteschi, *Chemical Society Reviews* **2011**, *40*, 3092.

[41] M. A. Sørensen, H. Weihe, M. G. Vinum, J. S. Mortensen, L. H. Doerrer, J. Bendix, *Chemical Science* **2017**, *8*, 3566–3575.

[42] J. J. Baldoví, S. Cardona-Serra, J. M. Clemente-Juan, E. Coronado, A. Gaita-Ariño, A. Palii, *Journal of Computational Chemistry* **2013**, *34*, 1961–1967.

[43] J. J. Baldoví, J. M. Clemente-Juan, E. Coronado, A. Gaita-Ariño, A. Palii, *Journal of Computational Chemistry* **2014**, *35*, 1930–1934.

[44] K. R. Vignesh, S. K. Langley, K. S. Murray, G. Rajaraman, *Inorganic Chemistry* **2017**, *56*, 2518–2532.

[45] J. D. Rinehart, J. R. Long, *Chemical Science* **2011**, *2*, 2078.

[46] C. Benelli, D. Gatteschi, *Chemical Reviews* **2002**, *102*, 2369–2388.

[47] K. S. Cole, R. H. Cole, *The Journal of Chemical Physics* **1941**, *9*, 341–351.

[48] M. Grahl, J. Kötzler, I. Seßler, *Journal of Magnetism and Magnetic Materials* **1990**, *90–91*, 187–188.

[49] S. V. Eliseeva, J.-C. G. Bünzli, *New Journal of Chemistry* **2011**, *35*, 1165.

[50] N. Ishikawa, M. Sugita, T. Okubo, N. Tanaka, T. Iino, Y. Kaizu, *Inorganic Chemistry* **2003**, *42*, 2440–2446.

4.7 Supporting Information

Experimental Section

All manipulations were performed under aerobic conditions using materials (reagent grade) and solvents as received. C, H and N elemental analyses were carried out on a Foss Heraeus Vario EL at the Institute of Organic Chemistry at the Johannes Gutenberg University Mainz. Infrared absorption spectra were recorded at room temperature in a range of 3,000-400 cm^{-1} on a Thermo Fischer NICOLET Nexus FT/IR-5700 spectrometer equipped with Smart Orbit ATR Diamond cell. UV-Vis absorption measurements were performed between for complexes 1, 2, 3 and 4 in MeCN between 200 and 1000 nm on a JASCO V-570 UV/Vis/NIR spectrophotometer (Fig.S10, ESI) Variable-temperature direct current (dc) magnetic susceptibility measurements were performed on polycrystalline samples with the use of Quantum Design SQUID magnetometer MPMS-7 equipped with a 7 T magnet. The samples were embedded in eicosane to avoid orientation of the crystallites under applied field. Experimental susceptibility data were corrected for the underlying diamagnetism using Pascal's constants.[114] The temperature dependent magnetic contribution of the holder and of the embedding matrix eicosane were experimentally determined and substracted from the measured susceptibility data. Variable temperature susceptibility data were collected in a temperature range of 2-300K under an applied field of 0.1 Tesla, while magnetization data were collected between 2 and 10 K and using magnetic fields up to 7 Tesla. Alternating-current (ac) measurements were performed with an oscillating magnetic field of 3 Oe at frequencies ranging from 1 to 1400 Hz. Field-dependence measurements were performed and they revealed an optimum dc field of 1000 Oe. Using that optimum field further magnetic measurements were performed as described in the text.

4.7.1 Synthesis of reported complex 1

(^{t}Bu$_4$N) {Ga$_8$Dy(OH)$_4$(shi)$_8$}·5MeOH·3H$_2$O (1): To a stirred almost colorless solution of shiH$_3$ (61.00 mg, 0.4 mmol) and piperidine (40 µL, 0.4 mmol) in MeOH, Ga(NO$_3$)$_3$·H$_2$O (109 mg, 0.4 mmol) was added and left for stirring for 5 min. To the resulting clear and colorless solution Dy(O$_2$CMe)$_3$•xH$_2$O (20.00 mg, 0.05 mmol) was added along with ^{t}Bu$_4$NClO$_4$ (52.00 mg, 0.15 mmol) and was stirred for further 1 h. Then, the solution was filtered and the filtrate was left for slow evaporation. Colorless, good diffraction quality crystals of **1** appeared after 2 weeks which were collected by filtration, washed with hexanes (3 × 5 mL) and dried in air. Yield: 0.060 g (24.9%) based on the Dy^{III} ion. The air-dried solid was analyzed as **1·5H$_2$O (Ga$_8$Dy$_1$H$_{84}$O$_{34}$C$_{72}$ N$_9$):** C, 36.96; H, 3.62; N, 5.39. Found: C, 36.92; H, 3.53; N, 5.38. Selected ATR data (cm^{-1}): 1603 (s), 1573 (s), 1507 (w), 1442 (w), 1410 (w), 1264 (s), 1247 (w), 939 (s), 863 (s), 683 (w), 660 (w), 448 (w).

4.7.2 Single-crystal X-ray diffraction studies

X-ray diffraction data for the structure analysis were collected from suitable single crystals on a STOE IPDS 2T[2] equipped with an Oxford cooling system operating at 120(2) K (1), respectively. Graphite-monochromated Mo-Kα radiation (λ = 0.71073 Å) from long-fine focus sealed X-ray tube was used throughout. Data indexing, reduction, integration and absorption correction were done with STOE X-AREA and STOE X-RED[2]. Structures were solved with SHELXT[3] and refined by full-matrix least-squares on F-squared using SHELXL[4], interfaced through OLEX2-1.2[5]. All non-hydrogen atoms were refined with anisotropic displacement parameters, while hydrogen atoms have been placed on idealized position using a riding model. For the solvent water molecules the hydrogen atoms cannot be located properly and were omitted. The tetrabutylammonium counter ion is highly disordered over several positions. Only the two main, symmetry related, positions were taken into account. CCDC 1903450 contains the supplementary crystallographic data for the structure reported in this paper. These data can be obtained free of charge via www.ccdc.cam.ac.uk/conts/retrieving.html (or from the Cambridge Crystallographic Data Centre, 12 Union Road, Cambridge CB21EZ, UK; fax: (+44)1223-336-033; or deposit@ccdc.cam.ac.uk).

Table S1. Crystallographic data for complex **1**.

Complex	**1**•5MeOH•3H_2O
Empirical formula	$C_{77}H_{92}Ga_8DyN_9O_{36}$
Formula weight	2439.85
Temperature/K	120 (2)
Crystal system	monoclinic
Space group	P 2/*c*
a/Å	13.6911 (4)
b/Å	18.1247(5)
c/Å	19.8116(5)
α/°	90
β/°	90.093 (2)
γ/°	90
Volume/$Å^3$	4916.2(2)
Z	2
$\rho_{calc}g/cm^3$	1.648
μ/mm^{-1}	2.990
F(000)	2438.0
Crystal size/mm^3	0.38 × 0.263 × 0.09
Radiation	MoK\α (λ = 0.71073)
2Θ range for data collection/°	5.072 to 53.772
Index ranges	-17 ≤ h ≤ 17 -23 ≤ k ≤ 22 -25≤ l ≤ 21
Reflections collected	24260
Independent reflections	R_{int} = 0.0375 R_{sigma} = 0.0341
Data/restraints/ parameters	10530 / 68 / 679
Goodness-of-fit on F^2	1.165
Final $R^{a,b}$ indexes [I>=2σ (I)]	R_1 = 0.0973 wR_2 = 0.2554
Final $R^{a,b}$ indexes [all data]	R_1 = 0.1082 wR_2 = 0.2648
Largest diff. peak /hole / e $Å^{-3}$	4.55/ -1.87

[a] $R_1 = \Sigma(||F_o| - |F_c||)/\Sigma|F_o|$. [b] $wR_2 = [\Sigma[w(F_o^2 - F_c^2)^2]/\Sigma[w(F_o^2)^2]]^{1/2}$, $w = 1/[\sigma^2(F_o^2) + (ap)^2 + bp]$, where $p = [\max(F_o^2, 0) + 2F_c^2]/3$.

Table S2. Selected Bond Lengths for complex **1.**

Atom	Atom	Length/Å
Dy1	O3	2.329(6)
Dy1	O6	2.342(7)
Dy1	O9	2.308(6)
Dy1	O12	2.312(6)
Ga1	O1	1.869(6)
Ga1	O11	1.915(7)
Ga1	O12	1.955(6)
Ga1	O13	1.865(7)
Ga1	N1	1.978(8)
Ga2	O2	1.923(7)
Ga2	O3	1.957(7)
Ga2	O4	1.870(7)
Ga2	O13[1]	1.865(7)
Ga2	N2	1.985(8)
Ga3	O5	1.956(8)
Ga3	O6	1.942(7)
Ga3	O7	1.840(8)
Ga3	O14[1]	1.866(8)
Ga3	N3	1.977(9)
Ga4	O8	1.913(8)
Ga4	O9	1.950(7)
Ga4	O10	1.870(7)
Ga4	O14	1.885(8)
Ga4	N4	1.959(8)
O1	C1	1.356(11)
O2	C7	1.295(12)
O3	N1	1.396(9)
O6	N2	1.424(10)
O9	N3	1.413(11)
O12	N4	1.422 (9)

[1]1-X,+Y,3/2-Z

Table S3 Selected Bond Angles for **1.**

Atom	Atom	Angle/°
O3[1]	Dy1	O3	80.7(3)
O3	Dy1	O6[1]	138.3(2)
O3	Dy1	O6	68.7(2)
O6	Dy1	O6[1]	150.9(3)
O9	Dy1	O3	107.9(2)
O9	Dy1	O3[1]	150.8(2)
O9[1]	Dy1	O6	88.5(2)
O9	Dy1	O6	68.7(2)
O9	Dy1	O9[1]	78.5(3)
O9[1]	Dy1	O12	135.8(2)
O9	Dy1	O12	71.7(2)
O12	Dy1	O3	71.4(2)
O12[1]	Dy1	O3	85.7(2)
O12	Dy1	O6[1]	78.5(2)
O12	Dy1	O6	109.3(2)
O12[1]	Dy1	O12	149.9(3)
O1	Ga1	O11	87.9(3)
O1	Ga1	O12	159.5(3)
O1	Ga1	N1	92.8(3)
O11	Ga1	O12	80.0(3)
O11	Ga1	N1	144.0(3)
O12	Ga1	N1	87.6(3)
O13	Ga1	O1	102.0(3)
O13	Ga1	O11	105.4(3)
O13	Ga1	O12	97.2(2)
O13	Ga1	N1	109.5(3)
O2	Ga2	O3	80.6(3)
O2	Ga2	N2	145.5(3)
N4	O12	Ga1	113.3(5)

[1]1-X,+Y,3/2-Z

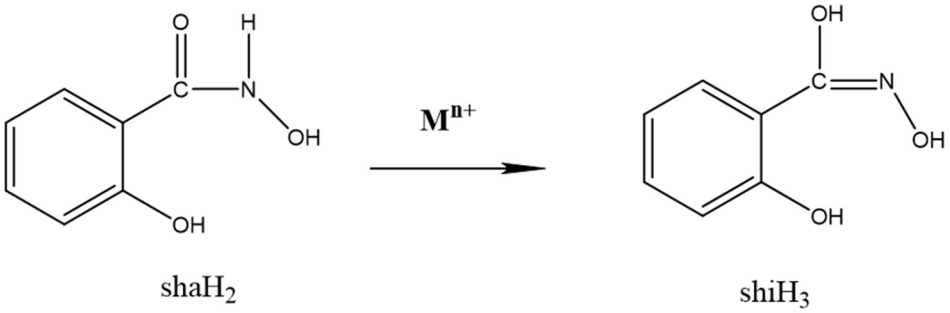

Scheme 1: Illustrative representation and abbreviation of the metal assisted 2-amide-iminol tautomerism of organic molecules discussed in the text.[40,49]

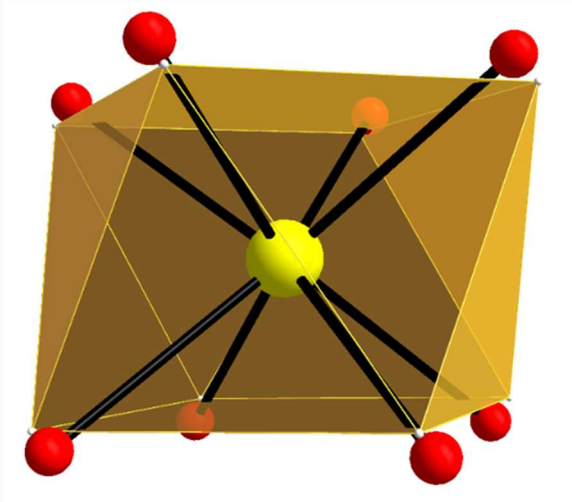

Figure S1: Square antiprismatic geometry of central lanthanide in complex **1**. The points connected by the lighter lines define the vertices of the ideal polyhedron**.** Color scheme: Ln, yellow; O, red.

Table S4. Shape measurements of the 8-coordinate lanthanide coordination polyhedra. The bold numbers indicate the closest polyhedron according to SHAPE calculations.[97]

Polyhedron[c]	Dy1
OP-8	34.44
HPY-8	22.71
HBPY-8	13.83
CU-8	6.56
SAPR-8	**1.18**
TDD-8	2.26
JGBF-8	16.57
JETBPY-8	28.70
JBTPR-8	3.85
BTPR-8	3.29
JSD-8	6.16
TT-8	7.45
ETBPY-8	25.63

[c] Abbreviations: OP-8, octagon; HPY-8, heptagonal pyramid; HBPY-8, hexagonal bipyramid; CU-8, cube; SAPR-8, square antiprism; TDD-8, triangular dodecahedron; JGBF-8, Johnson gyrobifastigium; JETBPY-8, Johnson elongated triangular bipyramid; JBTPR-8, Johnson biaugmented trigonal prism; BTPR-8, biaugmented trigonal prism; JSD-8, Johnson snub diphenoid; TT-8, triakis tetrahedron; ETBPY-8, elongated trigonal bipyramid.

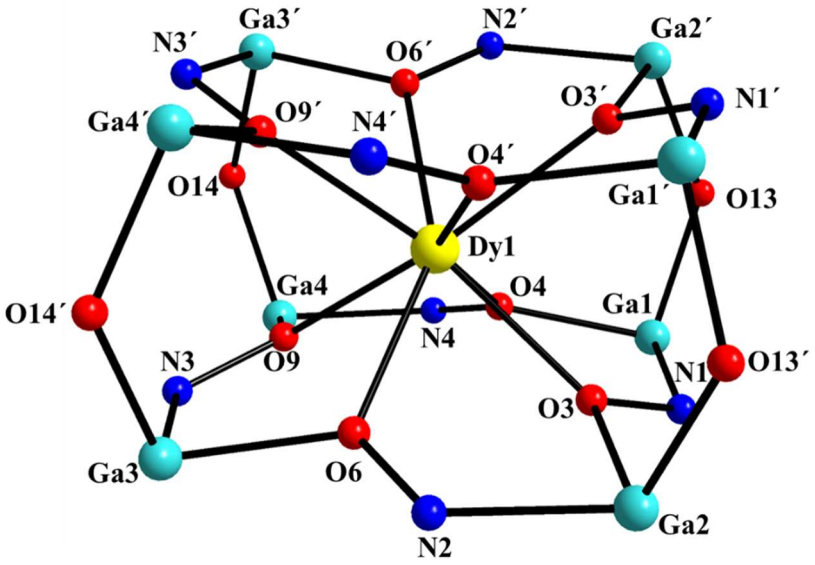

Figure S2: Labelled schematic representation of the core $\{Ga^{III}_8Dy^{III}(\mu\text{-}OH)_4(\mu\text{-}NO)_8\}^{15+}$ of **1**. Color scheme: Ga^{III}, aqua; Dy^{III}, yellow; N, blue; O, red; C, black. H atoms are omitted for clarity.

4.7.3 Magnetic Studies

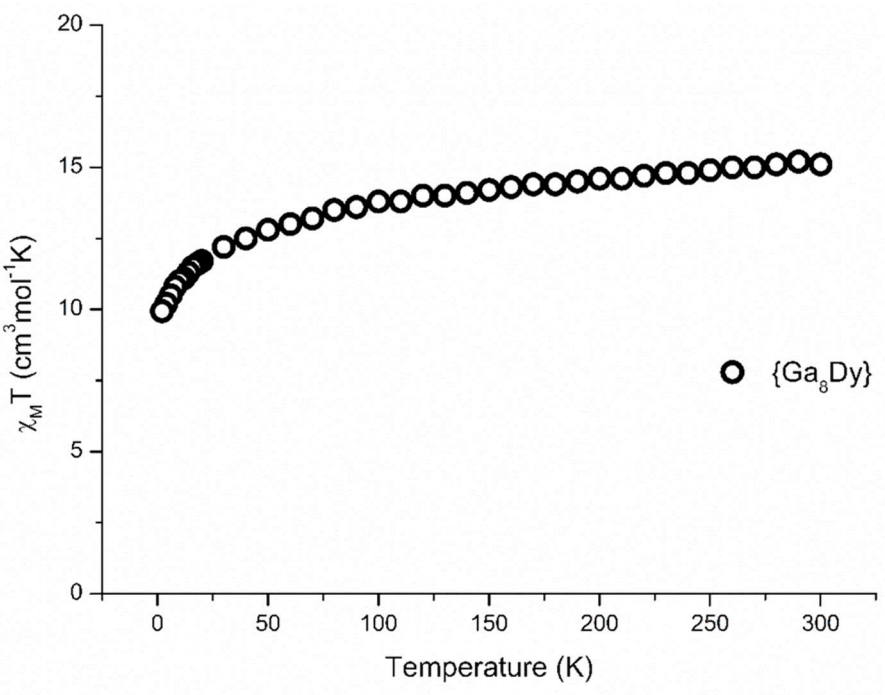

Figure S3: Temperature dependence of magnetic susceptibility of complex **1**.

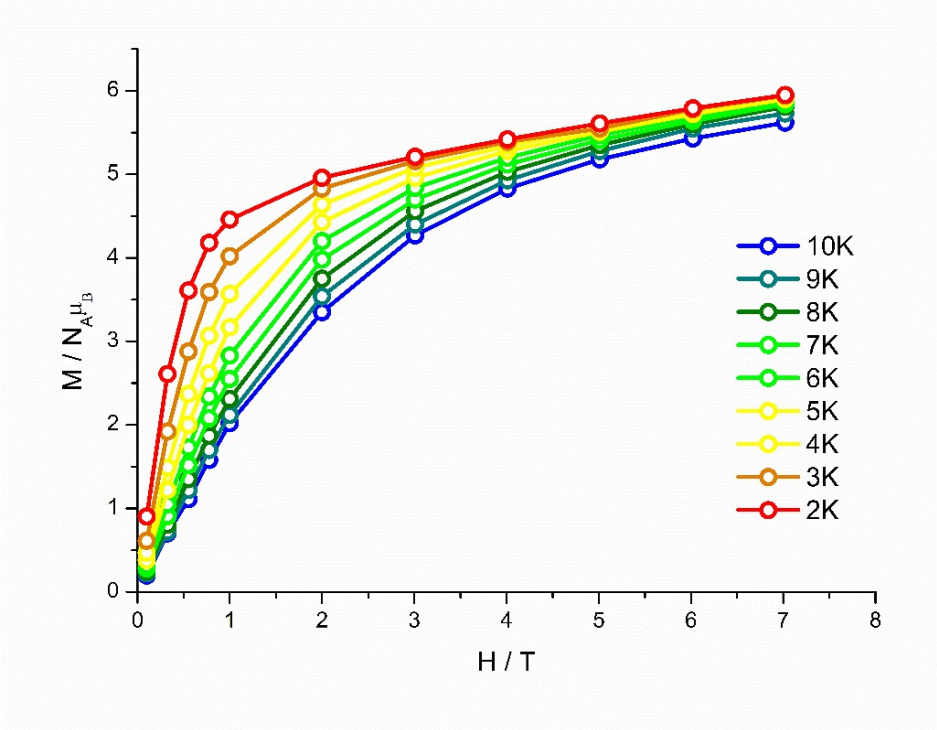

Figure S4: M vs H plots for complex **1** at various temperatures as indicated. Solid lines are guidelines for the eye.

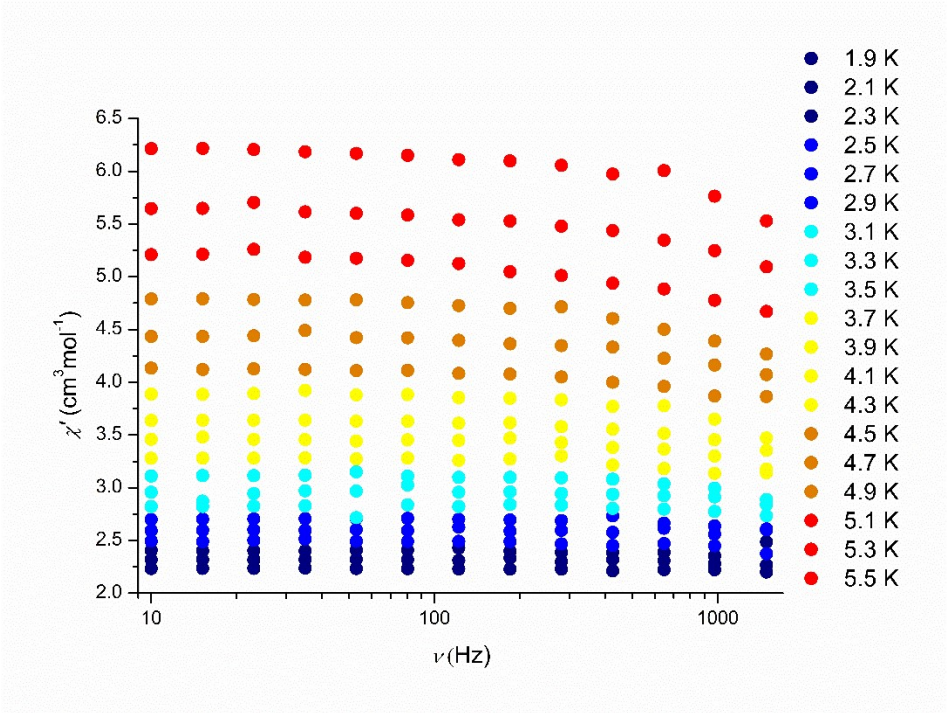

Figure S5: Frequency dependent in-phase susceptibility plot of for compound **1** (1.9 to 5.5 K) at zero field.

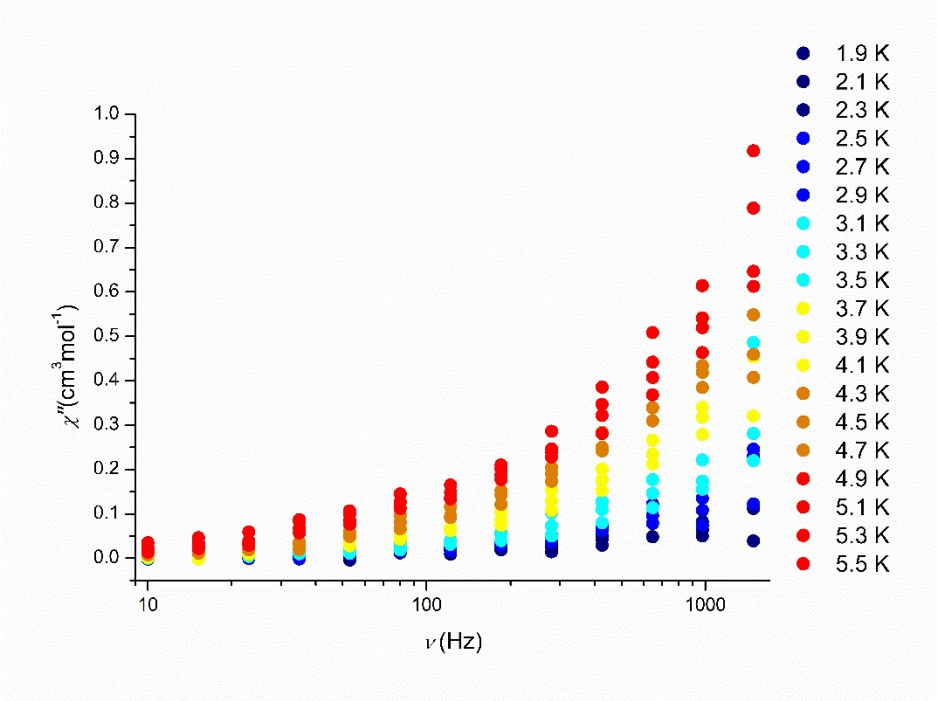

Figure S6: Frequency dependent out-of-phase susceptibility plot of for compound **1** (1.9 to 5.5 K) at zero field.

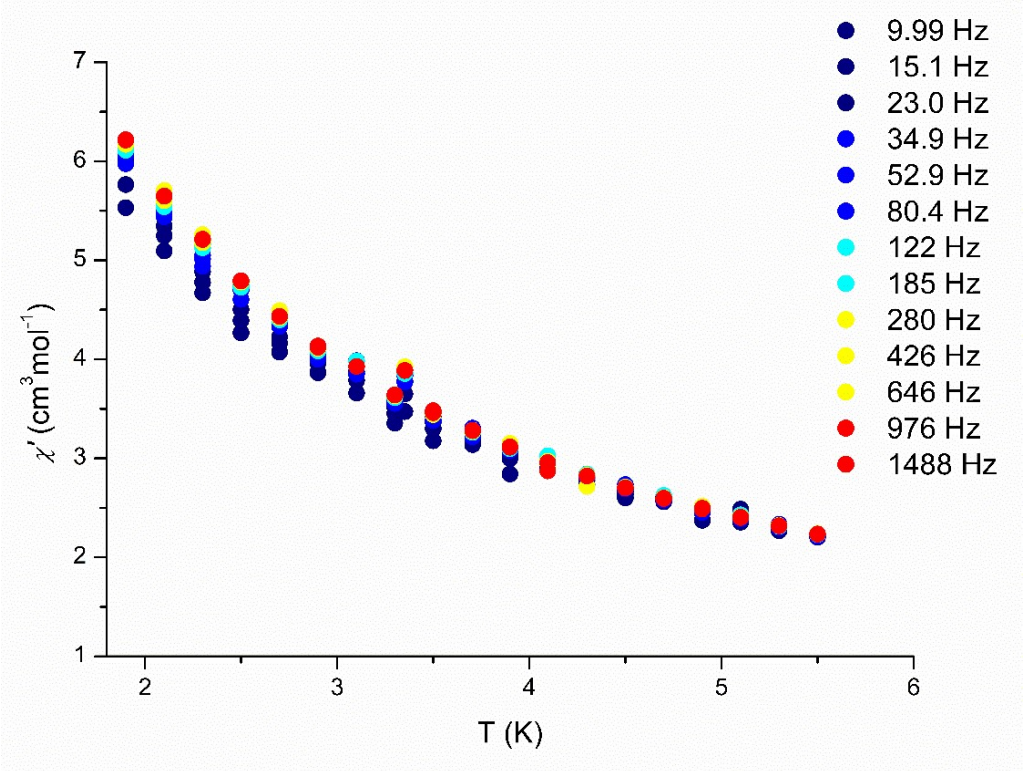

Figure S7: Temperature dependent in-phase susceptibility plot of for compound **1** (1.9 to 5.5 K) at 0 Oe.

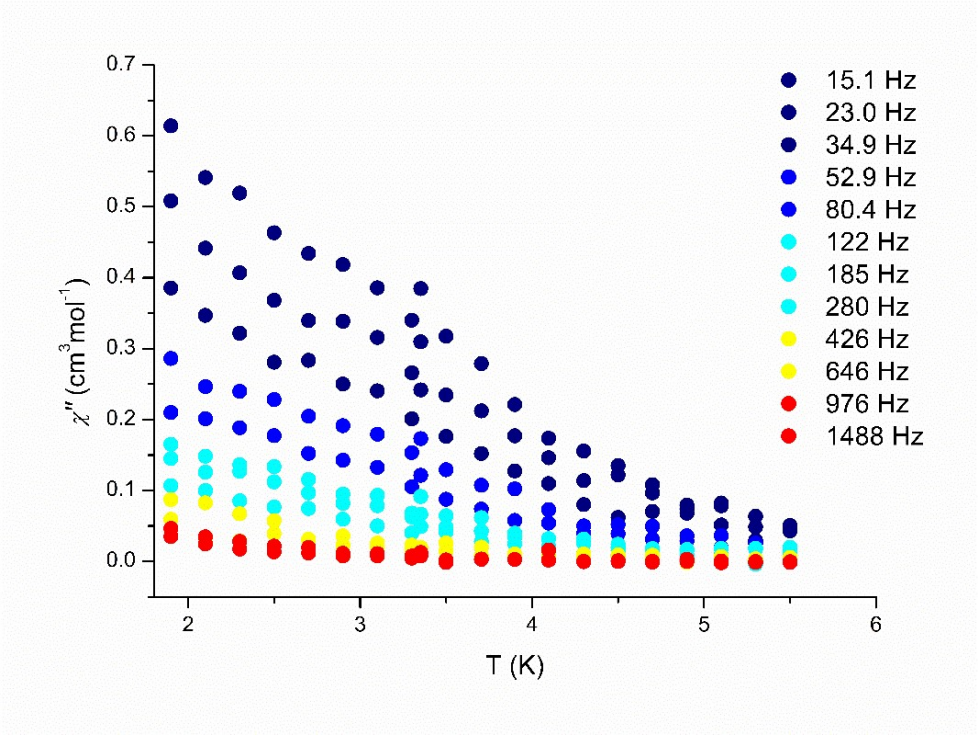

Figure S8: Temperature dependent in-phase susceptibility plot of for compound **1** (1.9 to 5.5 K) at 0 Oe**.**

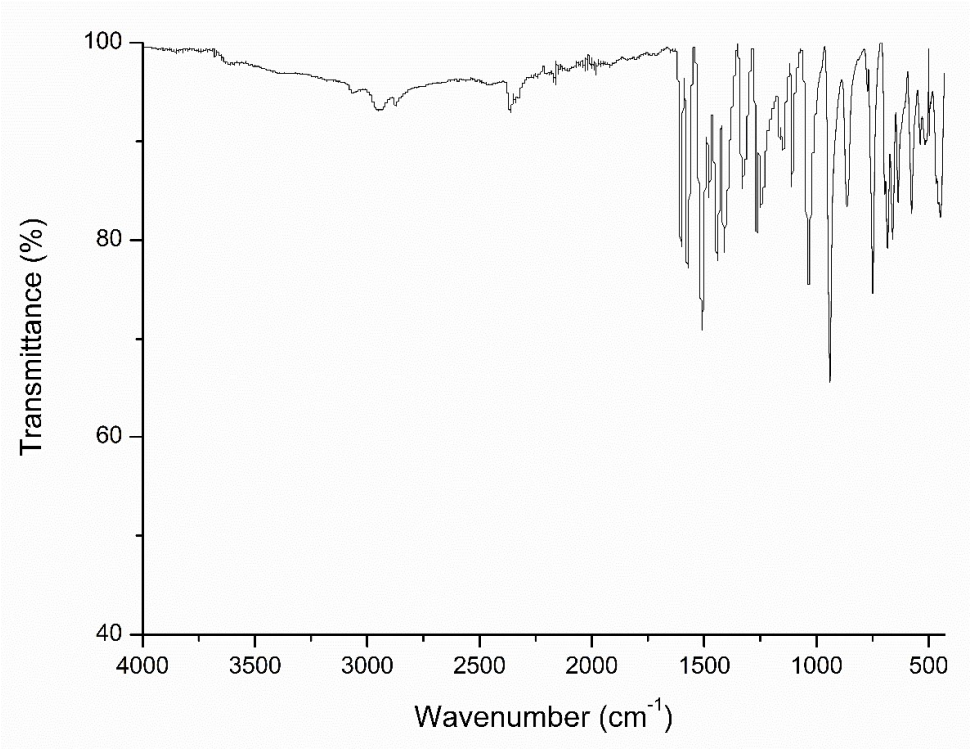

Figure S9: IR spectrum for complex **1.**

UV-Vis Absorption Spectroscopy

The ligand ($shiH_3$) has two main bands at 246 nm and 342 nm, which appear to be also present at all the complex. These ligand-centered transitions, that can be assigned to excitations within the delocalized π-system of the coordinated hydroxamic acid, are observed at 238 and 307 nm for **1**.

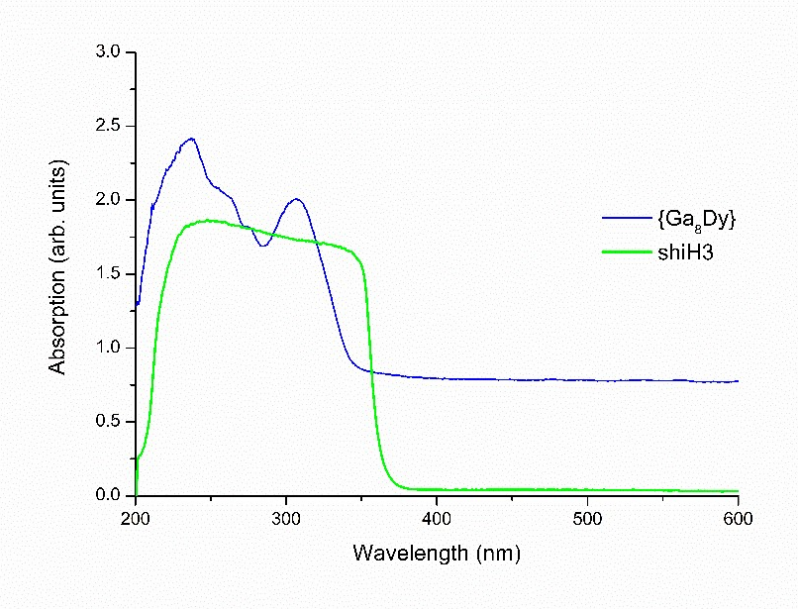

Figure S10: UV-vis studies for complex **1** and $shiH_3$ in MeCN.

4.7.4 Theoretical calculations

SIMPRE software

The static magnetic properties have been rationalized using the SIMPRE computational package.[9,10] The experimental atomic coordinates and magnetic susceptibility data have been introduced as an input; the two fitting parameters (D_r and Z_i) of the Radial Effective Charge (REC) model have been scanned.[11] A detailed explanation is provided in the Supporting Information.

Radial Effective Charge (REC) model

Theoretical approach

Our calculations start with the crystallographic atomic coordinates of the first coordination sphere. These are introduced as an input in the *simpre.dat* file of the portable *fortran77* software code SIMPRE.[9,12] This code parameterizes the electric field effect produced by the surrounding ligands, acting over the central ion, by using the following Crystal Field Hamiltonian expressed in terms of the Extended Stevens Operators (ESOs)[13–15]:

$$\hat{H}_{cf}(J) = \sum_{k=2,4,6}\sum_{q=-k}^{k} B_k^q O_k^q = \sum_{k=2,4,6}\sum_{q=-k}^{k} a_k(1-\sigma_k)A_k^q \left\langle r^k \right\rangle O_k^q$$

where k is the order (also called rank or degree) and q is the operator range, that varies between k and $-k$, of the Stevens operator equivalents O_k^q as defined by Ryabov in terms of the angular momentum operators $J_{\pm}$ and J_z,[16] where the components $O_k^q(c)$ and $O_k^q(s)$ correspond to the ESOs with $q \geq 0$ and $q < 0$ respectively.[16] Note that all the Stevens CF parameters B_k^q are real, whereas the matrix elements of O_k^q ($q < O$) are imaginary. a_k are the α, β and γ Stevens coefficients[17] for $k = 2, 4, 6$, respectively, which are tabulated and depend on the number of f electrons. σ_k are the Sternheimer shielding parameters of the $4f$ electronic shell, and $\langle r^k \rangle$ are the expectation values of the radius.[18]

In SIMPRE, the A_k^q CF parameters are determined by the following relations:

$$A_k^0 = \frac{4\pi}{2k+1}\sum_{i=1}^{N}\frac{Z_i e^2}{R_i^{k+1}} Z_{k0}(\theta_i,\varphi_i)p_{kq} \quad (2a)$$

$$A_k^q = \frac{4\pi}{2k+1}\sum_{i=1}^{N}\frac{Z_i e^2}{R_i^{k+1}} Z_{kq}^{c}(\theta_i,\varphi_i)p_{kq} \quad (q>0) \quad (2b)$$

$$A_k^q = \frac{4\pi}{2k+1}\sum_{i=1}^{N}\frac{Z_i e^2}{R_i^{k+1}} Z_{k|q|}^{s}(\theta_i,\varphi_i)p_{k|q|} \quad (q<0) \quad (2c)$$

where R_i, θ_i and φ_i are the effective polar coordinates of the point charges, and Z_i is the effective point charge, associated to the *i*-th donor atom with the lanthanoid at the origin, *N* is the number of ligands; *e* is the electron charge, p_{kq} are the prefactors of the spherical harmonics and Z_{kq} are the tesseral harmonics expressed in terms of the polar coordinates for the i-th donor atom.

In the REC model[157] the ligand is modeled through an effective point charge situated between the lanthanoid and the coordinated atom at a distance R_i from the magnetic centre, which is smaller than the real metal-ligand distance (r_i). To account for the effect of covalent electron sharing, a radial displacement vector (D_r) is defined, in which the polar coordinate *r* of each coordinated atom is collectively varied, $R_i = r_i - D_r$, and at the same time the charge value (Z_i) is scanned in order to achieve a minimum deviation between calculated and experimental data, whereas θ_i and φ_i remain constant. In the fitting procedures, we define the relative error *E* as:

$$E = \frac{1}{n}\sum_{i=1}^{n}\frac{\left[\chi_{theo,i} - \chi_{\exp,i}\right]^2}{\left[\chi_{\exp,i}\right]^2} \quad (3)$$

where χ_{exp} and χ_{theo} are experimental and theoretical magnetic susceptibility, respectively, and *n* is the number of points.

Table S5. Ground multiplet energy level scheme (cm^{-1}) and main $|M_J>$ contributions (more than 10%) to the wave function calculated for complex **1**.

Calculated Kramers doublets and wave function amplitudes	
0	79% |±11/2>
15	81% |±13/2>
148	61% |±9/2> + 19% |±7/2> + 10% |±11/2>
228	35% |±7/2> + 23% |±5/2> + 13% |±1/2> + 11% |±9/2>
270	22% |±3/2> + 19% |±5/2> + 16% |±1/2> + 13% |∓3/2> + 13% |∓7/2>
389	45% |±1/2> + 14% |±3/2>
441	37% |±5/2> + 33% |∓3/2> + 17% |±7/2>
549	93% |±15/2>

Table S6. Crystal-field parameters in cm^{-1} (Stevens notation) obtained for **1**.

k	q	$A_k^q\langle r^k\rangle$	B_k^q
2	0	30.61	-0.19434
2	1	51.67	-0.32805
2	-1	-228.01	1.44770
2	2	51.37	-0.32613
2	-2	24.52	-0.15566
4	0	-222.68	0.01318
4	1	-127.28	0.00754
4	-1	561.12	-0.03322
4	2	126.99	-0.00752
4	-2	60.68	-0.00359
4	3	341.91	-0.02024
4	-3	-433.66	0.02567
4	4	151.81	-0.00899
4	-4	187.62	-0.01111
6	0	76.76	0.00008
6	1	43.46	0.00004
6	-1	-191.32	-0.00020
6	2	-141.00	-0.00015
6	-2	-67.28	-0.00007

4.7.6 References

[1] G. A. Bain, J. F. Berry, *Journal of Chemical Education* **2008**, *85*, 532.

[2] Stoe & Cie X-AREA 2002, Stoe &Cie X-RED 2002, Stoe & Cie, Darmastadt, Germany.

[3] G. M. Sheldrick, *Acta Crystallographica Section A Foundations and Advances* **2015**, *71*, 3–8.

[4] G. M. Sheldrick, *Acta Crystallographica Section C Structural Chemistry* **2015**, *71*, 3–8.

[5] O. V. Dolomanov, L. J. Bourhis, R. J. Gildea, J. A. K. Howard, H. Puschmann, *Journal of Applied Crystallography* **2009**, *42*, 339–341.

[6] C. Y. Chow, E. R. Trivedi, V. Pecoraro, C. M. Zaleski, *Comments on Inorganic Chemistry* **2015**, *35*, 214–253.

[7] G. Mezei, C. M. Zaleski, V. L. Pecoraro, *Chemical Reviews* **2007**, *107*, 4933–5003.

[8] S. Alvarez, P. Alemany, D. Casanova, J. Cirera, M. Llunell, D. Avnir, *Coordination Chemistry Reviews* **2005**, *249*, 1693–1708.

[9] J. J. Baldoví, S. Cardona-Serra, J. M. Clemente-Juan, E. Coronado, A. Gaita-Ariño, A. Palii, *Journal of Computational Chemistry* **2013**, *34*, 1961–1967.

[10] J. J. Baldoví, J. M. Clemente-Juan, E. Coronado, A. Gaita-Ariño, A. Palii, *Journal of Computational Chemistry* **2014**, *35*, 1930–1934.

[11] J. J. Baldoví, J. J. Borrás-Almenar, J. M. Clemente-Juan, E. Coronado, A. Gaita-Ariño, *Dalton Transactions* **2012**, *41*, 13705.

[12] J. J. Baldoví, J. M. Clemente-Juan, E. Coronado, A. Gaita-Ariño, A. Palii, *Journal of Computational Chemistry* **2014**, *35*, 1930–1934.

[13] C Rudowicz, *J. Phys. C: Solid State Phys* **1985**, *18*, 3837.

[14] C. Y. C. C. Rudowicz, *J. Phys. Condes. Matter* **2004**, *16*, 5825.

[15] C. Rudowicz, *J. Phys. C: Solid State Phys.* **n.d.**, *18*, 1415.

[16] I. D. Ryabov, *Journal of Magnetic Resonance* **1999**, *140*, 141–145.

[17] K W H Stevens, *Proc. Phys. Soc. A* **1952**, *65*, 209.

[18] M. K. S. Edvardsson, *Journal of Alloys and Compounds* **1998**, *275*, 233.

Chapter 5 New Ga/Ln/shi^{3-} and Fe/Ln/shi^{3-} Complexes: Synthesis, Structural and Magnetic Studies.

In this chapter unpublished and lately obtained results will be presented and discussed. All complexes have been structurally and magnetically characterized and analyzed in detail. Most of the compounds that will be discussed are Ga(III)/Ln(III) complexes, while an Fe(III)/Ln(III) metallacrown-like molecule will be also presented. In all these compounds the organic ligand used is salicylhydroxamic acid ($shiH_3$), as the 12-MC-4 topology in all cases was intended.

5.1 Results and Discussion

Our synthetic efforts towards the isolation of 3d/4f or Ga(III)/4f 12-MC-4 complexes have not been an easy task. Inorganic synthetic chemistry of molecules is a challenging project and it has been proven to demand many considerations to be taken into account. The starting materials used, the organic ligand of choice, the external base and the reaction or crystallization solvent are some of the synthetic variables that need to be considered for the successful synthesis and isolation of polynuclear metal complexes. Upon changing one of the above variables at a reaction scheme, it is highly likely that a different product will be obtained. This is verified at the results that will be presented at this chapter.

The reaction of $Ga(NO_3)\cdot H_2O$, $Ln_2(piv)_6(Hpiv)_6$ (where pivH= HO_2CCMe_3), $shaH_2$, $^tBuNClO_4$ and NaOEt in a molar ratio of 8:1:8:3:8, in the solvent of MeOH, under the process of slow evaporation after seven days, led to the isolation of small light yellow plate crystals of $[Ga^{III}_8Ln^{III}_2Na^{I}_2(O_2CCMe_3)_8(shi)_8(MeOH)_4]\bullet 3H_2O$ (Ln = Dy (**1**), Tb (**2**)) in ~33 % yield. The chemical and structural identities of complexes **1** and **2** were determined by single-crystal X-ray crystallography, IR spectroscopy and elemental analyses (C, H, N).

Single-crystal diffraction studies showed that complex **1** and **2** are not isostructural since they crystallize in different space groups, nevertheless they possess the same molecular core (Table S1). Thus only the structure of complex **1** will be thoroughly discussed for simplicity reasons.

The oxidation states and the levels of protonation/deprotonation of the ligands have been determined based on metric parameters and charge balance considerations.

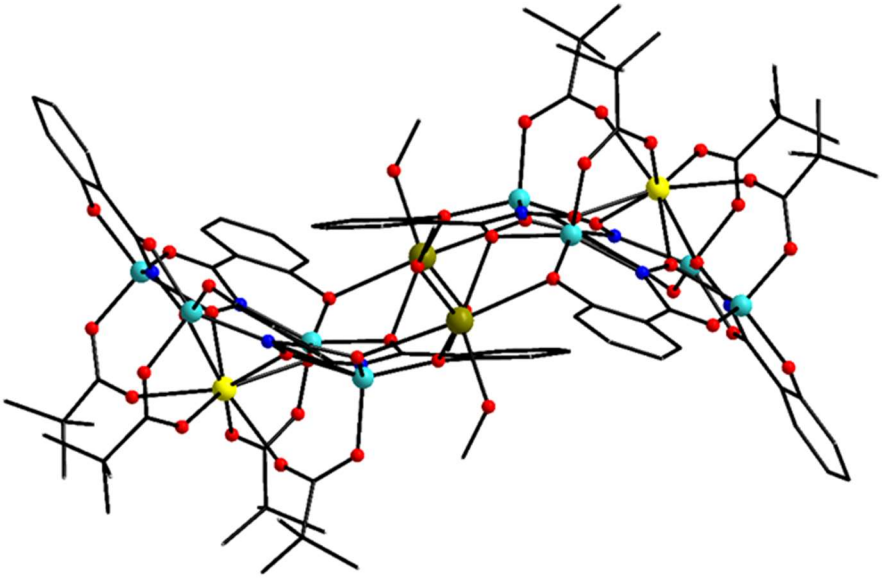

Figure 5.1.1: Schematic Representation of complex **1**. Color scheme: Ga^{III}, aqua; Dy^{III}, yellow; Na^{I} dark yellow; N, blue; O, red; C, black. H are omitted for clarity.

Complex **1** crystallizes in the triclinic $P\bar{1}$ space group and the detailed formula of the molecule is $[Ga^{III}_8Dy^{III}_2Na^{I}_2(O_2CCMe_3)_8(shi)_8(MeOH)_4]$ (**1**). The compound consists of eight Ga^{III} ions and two Dy^{III} atoms arranged in double 12-MC-4 topology, while two Na^{I} ions serve as linkers, connecting the two 12-MC-4 complexes to a whole. In each 12-MC-4 units, which are symmetry related, the Ga^{III} ions are held together via the oximato bridges provided by the triply deprotonated salicylhydroxamic acid (shi^{3-}) ligand in multiple coordination fashions (Scheme 1, SI), while the central Dy^{III} atoms lie 1.657(1) Å above the MC plane and its coordination sphere is completed by the oximato O atoms and the O atoms provided by the bridging pivalates. Dy^{III} is eight coordinate and possesses a square antiprismatic coordination geometry (CShM = 0.62, Figure S1, Table S2). The Na^{I} atoms are six coordinate with distorted octahedral geometries while all Ga(III) atoms are five-coordinate with distorted square pyramidal geometries ($\tau = 0.34 – 0.10$ and $\tau = 0.24 – 0.05$ for **2**) as it was defined by the trigonality index criteria, which -for five-coordinate metal ions- help us decide if the geometry is square

pyramidal or trigonal bipyramidal.[1] The closer the number is to 0, the closer the geometry is to the ideal square pyramidal configuration while the closer the number is to 1, the closer the geometry is to the trigonal bipyramidal geometrical arrangement.

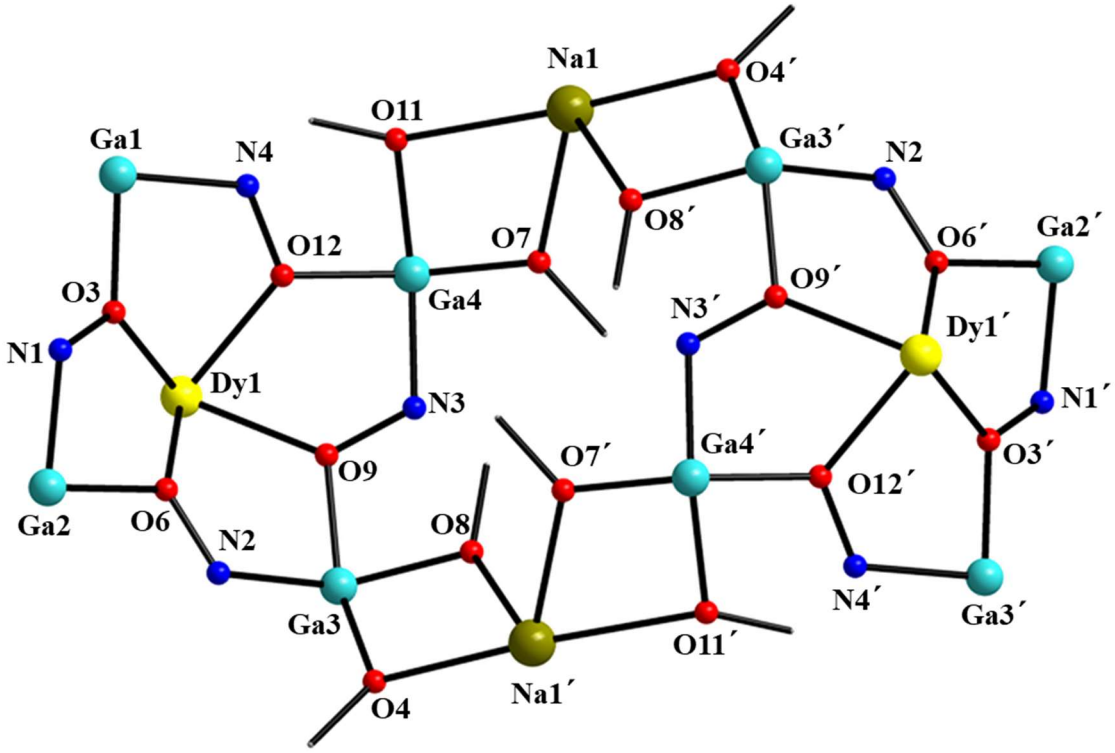

Figure 5.1.2: Schematic representation of labelled core of complex **1**. Color scheme: Ga^{III}, aqua; Dy^{III}, yellow; Na^{I}, dark yellow; O, red; N, blue; C, black.

Compound **1** possesses an overall inorganic core of $\{Ga^{III}_8Dy^{III}_2Na^{I}_2(\mu\text{-}OR)_8(\mu\text{-}NO)_8\}^{16+}$ as it is depicted in Figure 5.1.2. The basal Ga···Ga and the Ga···Dy separations lie in the range of 4.660(1) - 4.687(1) and 3.686(1) – 3.717(1) Å, respectively. The Dy···Dy distance is 11.495(1) Å and the Ga-O-N-Ga torsion angles lie in the range of 176.09 – 179.72°. As it depicted on Figure 5.1.1 and Figure 5.1.2, complex **1** consists of two 12-MC-4 units that are connected via the two sodium ions which serve as linkers, assisting in the assembly of the final compound. This structural motif is observed here for the first time within the reported 12-MC-4 metallacrown compounds. There have been quite a few pure 3*d* and 3*d*/4*f* 12-MC-4 MCs reported, having Na atoms participating in the structure but in none of them the Na atoms act as linker of 12-MC-4 units. In 2018 Pecoraro et *al*., reported a $\{Ga_8Ln_2\}$ complex having

two 12-MC-4 units linked via an organic moiety, which possesses a similar nuclearity with our compound, however no Na atoms participate in the molecular structure.[2] In most of the reported cases in which Na ions are present, the Na atoms act as coordinating ions, assisting with the charge balance of the overall complex. Thus, the novelty of this structural motif is undeniable compared to already existing reports. [3–5]

Solid state, direct-current (dc) magnetic susceptibility studies were carried out on freshly prepared and analytical pure (see Supporting Information for details) microcrystalline samples of **1** and **2** in the temperature range of 2 – 300 K under an applied field of 0.1 T. The $\chi_M T$ product of both compounds **1** and **2** is depicted in Figure 5.1.3. The experimental values at 300 K for both compounds (28.1 $cm^3mol^{-1}K$ for **1** and 23.1 $cm^3mol^{-1}K$ for **2**) are very close to the theoretical ones (28.34 $cm^3mol^{-1}K$ for **1** and 23.64 $cm^3mol^{-1}K$ for **2**) expected for two non-interacting Dy(III) ions ($^6H_{15/2}$, S = 5/2, L = 5, J = 15/2, g = 4/3) and two non-interacting Tb(III) ions ($^7F_6$, S = 3, L = 3, g = 3/2). Upon cooling down the magnetic susceptibility for both complexes remains almost steady till 50 K, while after that a rapid decrease is observed reaching a value of 14.8 $cm^3mol^{-1}K$ for **1** and 11.7 $cm^3mol^{-1}K$ for **2** at 2 K. The low temperature decrease can be attributed to the depopulation of the Zeeman split crystal field sublevels, zero-field splitting effects and the presence of intermolecular antiferromagnetic exchange interactions within the molecules in the crystal.

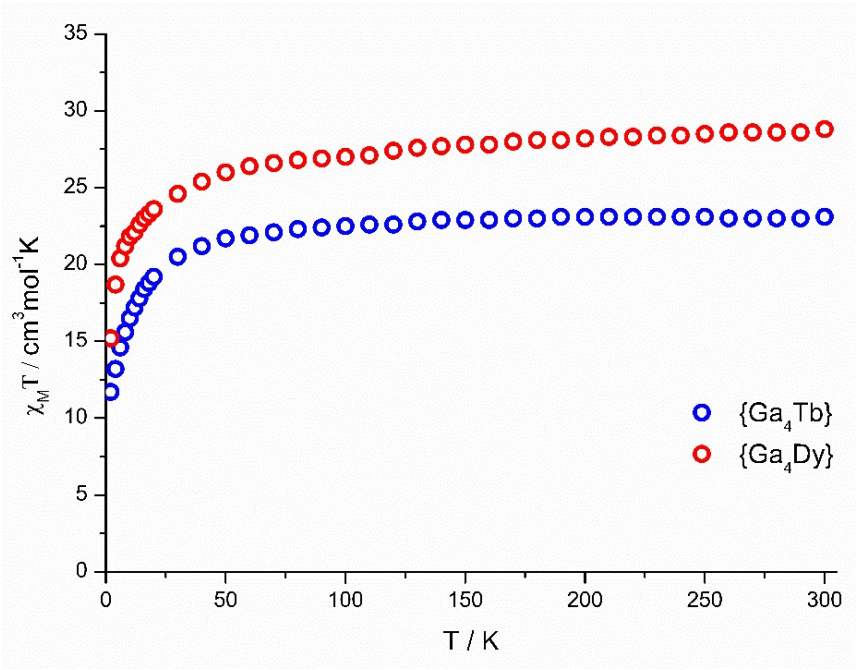

Figure 5.1.3: Temperature dependence of magnetic susceptibility for complexes **1** and **2**.

The field dependence of magnetization was also investigated and measured for both complexes in the temperature range of 2 – 10 K under a variety of magnetic fields (0 – 7 T, Figure 5.1.4, Figure S2). In both complexes, the magnetization values increase rapidly at low fields while a more continuous increase is observed at higher fields. The values of magnetization at 2 K under the applied field of 7 T are 13 μ_B for **1** and 11.33 μ_B for **2**, not reaching saturation. The lack of saturation can be an indication of the presence of magnetic anisotropy and/or population of the Ln(III) low-lying states.

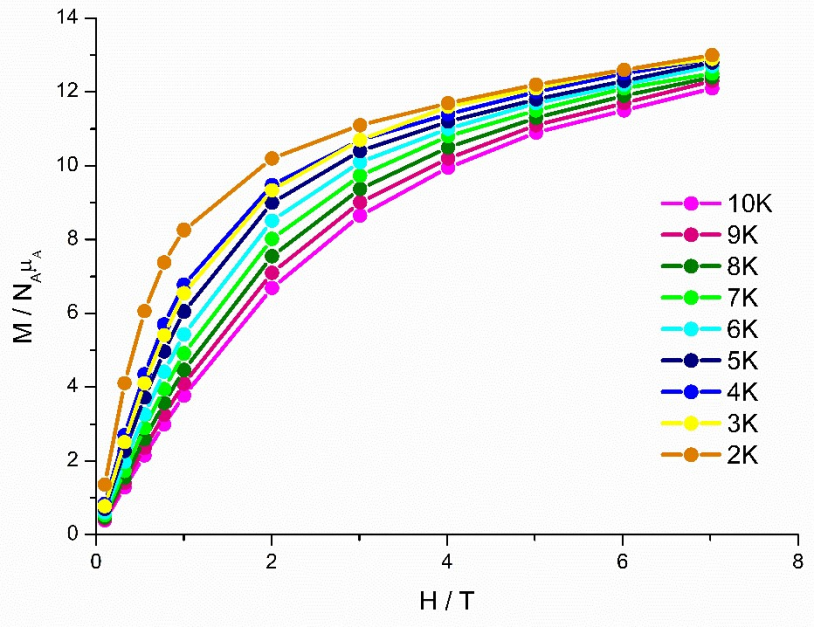

Figure 5.1.4: M vs H plots for complex 1 in various temperatures as indicated. Solid lines are guidelines for the eyes.

Alternating-current (ac) studies for complexes **1** and **2** were also performed in a zero-applied field, with a 3 Oe ac field oscillating at frequencies in the range of 1-1500 Hz and at temperatures of 1.9 – 4.1 K. Complex **2** does not show any frequency dependant ac signals neither at zero nor at an applied external magnetic field, declaring that the compound does not belong to the SMM family at the temperature ranges of investigation. However, complex **1** does possess frequency dependant ac signals under an applied magnetic field. The lack of observation of a χ'' peak maxima at zero field for complex **1**, led to the use of an external optimum field of 1600 Oe (at frequencies from 1 -1500 Hz and at a temperature range of 1.9 –

4-1 K) trying suppress the QTM, which is a negative effect to SMM behavior. After the application of the external dc field of 1600 Oe a not well-pronounced SMM behavior can be observed (Figure 5.1.5, S3,S4). The application of the external field was not adequate enough to supress the tunneling and thus, only a slight part of the frequency dependent out-of-phase tails of signals can be observed in Figure 5.1.5. Further, fitting of the data was not possible for complex **1**. The out-of-phase signals, as depicted in Figure 5.1.5, are weak and a reliable fitting was not possible to be obtained. However, in this case a magnetic investigation of the complex has been performed unlike the previously discussed {Ga_8Dy_2} compound for which no magnetic measurement has been described in the paper.[2]

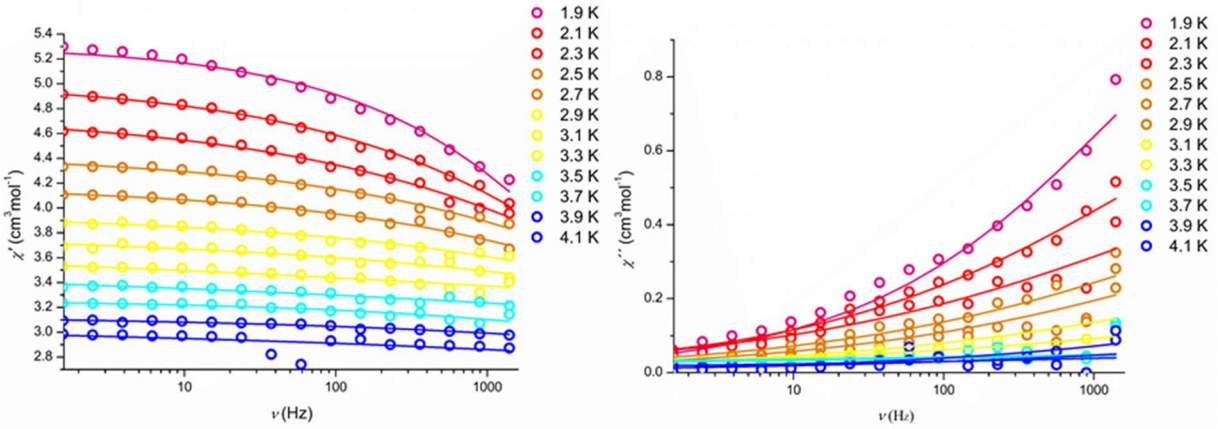

Figure 5.1.5: Frequency-dependent ac susceptibility studies in an applied field of 1600 Oe for complex **1**. The solid lines represent fitting of the data.

After having obtained the complexes described above it was clear enough, from a synthetic point of view, that changing the base to one that doesn't include Na(I) ions would lead to the isolation of a completely different product. That was exactly the next step of our synthetic attempts, which were directly focused on the use of organic bases that didn't contain ions that could compete with the Ga(III) or Ln(III) ions in solution and could potentially coordinate. As such, three new, different from complex **1** and **2**, molecules were obtained, while their structural and magnetic characterization is extensively analyzed below.

The reaction of $Ga(NO_3)\cdot H_2O$, $Dy_2(piv)_6(Hpiv)_6$ (where pivH= HO_2CCMe_3), $shaH_2$, $^tBu_4NClO_4$ and morpholine (C_4H_9NO) in a molar ratio of 8:1:8:3:8, in the solvent of MeOH, during the process of slow evaporation after five days, gave small colorless plate crystals of

(^{t}BuNClO$_4$)[Ga$^{III}_4$Dy^{III}(O$_2$CCMe$_3$)$_4$(shi)$_4$]•6H$_2$O (Ln = Dy (**3**)) in ~65 % yield. The chemical and structural identity of complex **3** was determined by single-crystal X-ray crystallography, IR spectroscopy and elemental analyses (C, H, N).

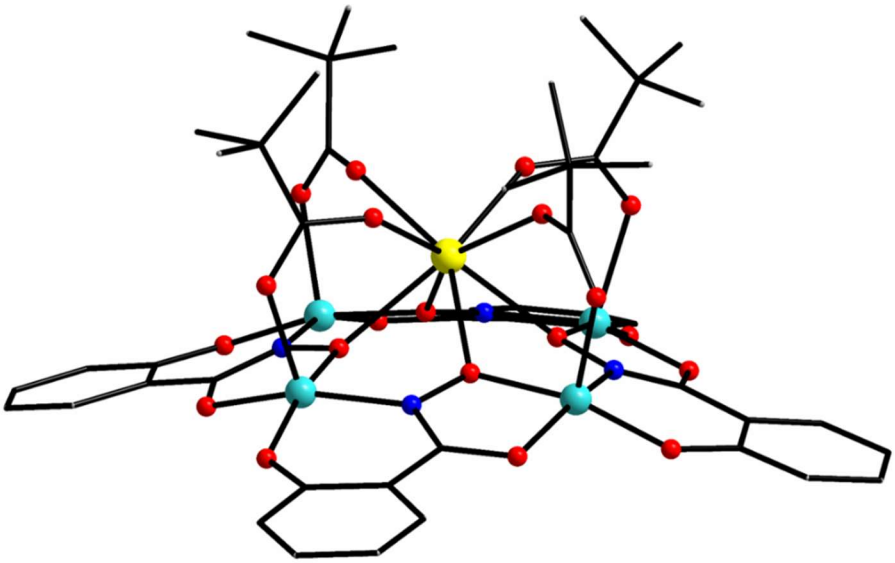

Figure 5.1.6: Schematic Representation of complex **3**. Color scheme: Ga^{III}, aqua; Dy^{III}, yellow; N, blue; O, red; C, black. H are omitted for clarity.

X-Ray diffraction studies were performed and revealed that complex **3** crystallizes in the Pnma orthorombic space group (Table S6). The final formula of the complex was derived based on charge balance considerations and metric parameters.[6] Complex **3** consists of a [Ga$^{III}_4$Dy^{III}(O$_2$CCMe$_3$)$_4$(shi)$_4$]$^{-}$ anion (Figure 5.1.6) and one ^{t}Bu$_4$NClO$_4$ cation that counterbalances the molecular structure. In that case, it is clear that the use of ^{t}Bu$_4$NClO$_4$ is of crucial importance since it acts as a countercation assisting in the formation of the final product. Selected interatomic distances and angles for complex **3** are listed in Table S7 and S8 at the Supporting Information. The core of **3** (Figure 1.5.7) contains four Ga(III) ions held together by the four triply deprotonated shi^{3-} ligands in a 12-MC-4 motif, while a Dy(III) ion sits in the cavity of the metallacrown.

The connection of $Ga^{III}\cdots Ga^{III}$ and $Ga^{III}\cdots Dy^{III}$ ions result in distance separations of 4.701(1) Å and 3.685(1)-3-714(1) Å, respectively. The Ga^{III} atoms are bridged by four oximate bridges provided by the shi^{3-} ligands, which all adopt the same η^1: η^1: η^1: η^2:μ_3 coordination mode (Scheme 2, SI), assisting in the formation of the characteristic 12-MC-4 motif. The Dy(III) sits 1.633(1) Å above the plane that is formed from the four Ga(III) ions, shaping this pyramide-like core. The basal positions of the pyramid are occupied by the four Ga(III) ions, while the Dy(III) atom sits on the apical position of the pyramid. All four Ga(III) ions are five-coordinate with distorted square pyramidal geometries (τ =0.08 – 0.26), while the central Dy(III) atom is eight-coordinate possessing a square antiprismatic geometry, as it was further established by SHAPE calculations (ChSM = 0.66, Table S9).[7,8] Finally, it is clear enough that the core of this complex is identical to the core of the $\{Mn_4Ln\}$ family of complexes discussed in Chapter 2 and as such confirmational details can be checked there as well.

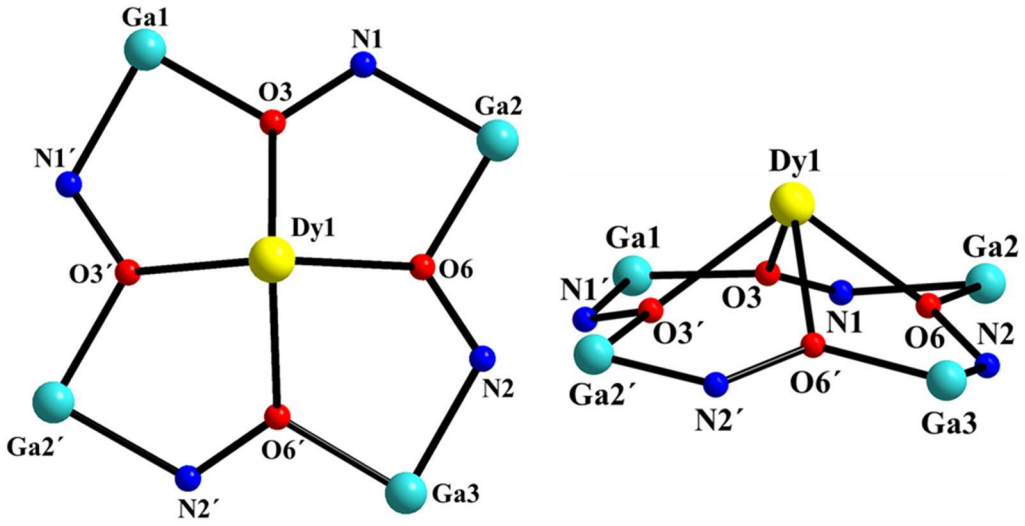

Figure 5.1.7: Schematic representation of inorganic core $\{Ga^{III}_4Dy^{III}(\mu\text{-}NO)_4\}^{11+}$ of complex **3**. Color scheme: Ga^{III}, aqua; Dy^{III}, yellow; O, red; N, blue; C, black.

Solid state, direct-current (dc) magnetic susceptibility studies of a freshly prepared sample of **3** were performed in the temperature range of 2 – 300 K, under an applied field of 0.1 T. The data derived from the above measurements, are presented as a $\chi_M T$ vs T plot in Figure 5.1.8. The experimental value of complex **3** at 300K is 13.9 $cm^3mol^{-1}K$ very close to the theoretical one

of 14.17 $cm^3mol^{-1}K$, expected for one non-interacting Dy(III) ion ($^6H_{15/2}$, S = 5/2, L = 5, J = 15/2, g = 4/3). Upon lowering the temperature, the magnetic susceptibility of the complex stays almost steady till 50 K, while after that a fast decrease is detected reaching a value of 8.74 $cm^3mol^{-1}K$ at 2 K. The low temperature decrease of the $\chi_M T$ can be attributed to the depopulation of the Dy(III) crystal field sublevels, zero-field splitting effects and the presence of intermolecular antiferromagnetic exchange interactions within the molecules of the crystal.

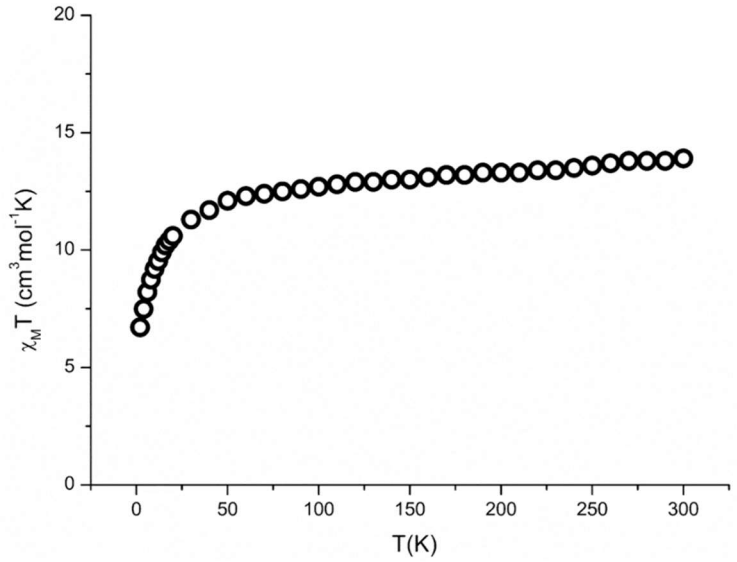

Figure 5.1.8: Temperature dependence of magnetic susceptibility for complex **3**.

Field-dependent magnetization measurements were performed for compound **3** at temperatures between 2 K and 10 K over the range of 0 – 7 T. As depicted in Figure 5.1.9 the values of magnetization increase rapidly at low field and upon increasing even further the field a more linear increase can be observed for complex **3**. At 7 T saturation is not reached with the magnetization value being 7.69 μ_B. The lack of saturation could hinder the presence of magnetic anisotropy and/or population of Dy(III) low-lying excited states.

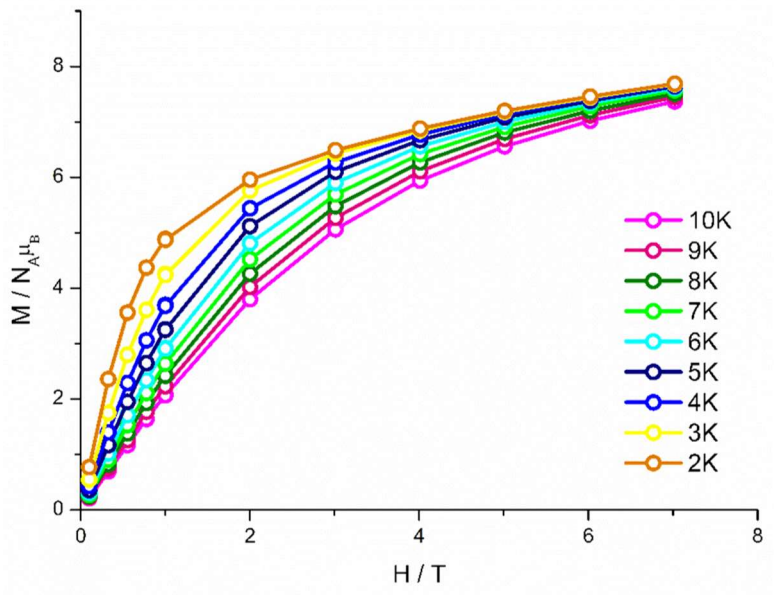

Figure 5. 1.9: M vs H plots for complex **3** in various temperatures as indicated. Solid lines are guidelines for the eyes.

Alternating-current (ac) magnetic susceptibility studies were performed for complex **3** in a zero and an applied dc field, with an 3 Oe ac field oscillating at frequencies from 1-1500 Hz in the temperature range of 1.9 – 5.5 K. No single-molecule magnetic behavior was observed for compound **3** at the temperatures reached by our SQUID. In previous examples of Dy-centered 12-MC-4 compounds no SMM properties have been reported. Pecoraro and coworkers published a similar Ga(III)/Dy(III) 12-MC-4 complex in 2016, with no ac signals reported.[9] Our group documented a report, which was investigating the same 12-MC-4 scaffold using paramagnetic Mn(III) as ring metal ions with Ln(III) (where Ln = various lanthanides) in the center, however no SMM behavior was observed for these complexes as well.[10] The most logic explanation for this lack of SMM properties can be the effect of the ligand field around the Dy metal ion in combination with its electronic shape. It seems that this 12-MC-4 arrangement does not stabilize a high multiplicity J term for dysprosium, having as an outcome the disappearance of SMM properties due to either ground state quantum tunneling effects or mixing of m_J states which are very close in energy and thus leading to tunneling from excited states.

Following the same synthetic principles discussed earlier, after obtaining complex **3** it was apparent enough that by avoiding the use of pivalates, from the initial synthetic scheme, we could force the system into the isolation of a different compound depending on the starting materials used. Thus, a new synthetic system was designed and multiple reactions and

crystallization techniques were employed towards the isolation of a new (possibly and desirably) 12-MC-4 compound.

The reaction of $Ga(NO_3)\cdot H_2O$, $Dy(O_2CCH_3)_3{\cdot}4H_2O$, $shaH_2$, $^tBu_4NClO_4$ and morpholine (C_4H_9NO) in a molar ratio of 8:1:8:3:8, in the solvent of MeOH, followed by layering with Et_2O/hexane for six days, led to the isolation of small colorless plate crystals of $[Ga^{III}_4Dy^{III}(NO_3)(shiH_2)_2(shi)_4(MeOH)(H_2O)_2]\bullet 2MeOH\bullet 5H_2O$ (**4**) in ~54 % yield. The chemical and structural identity of complex **4** were determined by single-crystal X-ray crystallography, IR spectroscopy and elemental analyses (C, H, N). X-Ray diffraction studies were performed and revealed that complex **4** crystallizes in the C2/c monoclinic space group (Table S10). The final formula of the complex was derived based on charge balance considerations and metric parameters.[6] Complex **4** comprises a $[Ga^{III}_4Dy^{III}(NO_3)(shiH_2)_2(shi)_4(MeOH)(H_2O)_2]$ (Figure 5.1.10) molecular structure, in which $BuNClO_4$ does not participate in the final formula. Most likely in this case, the use of $^tBu_4NClO_4$ is essential for the collection of the final product due to the fact that its presence in the reaction solution is necessary for the final crystallization, possibly due to concentration reasons.

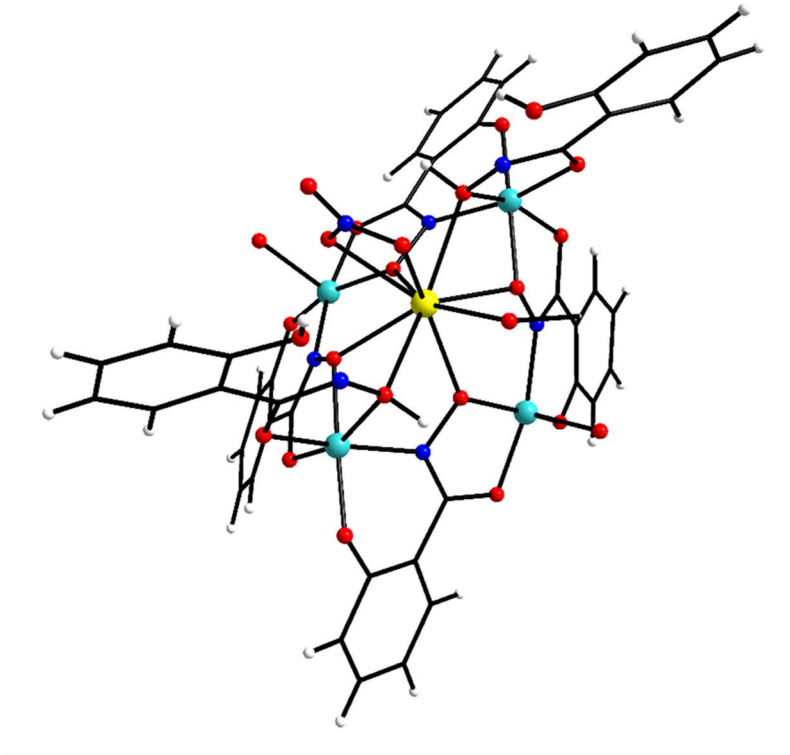

Figure 5.1.10: Schematic representation of molecular structure of complex **4**. Color scheme:Ga, aqua; Dy, yellow; O, red; N, blue; C,black; H, white.

Selected interatomic distances and angles for complex **4** are indexed in Table S11 and Table S12 at the Supporting Information. The core of **4** (Figure 1.5.7) contains four Ga(III) ions held together by the four triply deprotonated shi^{3-} and two singly-deprotonated $shiH_2^-$ ligands in a highly bend 12-MC-4 motif, while a Dy(III) ion sits in the cavity of this bend metallacrown. The coordination of the NO_3^- ions most likely is the driving force of this formed bend metallacrown motif, which had not been observed in the previous obtained structures.

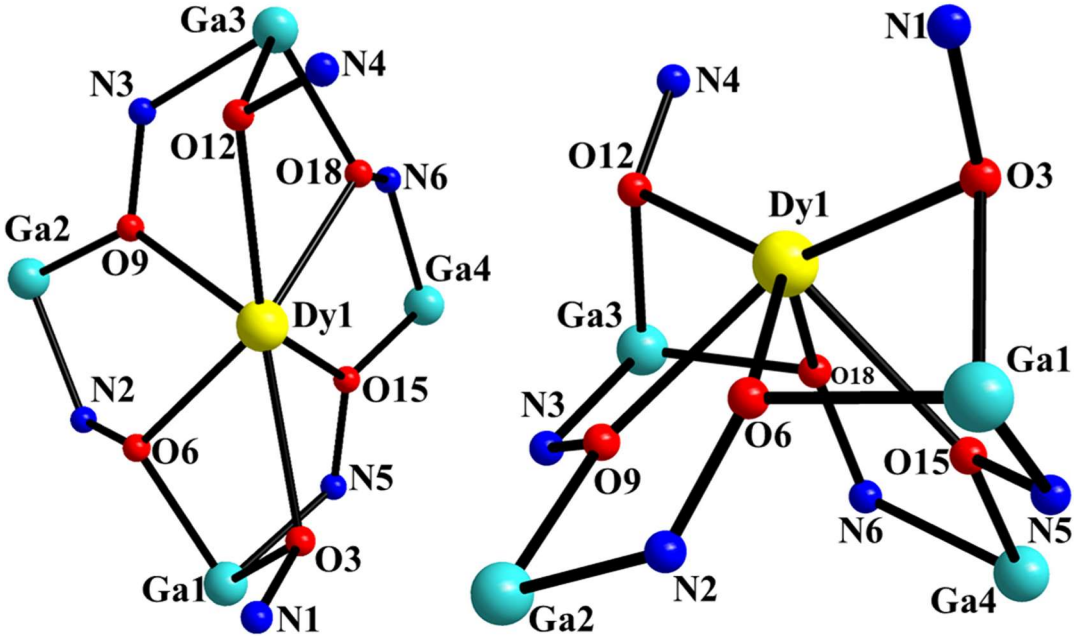

Figure 5.1.11: Labelled schematic representation of inorganic core $\{Ga^{III}_4Dy^{III}(\mu\text{-}NO)_6\}^{9+}$ of complex **4**. Color scheme: Ga^{III}, aqua; Dy^{III}, yellow; O, red; N, blue; C, black.

The connection of $Ga^{III}\cdots Ga^{III}$ result in the following distant separations of Ga1···Ga2 =4.666(1) Å, Ga2···Ga3 = 4.672(1) Å, Ga3···Ga4 = 4.632(1) Å and Ga4···Ga1 = 4.676(1) Å, while the distance separation of Dy(III) from the plane that is calculated between the four Ga(III) atoms is 1.914(1) Å (Figure S6). The Ga atoms are bridged by the oximate groups provided by salicylhydroxamic acid and the coordination modes that are adopted are η^1: η^1: η^1: η^2:μ_3 and η^1: η^2:μ (Scheme 3, SI). The core of compound **4** adopts a highly bend pyramid-like structure, where the Ga(III) ions occupy the base of the pyramid and the Dy(III) sits on the apical position forming the tip of the pyramid. Two Ga(III) are six-coordinate with distorted octahedral geometries, while the other two are five-coordinate possessing a square pyramidal geometry (τ = 0.17 for Ga2 and τ = 0.14 for Ga4). The central Dy(III) ion is nine-coordinate possessing a

spherical tricapped trigonal prism geometry with a CShM = 1.35 (Fig. S7, Table S13). Note that complex **4** is the first Ga/Ln/shi^{3-} complex, reported up to now, comprising this unique highly bend 12-MC-4 motif.

Variable-temperature direct current (dc) magnetic susceptibility measurements were performed on powdered polycrystalline sample of **4** in a 0.1 T field and in the 2.0–300 K range. The data are presented in a $\chi_M T$ versus T plot in Figure 5.1.12. For complex **4,** the experimental value (14.00 cm^{3}mol^{-1}K) is very close to the expected theoretical one of 14.17 cm^{3}mol^{-1}K for one non-interacting Dy(III) ion ($^6H_{15/2}$, S = 5/2, L = 5, J = 15/2, g = 4/3). The $\chi_M T$ product remains steady upon cooling of the temperature until approximately 50 K, while after that a sharp decrease is observed with the $\chi_M T$ product reaching the value of 10.3 cm^{3}mol^{-1}K at 2 K.

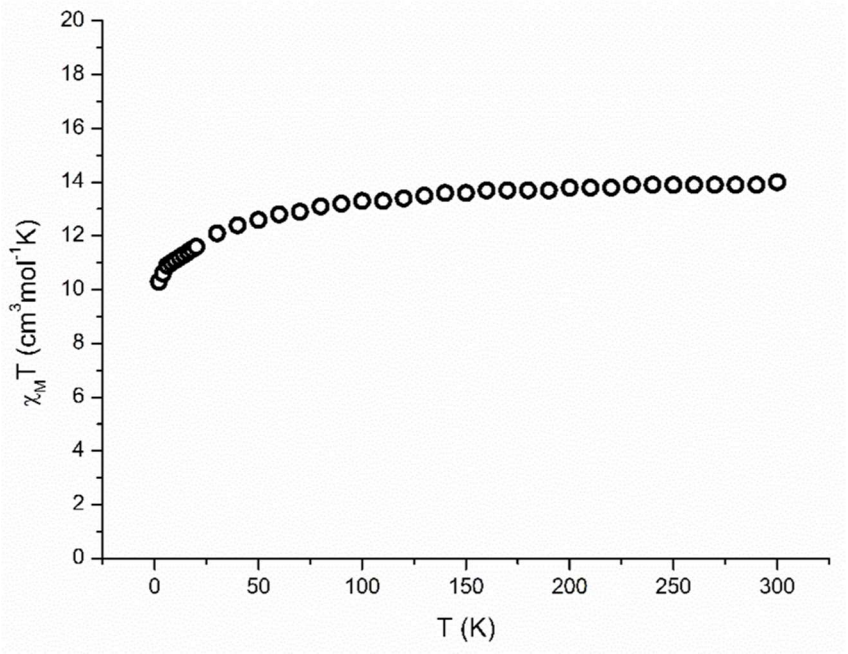

Figure 5.1.12: Temperature dependence of magnetic susceptibility for complex **4**.

This type of behavior is expected for systems where no interaction within metal centers is involved. The low temperature decrease can be attributed to Zeeman effects, zero-field splitting and the presence of intermolecular antiferromagnetic exchange interactions with the molecules of the crystal.

Magnetization vs field (M vs *H*) measurements were also performed and can be seen in Figure 5.1.13. The field dependant magnetization at 2 K shows a fast increase below 1 T, while after that a more gradual increase is observed till magnetization reaches the 4.33 μ_B at 7 T without saturation. The lack of saturation indicates the presence of magnetic anisotropy and/or population of Ln(III) low-lying excited states.[11]

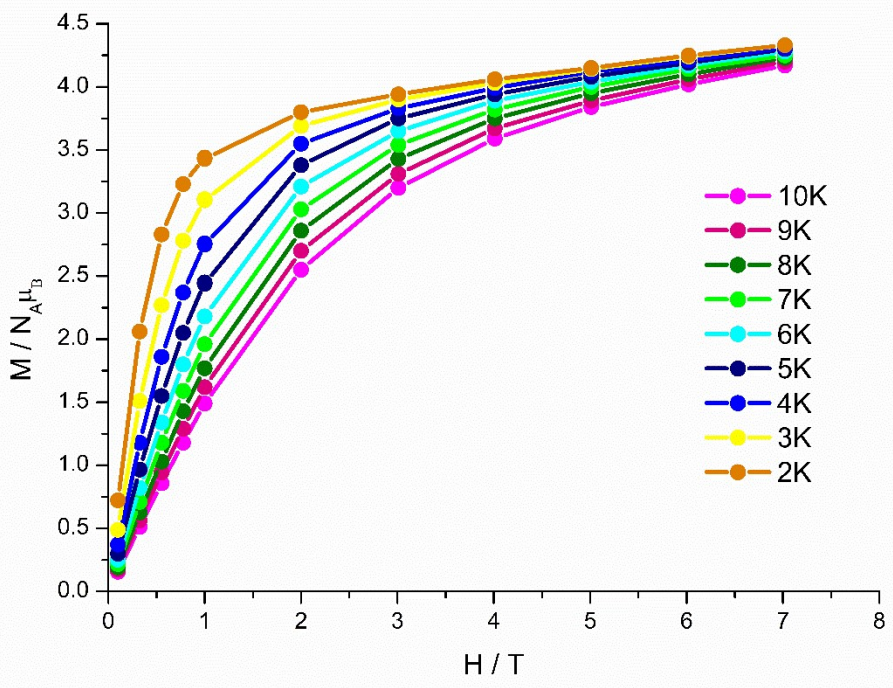

Figure 5.1.13: M vs H plots for complex **4** in various temperatures as indicated. Solid lines are guidelines for the eyes**.**

To test the magnetic dynamics of complex **4**, alternating-current (ac) magnetic susceptibility measurements were performed in a zero-applied field, with a 3 Oe ac field oscillating at frequencies in the range of 1-1500 Hz and at temperatures of 1.9 – 4.1 K. Compound **4** shows weak out-of-phase frequency dependant tails of signals below ~ 5 K at zero field, indicating the presence of a fast-relaxing SMM. That means that quantum tunneling of magnetization is strong and it coincides with the thermal relaxation pathway (Figure S8 - S11). Thus, since we were not able to observe any peak maxima at zero field, scan-field measurements were performed in order to find an optimum external dc field. Upon pursuing the aforementioned procedure an optimum field of 600 Oe was used for additional magnetic investigations. After the application of the external dc field of 600 Oe an increase at the χ' and χ'' is clearly observed as depicted in Figure 5.1.14. Fitting of the data was possible using a generalized Debye function and upon

constructing the Cole-Cole plots, we were able to observe that probably there is more than one main magnetization relaxation pathway for complex **4** since a wide distribution of the α values (α = 0.75 – 0.36) is clearly visible (Figure 5.1.15).[12–14] A fit was obtained taking into account all possible relaxation processes using the equation $\tau^{-1} = \tau_{QTM}^{-1} + CT^{n} + \tau_{0}^{-1}\exp(-U_{eff}/K_{B}T)$, where τ_{QTM}^{-1} corresponds to the quantum tunnelling relaxation process, CT^{n} corresponds to the Raman relaxation and the last terms relate to the Orbach relaxation pathway.[15] The best fit parameters are n = 9, C = 0.0079 $s^{-1}K^{-9}$, U_{eff} = 26.5 K, $\tau_0 = 9.46 \times 10^{-8}$ s and $\tau_{QTM} = 1.59 \times 10^{-4}$ s (Figure 5.1.15) with these values being in accordance with the values presented in the literature.[16] A reliable fitting using less terms was not feasible to be obtained. Fitting of the data without taking into account the quantum tunneling did not match our experimental data at all and thus it was also included into the equation.

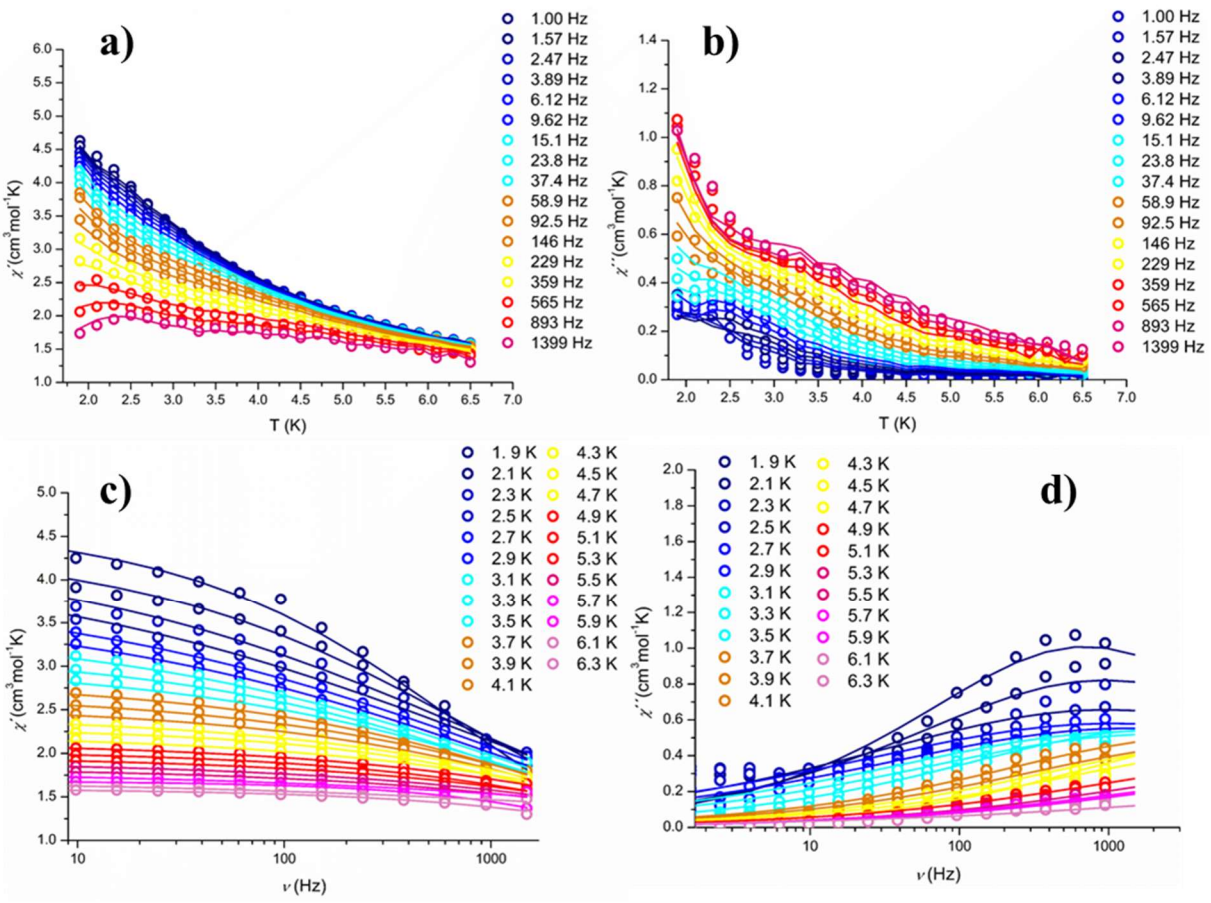

Figure 5.1.14: a) Temperature dependent in-phase susceptibility plot of for compound **4** (1.9 to 6.5 K) at 600 Oe. b) Temperature dependent out-of-phase susceptibility plot of for compound **4** (1.9 to 6.5 K) at 600 Oe. c) Frequency dependent in-phase susceptibility plot of for compound **4** (1.9 to 6.5 K) 600 Oe. d) Frequency dependent out-of-phase susceptibility plot of for compound **4** (1.9 to 6.5 K) at 600 Oe. Solid lines represent fit of the data.

On the occasion where Kramers ions, like Dy(III), are part of the molecular structure the dipole-dipole and hyperfine interactions as well as the presence of molecular anisotropy permit the mixing of the ground states of the Kramers ions in zero dc field, hence promoting the QTM over the thermal relaxation pathways.[17,18] In order to supress or even remove the QTM we applied an external (optimum dc field). The Cole-Cole plots, shown at Figure 5.1.15, for complex **4** in the temperature range of 1.9 – 5.7 K demonstrate semicircular shapes and fitting of the data was attempted using a Cole-Cole model.[19,20]

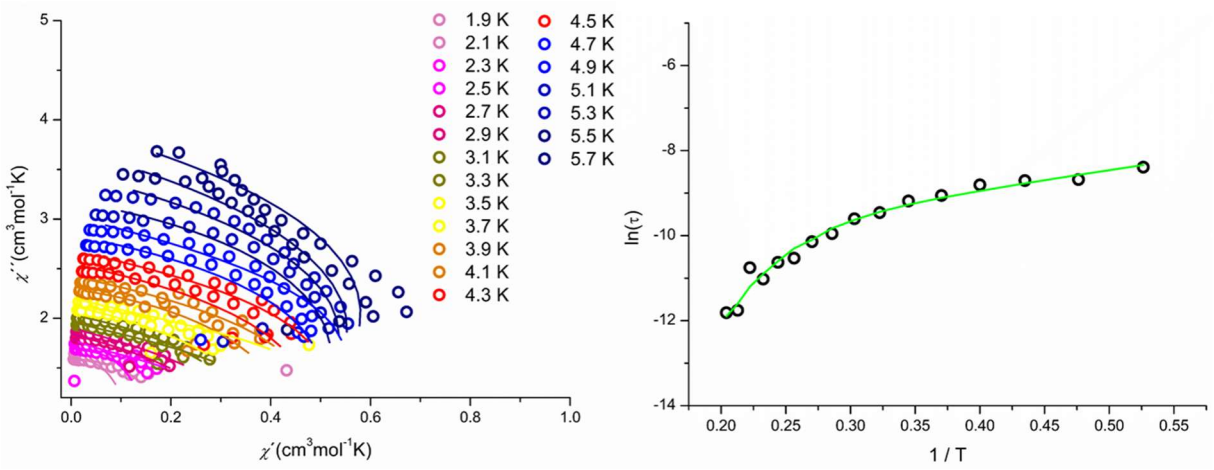

Figure 5.1.15: (left) Cole-Cole plots for complex **4** using the ac susceptibility data from 1.9 – 5.7 K under an external dc field of 600 Oe. The solid fines represent the best fit gained upon using the Cole-Cole model. (right) Arrhenius plot showing the magnetization relaxation of **4** under an applied field of 600 Oe.

The α values derived are in the range of 0.75 – 0.47, demonstrating a wide distribution of relaxation times, something that is being in accordance with the existence of more than one relaxation pathways, as it was also shown by the fitting reported above.

This is the first time that a complex like compound **4** is reported in the literature, possessing this highly bend 12-MC-4 motif. The novelty of that compound is based not only on the structural features but also the combination of metal ions used. This is the first time that a bend Ga(III)/Ln(III)/shi^{3-} 12-MC-4 complex is reported. It is very important to point out that complex **4** is an SMM and that behaviour can most likely be attributed to the bend or distorted geometry of the MC scaffold which led to the 9-coordination mode of the central lanthanide or vice versa. This can be further justified by the comparison of compound **4** to complex **3,** which shows no SMM behavior in its almost ideal 12-MC-4 arrangement of Ga(III) ring metal ions along with Dy(III) in the cavity. Finally, it is also important to point out that based on literature reports we

have also observed that the 9-coordination mode of lanthanides in spherical tricapped trigonal prism geometry often leads to single-molecule magnet behavior of considerable performance, further justifying the magnetic behavior of complex **4**.[21]

The last Ga(III)-based compound that will be discussed in this chapter, is complex **5** with a general formula of $(^{t}Bu_4N)[Ga^{III}_8Ho^{III}(OH)_4(shi)_8]\bullet 3MeOH\bullet 5H_2O$. This compound is the isostructural analogue of the double-decker complex discussed in Chapter 4, possessing Ho(III) instead of Dy(III). This complex was not included in the first communication paper since it was only obtained a few weeks ago. The reasons of interest towards complex **5** were mostly magnetic-based since we wanted to investigate whether the electronic shape of the central lanthanide would have an effect on magnetism. As it is known, Ho(III) is a $4f^{10}$ metal ion and it has a fairly distorted oblate form.[18] Dy(III) has a pure oblate shape and thus the isolation of the Ho(III) and Er(III) analogues of the complex discussed in Chapter 4, would assist us towards the finding of a rational to the question whether the electronic shape has an effect on the final relaxation of magnetization reversal. The Er(III) analogue has not been isolated so far and thus no further discussion will be held.

The reaction of $Ga(NO_3)_3\bullet H_2O$, $Ho_2(CO_3)_3\times H_2O$, shaH2, $^{t}Bu_4NClO_4$ and piperidine in 8:1:8:3:8 molar ration in the solvent of MeOH, yielded a pale pinkish suspension that under intensive stirring for one hour led to a colorless and almost clear solution. Upon filtration the solution was left for slow evaporation and after ten days small colorless plate crystals of $(^{t}Bu_4N)[Ga^{III}_8Ho^{III}(OH)_4(shi)_8]\bullet 3MeOH\bullet 5H_2O$ (**5**) were isolated in ~47 %. The chemical and structural identity of compound 5 was confirmed by X-Ray crystallography, elemental analyses and IR spectroscopy (Supporting Information).

Single-crystal diffraction studies revealed that compound **5** crystallizes in the monoclinic P2/c space group (Table S14). The oxidation states of the involved metal ions as well as the deprotonation level of the salicylhydroxamic ligands were based on metric parameters and charge balance considerations. The complex contains a $[Ga^{III}_8Ho^{III}(OH)_4(shi)_8]$ anion and a $^{t}Bu_4N$ cation which counterbalances the overall charge of the molecule, while MeOH and H_2O molecules are also present in the lattice. The complex comprises eigth Ga^{III} ions and one Ho^{III} arranged in a sandwich-like topology. The Ga^{III} atoms are forming two 12-MC-4 planes in which a central Ho^{III} atom is embedded. The basal Ga^{III} atoms are bridged via the oximato groups of eight triply deprotonated shi^{3-} ligands adopting a $\eta^1:\eta^1:\eta^1:\eta^2:\mu_3$ coordination mode, while the two deckers are linked via four μ-OH groups.

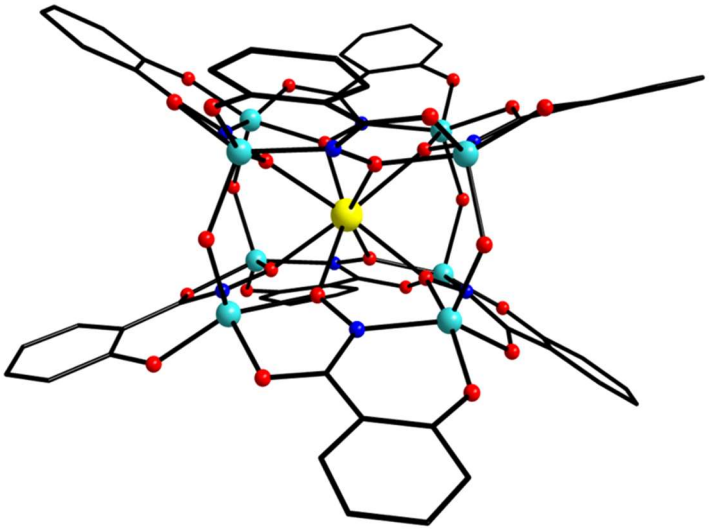

Figure 5.1.16: Schematic representation of molecular structure of complex **5**. Color scheme:Ga, aqua; Ho, yellow; O, red; N, blue; C,black; H, white.

All Ga^{III} atoms are five-coordinate with distorted to almost ideal square pyramidal geometries (τ = 0.28 – 0.03) as defined by the trigonality index criteria, while the central Ho^{III} ion is eight-coordinate possessing a square antiprismatic coordination geometry (CShM = 1.08, Table S17).

Complex **5** possesses an overall core of $\{Ga^{III}_8Ho^{III}(\mu\text{-}OH)_4(\mu\text{-}NO)_8\}^{15+}$ as depicted in Figure 5.1.17. The basal Ga•••Ga and the Ga•••Ho distances are found to be in the range of 4.687(1)-4.716(1) and 3.709(1)-3.750(1) Å, respectively, while the Ga•••Ga separation of the two deckers lies in the range of 3.379(1) – 3.408(2) Å. Finally, the Ga-O-N-Ga torsion angles are in the range of 165.67 - 176.98˚. Comparing the structural features of $\{Ga_8Ho\}$ with the isostructural compound presented in Chapter 4, we can directly see that all bond distances of complex **5** are shorter compared to the previous published compound, while the torsion angles are slightly larger. That means that the overall complex has a more compressed structural conformation that could potentially have an effect at the final magnetic properties of complex **5,** which will be described later on.

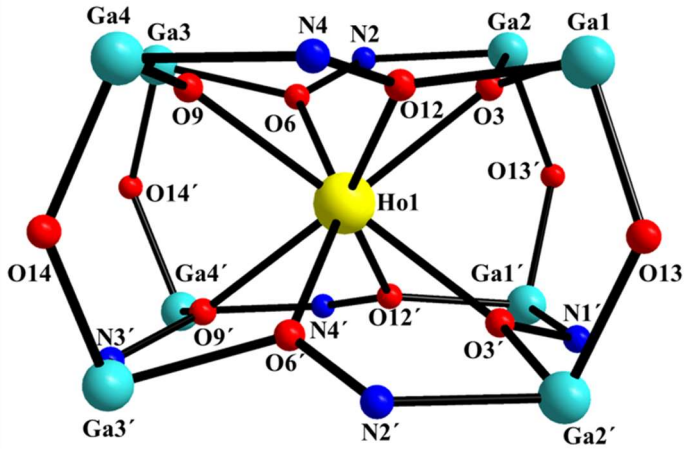

Figure 5.1.17: Labelled schematic representation of inorganic core $\{Ga^{III}_8Ho^{III}(\mu\text{-}OH)_4(\mu\text{-}NO)_8\}^{15+}$ of complex **5**. Color scheme: Ga^{III}, aqua; Ho^{III}, yellow; O, red; N, blue; C, black.

Solid state, direct-current (dc) magnetic susceptibility studies were recorded in the temperature range of 2 – 300 K on a freshly prepared and analytical pure (see SI) microcrystalline sample of **5** under an applied field of 0.1 T. The experimental value of the $\chi_M T$ product at 300 K is 13.08 $cm^3mol^{-1}K$, very close to the theoretical one of 14.08 $cm^3mol^{-1}K$ expected for one non-interacting Ho(III) atom ($^5I_8$, S = 2, L = 6, J = 8, g = 5/4) (Figure 5.1.18). As observed, the $\chi_M T$ product steadily and slightly decreases in the range of 300 K till 50 K, while upon further temperature lowering it more acutely decreases reaching a value of 13.08 $cm^3mol^{-1}K$ at 2 K. The sharp low temperature decrease is commonly attributed to the depopulation of the Zeeman split crystal field levels.

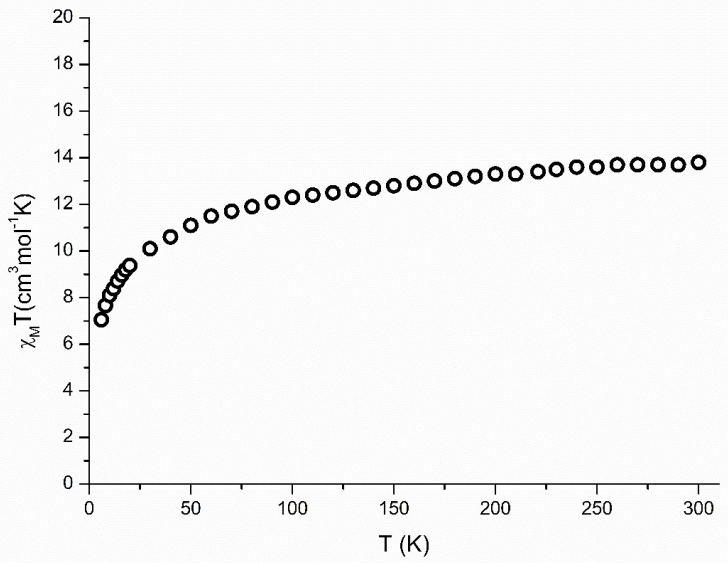

Figure 5.1.18: Temperature dependence of magnetic susceptibility for complex **5**.

The field dependence of magnetization of {Ga_8Ho} **(5)** was also monitored in the temperature range of 2 – 10 K under a variety of fields from 0 till 7 T (Figure 5.1.19). The values of magnetization increase rapidly at low fields while a higher fields at more continuous increase is observed. The magnetization value of complex **5,** at 2 K under the applied field of 7 T, is 5.16 μ_B not coming to saturation. The lack of saturation of magnetization can be suggestive of the presence of magnetic anisotropy and/or population of the Ho(III) low-lying excite states.

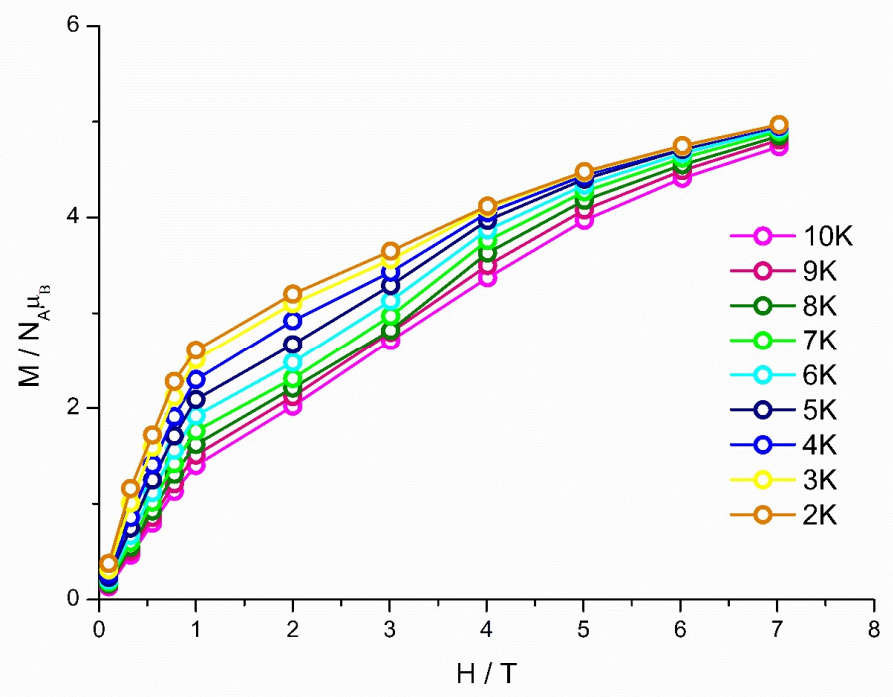

Figure 5.1.19: M vs H plots for complex **5** in various temperatures as indicated. Solid lines are guidelines for the eyes.

Alternating-current (ac) magnetic susceptibility studies were also performed for complex {Ga_8Ho} **(5)**. However we were not able to observe any ac signal either at zero or at any applied external dc field, meaning that compound **5** does not behave as an SMM at the temperatures of investigation of our SQUID magnetometer.

The last compound that will be discussed in this chapter is an Fe/Ln/shi^{3-} complex. Apart from working with diamagnetic periphery ring metal ions at the metallacrown scaffold, one of the targets of this Thesis was to use paramagnetic ones, in order to monitor the effect of the magnetic nature of the periphery metal ions on the magnetic behavior of the resulting complexes. The published papers from Chapter 2 and Chapter 3 are dealing with that, since in Chapter 2 a Mn/Ln/shi^{3-} family of complexes was structurally and magnetically investigated

while Chapter 3 deals with the synthesis and magnetic characterization of a fused 12-MC-4 or new metallacryptate family of compounds. In both cases, the change from diamagnetic Ga(III) atoms to highly paramagnetic Mn(III) and Fe(III) ions was intended. Fe(III) ions seemed promising for us since it has already been established in the literature that Ga(III) and Fe(III) behave quite similarly, thus it is quite often possible to substitute one another and isolate their isostructural compounds.[22,23] In this section, a Fe/Ln/shi^{3-} molecule will be discussed while magnetic studies of the compound will be also presented.

The reaction of $Fe(ClO)_4H_2O$, $Dy(NO_3)_3H_2O$, $shaH_2$, $^tBuNClO_4$ and piperidine ($C_5H_{11}N$) in a molar ratio of 8:1:8:3:8 in the solvent of MeOH, gave a dark red clear solution which upon the process of layering with hexanes, after three days, led to the isolation of dark red block crystals of complex $\{Fe_6Dy_2(shiH_2)_4(shiH)_2(shi)_6(MeOH)_4\}\bullet 2MeOH\bullet 12H_2O$ (**6**) in good yields ~72 % (Figure 5.1.20). The chemical and structural identity of complex **6** was determined by single-crystal X-ray crystallography, IR spectroscopy and elemental analyses (C, H, N).

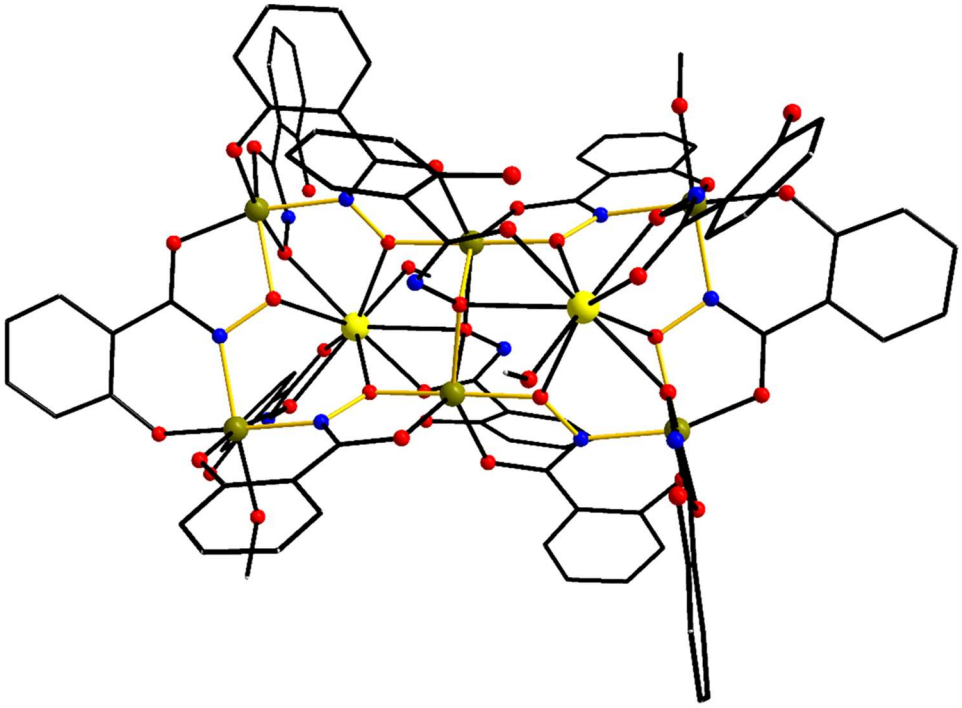

Figure 5.1.20: Schematic representation of molecular structure of complex **6**, highlighting the edge-sharing 12-MC-4 motif. Color scheme: Fe, dark yellow; Dy, yellow; O, red; N, blue; C,black; H, omitted for clarity.

Single-crystal diffraction studies revealed that compound **6** crystallizes at the monoclinic C2/c space group (Table S18). The oxidation states of the involved metal ions as well as the deprotonation level of the salicylhydroxamic ligands were based on metric parameters and charge balance considerations. Selected interatomic distances and angles are presented in Table S19 and S20. The structure of complex **6** possess a $\{Fe_6Dy_2(shiH_2)_4(shiH)_2(shi)_6(MeOH)_4\}$ general formula, while we can also observe MeOH and H_2O molecules present in the crystal lattice of the complex. The $\{Fe_6Dy_2\}$ complex comprises six Fe^{III} atoms held together via the hydroxide and oximate groups provided by the salicylhydroxamic acid ligand, while two Dy^{III} ions are positioned in the middle of the two vacant cavities present in the molecule. Fe1 and Fe1′ serve as the edge-sharing ring metal ions between the two fused 12-MC-4 crowns. This complex could be also considered as a cage-like structure since not a distinct 12-MC-4 topology is observed, however, the structural features that characterize metallacrowns are present, thus justifying even further this double edge-sharing 12-MC-4 description of the complex.

Compound **6** possesses an overall $\{Fe_6Dy_2(\mu_3\text{-}NO)_2(\mu\text{-}NO)_{10}\}^{12+}$ inorganic core (Figure 5.1.21). Fe1, Fe1′, Dy1 and Dy1′ are sitting at the vertices of a defective dicubane with two cubanes sharing a face [Fe(1)O(12′)Fe(1′)O(12)] and each missing a metal vertex. The central Fe^{III} ions are bridged by two μ_3-NO (N4O12, N4′O12′) and four μ-NO bridges (N3O9, N1O3, N3′O9′, N1′O3′). The ligand coordinates to the metal ions adopting three different coordination modes $\eta^1{:}\eta^1{:}\eta^2{:}\mu$, $\eta^1{:}\eta^1{:}\eta^3{:}\mu_3$ and $\eta^1{:}\eta^1{:}\eta^1{:}\eta^2{:}\mu_3$ shown in Scheme 4 of the Supporting Information. The core is completed by the outer F2, Fe3, F2′ and Fe3′ metal ions which are also linked with each other via the oximate groups provided by the organic ligand. Finally, peripheral ligation is provided by four MeOH molecules.

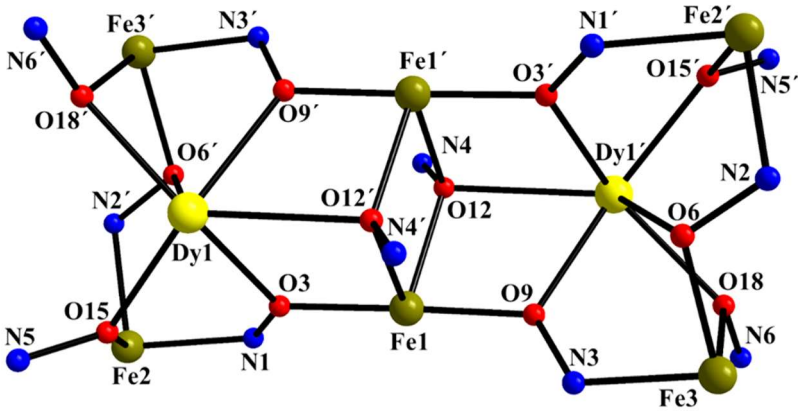

Figure 5.1.21: Labelled schematic representation of the inorganic core $\{Fe_6Dy_2(\mu_3\text{-}NO)_2(\mu\text{-}NO)_{10}\}^{12+}$ of complex **6**. Color scheme: Fe, dark yellow; Dy, yellow; O, red; N, blue; C,black.

All Fe^{III} centers are six-coordinate possessing a distorted octahedral geometry, while the central Dy^{III} atoms are nine-coordinate with a muffin-type coordination geometry as established by the use of program SHAPE (CShM = 1.28, Figure S13, Table S21).[7,8] This muffin-type coordination environment of the dysprosium ions is a commonly observed geometry for Dy(III) ions according to literature reviews.[24–26] There are quite a few examples reported so far and in most of the cases, this coordination environment of the Dy(III) ions is often accompanied by the appearance of SMM properties of the studied compounds.[24–26]

Solid state, direct-current magnetic susceptibility measurements were performed in the temperature range of 2 – 300 K and under an applied field of 0.1 T, for a freshly prepared microcrystalline sample of **6**. The obtained data are shown in the $\chi_M T$ vs T plot at Figure 5.1.22. The experimental value at 300 K for complex **6** (37.0 $cm^3mol^{-1}K$) is much lower than the theoretical spin only value of 54.59 $cm^3mol^{-1}K$ expected for six non-interacting Fe^{III} ions (S = 5/2, g = 2) and two Dy^{III} ($^6H_{15/2}$, S = 5/2, L = 5, J = 15/2, g = 4/3). The $\chi_M T$ product decreases with decreasing temperature demonstrating the presence of predominant antiferromagnetic exchange interactions within the metal spin carriers. This behaviour is further promoted by the fact that the $\chi_M T$ value at 300 K is much are lower than the expected theoretical one, indicating the presence of strong antiferromagnetic exchange interaction. Unfortunately, only the Dy-analogue of the complex has been isolated, hence we could not proceed with fitting of the magnetic susceptibility data since the Gd-analogue was not possible to be obtained up to now. Note that fitting of the data is possible using the Gadolinium analogue since Gd(III) is isotropic so we take into account only the S value at the spin Hamiltonian while for highly anisotropic Dy(III) the spin-orbit coupled term J is the sum of the spin contribution (S) and the orbital contribution (L) which makes the fitting procedure more complicated for the conventionally used fitting programs.[27]

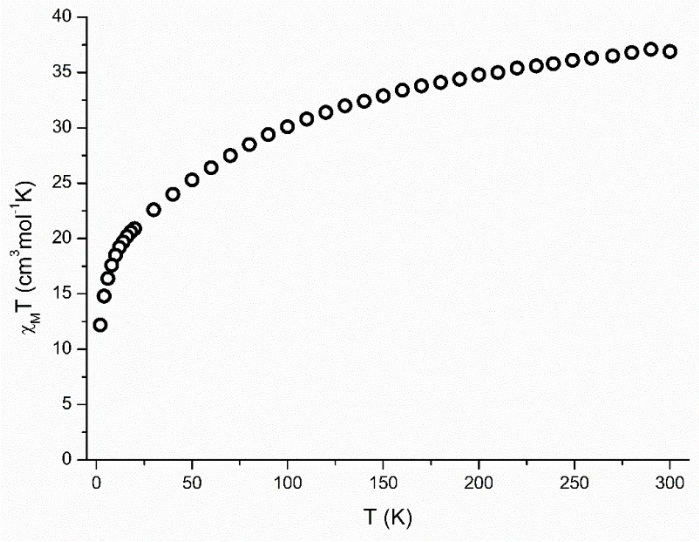

Figure 5.1.22: Temperature dependence of magnetic susceptibility for complex **6**.

The field dependence of magnetization for compound **6** was investigated in the temperature range of 2 - 10 K over the range of 0 - 7 T (Figure 5.1.23). As we can observe at the figure, the values of magnetization increase sharply at low field and after that a more linear/continuous increase is detected for complexes **6**. However, saturation is not reached at 7 T with the magnetization value being 10.4 μ_B at 2 K. The lack of saturation in magnetization is suggestive of the presence of magnetic anisotropy and/or population of the Ln^{III} low-lying excited states, while it can be also due to the presence antiferromagnetic exchange interactions between the metal ions.

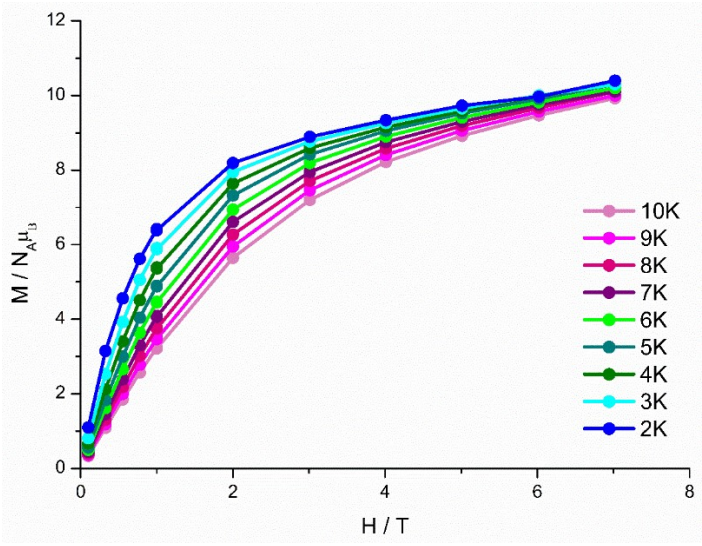

Figure 5.1.23: M vs H plots for complex **6** in various temperatures as indicated. Solid lines are guidelines for the eyes.

To probe the magnetic dynamics for our compound, alternating-current (ac) magnetic susceptibility studies were performed in zero-applied dc field, with a 3.0 Oe ac field oscillating at frequencies between 1-1500 Hz and in the temperature range of 1.9 - 5 K. Complex **6** shows frequency-dependent tails of signals below ~4 K at zero field, indicating that the magnetization relaxes very fast and as such the slow magnetic relaxation and quantum tunnelling most likely coexist. We were not able to observe any χ''_M peak maxima at zero field and thus in order to shift the peaks and supress the quantum tunnelling (QTM), an applied dc field was employed. After performing field-scan measurements, an optimum external field of 800 Oe was chosen to be used for further magnetic investigations. Upon application of the external field, we were able to slightly shift the peaks but apparently we were not able to supress the QTM, since no peak maxima could be observed (Figure 5.1.24).

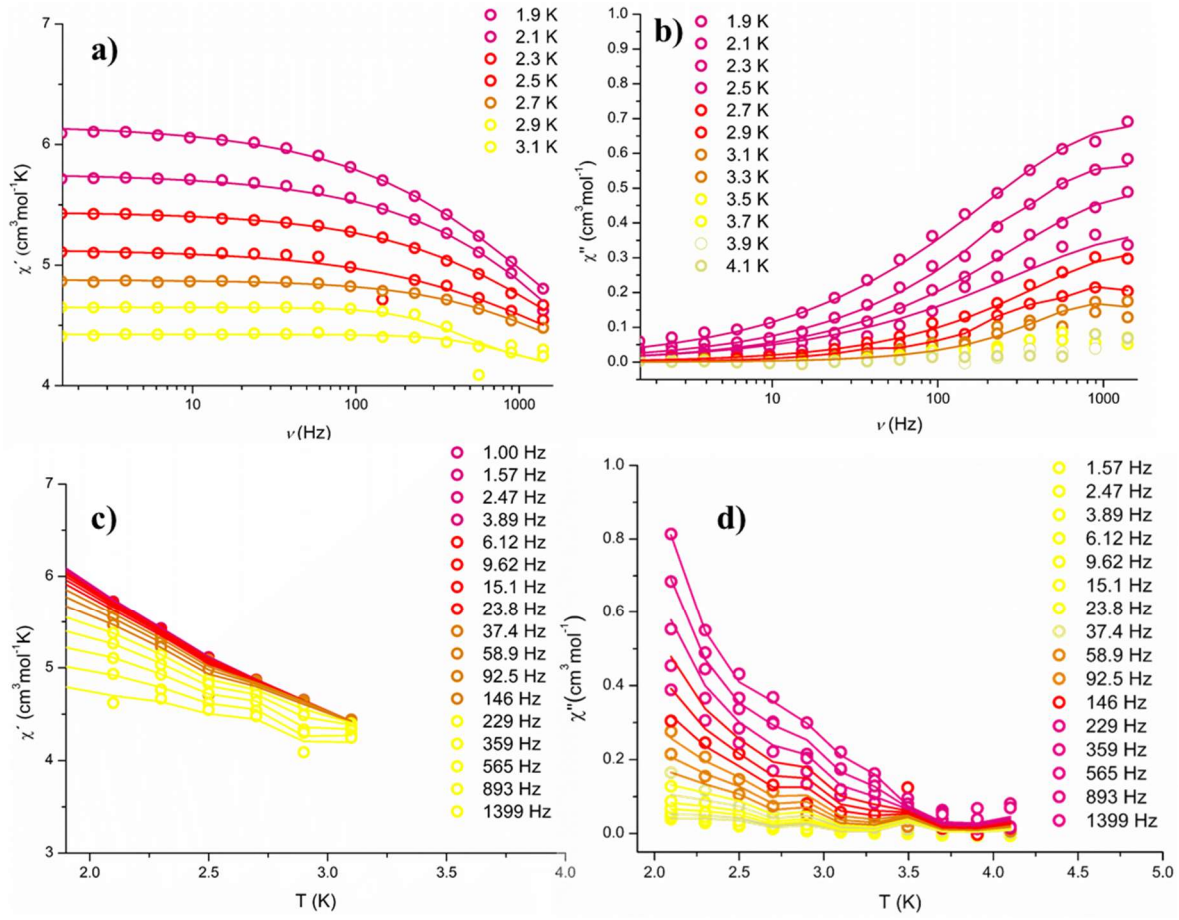

Figure 5.1.24: a) Temperature dependent in-phase susceptibility plot of for compound **6** (1.9 to 3.1 K) at 800 Oe. b) Temperature dependent out-of-phase susceptibility plot of for compound **6** (1.9 to 4.1 K) at 800 Oe. c) Frequency dependent in-phase susceptibility plot of for compound **6** (1.9 to 3.1 K) 800 Oe. d) Frequency dependent out-of-phase susceptibility plot of for compound **6** (1.9 to 4. 1 K) at 800 Oe. Solid lines represent fit of the data.

The SMM behavior of complex **6** is visible at very low temperatures (1.9 – 3.1 K) and unfortunately attempts to fit the data trying to evaluate and derive an estimation of the U_{eff} value of the complex were not feasible. That can be further supported by taking a look at the Cole-Cole plots depicted in Figure 5.1.25. The data of the diagram are very close to zero, not allowing us to proceed with a reliable attempt for constructing a ln(τ) vs 1/T plot.

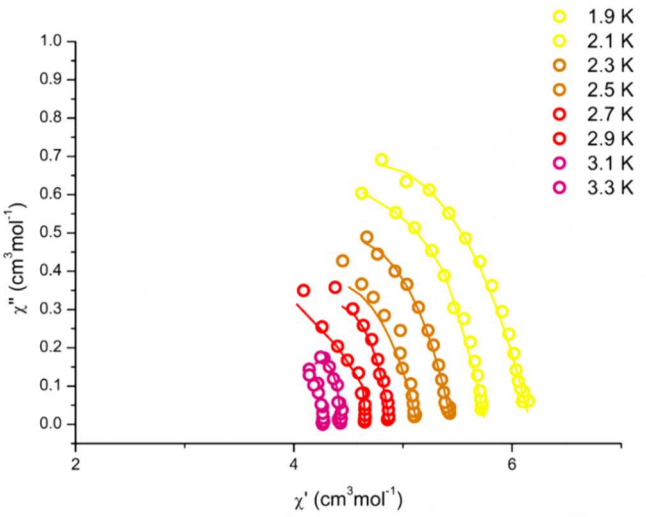

Figure 5.1.25: Cole-Cole diagram constructed for complex **6**. Solid lines represent fit of the data.

Even if compound **6** does not show the most exciting single-molecule magnet behavior in terms of giving us a chance to investigate this phenomena deeper, still the complex belongs to the SMM family. The most important and unique feature of complex **6** though, is its structural characteristics. This is the first time that a compound possesses this double-fused 12-MC-4 crown motif, which has an edge-sharing face containing two Fe(III) centers.

Trying to make an implication towards literature findings, it is quite interesting to make a correlation of this complex with the well-known and extensively studied Dysprosium dimers reported over the years.[28–30] The aforementioned complex can be potentially seen as an quasi-dimer compound meaning that future work can possibly include the isolation of a pure dimeric analogue of the complex, moving away from the strictly described MC motif. This could lead to the isolation of compounds with potentially improved and enhanced SMM properties since, up to now, it has been observed that the Dy dimeric motif leads to improved SMM performance due to the Dy-Dy interactions which lead to suppression of QTM.[31] Even though no indication of such interactions is present in the complex described above, it might be of interest to keep this possibility open for future investigations.

5.2 Conclusions and Perspectives

In Chapter 5, the synthesis, structural and magnetic characterization of five Ga^{III}/Ln^{III} compounds **1**, **2**, **3**, **4**, **5**, and one Fe^{III}/Ln^{III} **6** have been reported. Complexes **1** and **2** with the formula of $[Ga^{III}_8Ln^{III}_2Na^{I}_2(O_2CCMe_3)_8(shi)_8(MeOH)_4]\bullet 3H_2O$ (Ln = Dy (**1**), Tb (**2**)) possess the same core $\{Ga^{III}_8Ln^{III}_2Na^{I}_2(\mu\text{-}OR)_8(\mu\text{-}NO)_8\}^{16+}$ and for that reason only complex **1** (Dy-analogue) was extensively discussed. Complex **1** was found to be an SMM, while compound **2** (Tb-analogue) unfortunately showed no frequency dependent ac signals. The fact that only the Dy(III)-analogue (and not Tb(III)) showed SMM properties most likely means that the ligand field induced on the Tb(III) ion in combination with its electronic perfect oblate form was not enough to stabilize a high multiplicity m_J value which would create an appreciable energy U_{eff} barrier that could detected. The structural motif of compounds **1** and **2**, nevertheless, is of great significance since it is the first time that this scaffold is observed and reported, within metallacrown molecules. Complex $(^tBuNClO_4)[Ga^{III}_4Dy^{III}(O_2CCMe_3)_4(shi)_4]$ **(3)** possesses a pure 12-MC-4 motif and its structure was extensively studied and presented. Unfortunately, compound **3** does not behave as an SMM at the temperatures reached by our SQUID magnetometer. Considering that the central lanthanide has only a slightly distorted square antiprismatic geometry and that the diamagnetic periphery metal ions could potentially assist the SMM behaviour, not observing frequency dependant ac signals was not what we were expecting. However, a possible explanation could be that most likely a small multiplicity m_J state has been stabilized as a ground state, being very close in energy with the first excited state thus, either permitting very fast relaxation of magnetization from the ground state or from the first excited state. Still these are obviously very fast processes which occur at very low temperatures that we cannot detect. Compound $[Ga^{III}_4Dy^{III}(NO_3)(shiH_2)_2(shi)_4(MeOH)(H_2O)_2]$ **(4)** has a unique bend 12-MC-4 structural motif and this is the first time that such structural features are observed in the class of metallacrowns. The core of the complex is $\{Ga^{III}_4Dy^{III}(\mu\text{-}NO)_6\}^{9+}$, with the Dy(III) atom being 1.914(1) Å above the plane that is formed by the four Ga(III) ions. Compound **4**, in contrast to complex **3**, does behave as an SMM. Most likely, the SMM behavior of compound **4** is attributed to the 9-coordination mode of the central lanthanide, while surrounded by four Ga(III) which form the bent 12-MC-4 scaffold. Efforts towards isolating other members of anisotropic lanthanides have been performed and for some,

results are still being expected. Compound **5** with the structural formula of $(^{t}Bu_4N)[Ga^{III}_8Ho^{III}(OH)_4(shi)_8]\bullet 3MeOH\bullet 5H_2O$, is isostructural with the Dy(III)-complex described in Chapter 4, which has been submitted for publication. The structural characteristics of the complex have been analyzed, while it has been observed that no SMM behavior is present for our compound at the temperatures investigated by our SQUID. The reason of obtaining that complex was based on a methodical rational. We wanted to check how the electronic shape of the central lanthanide ion would affect the magnetic properties of the complex. As it has been already shown the Dy-analogue, discussed in Chapter 4, exhibits single-molecule magnet behavior unlike complex **5**. The reason for that is probably that the Dy(III) ion has an oblate electronic shape while Ho(III) possess a slightly distorted oblate shape leaning towards the prolate electronic form. That confirms the theory which was firstly discussed by Rinehart and Long[18], that the electronic shape of the central lanthanide in combination with the electronic charges provided by the ligand, play a crucial role to the final magnetic behavior of the molecules. The Tb-analogue has not been obtained yet, but this is the next synthetic step since according to this trend, a perfect oblate-shaped molecule (in this system) will most likely give the best SMM performance. Finally, an Fe/Dy/shi^{3-} complex (**6**) was synthesized and structurally and magnetically analyzed. The goal was to try and obtain the isostructural compounds of Ga(III) with Fe(III) instead since iron has quite similar coordination behavior with gallium as it was discussed in the text. The complex obtained, however, possesses a $\{Fe_6Dy_2(shiH_2)_4(shiH)_2(shi)_6(MeOH)_4\}\bullet 2MeOH\bullet 12H_2O$ formula and upon running alternating-current magnetic susceptibility studies, we were able to observe the presence of frequency-dependent ac signals. The structural advances of that complex have been described thoroughly and its magnetic behavior has been monitored and presented. Unfortunately, an estimation of the U_{eff} values was not deemed possible but attempts for the isolation of other analogues of the complex (such as Gd, Tb, etc) are in progress.

It is quite clear that synthesis of molecular complexes is not an easy task and the isolation and crystallization of them can be quite challenging. This is the main reason that some analogues from the family of complexes discussed, have not been yet isolated. The main focus of that project from now onwards would have to be the isolation and magnetic characterization of the isostructural compounds that are still needed, while at the same time a new path could be also followed. The isolation of the Mn-based double-decker or sandwich complex would be a great asset for further studying and deeper understanding of the SMM phenomena. In such a way, the

difference on the magnetic studies compared to the diamagnetic Ga(III) double decker could be monitored. Mn(III) ions, with a d^4 electron configuration, are highly paramagnetic and anisotropic metal ions. Surely, their use would bring a vast change on the magnetic properties compared to the Ga(III) analogue. Finally, the complexes that have been isolated with Ga(III) ions could be potentially also isolated by Al(III) ions, which is a above gallium at the periodic table and in such way the effect of spin-orbit coupling (SOC) could be analyzed, monitored and investigated.[32]

5.3 Supporting Information

Materials and Methods

General Information

All chemicals and solvents used for synthesis were of reagent grade and used as purchased without further purification. All manipulations were performed under aerobic conditions using chemicals and solvents as received. C, H and N elemental analyses were performed on a Foss Heraeus Vario EL at the Institute of Organic Chemistry at the Johannes Gutenberg University Mainz. Infrared absorption spectra were recorded at room temperature in a range of 3,000-400 cm^{-1} on a Thermo Fischer NICOLET Nexus FT/IR-5700 spectrometer equipped with Smart Orbit ATR Diamond cell. Variable-temperature direct current (dc) magnetic susceptibility measurements were accomplished on polycrystalline samples with the use of Quantum Design SQUID magnetometer MPMS-7 equipped with a 7 T magnet. The samples were embedded in eicosane to avoid orientation of the crystallites under applied field. Pascal´s constants were used to correct the experimental susceptibility data for the underlying diamagnetism.[11] The temperature dependent magnetic contribution of the holder and of the embedding matrix eicosane were experimentally determined and substracted from the measured susceptibility data. Variable temperature susceptibility data were obtained in a temperature range of 2-300K under an applied field of 0.1 Tesla. Magnetization data were collected between 2 and 10 K and using magnetic fields up to 7 Tesla. Alternating-current (ac) measurements were performed with an oscillating magnetic field of 3 Oe at frequencies spanning from 1 to 1400 Hz.

Synthesis of reported compounds 1 - 6:

[$Ga^{III}_8Dy^{III}_2Na^{I}_2(O_2CCMe_3)_8(shi)_8(MeOH)_4$]•$3H_2O$ (1)•$3H_2O$: To a stirred almost colorless solution of $shiH_3$ (61.00 mg, 0.4 mmol) and $Ga(NO_3)_3H_2O$ (109.00 mg, 0.4 mmol) in MeOH, $Dy_2(piv)_6(Hpiv)_6$ (154.00 mg, 0.1 mmol) and $^tBuNClO_4$ (52.00 mg, 0.15 mmol) was added and left stirring for 60 min. To the resulting clear and colorless solution NaOEt (27.00 mg, 0.4 mmol) was added was stirred for further 30 min. Then, the solution was filtered and the filtrate was left for slow evaporation. After 10 days, diffraction quality crystals of **1** were obtained, collected by filtration, washed with hexanes (3 × 5 mL) and dried in air. Yield: 0.0325 g (32.5%) based on the Dy^{III} ion. The air-dried solid was analyzed as **(1) ($Ga_8Dy_2Na_2H_{120}C_{100}O_{46}N_8$):** C, 38.76; H, 3.90; N, 3.61. Found: C, 38.77; H, 3.86; N, 3.65. Selected ATR data (cm^{-1}): 1605 (w), 1574 (s), 1530 (w), 1441 (w), 1406 (s), 1248 (w), 1065 (w), 953 (w), 789 (w), 697 (s), 587 (w), 545 (w).

[$Ga^{III}_8Tb^{III}_2Na^{I}_2(O_2CCMe_3)_8(shi)_8(MeOH)_4$]•$2H_2O$ (2) •$2H_2O$: To a stirred almost colorless solution of $shiH_3$ (61.00 mg, 0.4 mmol) and $Ga(NO_3)_3H_2O$ (109.00 mg, 0.4 mmol) in MeOH, $Tb_2(piv)_6(Hpiv)_6$ (157.00 mg, 0.1 mmol) and $^tBuNClO_4$ (52.00 mg, 0.15 mmol) was added and left stirring for 60 min. To the resulting clear and colorless solution NaOEt (27.00 mg, 0.4 mmol) was added and was stirred for further 30 min. Then, the solution was filtered and the filtrate was left for slow evaporation. After 12 days, diffraction quality crystals of **2** were obtained, collected by filtration, washed with hexanes (3 × 5 mL) and dried in air. Yield: 0.0335 g (33.5%) based on the Dy^{III} ion. The air-dried solid was analyzed as **(2) ($Ga_8Tb_2Na_2H_{124}C_{100}O_{46}N_8$):** C, 38.57; H, 4.08; N, 3.60. Found: C, 38.58; H, 4.15; N, 3.65. Selected ATR data (cm^{-1}): 1603 (w), 1574 (s), 1529 (w), 1441 (w), 1406 (s), 1248 (w), 1065 (w), 952 (w), 789 (w), 697 (s), 583 (w), 545 (w).

(^{t}BuNClO$_4$)[Ga$^{III}_4$Dy^{III}(O$_2$CCMe$_3$)$_4$(shi)$_4$] •6H$_2$O (3): To a stirred almost colorless solution of shiH$_3$ (61.00 mg, 0.4 mmol) and Ga(NO$_3$)$_3$H$_2$O (109.00 mg, 0.4 mmol) in MeOH, Dy$_2$(piv)$_6$(Hpiv)$_6$ (154.00 mg, 0.1 mmol) and ^{t}BuNClO$_4$ (52.00 mg, 0.15 mmol) was added and left stirring for 60 min. To the resulting clear and colorless solution morpholine (36.00 μL, 0.4 mmol) was added and was stirred for further 30 min. Then, the solution was filtered and the filtrate was left for slow evaporation. After 7 days, diffraction quality crystals of **3** were obtained, collected by filtration, washed with hexanes (3 × 5 mL) and dried in air. Yield: 0.066 g (66%) based on the Dy^{III} ion. The air-dried solid was analyzed as **(2)•6H$_2$O (Ga$_4$DyH$_{91.5}$C$_{70}$O$_{27}$N$_5$):** C, 44.80; H, 4.91; N, 3.73. Found: C, 44.76; H, 4.82; N, 3.80. Selected ATR data (cm^{-1}): 2691 (w) 1606 (w), 1570(w), 1454 (w), 1417 (w), 1322 (b), 1289 (s), 1097 (w), 907 (w), 883 (w), 592 (w), 540 (w), 511 (w).

[Ga$^{III}_4$Dy^{III}(NO$_3$)(shiH$_2$)$_2$(shi)$_4$(MeOH)(H$_2$O)$_2$]•2MeOH•5H$_2$O (4): To a stirred almost colorless solution of shiH$_3$ (61.00 mg, 0.4 mmol) and Ga(NO$_3$)$_3$H$_2$O (109.00 mg, 0.4 mmol) in MeOH, Dy(O$_2$CCH$_3$)$_3$•4H$_2$O (41.00 mg, 0.1 mmol) and ^{t}BuNClO$_4$ (52.00 mg, 0.15 mmol) was added and left stirring for 60 min. To the resulting clear and colorless solution morpholine (36.00 μL, 0.4 mmol) was added and was stirred for further 30 min. Then, the solution was filtered and the filtrate was layered in Et$_2$O/hexane (2 × 5 mL). After 15 days, diffraction quality crystals of **4** were obtained, collected by filtration, washed with hexanes (3 × 5 mL) and dried in air. Yield: 0. 489 g (49%) based on the Dy^{III} ion. The air-dried solid was analyzed as **(4)• 2MeOH•5H$_2$O (C$_{47}$H$_{20}$DyGa$_4$N$_7$O$_{32}$):** C, 34.81; H, 1.70; N, 5.92. Found: C, 34.92; H, 1.76; N, 5.84. Selected ATR data (cm^{-1}): 1602 (w), 1578 (w), 1510 (w), 1448 (w), 1315 (w), 1232 (w), 1044 (s), 949 (s), 855 (w), 762 (w), 652 (b), 573 (w).

(^{t}Bu$_4$N)[Ga$^{III}_8$Ho^{III}(OH)$_4$(shi)$_8$]•3MeOH•5H$_2$O (5): To a stirred almost colorless solution of shiH$_3$ (61.00 mg, 0.4 mmol) and Ga(NO$_3$)$_3$H$_2$O (109.00 mg, 0.4 mmol) in MeOH, Ho(CO$_3$)$_3$•H$_2$O (53.00 mg, 0.1 mmol) and ^{t}BuNClO$_4$ (52.00 mg, 0.15 mmol) was added (light pink suspension) and left stirring for 60 min. To the resulting clear and colorless solution morpholine (36.00 μL, 0.4 mmol) was added and was stirred for further 30 min. Then, the solution was filtered and the filtrate was left for slow evaporation. After 15 days, diffraction quality crystals of **5** were obtained, collected by filtration, washed with hexanes (3 × 5 mL) and dried in air. Yield: 0. 478 g (48%) based on the Ho^{III} ion. The air-dried solid was analyzed as **(5)•5H$_2$O (C$_{47}$H$_{20}$HoGa$_8$N$_7$O$_{32}$):** C, 35.55; H, 3.90; N, 5.18. Found: C, 35.46; H, 3.81; N, 5.24. Selected ATR data (cm^{-1}): 1602 (w), 1574 (w), 1507 (w), 1443 (w), 1315 (w), 1245 (w), 1035 (s), 942 (s), 863 (w), 750 (w), 682 (b), 576 (w).

{Fe$_6$Dy$_2$(shiH$_2$)$_4$(shiH)$_2$(shi)$_6$(MeOH)$_4$}•2MeOH•12H$_2$O (6): To a stirred almost colorless solution of shiH$_3$ (61.00 mg, 0.4 mmol) in MeOH, piperidine (40.00 μL, 0.4 mmol) was added and left for stirring. Afterwards, Fe(ClO$_4$)$_3$•H$_2$O (79.00 mg, 0.4 mmol) was inserted and the solution turned dark red. Upon addition of Dy(NO$_3$)$_3$•H$_2$O (18.00 mg, 0.05 mmol) and ^{t}BuNClO$_4$ (52.00 mg, 0.15 mmol) the solution remained clear and dark red and left stirring for 40 min. Then, the solution was filtered and the filtrate was layered with Et$_2$O/hexane. After 3 days, diffraction quality crystals of **6** were obtained, collected by filtration, washed with hexanes (3 × 5 mL) and dried in air. Yield: 0. 458 g (46%) based on the Dy^{III} ion. The air-dried solid was analyzed as **(6)•2MeOH•12H$_2$O (C$_{97}$H$_{99}$Dy$_2$Fe$_6$N$_{12}$O$_{61}$):** C, 37.99; H, 3.18; N, 5.48. Found: C, 37.92; H, 3.22; N, 5.49. Selected ATR data (cm^{-1}): 1594 (w), 1563 (w), 1487 (s), 1378 (w), 1306 (w), 1243 (w), 1097 (s), 922 (s), 853 (w), 749 (w), 666 (w), 608 (w).

Single-crystal X-ray diffraction studies

X-ray diffraction data for the structure analysis were collected from suitable single crystals on a STOE IPDS 2T [12–15] equipped with an Oxford cooling system operating at 296(2) K (**1, 2**), 293(2) K (**3**), 173(2) K (**4**), 100(2) K (**5**) and at 120(**2**) K [13–15]for (**6**). Graphite-monochromated Mo-Kα radiation (λ = 0.71073 Å) from long-fine focus sealed X-ray tube was used throughout. Data indexing, reduction, integration and absorption correction were done with STOE X-AREA and STOE X-RED[12]. Structures were solved with SHELXT[13] and refined by full-matrix least-squares on F-squared using SHELXL[14], interfaced through OLEX2[15]. All non-hydrogen atoms were refined with anisotropic displacement parameters, while hydrogen atoms belonging to the main core have been placed on idealized position using a riding model. The hydrogen atoms of the doubly deprotonated ligands were placed according to charge balance considerations and geometrical reasons. For the solvent water molecules the hydrogen atoms were placed geometrical. For the solvent water molecules the hydrogen atoms cannot be located satisfactorily and were omitted. Although some water molecules can be located, still large solvent accessible voids are present in the structures. The highly disordered solvent molecules in these voids were squeezed with the routine SQUEEZE[16–18] implemented in Platon[17].

Table S1 Crystallographic data for complexes **1-2**.

Complex	**1**	**2**
Empirical formula	$C_{100}H_{120}Dy_2Ga_8N_8Na_2O_{46}$	$C_{100}H_{124}Ga_8N_8Na_2O_{46}Tb_2$
Formula weight	3098.77	3095.74
Temperature/K	296.15	296(2)
Crystal system	triclinic	monoclinic
Space group	$P\bar{1}$	$P2_1/n$
a/Å	12.6090(10)	14.661(7)
b/Å	14.4374(13)	25.102(12)
c/Å	18.0035(17)	16.005(8)
α/°	102.134(3)	90
β/°	106.916(3)	98.027(6)
γ/°	92.134(2)	90
Volume/Å^3	3048.5(5)	5833(5)
Z	1	2
ρ_{calc}g/cm^3	1.688	1.7626
μ/mm^{-1}	3.041	3.111
F(000)	1546.0	3101.2
Crystal size/mm^3	0.2 × 0.14 × 0.07	0.2 × 0.12 × 0.06
Radiation	MoK\α (λ = 0.71073)	MoK\α (λ = 0.71073)
2Θ range for data collection/°	2.902 to 55.906	3.04 to 56.06
Index ranges	-16 ≤ h ≤ 15 -19 ≤ k ≤ 19 -23 ≤ l ≤ 22	-19 ≤ h ≤ 19 -33 ≤ k ≤ 32 -21 ≤ l ≤ 13
Reflections collected	29003	37030
Independent reflections	R_{int} = 0.0741 R_{sigma} = 0.1539	R_{int} = 0.3510 R_{sigma} = 0.5754
Data/restraints/ parameters	14624 / 30/ 798	14021/ 6/ 361
Goodness-of-fit on F^2	0.929	0.724
Final R^{a,b} indexes [I>=2σ (I)]	R_1 = 0.0557 wR_2 = 0.1186	R_1 = 0.0783 wR_2 = 0.1501
Final R^{a,b} indexes [all data]	R_1 = 0.1104 wR_2 = 0.1330	R_1 = 0.3050 wR_2 = 0.2475
Largest diff. peak /hole / e Å^{-3}	1.10/ -1.16	5.68/ -4.91

$^a R_1 = \Sigma(||F_o| - |F_c||)/\Sigma|F_o|$. $^b wR_2 = [\Sigma[w(F_o^2 - F_c^2)^2]/\Sigma[w(F_o^2)^2]]^{1/2}$, $w = 1/[\sigma^2(F_o^2) + (ap)^2 + bp]$, where $p = [\max(F_o^2, 0) + 2F_c^2]/3$.

Table S2 Selected Bond Lengths for complexes **1-2.**

Atom	Atom	Length/Å
Dy1	O3	2.328(5)
Dy1	O6	2.312(5)
Dy1	O9	2.325(5)
Dy1	O12	2.358(5)
Dy1	O13	2.356(5)
Dy1	O15	2.335(5)
Dy1	O17	2.316(6)
Dy1	N19	2.346(6)
Ga1	O2	1.927(6)
Ga1	O3	1.946(5)
Ga1	O10	1.838(6)
Ga1	O14	1.890(5)
Ga1	N4	1.962(6)
Ga2	O1	1.849(6)
Ga2	O5	1.912(6)
Ga2	O6	1.951(5)
Ga2	O16	1.882(5)
Ga2	N1	1.948(7)
Ga3	O4	1.817(6)
Ga3	O8	1.962(5)
Ga3	O9	1.931(5)
Ga3	O18	1.872(6)
Ga3	N2	1.933(6)
Ga4	O7	1.842(5)
Ga4	O11	1.987(6)
Ga4	O12	1.939(5)
Ga4	O20	1.879(5)
Ga4	N3	1.935(6)
Na1	O4[1]	2.348(6)
Na1	O7	2.378(6)
Na1	O8[1]	2.559(6)
Na1	O11	2.642(6)
Na1	O21	2.326(7)
Na1	O23	2.209(12)
O3	N1	1.419(7)
O6	N2	1.437(7)

O9	N3	1.425(7)
O12	N4	1.410(7)
Tb1	O10	2.348(12)
Tb1	O18[1]	2.328(13)
Tb1	O14	2.375(12)
Tb1	O19[1]	2.364(12)
Tb1	O1[1]	2.386(13)
Tb1	O3[1]	2.345(12)
Tb1	O12	2.352(14)
Tb1	O9	2.341(12)
Ga1	O1	1.912(12)
Ga1	O2	1.834(12)
Ga1	O21[1]	1.884(14)
Ga1	O20	1.857(14)
Ga1	N1	1.967(15)
Ga2	O3	1.936(13)
Ga2	O4	1.908(12)
Ga2	O17	1.892(13)
Ga2	N2	2.951(13)
Ga2	O5	2.830(13)
Ga3	O10	1.904(11)
Ga3	O13	1.885(13)
Ga3	O6	1.963(13)
Ga3	O7	1.869(12)
Ga3	N3	1.981(16)
Ga4	O11	1.865(13)
Ga4	O9	1.962(13)
Ga4	O15	1.856(14)
Ga4	O8	1.916(12)
Ga4	N4	1.961(14)
Na1	O4	2.620(15)
Na1	O6	2.521(13)
Na1	O23	2.351(14)
Na1	O7	2.491(15)
Na1	O5	2.508(13)
Na1	O16	2.325(16)

[1]-X,1-Y,1-Z

Table S3 Selected Bond Angles for **1-2**.

Atom	Atom	Atom	Angle/°
$O^{(3)}$	$Dy^{(1)}$	$O^{(12)}$	68.22(18)
$O^{(3)}$	$Dy^{(1)}$	$O^{(13)}$	72.88(18)
$O^{(3)}$	$Dy^{(1)}$	$O^{(15)}$	80.57(19)
$O^{(3)}$	$Dy^{(1)}$	$O^{(19)}$	134.4(2)
$O^{(6)}$	$Dy^{(1)}$	$O^{(3)}$	68.74(18)
$O^{(6)}$	$Dy^{(1)}$	$O^{(9)}$	69.16(18)
$O^{(6)}$	$Dy^{(1)}$	$O^{(12)}$	101.85(17)
$O^{(6)}$	$Dy^{(1)}$	$O^{(13)}$	136.43(19)
$O^{(6)}$	$Dy^{(1)}$	$O^{(15)}$	76.37(18)
$O^{(6)}$	$Dy^{(1)}$	$O^{(17)}$	82.59(19)
$O^{(6)}$	$Dy^{(1)}$	$O^{(19)}$	147.35(19)
$O^{(9)}$	$Dy^{(1)}$	$O^{(3)}$	109.13(18)
$O^{(9)}$	$Dy^{(1)}$	$O^{(12)}$	68.15(18)
$O^{(9)}$	$Dy^{(1)}$	$O^{(13)}$	145.46(19)
$O^{(9)}$	$Dy^{(1)}$	$O^{(15)}$	136.71(19)
$O^{(9)}$	$Dy^{(1)}$	$O^{(19)}$	79.97(19)
$O^{(13)}$	$Dy^{(1)}$	$O^{(12)}$	81.86(17)
$O^{(15)}$	$Dy^{(1)}$	$O^{(12)}$	146.61(19)
$O^{(15)}$	$Dy^{(1)}$	$O^{(13)}$	77.78(18)
$O^{(15)}$	$Dy^{(1)}$	$O^{(19)}$	123.93(18)
$O^{(17)}$	$Dy^{(1)}$	$O^{(3)}$	146.94(19)
$O^{(17)}$	$Dy^{(1)}$	$O^{(9)}$	73.52(18)
$O^{(17)}$	$Dy^{(1)}$	$O^{(12)}$	136.44(18)
$O^{(17)}$	$Dy^{(1)}$	$O^{(13)}$	124.25(18)
$O^{(17)}$	$Dy^{(1)}$	$O^{(15)}$	76.85(19)
$O^{(17)}$	$Dy^{(1)}$	$O^{(19)}$	78.6(2)
$O^{(19)}$	$Dy^{(1)}$	$O^{(12)}$	75.14(18)
$O^{(19)}$	$Dy^{(1)}$	$O^{(13)}$	75.97(19)
$O^{(2)}$	$Ga^{(1)}$	$O^{(3)}$	80.5(2)
$O^{(2)}$	$Ga^{(1)}$	$N^{(4)}$	140.2(2)
$O^{(3)}$	$Ga^{(1)}$	$N^{(4)}$	87.0(2)
$O^{(10)}$	$Ga^{(1)}$	$O^{(2)}$	89.5(2)
$O^{(10)}$	$Ga^{(1)}$	$O^{(3)}$	160.6(2)
$O^{(10)}$	$Ga^{(1)}$	$O^{(14)}$	101.8(2)
$O^{(10)}$	$Ga^{(1)}$	$N^{(4)}$	90.4(2)
$O^{(14)}$	$Ga^{(1)}$	$O^{(2)}$	111.1(2)
$O^{(14)}$	$Ga^{(1)}$	$O^{(3)}$	97.3(2)
$O^{(14)}$	$Ga^{(1)}$	$N^{(4)}$	107.8(2)
$O^{(1)}$	$Ga^{(2)}$	$O^{(5)}$	90.0(2)
$O^{(1)}$	$Ga^{(2)}$	$O^{(6)}$	157.3(2)
$O^{(1)}$	$Ga^{(2)}$	$O^{(16)}$	101.9(2)
$O^{(1)}$	$Ga^{(2)}$	$N^{(1)}$	91.1(2)
$O^{(5)}$	$Ga^{(2)}$	$O^{(6)}$	81.2(2)

$O^{(5)}$	$Ga^{(2)}$	$N^{(1)}$	145.3(2)
$O^{(16)}$	$Ga^{(2)}$	$O^{(5)}$	101.7(2)
$O^{(16)}$	$Ga^{(2)}$	$O^{(6)}$	100.3(2)
$O^{(16)}$	$Ga^{(2)}$	$N^{(1)}$	112.0(2)
$N^{(1)}$	$Ga^{(2)}$	$O^{(6)}$	84.6(2)
$O^{(4)}$	$Ga^{(3)}$	$O^{(8)}$	84.8(2)
$O^{(4)}$	$Ga^{(3)}$	$O^{(9)}$	153.8(2)
$O^{(4)}$	$Ga^{(3)}$	$O^{(18)}$	106.4(3)
$O^{(4)}$	$Ga^{(3)}$	$N^{(2)}$	91.3(3)
$O^{(9)}$	$Ga^{(3)}$	$O^{(8)}$	81.5(2)
$O^{(9)}$	$Ga^{(3)}$	$N^{(2)}$	87.5(2)
$O^{(18)}$	$Ga^{(3)}$	$O^{(8)}$	105.1(2)
$O^{(18)}$	$Ga^{(3)}$	$O^{(9)}$	98.7(2)
$O^{(18)}$	$Ga^{(3)}$	$N^{(2)}$	109.0(2)
$N^{(2)}$	$Ga^{(3)}$	$O^{(8)}$	145.4(2)
$O^{(7)}$	$Ga^{(4)}$	$O^{(11)}$	88.3(2)
$O^{(7)}$	$Ga^{(4)}$	$O^{(12)}$	149.8(2)
$O^{(7)}$	$Ga^{(4)}$	$O^{(20)}$	106.5(2)
$O^{(7)}$	$Ga^{(4)}$	$N^{(3)}$	92.0(2)
$O^{(12)}$	$Ga^{(4)}$	$O^{(11)}$	81.1(2)
$O^{(20)}$	$Ga^{(4)}$	$O^{(11)}$	96.3(2)
$O^{(20)}$	$Ga^{(4)}$	$O^{(12)}$	102.8(2)
$O^{(20)}$	$Ga^{(4)}$	$N^{(3)}$	106.5(2)
$N^{(3)}$	$Ga^{(4)}$	$O^{(11)}$	156.1(2)
$N^{(3)}$	$Ga^{(4)}$	$O^{(12)}$	86.9(2)
$Ga^{(4)}$	$Na^{(1)}$	$Ga^{(3)1}$	124.10(9)
$O^{(4)1}$	$Na^{(1)}$	$Ga^{(3)1}$	29.29(14)
$O^{(4)1}$	$Na^{(1)}$	$Ga^{(4)}$	150.07(18)
$O^{(4)1}$	$Na^{(1)}$	$O^{(8)1}$	60.62(19)
$O^{(4)1}$	$Na^{(1)}$	$O^{(11)}$	174.2(2)
$O^{(7)}$	$Na^{(1)}$	$Ga^{(3)1}$	99.12(15)
$O^{(7)}$	$Na^{(1)}$	$Ga^{(4)}$	29.68(13)
$O^{(7)}$	$Na^{(1)}$	$O^{(4)1}$	121.0(2)
$O^{(7)}$	$Na^{(1)}$	$O^{(8)1}$	84.4(2)
$O^{(7)}$	$Na^{(1)}$	$O^{(11)}$	63.97(19)
$O^{(8)1}$	$Na^{(1)}$	$Ga^{(3)1}$	33.11(13)
$O^{(8)1}$	$Na^{(1)}$	$Ga^{(4)}$	99.38(16)
$O^{(8)1}$	$Na^{(1)}$	$O^{(11)}$	118.9(2)
$N^{(1)}$	$O^{(3)}$	$Dy^{(1)}$	125.4(4)
$N^{(1)}$	$O^{(3)}$	$Ga^{(1)}$	113.7(4)
$N^{(4)}$	$O^{(12)}$	$Dy^{(1)}$	120.2(3)
$N^{(4)}$	$O^{(12)}$	$Ga^{(4)}$	113.2(4)
$O^{(3)}$	$N^{(1)}$	$Ga^{(2)}$	118.1(4)

$O^{(18)1}$	$Tb^{(1)}$	$O^{(10)}$	79.7(4)
$O^{(14)}$	$Tb^{(1)}$	$O^{(10)}$	73.0(4)
$O^{(14)}$	$Tb^{(1)}$	$O^{(18)1}$	77.0(4)
$O^{(19)1}$	$Tb^{(1)}$	$O^{(10)}$	144.7(4)
$O^{(19)1}$	$Tb^{(1)}$	$O^{(18)1}$	78.1(4)
$O^{(19)1}$	$Tb^{(1)}$	$O^{(14)}$	127.0(4)
$O^{(1)1}$	$Tb^{(1)}$	$O^{(10)}$	106.4(4)
$O^{(1)1}$	$Tb^{(1)}$	$O^{(18)1}$	138.3(4)
$O^{(1)1}$	$Tb^{(1)}$	$O^{(14)}$	144.7(4)
$O^{(1)1}$	$Tb^{(1)}$	$O^{(19)1}$	74.3(4)
$O^{(3)1}$	$Tb^{(1)}$	$O^{(10)}$	68.7(4)
$O^{(3)1}$	$Tb^{(1)}$	$O^{(18)1}$	77.1(4)
$O^{(3)1}$	$Tb^{(1)}$	$O^{(14)}$	136.8(4)
$O^{(3)1}$	$Tb^{(1)}$	$O^{(19)1}$	79.7(4)
$O^{(3)1}$	$Tb^{(1)}$	$O^{(1)1}$	67.7(4)
$O^{(12)}$	$Tb^{(1)}$	$O^{(10)}$	137.5(4)
$O^{(12)}$	$Tb^{(1)}$	$O^{(18)1}$	122.7(5)
$O^{(12)}$	$Tb^{(1)}$	$O^{(14)}$	77.7(4)
$O^{(12)}$	$Tb^{(1)}$	$O^{(19)1}$	77.9(4)
$O^{(12)}$	$Tb^{(1)}$	$O^{(1)1}$	81.1(5)
$O^{(12)}$	$Tb^{(1)}$	$O^{(3)1}$	145.5(4)
$O^{(9)}$	$Tb^{(1)}$	$O^{(10)}$	68.6(4)
$O^{(9)}$	$Tb^{(1)}$	$O^{(18)1}$	144.7(4)
$O^{(9)}$	$Tb^{(1)}$	$O^{(14)}$	79.2(4)
$O^{(9)}$	$Tb^{(1)}$	$O^{(19)1}$	137.2(5)
$O^{(9)}$	$Tb^{(1)}$	$O^{(1)1}$	68.5(4)
$O^{(9)}$	$Tb^{(1)}$	$O^{(3)1}$	104.2(4)
$O^{(9)}$	$Tb^{(1)}$	$O^{(12)}$	76.2(4)
$O^{(4)}$	$Ga^{(2)}$	$O^{(3)}$	80.2(5)
$O^{(17)}$	$Ga^{(2)}$	$O^{(3)}$	102.3(5)
$O^{(17)}$	$Ga^{(2)}$	$O^{(4)}$	102.5(5)
$N^{(2)}$	$Ga^{(2)}$	$O^{(3)}$	86.6(6)
$N^{(2)}$	$Ga^{(2)}$	$O^{(4)}$	150.1(6)
$N^{(2)}$	$Ga^{(2)}$	$O^{(17)}$	106.4(6)
$O^{(5)}$	$Ga^{(2)}$	$O^{(3)}$	153.0(5)
$O^{(5)}$	$Ga^{(2)}$	$O^{(4)}$	87.4(5)
$O^{(5)}$	$Ga^{(2)}$	$O^{(17)}$	103.7(6)
$O^{(5)}$	$Ga^{(2)}$	$N^{(2)}$	92.8(6)
$O^{(9)}$	$Ga^{(4)}$	$O^{(11)}$	98.9(6)
$O^{(15)}$	$Ga^{(4)}$	$O^{(11)}$	101.1(6)
$O^{(15)}$	$Ga^{(4)}$	$O^{(9)}$	159.4(6)
$O^{(8)}$	$Ga^{(4)}$	$O^{(11)}$	104.6(6)
$O^{(8)}$	$Ga^{(4)}$	$O^{(9)}$	79.6(5)
$O^{(8)}$	$Ga^{(4)}$	$O^{(15)}$	90.3(6)
$N^{(4)}$	$Ga^{(4)}$	$O^{(11)}$	111.3(6)
$N^{(4)}$	$Ga^{(4)}$	$O^{(9)}$	86.8(6)
$N^{(4)}$	$Ga^{(4)}$	$O^{(15)}$	90.8(6)

$N^{(4)}$	$Ga^{(4)}$	$O^{(8)}$	143.1(6)
$O^{(13)}$	$Ga^{(3)}$	$O^{(10)}$	100.3(5)
$O^{(6)}$	$Ga^{(3)}$	$O^{(10)}$	80.8(5)
$O^{(6)}$	$Ga^{(3)}$	$O^{(13)}$	103.0(5)
$O^{(7)}$	$Ga^{(3)}$	$O^{(10)}$	154.9(5)
$O^{(7)}$	$Ga^{(3)}$	$O^{(13)}$	103.9(5)
$O^{(7)}$	$Ga^{(3)}$	$O^{(6)}$	87.4(5)
$N^{(3)}$	$Ga^{(3)}$	$O^{(10)}$	87.1(5)
$N^{(3)}$	$Ga^{(3)}$	$O^{(13)}$	107.2(6)
$N^{(3)}$	$Ga^{(3)}$	$O^{(6)}$	149.0(6)
$N^{(3)}$	$Ga^{(3)}$	$O^{(7)}$	92.0(6)
$O^{(2)}$	$Ga^{(1)}$	$O^{(1)}$	159.8(6)
$O^{(21)1}$	$Ga^{(1)}$	$O^{(1)}$	79.4(5)
$O^{(21)1}$	$Ga^{(1)}$	$O^{(2)}$	91.3(6)
$O^{(20)}$	$Ga^{(1)}$	$O^{(1)}$	99.3(5)
$O^{(20)}$	$Ga^{(1)}$	$O^{(2)}$	100.6(5)
$O^{(20)}$	$Ga^{(1)}$	$O^{(21)1}$	106.8(6)
$N^{(1)}$	$Ga^{(1)}$	$O^{(1)}$	87.3(5)
$N^{(1)}$	$Ga^{(1)}$	$O^{(2)}$	90.5(6)
$N^{(1)}$	$Ga^{(1)}$	$O^{(21)1}$	145.4(6)
$N^{(1)}$	$Ga^{(1)}$	$O^{(20)}$	106.8(6)
$O^{(6)}$	$Na^{(1)}$	$O^{(4)}$	117.7(5)
$O^{(23)}$	$Na^{(1)}$	$O^{(4)}$	91.3(5)
$O^{(23)}$	$Na^{(1)}$	$O^{(6)}$	91.1(5)
$O^{(7)}$	$Na^{(1)}$	$O^{(4)}$	171.1(5)
$O^{(7)}$	$Na^{(1)}$	$O^{(6)}$	63.8(4)
$O^{(7)}$	$Na^{(1)}$	$O^{(23)}$	97.5(5)
$O^{(5)}$	$Na^{(1)}$	$O^{(4)}$	60.4(4)
$O^{(5)}$	$Na^{(1)}$	$O^{(6)}$	81.3(4)
$O^{(5)}$	$Na^{(1)}$	$O^{(23)}$	141.3(6)
$O^{(5)}$	$Na^{(1)}$	$O^{(7)}$	112.3(5)
$O^{(16)}$	$Na^{(1)}$	$O^{(4)}$	83.2(5)
$O^{(16)}$	$Na^{(1)}$	$O^{(6)}$	149.1(6)
$O^{(16)}$	$Na^{(1)}$	$O^{(23)}$	112.1(5)
$O^{(16)}$	$Na^{(1)}$	$O^{(7)}$	92.1(5)
$O^{(16)}$	$Na^{(1)}$	$O^{(5)}$	91.5(5)
$N^{(2)1}$	$O^{(10)}$	$Tb^{(1)}$	122.3(9)
$N^{(2)1}$	$O^{(10)}$	$Ga^{(3)}$	114.7(9)
$N^{(4)1}$	$O^{(1)}$	$Ga^{(1)}$	114.3(10)
$N^{(1)}$	$O^{(3)}$	$Tb^{(1)1}$	123.4(10)
$N^{(1)}$	$O^{(3)}$	$Ga^{(2)}$	113.5(9)
$N^{(3)}$	$O^{(9)}$	$Tb^{(1)}$	125.2(10)
$N^{(3)}$	$O^{(9)}$	$Ga^{(4)}$	113.7(10)

[1]1-X,1-Y,1-Z

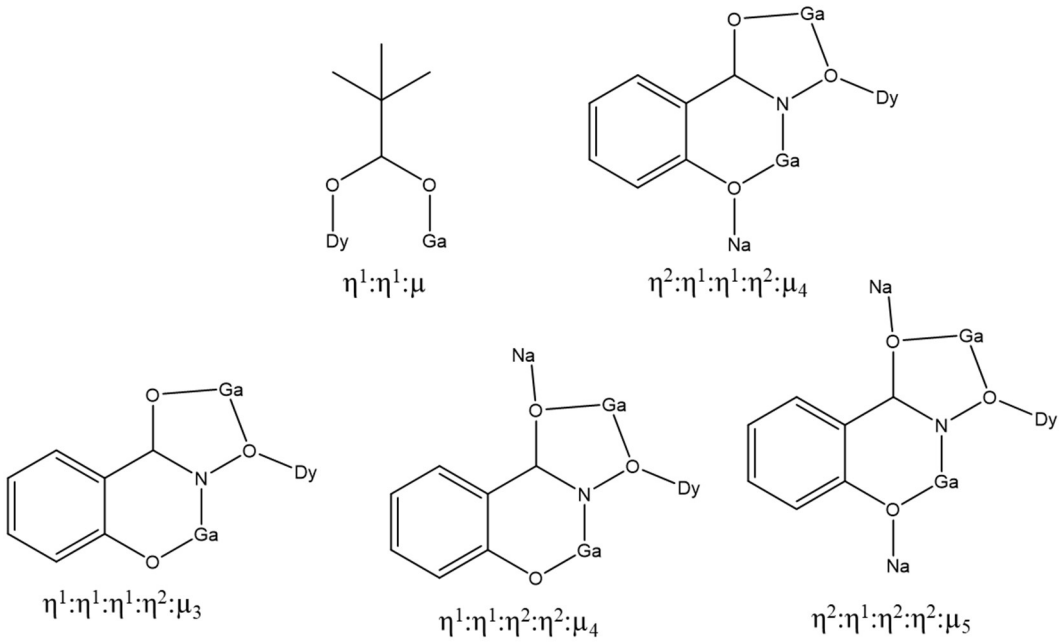

Scheme 1: Schematic representation of coordination modes of the ligands discussed in the text for complex **1**.

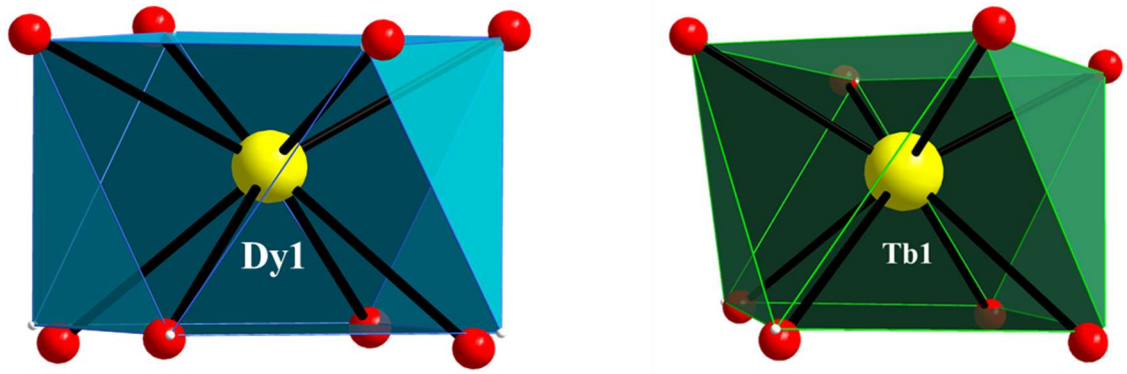

Figure S1: Square antiprismatic geometry of central lanthanide in complex **1** and **2**. The points connected by the lighter lines define the vertices of the ideal polyhedron**.** Color scheme: Ln, yellow; O, red.

Table S4 Shape measurements of the 8-coordinate lanthanide coordination polyhedra. The bold numbers indicate the closest polyhedron according to SHAPE calculations.[3]

Polyhedron[c]	Dy1
OP-8	29.56
HPY-8	23.87
HBPY-8	15.42
CU-8	8.17
SAPR-8	**0.62**
TDD-8	2.10
JGBF-8	15.94
JETBPY-8	29.50
JBTPR-8	2.69
BTPR-8	1.48
JSD-8	5.38
TT-8	8.99
ETBPY-8	24.40

[c] Abbreviations: OP-8, octagon; HPY-8, heptagonal pyramid; HBPY-8, hexagonal bipyramid; CU-8, cube; SAPR-8, square antiprism; TDD-8, triangular dodecahedron; JGBF-8, Johnson gyrobifastigium; JETBPY-8, Johnson elongated triangular bipyramid; JBTPR-8, Johnson biaugmented trigonal prism; BTPR-8, biaugmented trigonal prism; JSD-8, Johnson snub diphenoid; TT-8, triakis tetrahedron; ETBPY-8, elongated trigonal bipyramid.

Table S5 Shape measurements of the 8-coordinate lanthanide coordination polyhedra. The bold numbers indicate the closest polyhedron according to SHAPE calculations.[3]

Polyhedron[c]	Tb1
OP-8	29.12
HPY-8	23.62
HBPY-8	15.96
CU-8	8.75
SAPR-8	**0.51**
TDD-8	2.40
JGBF-8	16.00
JETBPY-8	28.92
JBTPR-8	2.72
BTPR-8	1.63
JSD-8	5.38
TT-8	9.61
ETBPY-8	24.37

[c] Abbreviations: OP-8, octagon; HPY-8, heptagonal pyramid; HBPY-8, hexagonal bipyramid; CU-8, cube; SAPR-8, square antiprism; TDD-8, triangular dodecahedron; JGBF-8, Johnson gyrobifastigium; JETBPY-8, Johnson elongated triangular bipyramid; JBTPR-8, Johnson biaugmented trigonal prism; BTPR-8, biaugmented trigonal prism; JSD-8, Johnson snub diphenoid; TT-8, triakis tetrahedron; ETBPY-8, elongated trigonal bipyramid.

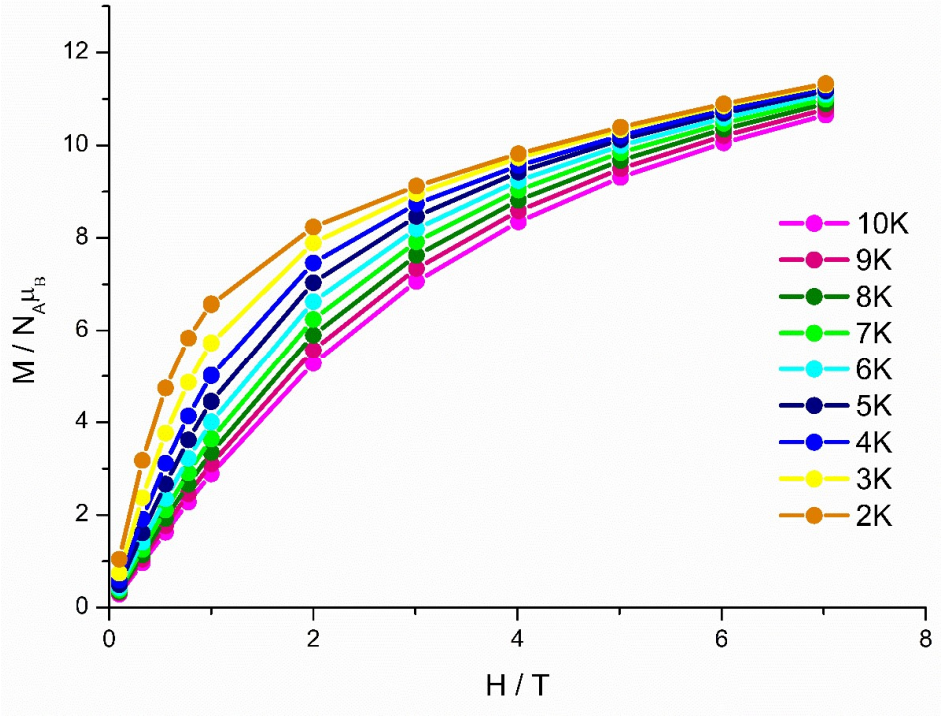

Figure S2: M vs H plots for complex **2** in various temperatures as indicated. Solid lines are guidelines for the eyes.

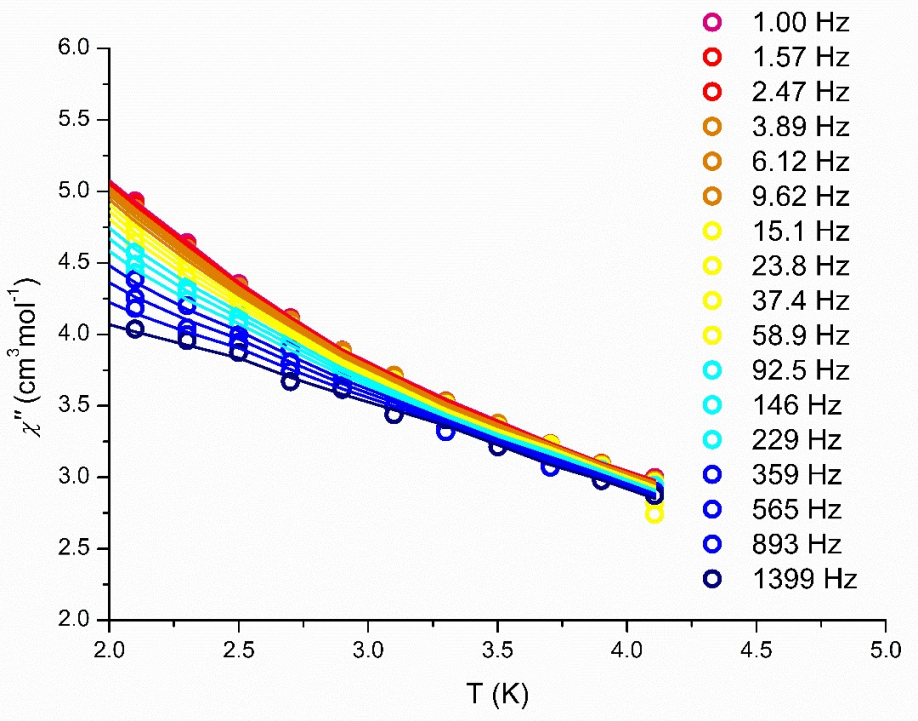

Figure S3: Temperature dependent in-phase susceptibility plot of for compound **1** (1.9 to 4.1 K) at 1600 Oe. Solid lines represent fit of the data.

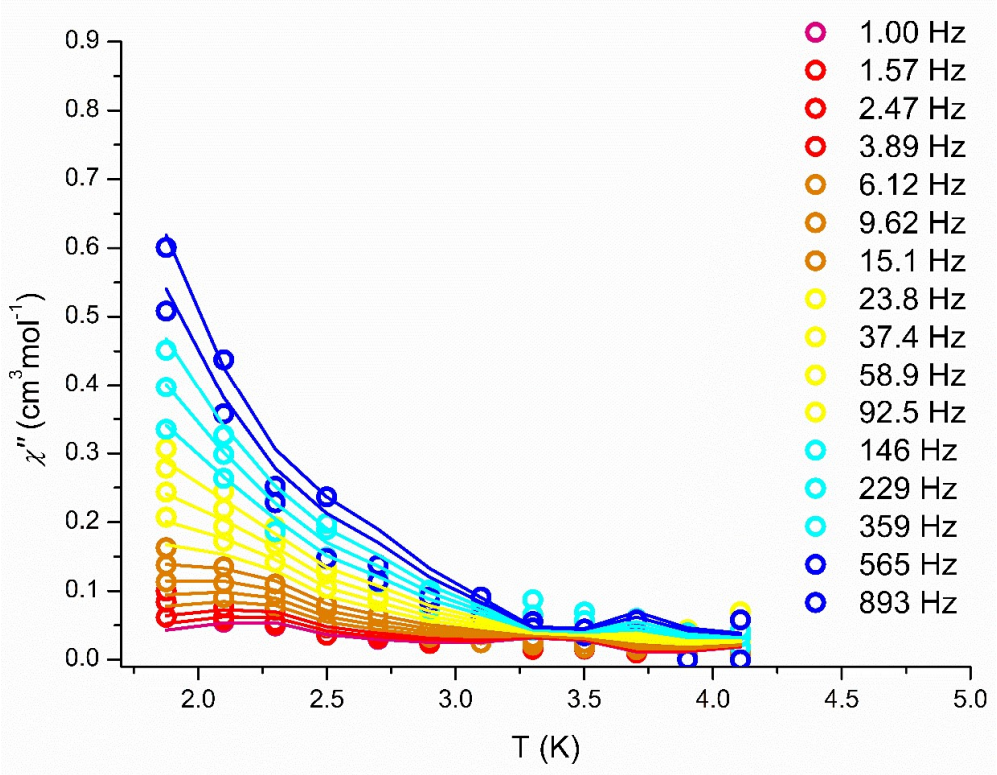

Figure S4: Temperature dependent out-of-phase susceptibility plot of for compound **1** (1.9 to 4.1 K) at 1600 Oe. Solid lines represent fit of the data.

Table S6 Crystallographic data for complex **3**.

Complex	**3**
Empirical formula	$C_{70}H_{110}DyGa_4N_5O_{27}$
Formula weight	1895.00
Temperature/K	293(2)
Crystal system	orthorhombic
Space group	Pnma
a/Å	35.505(7)
b/Å	18.592(4)
c/Å	12.753(3)
α/°	90
β/°	90
γ/°	90
Volume/Å^3	8419(3)
Z	4
ρ_{calc}g/cm^3	1.495
μ/mm^{-1}	2.216
F(000)	3884.0
Crystal size/mm^3	0.75 × 0.43 × 0.14
Radiation	MoK\α (λ = 0.71073)
2Θ range for data collection/°	2.294 to 55.49
Index ranges	-46 ≤ h ≤ 43 -24 ≤ k ≤ 24 -16 ≤ l ≤ 16
Reflections collected	74309
Independent reflections	R_{int} = 0.0694 R_{sigma} = 0.0464
Data/restraints/ parameters	10200 /345 /835
Goodness-of-fit on F^2	1.237
Final R^{a,b} indexes [I>=2σ (I)]	R_1 = 0.0649 wR_2 = 0.1569
Final R^{a,b} indexes [all data]	R_1 = 0.0770 wR_2 = 0.1634
Largest diff. peak /hole / e Å^{-3}	0.85/-2.92

$^a R_1 = \Sigma(||F_o| - |F_c||)/\Sigma|F_o|$. $^b wR_2 = [\Sigma[w(F_o^2 - F_c^2)^2]/\Sigma[w(F_o^2)^2]]^{1/2}$, $w = 1/[\sigma^2(F_o^2) + (ap)^2 + bp]$, where $p = [\max(F_o^2, 0) + 2F_c^2]/3$.

Table S7 Selected Bond Lengths for complex **3**.

$Dy^{(1)}$	$O^{(3)}$	2.352(7)
$Dy^{(1)}$	$O^{(3)1}$	2.352(7)
$Dy^{(1)}$	$O^{(3)1}$	2.352(7)
$Dy^{(1)}$	$O^{(6)}$	2.328(7)
$Dy^{(1)}$	$O^{(6)1}$	2.328(7)
$Dy^{(1)}$	$O^{(8)}$	2.341(8)
$Dy^{(1)}$	$O^{(8)1}$	2.341(8)
$Dy^{(1)}$	$O^{(10)}$	2.332(7)
$Dy^{(1)}$	$O^{(10)1}$	2.332(7)
$Ga^{(2)}$	$O^{(1)}$	1.836(10)
$Ga^{(2)}$	$O^{(5)}$	1.922(10)
$Ga^{(2)}$	$O^{(6)}$	1.942(8)
$Ga^{(2)}$	$O^{(7)}$	1.888(8)
$Ga^{(2)}$	$N^{(1)}$	1.99(2)
$Ga^{(3)}$	$O^{(4)}$	1.852(10)
$Ga^{(3)}$	$O^{(9)1}$	2.305(8)
$Ga^{(3)}$	$O^{(9)}$	1.890(8)
$Ga^{(3)}$	$N^{(2)}$	1.98(3)
$O^{(3)}$	$N^{(1)}$	1.38(3)
$O^{(6)}$	$N^{(2)}$	1.41(4)
$O^{(7)}$	$C^{(15)}$	1.271(15)
$O^{(9)}$	$Ga^{(3)1}$	2.305(8)
$Ga^{(1B)}$	$N^{(1B)}$	2.02(2)
$Ga^{(2B)}$	$O^{(2B)}$	1.920(9)
$Ga^{(2B)}$	$O^{(3B)}$	1.947(8)
$Ga^{(2B)}$	$O^{(4B)}$	1.844(10)
$Ga^{(2B)}$	$O^{(7B)}$	1.896(8)
$Ga^{(2B)}$	$N^{(2B)}$	2.00(3)
$O^{(3B)}$	$N^{(1B)}$	1.40(3)
$O^{(6B)}$	$N^{(2B)}$	1.37(3)
$O^{(9B)}$	$Ga^{(1B)1}$	2.322(9)
$Ga^{(1B)}$	$Ga^{(1B)1}$	1.354(3)
$Ga^{(1B)}$	$O^{(1B)}$	1.860(10)
$Ga^{(1B)}$	$O^{(9B)1}$	2.322(9)
$Ga^{(1B)}$	$O^{(9B)}$	1.872(8)

^{1}+X,1/2-Y,+Z; ^{2}+X,3/2-Y,+Z

Table S8 Selected Bond Angles for **3**.

$O^{(3)1}$	$Dy^{(1)}$	$O^{(3)}$	27.1(4)
$O^{(6)1}$	$Dy^{(1)}$	$O^{(3)}$	88.7(3)
$O^{(6)1}$	$Dy^{(1)}$	$O^{(3)1}$	68.2(3)
$O^{(6)}$	$Dy^{(1)}$	$O^{(3)1}$	88.7(3)
$O^{(6)}$	$Dy^{(1)}$	$O^{(3)}$	68.2(3)
$O^{(6)}$	$Dy^{(1)}$	$O^{(6)1}$	96.1(4)
$O^{(6)}$	$Dy^{(1)}$	$O^{(8)1}$	168.1(3)
$O^{(6)1}$	$Dy^{(1)}$	$O^{(8)1}$	74.3(3)
$O^{(6)}$	$Dy^{(1)}$	$O^{(8)}$	74.3(3)
$O^{(6)1}$	$Dy^{(1)}$	$O^{(8)}$	168.1(3)
$O^{(6)}$	$Dy^{(1)}$	$O^{(10)1}$	109.9(3)
$O^{(6)}$	$Dy^{(1)}$	$O^{(10)}$	83.8(3)
$O^{(6)1}$	$Dy^{(1)}$	$O^{(10)1}$	83.8(3)
$O^{(6)1}$	$Dy^{(1)}$	$O^{(10)}$	109.9(3)
$O^{(8)1}$	$Dy^{(1)}$	$O^{(3)1}$	81.2(3)
$O^{(8)1}$	$Dy^{(1)}$	$O^{(3)}$	103.9(3)
$O^{(8)}$	$Dy^{(1)}$	$O^{(3)}$	81.2(3)
$O^{(8)}$	$Dy^{(1)}$	$O^{(3)1}$	103.9(3)
$O^{(8)}$	$Dy^{(1)}$	$O^{(8)1}$	114.2(4)
$O^{(10)1}$	$Dy^{(1)}$	$O^{(3)}$	172.1(3)
$O^{(10)}$	$Dy^{(1)}$	$O^{(3)1}$	172.1(3)
$O^{(10)}$	$Dy^{(1)}$	$O^{(3)}$	148.2(3)
$O^{(10)1}$	$Dy^{(1)}$	$O^{(3)1}$	148.2(3)
$O^{(10)}$	$Dy^{(1)}$	$O^{(8)1}$	105.9(3)
$O^{(10)1}$	$Dy^{(1)}$	$O^{(8)1}$	76.6(3)
$O^{(10)1}$	$Dy^{(1)}$	$O^{(8)}$	105.9(3)
$O^{(10)}$	$Dy^{(1)}$	$O^{(8)}$	76.6(3)
$O^{(10)1}$	$Dy^{(1)}$	$O^{(10)}$	35.0(4)
$O^{(1)}$	$Ga^{(2)}$	$O^{(5)}$	88.7(5)
$O^{(1)}$	$Ga^{(2)}$	$O^{(6)}$	154.9(5)
$O^{(1)}$	$Ga^{(2)}$	$O^{(7)}$	105.5(5)
$O^{(1)}$	$Ga^{(2)}$	$N^{(1)}$	91.7(9)
$O^{(5)}$	$Ga^{(2)}$	$O^{(6)}$	80.9(3)
$O^{(5)}$	$Ga^{(2)}$	$N^{(1)}$	150.2(8)
$O^{(6)}$	$Ga^{(2)}$	$N^{(1)}$	86.4(8)
$O^{(7)}$	$Ga^{(2)}$	$O^{(5)}$	101.1(4)
$O^{(7)}$	$Ga^{(2)}$	$O^{(6)}$	99.0(3)
$O^{(7)}$	$Ga^{(2)}$	$N^{(1)}$	107.5(8)
$O^{(4)}$	$Ga^{(3)}$	$O^{(9)}$	102.8(5)
$O^{(4)}$	$Ga^{(3)}$	$O^{(9)1}$	120.9(4)
$O^{(4)}$	$Ga^{(3)}$	$N^{(2)}$	90.6(10)
$O^{(9)}$	$Ga^{(3)}$	$O^{(9)1}$	35.8(5)
$O^{(9)}$	$Ga^{(3)}$	$N^{(2)}$	108.7(10)
$N^{(2)}$	$Ga^{(3)}$	$O^{(9)1}$	132.7(10)
$O^{(3)1}$	$O^{(3)}$	$N^{(1)}$	160.3(13)

$O^{(1B)}$	$Ga^{(1B)}$	$O^{(9B)1}$	120.8(4)
$O^{(1B)}$	$Ga^{(1B)}$	$O^{(9B)}$	102.9(4)
$O^{(1B)}$	$Ga^{(1B)}$	$N^{(1B)}$	90.8(9)
$O^{(9B)}$	$Ga^{(1B)}$	$O^{(9B)1}$	36.9(6)
$O^{(9B)}$	$Ga^{(1B)}$	$N^{(1B)}$	112.4(9)
$N^{(1B)}$	$Ga^{(1B)}$	$O^{(9B)1}$	136.3(9)
$O^{(2B)}$	$Ga^{(2B)}$	$O^{(3B)}$	79.5(3)
$O^{(2B)}$	$Ga^{(2B)}$	$N^{(2B)}$	144.4(12)
$O^{(3B)}$	$Ga^{(2B)}$	$N^{(2B)}$	86.5(11)
$O^{(4B)}$	$Ga^{(2B)}$	$O^{(2B)}$	89.4(4)
$O^{(4B)}$	$Ga^{(2B)}$	$O^{(3B)}$	157.3(4)
$O^{(4B)}$	$Ga^{(2B)}$	$O^{(7B)}$	102.4(4)
$O^{(4B)}$	$Ga^{(2B)}$	$N^{(2B)}$	91.3(11)
$O^{(7B)}$	$Ga^{(2B)}$	$O^{(2B)}$	105.8(4)
$O^{(7B)}$	$Ga^{(2B)}$	$O^{(3B)}$	99.7(3)
$O^{(7B)}$	$Ga^{(2B)}$	$N^{(2B)}$	108.7(12)
$O^{(3B)}$	$N^{(1B)}$	$Ga^{(1B)}$	115.8(16)
$O^{(6B)}$	$N^{(2B)}$	$Ga^{(2B)}$	118(2)
$O^{(3)}$	$N^{(1)}$	$Ga^{(2)}$	117.8(18)
$O^{(6)}$	$N^{(2)}$	$Ga^{(3)}$	117.9(19)
$O^{(2)}$	$C^{(7)}$	$N^{(1)}$	120.4(14)
$N^{(1)}$	$O^{(3)}$	$Dy^{(1)}$	123.1(13)
$Ga^{(2)}$	$O^{(6)}$	$Dy^{(1)}$	119.8(4)
$N^{(2)}$	$O^{(6)}$	$Dy^{(1)}$	123.0(14)
$N^{(2)}$	$O^{(6)}$	$Ga^{(2)}$	112.9(13)

[1]+X,1/2-Y,+Z; [2]+X,3/2-Y,+Z

Table S9 Shape measurements of the 8-coordinate lanthanide coordination polyhedra. The bold numbers indicate the closest polyhedron according to SHAPE calculations.[3]

Polyhedron[c]	Dy1
OP-8	30.06
HPY-8	23.51
HBPY-8	15.09
CU-8	7.89
SAPR-8	**0.67**
TDD-8	1.98
JGBF-8	16.07
JETBPY-8	29.45
JBTPR-8	2.99
BTPR-8	1.88
JSD-8	5.13
TT-8	8.70
ETBPY-8	24.53

[c] Abbreviations: OP-8, octagon; HPY-8, heptagonal pyramid; HBPY-8, hexagonal bipyramid; CU-8, cube; SAPR-8, square antiprism; TDD-8, triangular dodecahedron; JGBF-8, Johnson gyrobifastigium; JETBPY-8, Johnson elongated triangular bipyramid; JBTPR-8, Johnson biaugmented trigonal prism; BTPR-8, biaugmented trigonal prism; JSD-8, Johnson snub diphenoid; TT-8, triakis tetrahedron; ETBPY-8, elongated trigonal bipyramid.

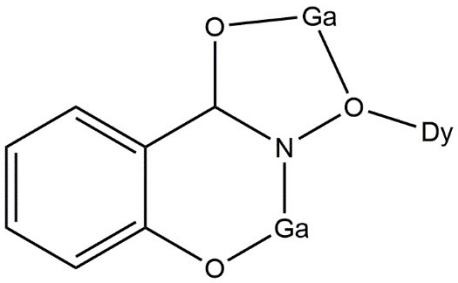

Scheme 2: Coordination mode of complex **3** with the shi^{3-} ligand adopting a η^1: η^1: η^1: η^2:μ_3 coordination mode.

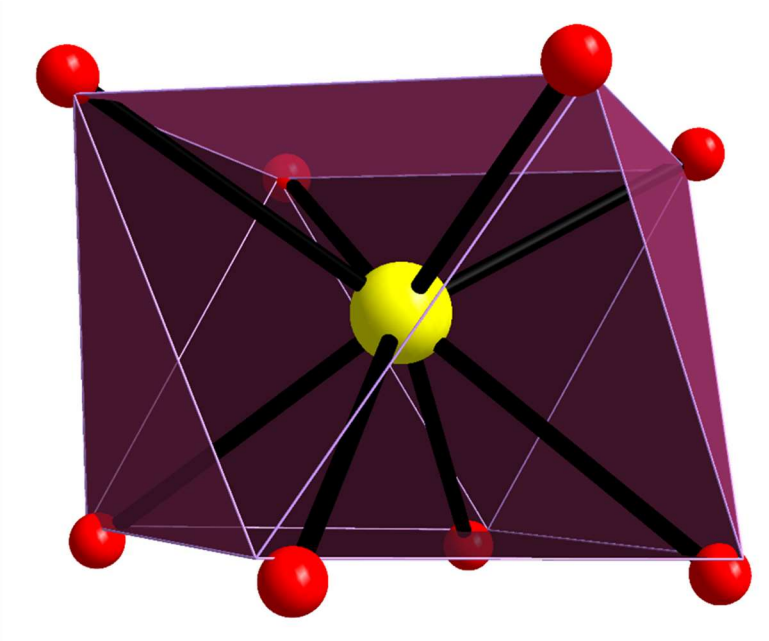

Figure S5: Square antiprismatic geometry of central lanthanide in complex **3**. The points connected by the lighter lines define the vertices of the ideal polyhedron**.** Color scheme: Ln, yellow; O, red.

Table S10 Crystallographic data for complex **3**.

Complex	**4**
Empirical formula	$C_{47}H_{20}DyGa_4N_7O_{32}$
Formula weight	1636.08
Temperature/K	173.15
Crystal system	monoclinic
Space group	C2/c
a/Å	26.378(5)
b/Å	27.509(6)
c/Å	24.815(5)
α/°	90
β/°	113.676(6)
γ/°	90
Volume/Å^3	16491(6)
Z	8
ρ_{calc}g/cm^3	1.318
μ/mm^{-1}	2.257
F(000)	6376.0
Crystal size/mm^3	0.06 × 0.05 × 0.02
Radiation	MoK\α (λ = 0.71073)
2Θ range for data collection/°	3.266 to 56.126
Index ranges	-34 ≤ h ≤ 34 -36 ≤ k ≤ 33 -32 ≤ l ≤ 32
Reflections collected	82097
Independent reflections	R_{int} = 0.4753 R_{sigma} = 0.7009
Data/restraints/ parameters	19956 / 0/ 846
Goodness-of-fit on F^2	0.737
Final R^{a,b} indexes [I>=2σ (I)]	R_1 = 0.0727 wR_2 = 0.1589
Final R^{a,b} indexes [all data]	R_1 = 0.3377 wR_2 = 0.2227
Largest diff. peak /hole / e Å^{-3}	1.13/-0.98

$^{a}R_1 = \Sigma(||F_o| - |F_c||)/\Sigma|F_o|$. $^{b}wR_2 = [\Sigma[w(F_o^2 - F_c^2)^2]/\Sigma[w(F_o^2)^2]]^{1/2}$, $w = 1/[\sigma^2(F_o^2) + (ap)^2 + bp]$, where $p = [\max(F_o^2, 0) + 2F_c^2]/3$.

Table S11 Selected Bond Lengths for complex **4**.

$Dy^{(1)}$	$O^{(18)}$	2.378(10)
$Dy^{(1)}$	$O^{(19)}$	2.476(10)
$Dy^{(1)}$	$O^{(20)}$	2.462(11)
$Dy^{(1)}$	$O^{(22)}$	2.350(11)
$Dy^{(1)}$	$N^{(7)}$	2.895(16)
$Ga^{(1)}$	$O^{(2)}$	1.945(10)
$Ga^{(1)}$	$O^{(3)}$	1.994(9)
$Ga^{(1)}$	$O^{(5)}$	1.981(11)
$Ga^{(1)}$	$O^{(6)}$	2.005(9)
$Ga^{(1)}$	$O^{(13)}$	1.914(10)
$Ga^{(1)}$	$N^{(5)}$	1.993(14)
$Ga^{(2)}$	$O^{(4)}$	1.849(11)
$Ga^{(2)}$	$O^{(8)}$	1.908(9)
$Ga^{(2)}$	$O^{(9)}$	1.903(9)
$Ga^{(2)}$	$O^{(23)}$	2.050(13)
$Ga^{(2)}$	$N^{(2)}$	1.956(11)
$Ga^{(3)}$	$O^{(7)}$	1.911(9)
$Ga^{(3)}$	$O^{(11)}$	1.970(10)
$Ga^{(3)}$	$O^{(12)}$	2.060(9)
$Ga^{(3)}$	$O^{(17)}$	1.912(9)
$Ga^{(3)}$	$O^{(18)}$	1.980(9)
$Ga^{(3)}$	$N^{(3)}$	1.992(12)
$Ga^{(4)}$	$O^{(14)}$	1.906(12)
$Ga^{(4)}$	$O^{(15)}$	1.913(10)
$Ga^{(4)}$	$O^{(16)}$	1.824(12)
$Ga^{(4)}$	$O^{(26)}$	2.043(13)
$Ga^{(4)}$	$N^{(6)}$	1.903(12)
$O^{(3)}$	$N^{(1)}$	1.391(13)
$O^{(6)}$	$N^{(2)}$	1.404(13)
$O^{(9)}$	$N^{(3)}$	1.422(13)
$O^{(12)}$	$N^{(4)}$	1.400(13)
$O^{(15)}$	$N^{(5)}$	1.440(15)
$O^{(18)}$	$N^{(6)}$	1.393(13)
$O^{(19)}$	$N^{(7)}$	1.265(17)
$O^{(20)}$	$N^{(7)}$	1.306(16)
$O^{(21)}$	$N^{(7)}$	1.217(16)

^{1}+X,1/2-Y,+Z; ^{2}+X,3/2-Y,+Z

Table S12 Selected Bond Angles for **4**.

$O^{(3)}$	$Dy^{(1)}$	$O^{(12)}$	146.8(3)
$O^{(3)}$	$Dy^{(1)}$	$O^{(19)}$	71.5(3)
$O^{(3)}$	$Dy^{(1)}$	$O^{(20)}$	77.0(3)
$O^{(3)}$	$Dy^{(1)}$	$N^{(7)}$	72.7(3)
$O^{(6)}$	$Dy^{(1)}$	$O^{(3)}$	63.6(3)
$O^{(6)}$	$Dy^{(1)}$	$O^{(9)}$	68.5(3)
$O^{(6)}$	$Dy^{(1)}$	$O^{(12)}$	133.6(3)
$O^{(6)}$	$Dy^{(1)}$	$O^{(18)}$	126.4(3)
$O^{(6)}$	$Dy^{(1)}$	$O^{(19)}$	122.8(4)
$O^{(6)}$	$Dy^{(1)}$	$O^{(20)}$	136.9(3)
$O^{(6)}$	$Dy^{(1)}$	$N^{(7)}$	135.3(3)
$O^{(9)}$	$Dy^{(1)}$	$O^{(3)}$	131.9(3)
$O^{(9)}$	$Dy^{(1)}$	$O^{(12)}$	74.2(3)
$O^{(9)}$	$Dy^{(1)}$	$O^{(18)}$	73.5(3)
$O^{(9)}$	$Dy^{(1)}$	$O^{(19)}$	144.3(3)
$O^{(9)}$	$Dy^{(1)}$	$O^{(20)}$	145.0(3)
$O^{(9)}$	$Dy^{(1)}$	$N^{(7)}$	155.1(4)
$O^{(12)}$	$Dy^{(1)}$	$N^{(7)}$	81.5(4)
$O^{(15)}$	$Dy^{(1)}$	$O^{(3)}$	74.4(3)
$O^{(15)}$	$Dy^{(1)}$	$O^{(6)}$	74.3(3)
$O^{(15)}$	$Dy^{(1)}$	$O^{(9)}$	90.0(3)
$O^{(15)}$	$Dy^{(1)}$	$O^{(12)}$	132.9(3)
$O^{(15)}$	$Dy^{(1)}$	$O^{(19)}$	125.1(4)
$O^{(15)}$	$Dy^{(1)}$	$O^{(20)}$	79.0(4)
$O^{(15)}$	$Dy^{(1)}$	$O^{(22)}$	150.5(4)
$O^{(15)}$	$Dy^{(1)}$	$N^{(7)}$	102.9(4)
$O^{(18)}$	$Dy^{(1)}$	$O^{(3)}$	135.4(3)
$O^{(18)}$	$Dy^{(1)}$	$O^{(19)}$	110.2(4)
$O^{(18)}$	$Dy^{(1)}$	$O^{(20)}$	71.5(4)
$O^{(18)}$	$Dy^{(1)}$	$N^{(7)}$	91.0(4)
$O^{(19)}$	$Dy^{(1)}$	$O^{(12)}$	76.2(3)
$O^{(19)}$	$Dy^{(1)}$	$N^{(7)}$	25.8(4)
$O^{(20)}$	$Dy^{(1)}$	$O^{(12)}$	89.2(3)
$O^{(20)}$	$Dy^{(1)}$	$O^{(19)}$	52.4(4)
$O^{(20)}$	$Dy^{(1)}$	$N^{(7)}$	26.7(4)
$O^{(22)}$	$Dy^{(1)}$	$O^{(3)}$	87.3(3)
$O^{(22)}$	$Dy^{(1)}$	$O^{(6)}$	76.9(3)
$O^{(22)}$	$Dy^{(1)}$	$O^{(9)}$	85.3(4)
$O^{(22)}$	$Dy^{(1)}$	$O^{(12)}$	73.5(3)
$O^{(22)}$	$Dy^{(1)}$	$O^{(18)}$	135.9(3)
$O^{(22)}$	$Dy^{(1)}$	$O^{(19)}$	67.3(4)
$O^{(22)}$	$Dy^{(1)}$	$O^{(20)}$	119.7(4)
$O^{(2)}$	$Ga^{(1)}$	$O^{(3)}$	81.7(4)
$O^{(2)}$	$Ga^{(1)}$	$O^{(5)}$	96.3(5)
$O^{(2)}$	$Ga^{(1)}$	$O^{(6)}$	96.7(4)

$O^{(2)}$	$Ga^{(1)}$	$N^{(5)}$	163.7(5)
$O^{(3)}$	$Ga^{(1)}$	$O^{(6)}$	78.9(4)
$O^{(5)}$	$Ga^{(1)}$	$O^{(3)}$	158.6(4)
$O^{(5)}$	$Ga^{(1)}$	$O^{(6)}$	80.2(4)
$O^{(5)}$	$Ga^{(1)}$	$N^{(5)}$	99.9(5)
$O^{(13)}$	$Ga^{(1)}$	$O^{(2)}$	88.3(4)
$O^{(13)}$	$Ga^{(1)}$	$O^{(3)}$	107.2(4)
$O^{(13)}$	$Ga^{(1)}$	$O^{(5)}$	93.9(5)
$O^{(13)}$	$Ga^{(1)}$	$O^{(6)}$	172.6(4)
$O^{(13)}$	$Ga^{(1)}$	$N^{(5)}$	87.9(5)
$N^{(5)}$	$Ga^{(1)}$	$O^{(6)}$	88.7(5)
$O^{(4)}$	$Ga^{(2)}$	$O^{(8)}$	93.8(5)
$O^{(4)}$	$Ga^{(2)}$	$O^{(9)}$	157.0(5)
$O^{(4)}$	$Ga^{(2)}$	$O^{(23)}$	101.7(6)
$O^{(4)}$	$Ga^{(2)}$	$N^{(2)}$	92.6(5)
$O^{(8)}$	$Ga^{(2)}$	$O^{(23)}$	92.9(4)
$O^{(8)}$	$Ga^{(2)}$	$N^{(2)}$	167.3(5)
$O^{(9)}$	$Ga^{(2)}$	$O^{(8)}$	83.1(4)
$O^{(9)}$	$Ga^{(2)}$	$O^{(23)}$	101.3(4)
$O^{(9)}$	$Ga^{(2)}$	$N^{(2)}$	86.8(5)
$N^{(2)}$	$Ga^{(2)}$	$O^{(23)}$	96.5(5)
$O^{(7)}$	$Ga^{(3)}$	$O^{(11)}$	90.4(4)
$O^{(7)}$	$Ga^{(3)}$	$O^{(12)}$	104.8(4)
$O^{(7)}$	$Ga^{(3)}$	$O^{(17)}$	95.5(4)
$O^{(7)}$	$Ga^{(3)}$	$O^{(18)}$	173.0(4)
$O^{(7)}$	$Ga^{(3)}$	$N^{(3)}$	87.5(4)
$O^{(11)}$	$Ga^{(3)}$	$O^{(12)}$	79.7(4)
$O^{(11)}$	$Ga^{(3)}$	$O^{(18)}$	95.7(4)
$O^{(11)}$	$Ga^{(3)}$	$N^{(3)}$	163.2(5)
$O^{(17)}$	$Ga^{(3)}$	$O^{(11)}$	98.2(4)
$O^{(17)}$	$Ga^{(3)}$	$O^{(12)}$	159.6(4)
$O^{(17)}$	$Ga^{(3)}$	$O^{(18)}$	80.3(4)
$O^{(17)}$	$Ga^{(3)}$	$N^{(3)}$	98.6(4)
$O^{(18)}$	$Ga^{(3)}$	$O^{(12)}$	79.7(4)
$O^{(18)}$	$Ga^{(3)}$	$N^{(3)}$	87.7(5)
$N^{(3)}$	$Ga^{(3)}$	$O^{(12)}$	84.8(4)
$O^{(14)}$	$Ga^{(4)}$	$O^{(15)}$	82.8(5)
$O^{(14)}$	$Ga^{(4)}$	$O^{(26)}$	90.9(6)
$O^{(15)}$	$Ga^{(4)}$	$O^{(26)}$	100.7(5)
$O^{(16)}$	$Ga^{(4)}$	$O^{(14)}$	93.6(5)
$O^{(16)}$	$Ga^{(4)}$	$O^{(15)}$	160.5(6)
$O^{(16)}$	$Ga^{(4)}$	$O^{(26)}$	98.5(6)
$O^{(16)}$	$Ga^{(4)}$	$N^{(6)}$	94.8(5)
$N^{(6)}$	$Ga^{(4)}$	$O^{(14)}$	169.0(6)
$N^{(6)}$	$Ga^{(4)}$	$O^{(15)}$	87.0(5)

[1]+X,1/2-Y,+Z; [2]+X,3/2-Y,+Z

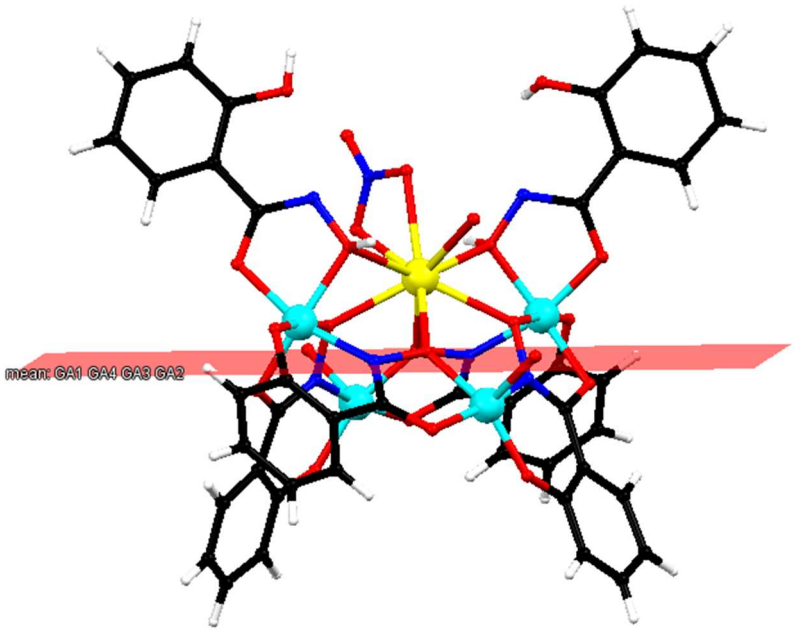

Figure S6: Schematic representation of complex **4** emphasizing on the mean plane calculated by the four Ga(III) atoms. Color scheme: Ga, aqua; Dy, yellow; O, red; N, blue; C, black; H, white.

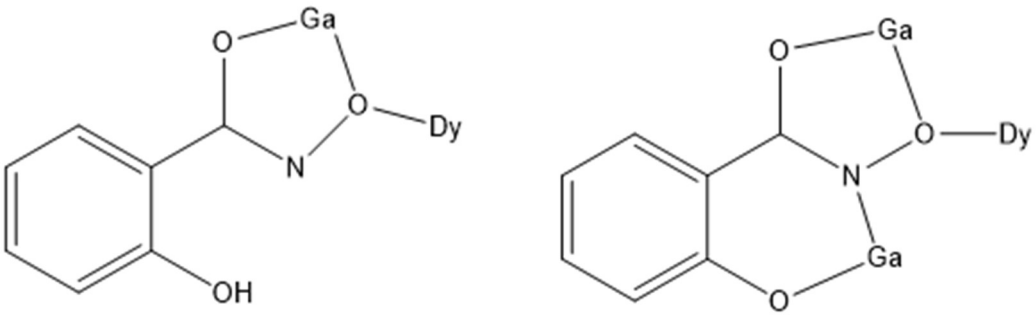

Scheme 3: Coordination modes of organic ligand in complex **4.**

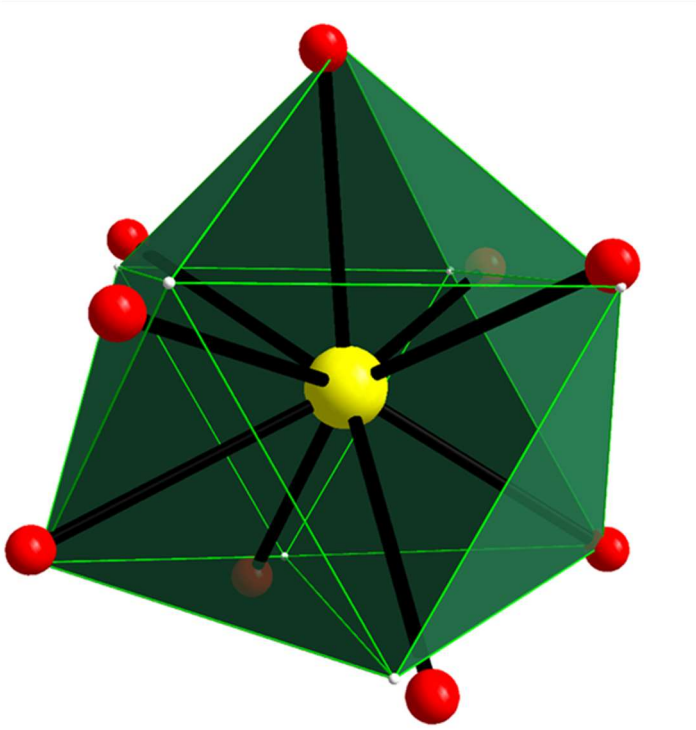

Figure S7: Spherical tricapped trigonal prismatic geometry of central lanthanide in complex **4**. The points connected by the lighter lines define the vertices of the ideal polyhedron**.** Color scheme: Ln, yellow; O, red.

Table S13 Shape measurements of the 9-coordinate lanthanide coordination polyhedra. The bold numbers indicate the closest polyhedron according to SHAPE calculations.[3]

Polyhedron[c]	Dy1
EP-9	34.27
OPY-9	23.37
HBPY-9	18.42
JTC-9	14.38
JCCU-9	9.12
CCU-9	7.45
JCSAPR-9	2.59
CSAPR-9	1.44
JTCTPR-9	2.88
TCTPR-9	**1.35**
JTDIC-9	10.84
HH-9	10.30
MFF-9	1.69

[c] Abbreviations: EP-9, enneagon; OPY-9, Octagonal pyramid; HBPY-9, Heptagonal bipyramid; JTC-9, Johnson triangular cupola J3; JCCU-9, Capped cube J8; CCU-9, Spherical-relaxed capped cube; JCSAPR-9, Capped square antiprism J10; CSAPR-9, Spherical capped square antiprism; JTCTPR-9, Tricapped trigonal prism J51; TCTPR-9, Spherical tricapped trigonal prism; JTDIC-9, Tridiminished icosahedron J63; HH-9, Hula-hoop; MFF-9, Muffin.

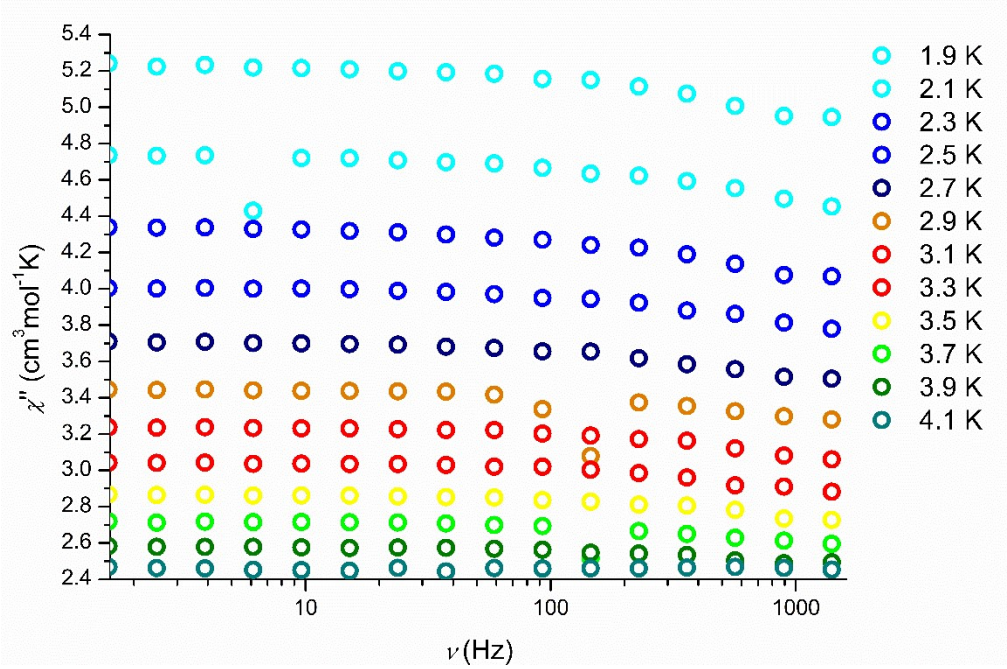

Figure S8: Frequency dependent in-phase susceptibility plot of for compound **4** (1.9 to 4.1 K) at zero field.

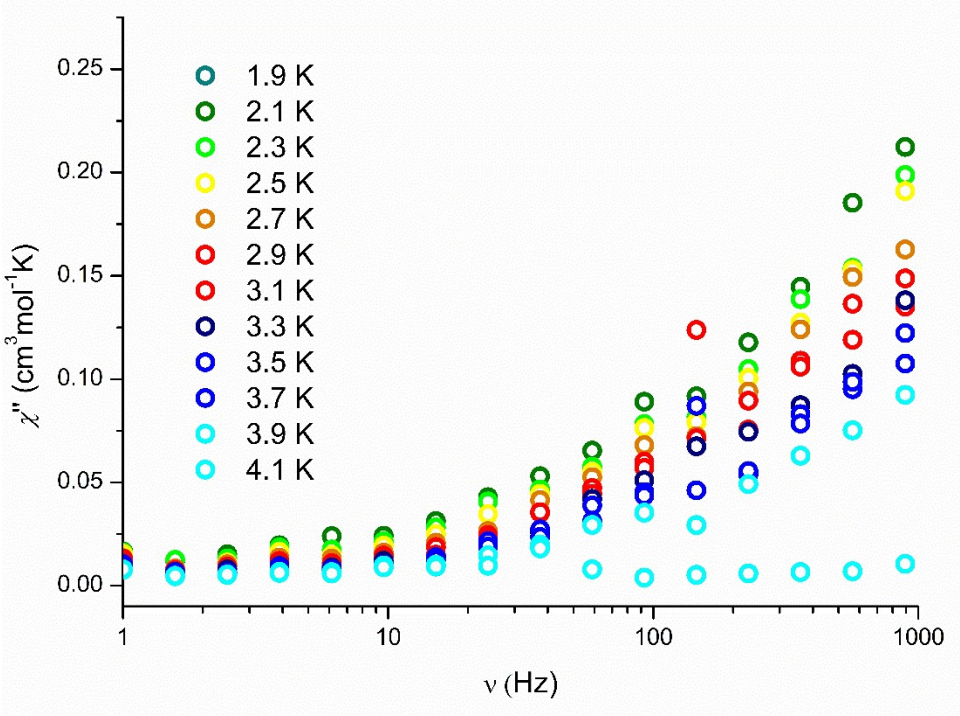

Figure S9: Frequency dependent out-of-phase susceptibility plot of for compound **4** (1.9 to 4.1 K) at zero field.

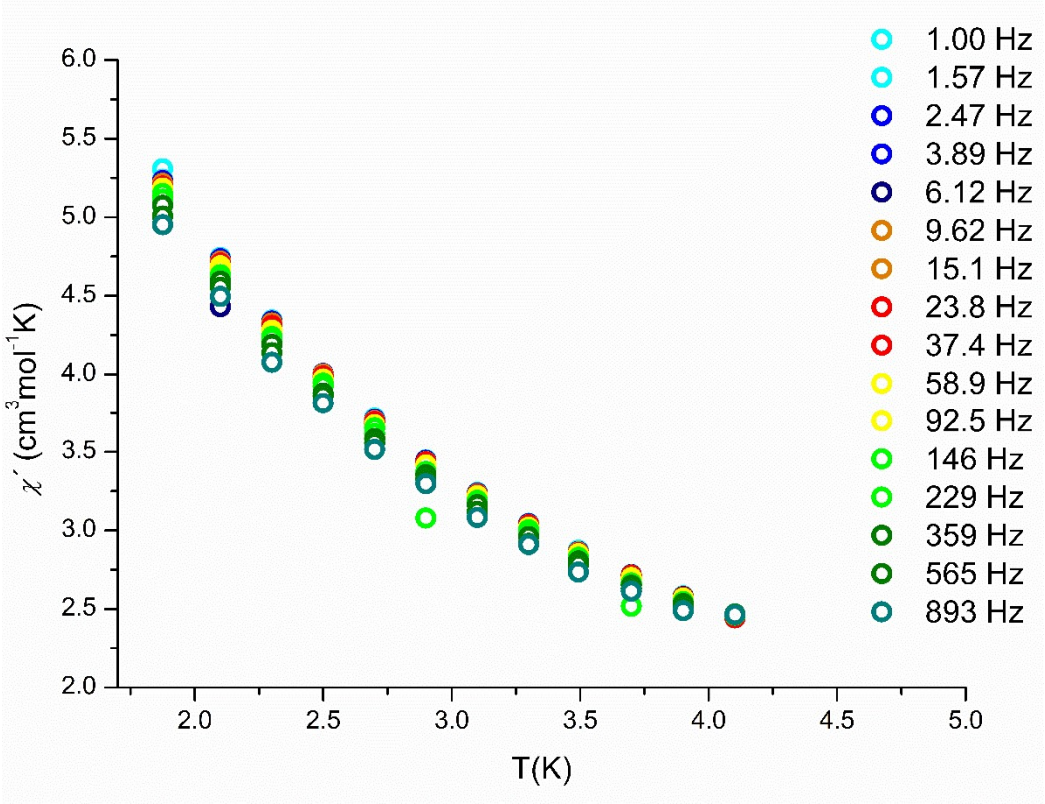

Figure 10: Temperature dependent in-phase susceptibility plot of for compound **4** (1.9 to 4.1 K) at 0 Oe.

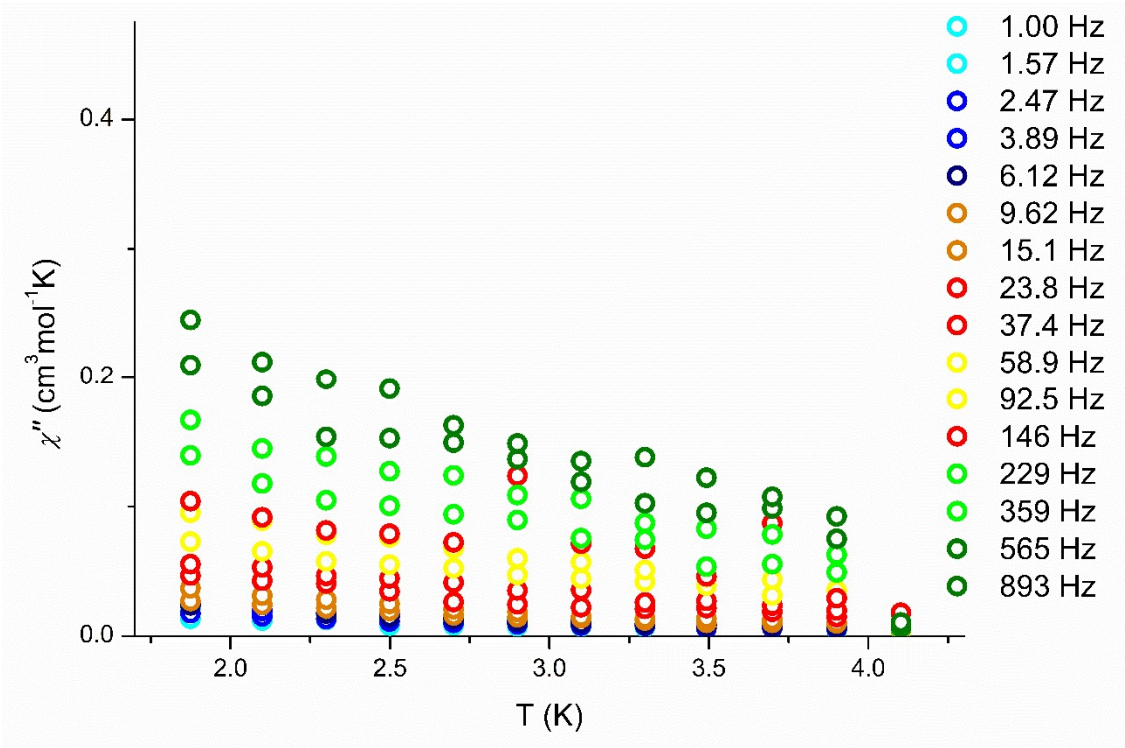

Figure S11: Temperature dependent in-phase susceptibility plot of for compound **4** (1.9 to 4.1 K) at 0 Oe.

Table S14 Crystallographic data for complex **5**.

Complex	**5**
Empirical formula	$C_{76}H_{88}HoGa_8N_9O_{37}$
Formula weight	2442.24
Temperature/K	120(2)
Crystal system	monoclinic
Space group	P2/c
a/Å	13.6829(5)
b/Å	18.1050(6)
c/Å	19.7347(7)
α/°	90
β/°	90.130(3)
γ/°	90
Volume/Å^3	4888.8(3)
Z	2
ρ_{calc}g/cm^3	1.659
μ/mm^{-1}	3.04
F(000)	2436.0
Crystal size/mm^3	0.26 × 0.19 × 0.08
Radiation	MoK\α (λ = 0.71073)
2Θ range for data collection/°	4.95 to 56.322
Index ranges	-18 ≤ h ≤ 18 -23 ≤ k ≤ 23 -23 ≤ l ≤ 26
Reflections collected	27438
Independent reflections	R_{int} = 0.0529 R_{sigma} = 0.0616
Data/restraints/ parameters	11830 /104 /677
Goodness-of-fit on F^2	1.134
Final R^{a,b} indexes [I>=2σ (I)]	R_1 = 0.0948 wR_2 = 0.2418
Final R^{a,b} indexes [all data]	R_1 = 0.1382 wR_2 = 0.2658
Largest diff. peak /hole / e Å^{-3}	2.38 / -1.48

$^a R_1 = \Sigma(||F_o| - |F_c||)/\Sigma|F_o|$. $^b wR_2 = [\Sigma[w(F_o^2 - F_c^2)^2]/\Sigma[w(F_o^2)^2]]^{1/2}$, $w = 1/[\sigma^2(F_o^2) + (ap)^2 + bp]$, where $p = [\max(F_o^2, 0) + 2F_c^2]/3$.

Table S15 Selected Bond Lengths for complex **5**.

$Ho^{(1)}$	$O^{(3)}$	2.327(7)
$Ho^{(1)}$	$O^{(3)1}$	2.327(7)
$Ho^{(1)}$	$O^{(6)1}$	2.338(8)
$Ho^{(1)}$	$O^{(6)}$	2.338(8)
$Ho^{(1)}$	$O^{(9)1}$	2.281(7)
$Ho^{(1)}$	$O^{(9)}$	2.281(7)
$Ho^{(1)}$	$O^{(12)}$	2.289(6)
$Ho^{(1)}$	$O^{(12)1}$	2.289(6)
$Ga^{(1)}$	$O^{(1)}$	1.849(7)
$Ga^{(1)}$	$O^{(11)}$	1.909(7)
$Ga^{(1)}$	$O^{(12)}$	1.956(7)
$Ga^{(1)}$	$O^{(13)}$	1.861(8)
$Ga^{(1)}$	$N^{(1)}$	1.979(9)
$Ga^{(2)}$	$O^{(2)}$	1.895(8)
$Ga^{(2)}$	$O^{(3)}$	1.957(7)
$Ga^{(2)}$	$O^{(4)}$	1.882(8)
$Ga^{(2)}$	$O^{(13)1}$	1.860(7)
$Ga^{(2)}$	$N^{(2)}$	1.981(9)
$Ga^{(3)}$	$O^{(5)}$	1.954(9)
$Ga^{(3)}$	$O^{(6)}$	1.936(7)
$Ga^{(3)}$	$O^{(7)}$	1.844(8)
$Ga^{(3)}$	$O^{(14)1}$	1.855(8)
$Ga^{(3)}$	$N^{(3)}$	1.994(11)
$Ga^{(4)}$	$O^{(8)}$	1.905(8)
$Ga^{(4)}$	$O^{(9)}$	1.939(7)
$Ga^{(4)}$	$O^{(10)}$	1.852(8)
$Ga^{(4)}$	$O^{(14)}$	1.892(9)
$Ga^{(4)}$	$N^{(4)}$	1.951(9)
$Ga^{(4)}$	$O^{(15)}$	2.35(2)
$O^{(3)}$	$N^{(1)}$	1.409(10)
$O^{(6)}$	$N^{(2)}$	1.415(12)
$O^{(9)}$	$N^{(3)}$	1.447(12)
$O^{(12)}$	$N^{(4)}$	1.433(11)

[1]1-X,+Y,3/2-Z

Table S16 Selected Bond Angles for **5**.

$O^{(3)1}$	$Ho^{(1)}$	$O^{(3)}$	81.2(4)
$O^{(3)1}$	$Ho^{(1)}$	$O^{(6)1}$	68.7(3)
$O^{(3)}$	$Ho^{(1)}$	$O^{(6)}$	68.7(3)
$O^{(3)1}$	$Ho^{(1)}$	$O^{(6)}$	138.5(3)
$O^{(3)}$	$Ho^{(1)}$	$O^{(6)1}$	138.5(3)
$O^{(6)1}$	$Ho^{(1)}$	$O^{(6)}$	150.6(4)
$O^{(9)}$	$Ho^{(1)}$	$O^{(3)1}$	150.1(3)
$O^{(9)}$	$Ho^{(1)}$	$O^{(3)}$	107.7(3)
$O^{(9)1}$	$Ho^{(1)}$	$O^{(3)1}$	107.7(3)
$O^{(9)1}$	$Ho^{(1)}$	$O^{(3)}$	150.1(3)
$O^{(9)}$	$Ho^{(1)}$	$O^{(6)1}$	87.8(3)
$O^{(9)1}$	$Ho^{(1)}$	$O^{(6)}$	87.8(3)
$O^{(9)}$	$Ho^{(1)}$	$O^{(6)}$	69.3(3)
$O^{(9)1}$	$Ho^{(1)}$	$O^{(6)1}$	69.3(3)
$O^{(9)}$	$Ho^{(1)}$	$O^{(9)1}$	79.2(4)
$O^{(9)1}$	$Ho^{(1)}$	$O^{(12)1}$	71.5(3)
$O^{(9)}$	$Ho^{(1)}$	$O^{(12)1}$	136.6(3)
$O^{(9)1}$	$Ho^{(1)}$	$O^{(12)}$	136.6(3)
$O^{(9)}$	$Ho^{(1)}$	$O^{(12)}$	71.5(3)
$O^{(12)1}$	$Ho^{(1)}$	$O^{(3)1}$	71.4(2)
$O^{(12)}$	$Ho^{(1)}$	$O^{(3)}$	71.4(2)
$O^{(12)}$	$Ho^{(1)}$	$O^{(3)1}$	85.2(3)
$O^{(12)1}$	$Ho^{(1)}$	$O^{(3)}$	85.2(3)
$O^{(12)}$	$Ho^{(1)}$	$O^{(6)1}$	78.1(3)
$O^{(12)1}$	$Ho^{(1)}$	$O^{(6)}$	78.1(3)
$O^{(12)}$	$Ho^{(1)}$	$O^{(6)}$	109.9(3)
$O^{(12)1}$	$Ho^{(1)}$	$O^{(6)1}$	109.9(3)
$O^{(12)}$	$Ho^{(1)}$	$O^{(12)1}$	149.2(4)
$O^{(1)}$	$Ga^{(1)}$	$O^{(11)}$	87.3(3)
$O^{(1)}$	$Ga^{(1)}$	$O^{(12)}$	159.3(3)
$O^{(1)}$	$Ga^{(1)}$	$O^{(13)}$	102.4(3)
$O^{(1)}$	$Ga^{(1)}$	$N^{(1)}$	92.5(3)
$O^{(11)}$	$Ga^{(1)}$	$O^{(12)}$	80.3(3)
$O^{(11)}$	$Ga^{(1)}$	$N^{(1)}$	142.7(4)
$O^{(12)}$	$Ga^{(1)}$	$N^{(1)}$	87.4(3)
$O^{(13)}$	$Ga^{(1)}$	$O^{(11)}$	106.2(3)
$O^{(13)}$	$Ga^{(1)}$	$O^{(12)}$	97.0(3)
$O^{(13)}$	$Ga^{(1)}$	$N^{(1)}$	110.2(3)
$O^{(2)}$	$Ga^{(2)}$	$O^{(3)}$	80.0(3)
$O^{(2)}$	$Ga^{(2)}$	$N^{(2)}$	145.3(4)
$O^{(3)}$	$Ga^{(2)}$	$N^{(2)}$	85.6(3)
$O^{(4)}$	$Ga^{(2)}$	$O^{(2)}$	89.1(4)
$O^{(4)}$	$Ga^{(2)}$	$O^{(3)}$	156.6(3)
$O^{(4)}$	$Ga^{(2)}$	$N^{(2)}$	92.0(4)
$O^{(13)1}$	$Ga^{(2)}$	$O^{(2)}$	103.2(3)
$O^{(13)1}$	$Ga^{(2)}$	$O^{(3)}$	98.6(3)

$O^{(13)1}$	$Ga^{(2)}$	$O^{(4)}$	104.0(4)
$O^{(13)1}$	$Ga^{(2)}$	$N^{(2)}$	110.2(4)
$O^{(5)}$	$Ga^{(3)}$	$N^{(3)}$	151.3(4)
$O^{(6)}$	$Ga^{(3)}$	$O^{(5)}$	80.8(3)
$O^{(6)}$	$Ga^{(3)}$	$N^{(3)}$	85.8(4)
$O^{(7)}$	$Ga^{(3)}$	$O^{(5)}$	88.3(4)
$O^{(7)}$	$Ga^{(3)}$	$O^{(6)}$	149.6(4)
$O^{(7)}$	$Ga^{(3)}$	$O^{(14)1}$	106.9(4)
$O^{(7)}$	$Ga^{(3)}$	$N^{(3)}$	90.8(4)
$O^{(14)1}$	$Ga^{(3)}$	$O^{(5)}$	98.3(4)
$O^{(14)1}$	$Ga^{(3)}$	$O^{(6)}$	102.8(4)
$O^{(14)1}$	$Ga^{(3)}$	$N^{(3)}$	109.4(4)
$O^{(8)}$	$Ga^{(4)}$	$O^{(9)}$	82.0(3)
$O^{(8)}$	$Ga^{(4)}$	$N^{(4)}$	154.7(4)
$O^{(8)}$	$Ga^{(4)}$	$O^{(15)}$	76.1(5)
$O^{(9)}$	$Ga^{(4)}$	$N^{(4)}$	87.6(3)
$O^{(9)}$	$Ga^{(4)}$	$O^{(15)}$	83.3(5)
$O^{(10)}$	$Ga^{(4)}$	$O^{(8)}$	90.6(4)
$O^{(10)}$	$Ga^{(4)}$	$O^{(9)}$	165.2(4)
$O^{(10)}$	$Ga^{(4)}$	$O^{(14)}$	97.7(4)
$O^{(10)}$	$Ga^{(4)}$	$N^{(4)}$	93.9(4)
$O^{(10)}$	$Ga^{(4)}$	$O^{(15)}$	82.5(5)
$O^{(14)}$	$Ga^{(4)}$	$O^{(8)}$	98.4(4)
$O^{(14)}$	$Ga^{(4)}$	$O^{(9)}$	96.1(4)
$O^{(14)}$	$Ga^{(4)}$	$N^{(4)}$	105.6(4)
$O^{(14)}$	$Ga^{(4)}$	$O^{(15)}$	174.5(5)
$N^{(4)}$	$Ga^{(4)}$	$O^{(15)}$	79.8(5)
$Ga^{(2)}$	$O^{(3)}$	$Ho^{(1)}$	121.9(3)
$N^{(1)}$	$O^{(3)}$	$Ho^{(1)}$	123.8(6)
$N^{(1)}$	$O^{(3)}$	$Ga^{(2)}$	112.3(5)
$Ga^{(3)}$	$O^{(6)}$	$Ho^{(1)}$	120.1(4)
$N^{(2)}$	$O^{(6)}$	$Ga^{(3)}$	113.1(6)

[1]1-X,+Y,3/2-Z

Table S17 Shape measurements of the 8-coordinate lanthanide coordination polyhedra. The bold numbers indicate the closest polyhedron according to SHAPE calculations.[3]

Polyhedron[c]	Ho1
OP-8	34.19
HPY-8	22.80
HBPY-8	14.29
CU-8	6.84
SAPR-8	**1.08**
TDD-8	2.27
JGBF-8	16.49
JETBPY-8	28.70
JBTPR-8	3.70
BTPR-8	3.14
JSD-8	6.09
TT-8	7.73
ETBPY-8	25.70

[c] Abbreviations: OP-8, octagon; HPY-8, heptagonal pyramid; HBPY-8, hexagonal bipyramid; CU-8, cube; SAPR-8, square antiprism; TDD-8, triangular dodecahedron; JGBF-8, Johnson gyrobifastigium; JETBPY-8, Johnson elongated triangular bipyramid; JBTPR-8, Johnson biaugmented trigonal prism; BTPR-8, biaugmented trigonal prism; JSD-8, Johnson snub diphenoid; TT-8, triakis tetrahedron; ETBPY-8, elongated trigonal bipyramid.

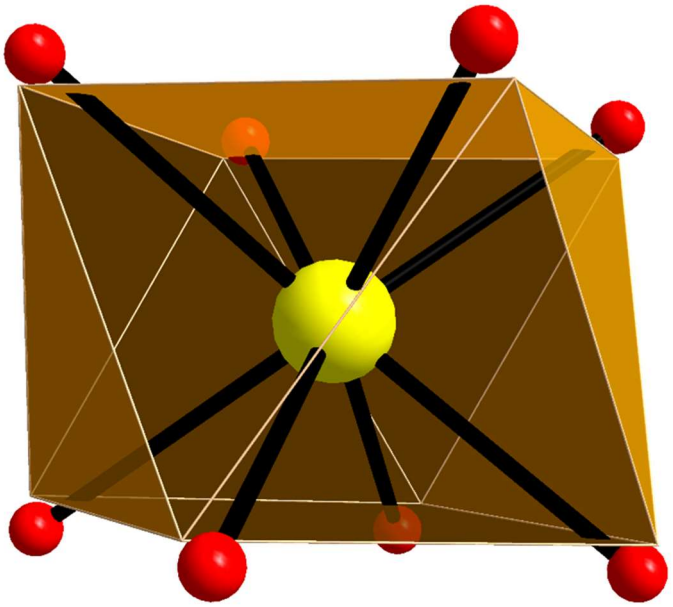

Figure S12: Square antiprismatic geometry of central lanthanide in complex **5**. The points connected by the lighter lines define the vertices of the ideal polyhedron. Color scheme: Ln, yellow; O, red.

Table S18 Crystallographic data for complex **6**.

Complex	**6**
Empirical formula	$C_{97}H_{99}Dy_2Fe_6N_{12}O_{61}$
Formula weight	3068.98
Temperature/K	100.0
Crystal system	monoclinic
Space group	C2/c
a/Å	18.8969(19)
b/Å	28.981(3)
c/Å	28.579(3)
α/°	90
β/°	94.556(3)
γ/°	90
Volume/Å^3	15602 (3)
Z	4
ρ_{calc}g/cm^3	1.307
μ/mm^{-1}	1.567
F(000)	6164.0
Crystal size/mm^3	0.31 × 0.19 × 0.09
Radiation	MoK\α (λ = 0.71073)
2Θ range for data collection/°	3.154 to 42.594
Index ranges	-19 ≤ h ≤ 19 -29 ≤ k ≤ 29 -29 ≤ l ≤ 27
Reflections collected	25142
Independent reflections	R_{int} = 0.0820 R_{sigma} = 0.1004
Data/restraints/ parameters	8571 /220 /909
Goodness-of-fit on F^2	1.068
Final R^{a,b} indexes [I>=2σ (I)]	R_1 = 0.0864 wR_2 = 0.2391
Final R^{a,b} indexes [all data]	R_1 = 0.1461 wR_2 = 0.2903
Largest diff. peak /hole / e Å^{-3}	1.67 / -0.90

$^a R_1 = \Sigma(||F_o| - |F_c||)/\Sigma|F_o|$. $^b wR_2 = [\Sigma[w(F_o^2 - F_c^2)^2]/\Sigma[w(F_o^2)^2]]^{1/2}$, $w = 1/[\sigma^2(F_o^2) + (ap)^2 + bp]$, where $p = [\max(F_o^2, 0) + 2F_c^2]/3$.

Table S19 Selected Bond Lengths for complex **6**.

$Dy^{(1)}$	$O^{(3)}$	2.348(12)
$Dy^{(1)}$	$O^{(6)1}$	2.560(11)
$Dy^{(1)}$	$O^{(9)1}$	2.372(10)
$Dy^{(1)}$	$O^{(11)1}$	2.373(14)
$Dy^{(1)}$	$O^{(12)1}$	2.663(12)
$Dy^{(1)}$	$O^{(14)}$	2.385(12)
$Dy^{(1)}$	$O^{(15)}$	2.339(10)
$Dy^{(1)}$	$O^{(18)1}$	2.396(12)
$Dy^{(1)}$	$O^{(20)}$	2.395(11)
$Fe^{(1)}$	$O^{(2)}$	1.947(12)
$Fe^{(1)}$	$O^{(3)}$	1.960(11)
$Fe^{(1)}$	$O^{(8)}$	1.986(11)
$Fe^{(1)}$	$O^{(9)}$	1.941(11)
$Fe^{(1)}$	$O^{(12)1}$	2.125(12)
$Fe^{(1)}$	$O^{(12)}$	2.098(10)
$Fe^{(2)}$	$O^{(1)}$	1.893(13)
$Fe^{(2)}$	$O^{(4)1}$	1.958(13)
$Fe^{(2)}$	$O^{(15)}$	2.037(10)
$Fe^{(2)}$	$O^{(19)}$	2.117(12)
$Fe^{(2)}$	$N^{(1)}$	2.080(13)
$Fe^{(2)}$	$N^{(2)1}$	2.035(15)
$Fe^{(3)}$	$O^{(5)}$	1.946(13)
$Fe^{(3)}$	$O^{(6)}$	2.042(11)
$Fe^{(3)}$	$O^{(7)}$	1.933(12)
$Fe^{(3)}$	$O^{(17)}$	2.006(13)
$Fe^{(3)}$	$O^{(18)}$	2.073(12)
$Fe^{(3)}$	$N^{(3)}$	2.039(15)
$O^{(3)}$	$N^{(1)}$	1.388(17)
$O^{(6)}$	$N^{(2)}$	1.414(17)
$O^{(9)}$	$N^{(3)}$	1.412(17)
$O^{(12)}$	$N^{(4)}$	1.40(2)
$O^{(15)}$	$N^{(5)}$	1.403(18)
$O^{(18)}$	$N^{(6)}$	1.324(17)

[1]1/2-X,3/2-Y,1-Z

Table S20 Selected Bond Angles for **6**.

$O^{(3)}$	$Dy^{(1)}$	$O^{(6)1}$	72.4(4)
$O^{(3)}$	$Dy^{(1)}$	$O^{(9)1}$	90.1(4)
$O^{(3)}$	$Dy^{(1)}$	$O^{(11)1}$	80.1(5)
$O^{(3)}$	$Dy^{(1)}$	$O^{(12)1}$	62.0(4)
$O^{(3)}$	$Dy^{(1)}$	$O^{(14)}$	128.5(4)
$O^{(3)}$	$Dy^{(1)}$	$O^{(18)1}$	133.3(4)
$O^{(3)}$	$Dy^{(1)}$	$O^{(20)}$	140.6(4)
$O^{(6)1}$	$Dy^{(1)}$	$O^{(12)1}$	110.0(4)
$O^{(9)1}$	$Dy^{(1)}$	$O^{(6)1}$	69.8(4)
$O^{(9)1}$	$Dy^{(1)}$	$O^{(11)1}$	119.9(5)
$O^{(9)1}$	$Dy^{(1)}$	$O^{(12)1}$	60.7(3)
$O^{(9)1}$	$Dy^{(1)}$	$O^{(14)}$	141.4(4)
$O^{(9)1}$	$Dy^{(1)}$	$O^{(18)1}$	77.0(4)
$O^{(9)1}$	$Dy^{(1)}$	$O^{(20)}$	74.2(4)
$O^{(11)1}$	$Dy^{(1)}$	$O^{(6)1}$	151.0(5)
$O^{(11)1}$	$Dy^{(1)}$	$O^{(12)1}$	62.5(4)
$O^{(11)1}$	$Dy^{(1)}$	$O^{(14)}$	73.1(5)
$O^{(11)1}$	$Dy^{(1)}$	$O^{(18)1}$	145.0(5)
$O^{(11)1}$	$Dy^{(1)}$	$O^{(20)}$	77.4(5)
$O^{(14)}$	$Dy^{(1)}$	$O^{(6)1}$	117.8(4)
$O^{(14)}$	$Dy^{(1)}$	$O^{(12)1}$	132.0(4)
$O^{(14)}$	$Dy^{(1)}$	$O^{(18)1}$	75.8(4)
$O^{(14)}$	$Dy^{(1)}$	$O^{(20)}$	74.1(4)
$O^{(15)}$	$Dy^{(1)}$	$O^{(3)}$	68.2(4)
$O^{(15)}$	$Dy^{(1)}$	$O^{(6)1}$	75.6(3)
$O^{(15)}$	$Dy^{(1)}$	$O^{(9)1}$	143.5(4)
$O^{(15)}$	$Dy^{(1)}$	$O^{(11)1}$	86.1(5)
$O^{(15)}$	$Dy^{(1)}$	$O^{(12)1}$	124.2(3)
$O^{(15)}$	$Dy^{(1)}$	$O^{(14)}$	66.8(4)
$O^{(15)}$	$Dy^{(1)}$	$O^{(18)1}$	96.4(4)
$O^{(15)}$	$Dy^{(1)}$	$O^{(20)}$	140.6(4)
$O^{(18)1}$	$Dy^{(1)}$	$O^{(6)1}$	61.0(4)
$O^{(18)1}$	$Dy^{(1)}$	$O^{(12)1}$	136.2(3)
$O^{(20)}$	$Dy^{(1)}$	$O^{(6)1}$	130.5(4)
$O^{(20)}$	$Dy^{(1)}$	$O^{(12)1}$	79.0(4)
$O^{(20)}$	$Dy^{(1)}$	$O^{(18)1}$	78.9(4)
$O^{(2)}$	$Fe^{(1)}$	$O^{(3)}$	78.7(5)
$O^{(2)}$	$Fe^{(1)}$	$O^{(8)}$	103.7(5)
$O^{(2)}$	$Fe^{(1)}$	$O^{(12)1}$	153.5(5)
$O^{(2)}$	$Fe^{(1)}$	$O^{(12)}$	96.0(5)
$O^{(3)}$	$Fe^{(1)}$	$O^{(8)}$	98.7(5)
$O^{(3)}$	$Fe^{(1)}$	$O^{(12)1}$	78.8(5)
$O^{(3)}$	$Fe^{(1)}$	$O^{(12)}$	104.2(5)
$O^{(8)}$	$Fe^{(1)}$	$O^{(12)}$	152.3(5)
$O^{(8)}$	$Fe^{(1)}$	$O^{(12)1}$	93.3(5)
$O^{(9)}$	$Fe^{(1)}$	$O^{(2)}$	103.9(5)

$O^{(9)}$	$Fe^{(1)}$	$O^{(3)}$	176.2(5)
$O^{(9)}$	$Fe^{(1)}$	$O^{(8)}$	78.0(5)
$O^{(9)}$	$Fe^{(1)}$	$O^{(12)1}$	99.4(5)
$O^{(9)}$	$Fe^{(1)}$	$O^{(12)}$	78.5(5)
$O^{(12)}$	$Fe^{(1)}$	$O^{(12)1}$	76.3(5)
$O^{(1)}$	$Fe^{(2)}$	$O^{(4)1}$	94.3(5)
$O^{(1)}$	$Fe^{(2)}$	$O^{(15)}$	166.5(5)
$O^{(1)}$	$Fe^{(2)}$	$O^{(19)}$	93.7(6)
$O^{(1)}$	$Fe^{(2)}$	$N^{(1)}$	85.8(5)
$O^{(1)}$	$Fe^{(2)}$	$N^{(2)1}$	102.9(6)
$O^{(4)1}$	$Fe^{(2)}$	$O^{(15)}$	97.7(5)
$O^{(4)1}$	$Fe^{(2)}$	$O^{(19)}$	88.6(5)
$O^{(4)1}$	$Fe^{(2)}$	$N^{(1)}$	179.5(6)
$O^{(4)1}$	$Fe^{(2)}$	$N^{(2)1}$	85.8(6)
$O^{(15)}$	$Fe^{(2)}$	$O^{(19)}$	80.5(5)
$O^{(15)}$	$Fe^{(2)}$	$N^{(1)}$	82.3(5)
$N^{(1)}$	$Fe^{(2)}$	$O^{(19)}$	91.9(5)
$N^{(2)1}$	$Fe^{(2)}$	$O^{(15)}$	84.2(5)
$N^{(2)1}$	$Fe^{(2)}$	$O^{(19)}$	162.8(6)
$N^{(2)1}$	$Fe^{(2)}$	$N^{(1)}$	93.7(5)
$O^{(5)}$	$Fe^{(3)}$	$O^{(6)}$	78.4(5)
$O^{(5)}$	$Fe^{(3)}$	$O^{(17)}$	103.9(6)
$O^{(5)}$	$Fe^{(3)}$	$O^{(18)}$	96.4(5)
$O^{(5)}$	$Fe^{(3)}$	$N^{(3)}$	155.4(6)
$O^{(6)}$	$Fe^{(3)}$	$O^{(18)}$	75.5(5)
$O^{(7)}$	$Fe^{(3)}$	$O^{(5)}$	90.3(6)
$O^{(7)}$	$Fe^{(3)}$	$O^{(6)}$	115.6(5)
$O^{(7)}$	$Fe^{(3)}$	$O^{(17)}$	93.2(6)
$O^{(7)}$	$Fe^{(3)}$	$O^{(18)}$	168.1(5)
$O^{(7)}$	$Fe^{(3)}$	$N^{(3)}$	85.3(5)
$O^{(17)}$	$Fe^{(3)}$	$O^{(6)}$	151.2(5)
$O^{(17)}$	$Fe^{(3)}$	$O^{(18)}$	75.7(5)
$O^{(17)}$	$Fe^{(3)}$	$N^{(3)}$	100.5(6)
$N^{(3)}$	$Fe^{(3)}$	$O^{(6)}$	81.8(5)
$N^{(3)}$	$Fe^{(3)}$	$O^{(18)}$	92.5(5)
$N^{(1)}$	$O^{(3)}$	$Dy^{(1)}$	124.4(9)
$N^{(1)}$	$O^{(3)}$	$Fe^{(1)}$	115.4(9)
$N^{(2)}$	$O^{(6)}$	$Dy^{(1)1}$	112.4(8)
$N^{(2)}$	$O^{(6)}$	$Fe^{(3)}$	112.2(9)
$N^{(3)}$	$O^{(9)}$	$Dy^{(1)1}$	121.4(8)
$N^{(3)}$	$O^{(9)}$	$Fe^{(1)}$	117.0(8)
$N^{(4)}$	$O^{(12)}$	$Fe^{(1)1}$	114.8(9)
$N^{(4)}$	$O^{(12)}$	$Fe^{(1)}$	122.7(10)

[1]1/2-X,3/2-Y,1-Z

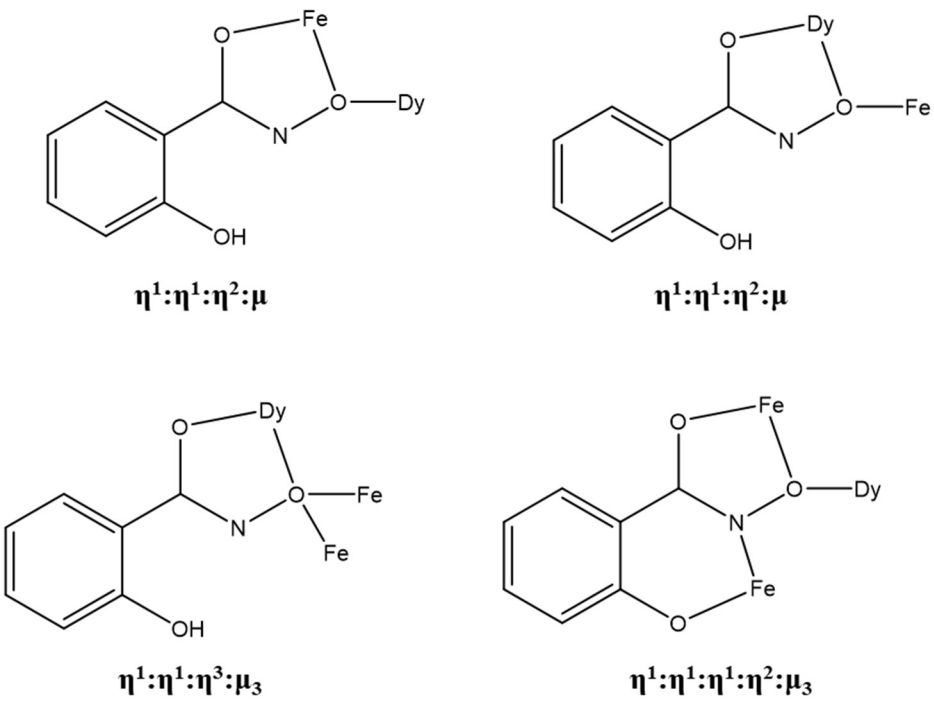

Scheme 4: Coordination modes of organic ligand in complex **6**.

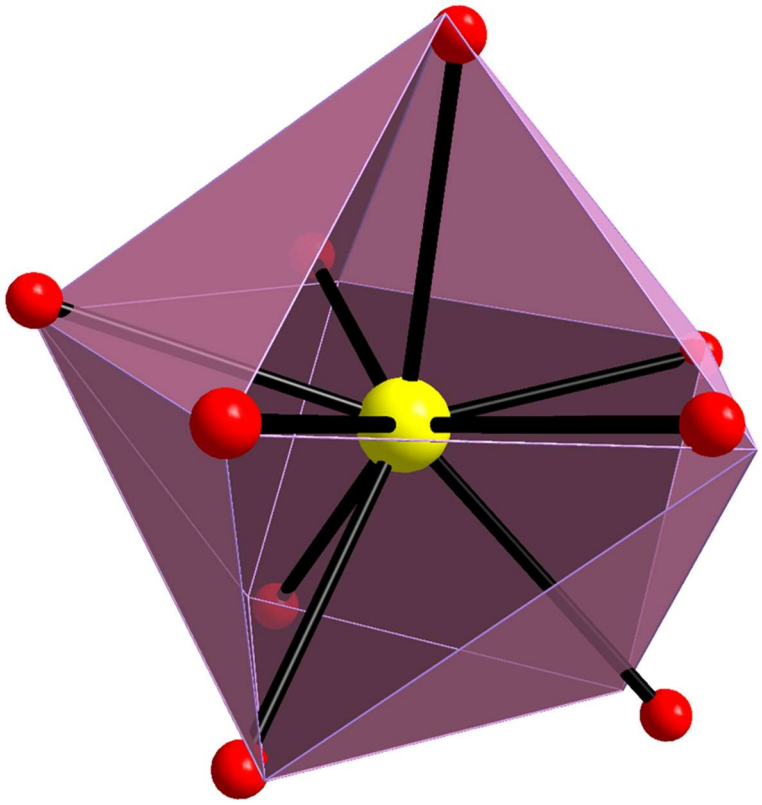

Figure S13: Muffin type geometry of central lanthanide in complex **6**. The points connected by the lighter lines define the vertices of the ideal polyhedron. Color scheme: Ln, yellow; O, red.

Table S21 Shape measurements of the 9-coordinate lanthanide coordination polyhedra. The bold numbers indicate the closest polyhedron according to SHAPE calculations.[3]

Polyhedron[c]	Dy1
EP-9	35.25
OPY-9	23.34
HBPY-9	16.93
JTC-9	14.75
JCCU-9	8.36
CCU-9	6.88
JCSAPR-9	2.20
CSAPR-9	1.73
JTCTPR-9	2.55
TCTPR-9	1.90
JTDIC-9	11.82
HH-9	10.77
MFF-9	**1.28**

[c] Abbreviations: EP-9, enneagon; OPY-9, Octagonal pyramid; HBPY-9, Heptagonal bipyramid; JTC-9, Johnson triangular cupola J3; JCCU-9, Capped cube J8; CCU-9, Spherical-relaxed capped cube; JCSAPR-9, Capped square antiprism J10; CSAPR-9, Spherical capped square antiprism; JTCTPR-9, Tricapped trigonal prism J51; TCTPR-9, Spherical tricapped trigonal prism; JTDIC-9, Tridiminished icosahedron J63; HH-9, Hula-hoop; MFF-9, Muffin.

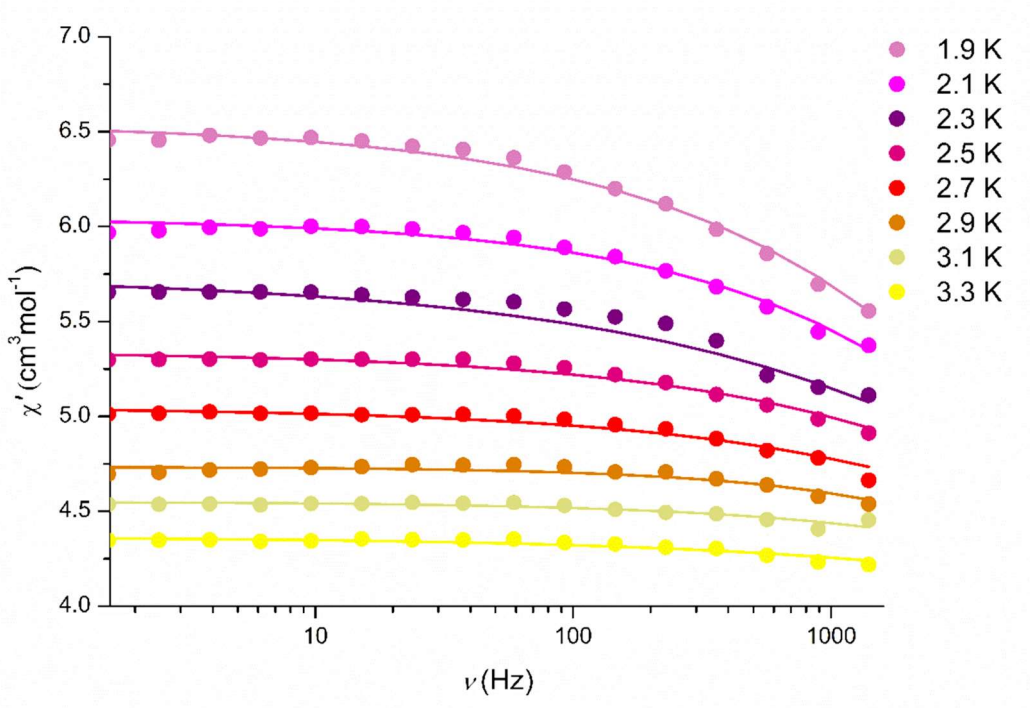

Figure S14: Frequency dependent in-phase susceptibility plot of for compound **6** (1.9 to 3.3 K) at zero field. Lines represent fitting of the data.

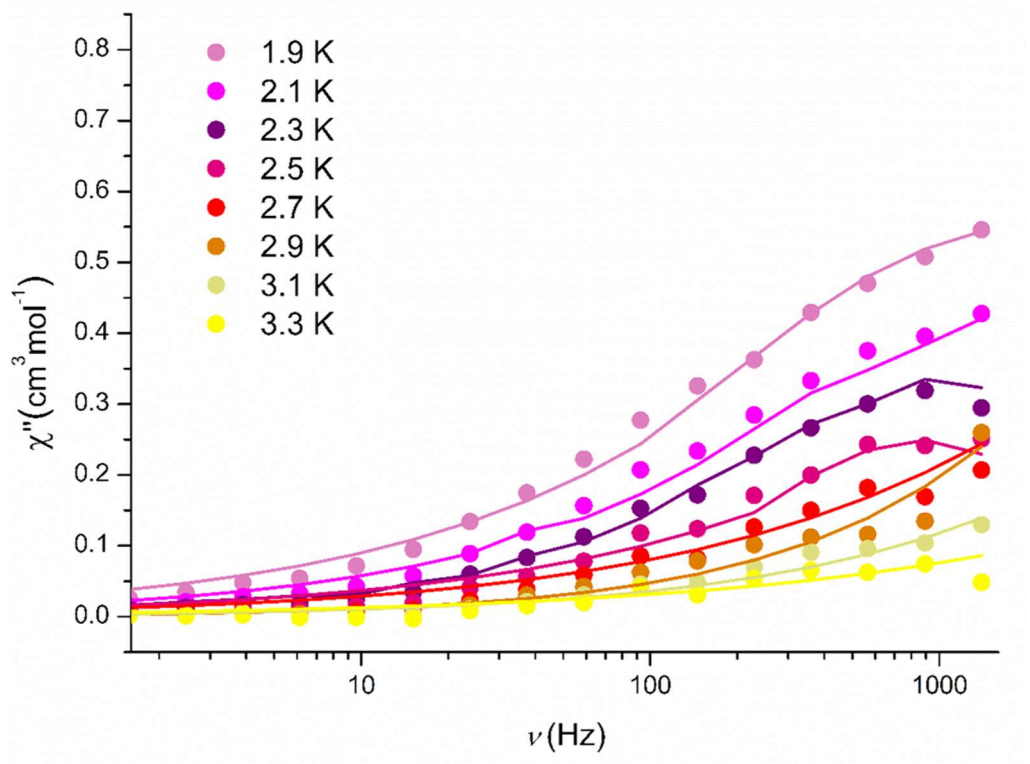

Figure S15: Frequency dependent out-of-phase susceptibility plot of for compound **6** (1.9 to 3.3 K) at zero field. Lines represent fitting of the data.

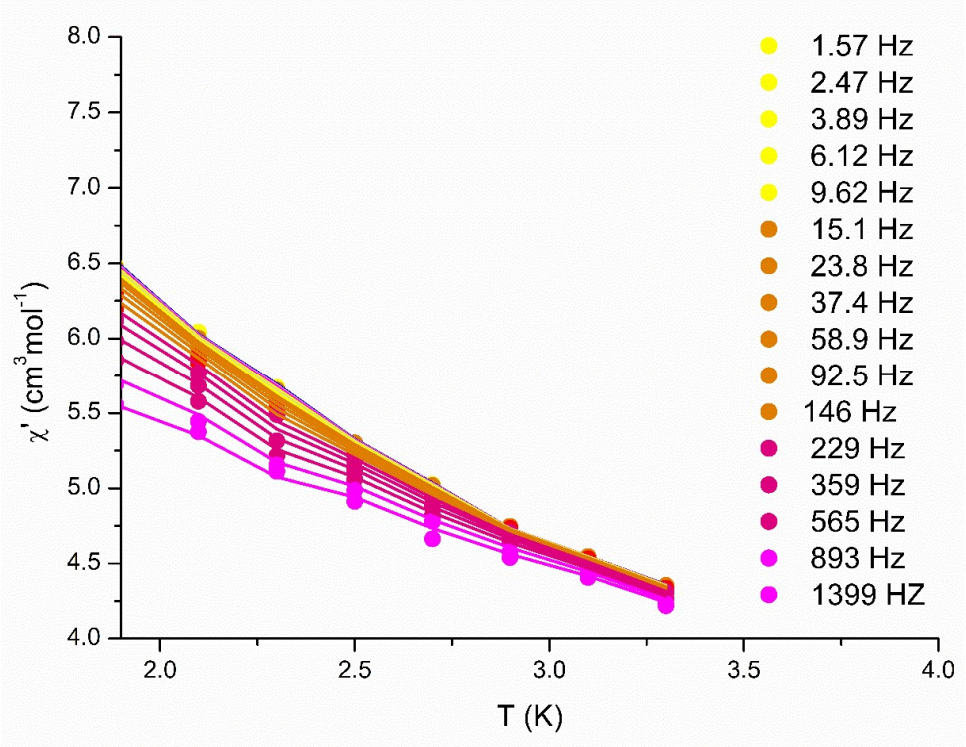

Figure S16: Temperature dependent in-phase susceptibility plot of for compound **6** (1.9 to 3.3 K) at 0 Oe.

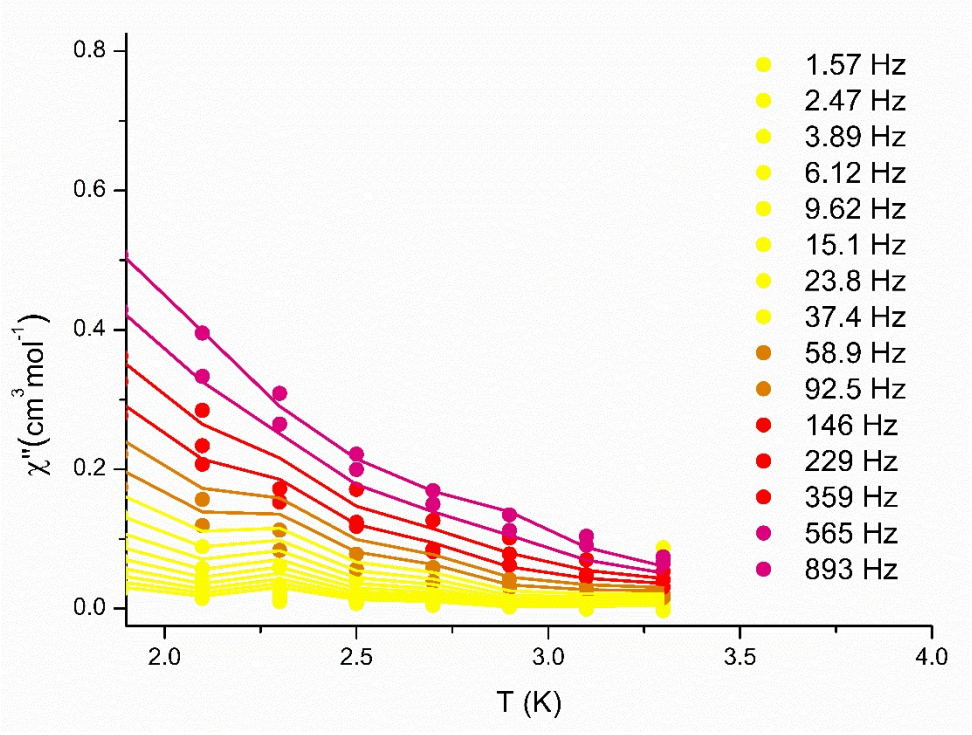

Figure S17: Temperature dependent out-of-phase susceptibility plot of for compound **6** (1.9 to 3.3 K) at 0 Oe.

IR Spectroscopy

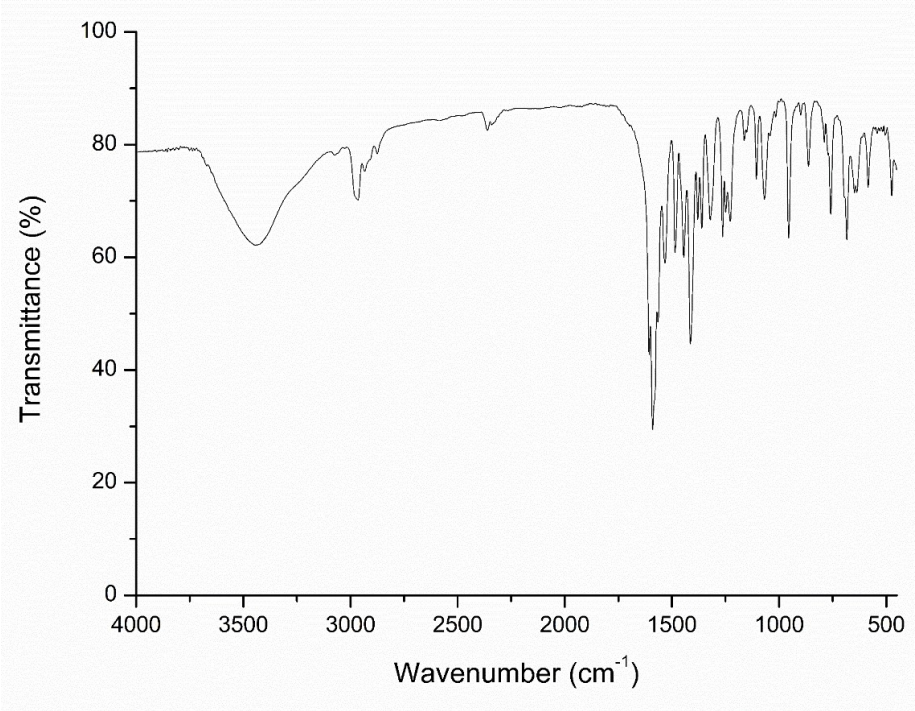

Figure S18: IR spectrum for complex **1**.

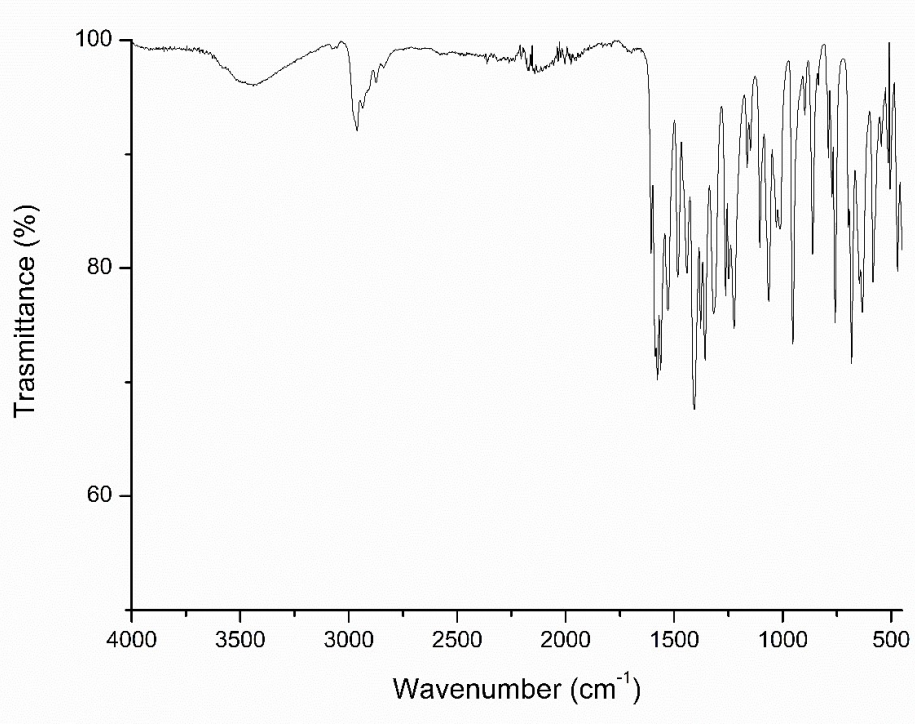

Figure S19: IR spectrum for complex **2**.

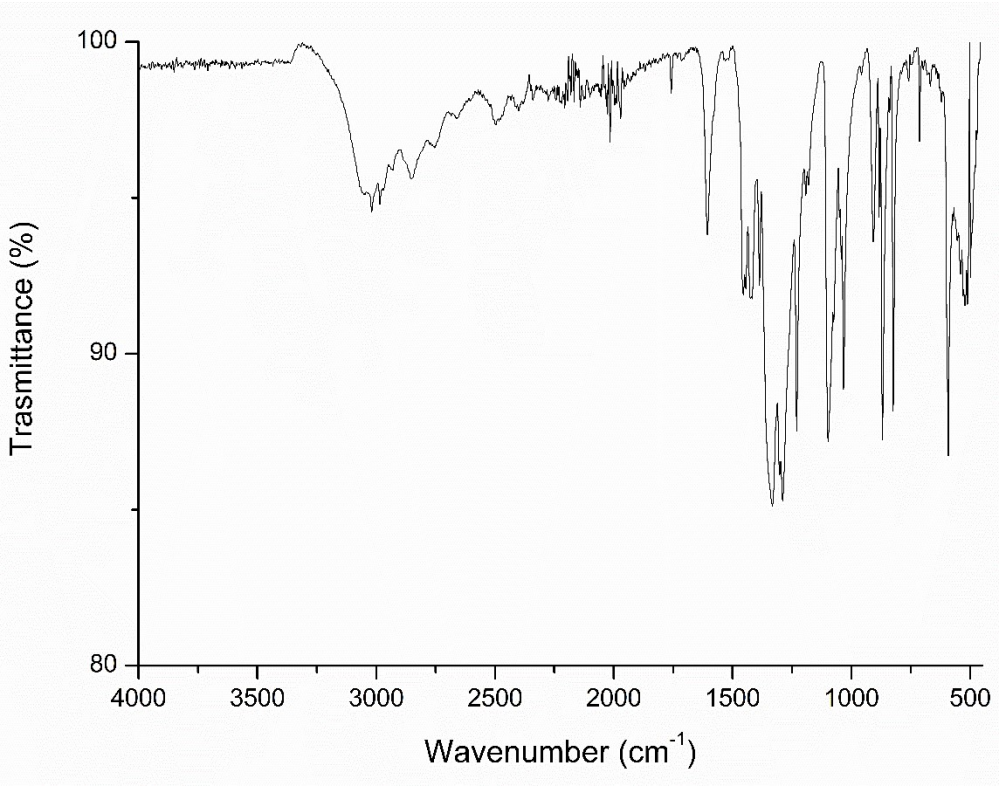

Figure S20: IR spectrum for complex **3**.

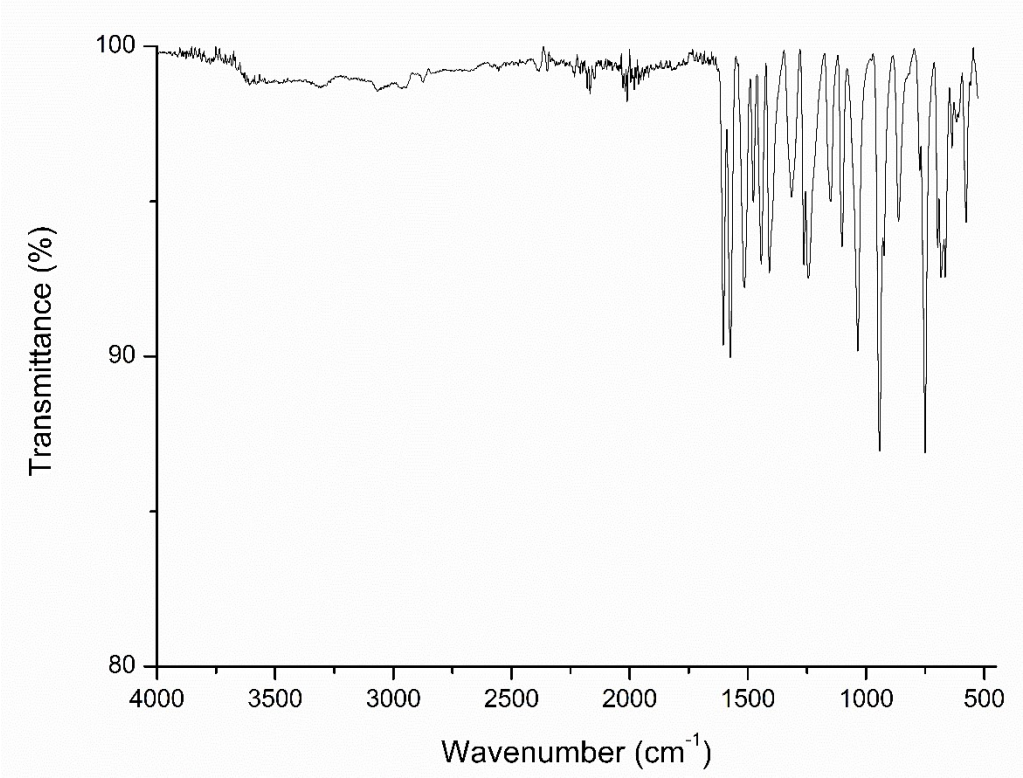

Figure S21: IR spectrum for complex **4**.

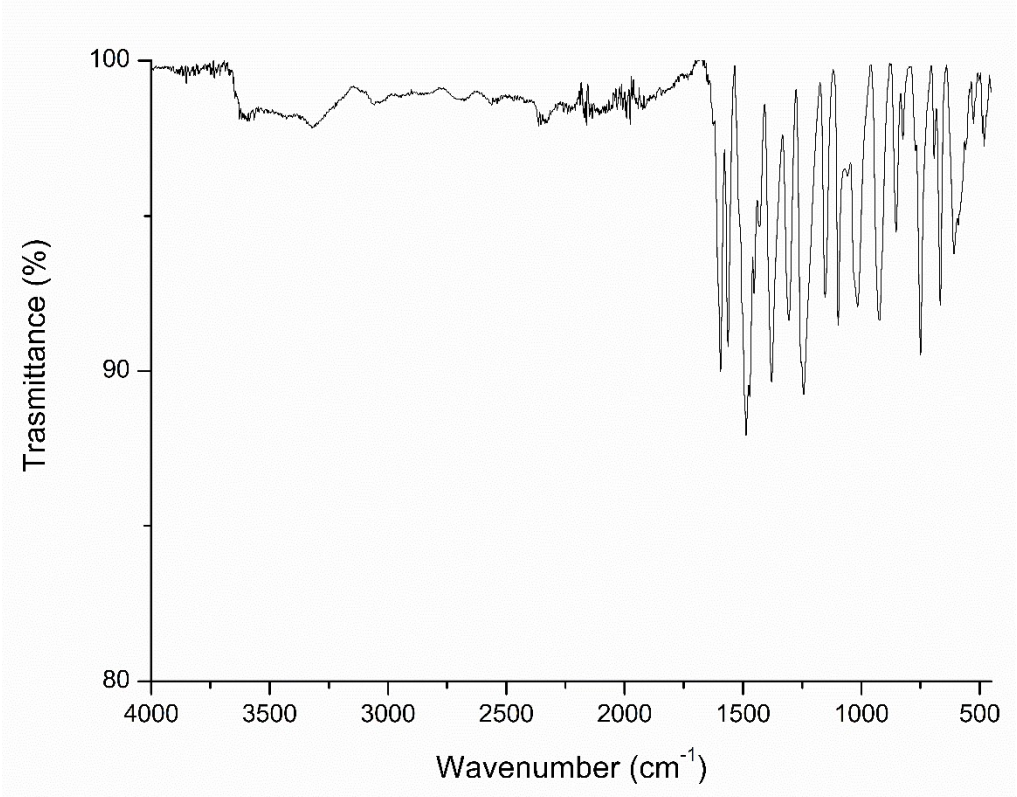

Figure S22: IR spectrum for complex **5**.

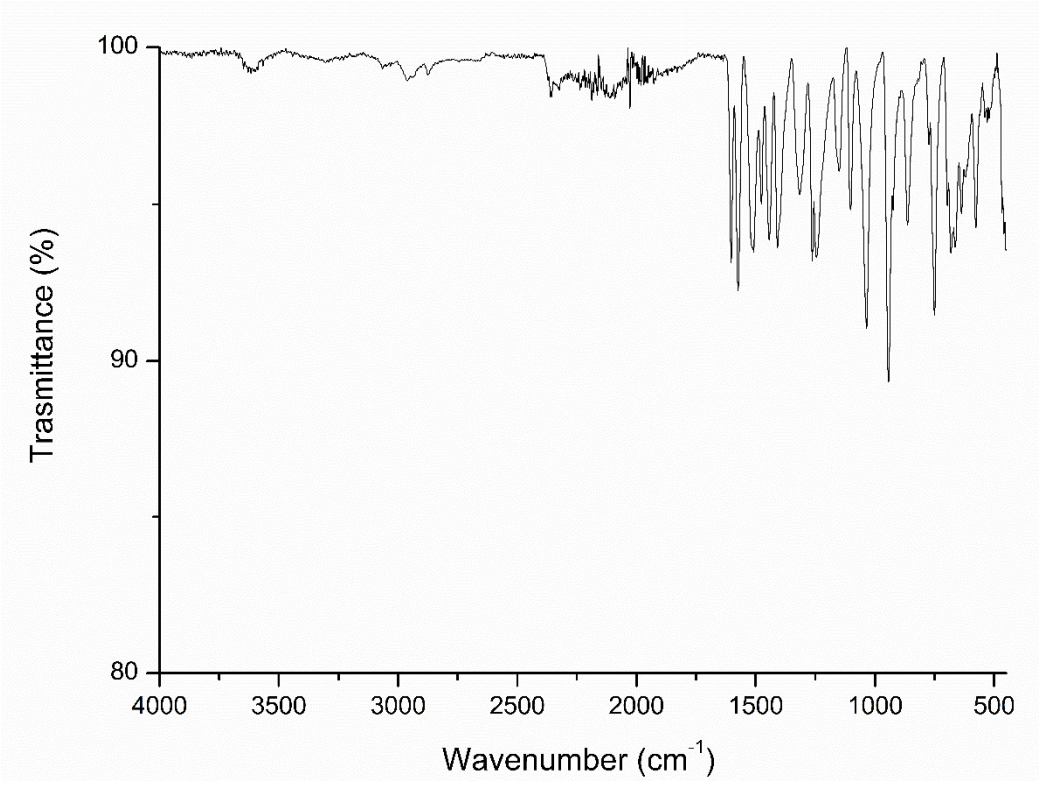

Figure S23*:* IR spectrum for complex **6**.

5.4 References

[1] A. W. Addison, T. N. Rao, J. Reedijk, J. van Rijn, G. C. Verschoor, *J. Chem. Soc., Dalton Trans.* **1984**, 1349–1356.

[2] T. N. Nguyen, C. Y. Chow, S. V. Eliseeva, E. R. Trivedi, J. W. Kampf, I. Martinić, S. Petoud, V. L. Pecoraro, *Chemistry - A European Journal* **2018**, *24*, 1031–1035.

[3] M. R. Azar, T. T. Boron, J. C. Lutter, C. I. Daly, K. A. Zegalia, R. Nimthong, G. M. Ferrence, M. Zeller, J. W. Kampf, V. L. Pecoraro, et al., *Inorganic Chemistry* **2014**, *53*, 1729–1742.

[4] D. P. Kessissoglou, J. J. Bodwin, J. Kampf, C. Dendrinou-Samara, V. L. Pecoraro, *Inorganica Chimica Acta* **2002**, *331*, 73–80.

[5] J. R. Travis, M. Zeller, C. M. Zaleski, *Polyhedron* **2016**, *114*, 29–36.

[6] W. Liu, H. H. Thorp, *Inorganic Chemistry* **1993**, *32*, 4102–4105.

[7] S. Alvarez, P. Alemany, D. Casanova, J. Cirera, M. Llunell, D. Avnir, *Coordination Chemistry Reviews* **2005**, *249*, 1693–1708.

[8] A. Ruiz-Martínez, D. Casanova, S. Alvarez, *Chemistry - A European Journal* **2008**, *14*, 1291–1303.

[9] C. Y. Chow, S. V. Eliseeva, E. R. Trivedi, T. N. Nguyen, J. W. Kampf, S. Petoud, V. L. Pecoraro, *Journal of the American Chemical Society* **2016**, *138*, 5100–5109.

[10] A. Athanasopoulou, L. Carrella, E. Rentschler, *Inorganics* **2018**, *6*, 66.

[11] J. Wu, J. Jung, P. Zhang, H. Zhang, J. Tang, B. Le Guennic, *Chemical Science* **2016**, *7*, 3632–3639.

[12] F. Habib, G. Brunet, V. Vieru, I. Korobkov, L. F. Chibotaru, M. Murugesu, *J. Am. Chem. Soc.* **2013**, *135*, 13242–13245.

[13] A. Watanabe, A. Yamashita, M. Nakano, T. Yamamura, T. Kajiwara, *Chem. Eur. J.* **2011**, *17*, 7428–7432.

[14] A. A. Athanasopoulou, L. M. Carrella, E. Rentschler, *Dalton Trans.* **2019**, *48*, 4779–4783.

[15] K. R. Vignesh, S. K. Langley, K. S. Murray, G. Rajaraman, *Inorganic Chemistry* **2017**, *56*, 2518–2532.

[16] A. Abragam, B. Bleaney, *Electron Paramagnetic Resonance of Transition Ions*, Oxford University Press, Oxford, **2012**.

[17] C. Benelli, D. Gatteschi, *Chemical Reviews* **2002**, *102*, 2369–2388.

[18] J. D. Rinehart, J. R. Long, *Chemical Science* **2011**, *2*, 2078.

[19] K. S. Cole, R. H. Cole, *The Journal of Chemical Physics* **1941**, *9*, 341–351.

[20] M. Grahl, J. Kötzler, I. Seßler, *Journal of Magnetism and Magnetic Materials* **1990**, *90–91*, 187–188.

[21] E. C. Mazarakioti, J. Regier, L. Cunha-Silva, W. Wernsdorfer, M. Pilkington, J. Tang, T. C. Stamatatos, *Inorganic Chemistry* **2017**, *56*, 3568–3578.

[22] P. King, T. C. Stamatatos, K. A. Abboud, G. Christou, *Angew. Chem. Int. Ed.* **2006**, *45*, 7379–7383.

[23] T. C. Stamatatos, S. Mukherjee, K. A. Abboud, G. Christou, *Chem. Commun.* **2009**, 62–64.

[24] C.-L. Yin, Z.-B. Hu, Q.-Q. Long, H.-S. Wang, J. Li, Y. Song, Z.-C. Zhang, Y.-Q. Zhang, Z.-Q. Pan, *Dalton Trans.* **2019**, *48*, 512–522.

[25] A. Mondal, V. Parmar, S. Konar, *Magnetochemistry* **2016**, *2*, 35.

[26] P. Antal, B. Drahoš, R. Herchel, Z. Trávníček, *Dalton Trans.* **2016**, *45*, 15114–15121.

[27] N. F. Chilton, R. P. Anderson, L. D. Turner, A. Soncini, K. S. Murray, *Journal of Computational Chemistry* **2013**, *34*, 1164–1175.

[28] M. Guo, Y. Xu, J. Wu, L. Zhao, J. Tang, *Dalton Trans.* **2017**, *46*, 8252–8258.

[29] T. Pugh, N. F. Chilton, R. A. Layfield, *Angew. Chem. Int. Ed.* **2016**, *55*, 11082–11085.

[30] Y.-N. Guo, G.-F. Xu, W. Wernsdorfer, L. Ungur, Y. Guo, J. Tang, H.-J. Zhang, L. F. Chibotaru, A. K. Powell, *J. Am. Chem. Soc.* **2011**, *133*, 11948–11951.

[31] J. Xiong, H.-Y. Ding, Y.-S. Meng, C. Gao, X.-J. Zhang, Z.-S. Meng, Y.-Q. Zhang, W. Shi, B.-W. Wang, S. Gao, *Chem. Sci.* **2017**, *8*, 1288–1294.

[32] R. Arratia-Pérez, L. Hernández-Acevedo, *Journal of Molecular Structure: THEOCHEM* **1993**, *282*, 131–141.

[33] G. A. Bain, J. F. Berry, *Journal of Chemical Education* **2008**, *85*, 532.

[34] **N.d.**

[35] G. M. Sheldrick, *Acta Crystallographica Section A Foundations and Advances* **2015**, *71*, 3–8.

[36] G. M. Sheldrick, *Acta Crystallographica Section C Structural Chemistry* **2015**, *71*, 3–8.

[37] O. V. Dolomanov, L. J. Bourhis, R. J. Gildea, J. A. K. Howard, H. Puschmann, *Journal of Applied Crystallography* **2009**, *42*, 339–341.

[38] A. L. Spek, *Acta Crystallographica Section D Biological Crystallography* **2009**, *65*, 148–155.

[39] A. L. Spek, *Journal of Applied Crystallography* **2003**, *36*, 7–13.

[40] A. L. Spek, *Acta Crystallographica Section C Structural Chemistry* **2015**, *71*, 9–18.